MEASUREMENT OF THE COSMIC RAY COMPOSITION WITH AIR SHOWERS DETECTED BY THE AMIGA EXTENSION AT THE PIERRE AUGER OBSERVATORY

Zur Erlangung des akademischen Grades eines
DOKTORS DER NATURWISSENSCHAFTEN
an der Fakultät für Physik des
Karlsruher Instituts für Technologie (KIT)
und der
Universidad Nacional de San Martín (UNSAM)

vorgelegte

DISSERTATION

von

DIPL.-PHYS. SARAH NICOLA MÜLLER

aus Seligenstadt

Tag der mündlichen Prüfung: 30. November 2018

Referent	Prof. Dr. Dr. h.c. Johannes Blümer
Koreferent	Prof. Dr. Alberto Etchegoyen
Betreuer	Dr. Markus Roth
	Dr. Federico Sanchez

MEASUREMENT OF THE COSMIC RAY COMPOSITION WITH AIR SHOWERS DETECTED BY THE AMIGA EXTENSION AT THE PIERRE AUGER OBSERVATORY

TESIS

presentada para optar por el título de

DOCTORA EN ASTROFÍSICA

del Instituto de Tecnología "Prof. Jorge A. Sábato" de la
Universidad Nacional de San Martín (UNSAM)
y del
Karlsruher Institut für Technologie (KIT)

por

DIPL.-PHYS. SARAH NICOLA MÜLLER

Fecha de la defensa oral: 30 de Noviembre 2018

Director	Prof. Dr. Dr. h.c. Johannes Blümer
Co-director	Prof. Dr. Alberto Etchegoyen
Collaborador	Dr. Markus Roth
	Dr. Federico Sanchez

ABSTRACT

The questions of the origin, acceleration, and propagation of ultra-high energy cosmic rays have still not been settled. To discriminate between astrophysical scenarios, a precise measurement of the mass composition in the transition region of galactic to extragalactic cosmic rays up to the highest energies is of key importance.

A crucial observable for the differentiation of mass groups of cosmic rays is the number of muons in extensive air showers. The Pierre Auger Observatory is therefore currently being upgraded with new detectors which will allow to measure the muonic shower component on an event-by-event basis. As part of the upgrade, the AMIGA extension, consisting of buried segmented scintillation counters, will provide the possibility of direct muon density measurements. Additionally, it will be used to validate the indirect muon measurements of the main upgrade detectors.

To define the specifics of the now deployed upgrade detectors, we study the impact of the energy detection threshold of muons on the mass separability of primary cosmic rays with detector-independent simulations. We find that, although the number of detected muons decreases, the mass separability increases for detection thresholds of few GeV. A good composition-sensitivity is, however, only achieved for large muon detection areas, or if the depth of shower maximum can be additionally inferred from the measurements. Considering these results, Auger has decided to deploy scintillators with an area of $3.8\,\mathrm{m}^2$ on top of the existing water-Cherenkov detectors.

In order to guarantee an unbiased estimate of the muon density based on the measurements of the AMIGA muon counters, we optimize and extend the existing reconstruction procedure. In this context, we develop a geometrical correction for muons leaving

a signal in multiple detector strips due to their inclined momentum. Furthermore, we derive a new unbiased parametrization of the muon lateral distribution function and ascertain that the optimum distance for its evaluation remains unchanged.

The engineering array for AMIGA, consisting of a hexagon of seven muon detectors of $30\,\mathrm{m}^2$ area each, has been operational since February 2015. We select a sample of one year of calibrated data taken with the engineering array, and, to ensure a high quality of the data set, develop a bad period rejection for AMIGA, exclude faulty detector modules, and correct for the area-dependent module efficiencies. Parametrizing the attenuation of the muonic signal due to the atmosphere and soil layer above the buried muon detectors for both simulations and data, we derive a zenith-independent estimator ρ_{35} of the muon density.

The main systematic uncertainties for AMIGA arise from the module area-dependent efficiency correction, the setting of the discriminator thresholds of the individual scintillator channels, the soil density, the parametrization of the muon lateral distribution function, and the attenuation correction. We estimate the individual contributions and obtain a total systematic uncertainty of about 14% of ρ_{35}.

A "muon excess" in data has been observed by multiple experiments. Our results for AMIGA confirm this disagreement of the muon content between simulations and data at somewhat different energies. Using Auger measurements of the depth of shower maximum as proxy for the mean logarithmic mass in data, we find that, depending on the hadronic interaction model, the muon content in simulations would need to be increased by 38% to 53% to match the AMIGA results.

We analyze the evolution of the mass composition based on the muon density measurements of the AMIGA engineering array by fitting the corrected muon densities ρ_{35} with a power law parametrization as a function of energy. Additionally, we compute the energy-dependent mean logarithmic mass. In agreement with previous Auger measurements of the depth of shower max-

imum, the results indicate a lightening of the mass composition in the energy range from $10^{17.4}$ eV to $10^{18.3}$ eV.

AMIGA will be fully completed at the end of 2019 and record data until 2025. Although the final detector design will be slightly changed compared to the engineering array by replacing photomultiplier tubes by silicon photomultipliers, most of the reconstruction improvements developed in this thesis are applicable. The presented first systematic analysis of data from the engineering array shows that AMIGA is on its way to perform composition measurements that will help to constrain astrophysical models of the origin and propagation of ultra-high energy cosmic rays.

ZUSAMMENFASSUNG

Die Fragen nach dem Ursprung, der Beschleunigung und der Propagation kosmischer Strahlung bei extrem hohen Energien sind noch immer nicht beantwortet. Um verschiedene astrophysikalische Szenarien zu unterscheiden, ist eine präzise Messung der Massenzusammensetzung der kosmischen Strahlung in der Übergangsregion zwischen galaktischer und extragalaktischer kosmischer Strahlung bis zu den höchsten Energien von größter Bedeutung.

Die Anzahl von Myonen in ausgedehnten Luftschauern ist eine wichtige Observable um verschiedene Massengruppen der kosmischen Strahlung zu unterscheiden. Aus diesem Grund wird das Pierre-Auger-Observatorium derzeit mit neuen Detektoren erweitert, die es erlauben werden, die myonische Schauerkomponente auf einer Ereignis-zu-Ereignis-Basis zu messen. Als Teil dieses Upgrades wird die AMIGA-Erweiterung, bestehend aus vergrabenen segmentierten Szintillationszählern, direkte Myondichtemessungen ermöglichen. Außerdem wird sie dazu dienen, die indirekten Myonmessungen der Upgradedetektoren zu validieren.

Um die Spezifikationen der mittlerweile installierten Upgradedetektoren zu definieren, untersuchen wir den Einfluss des Myonenergiedetektionsschwellwerts auf die Unterscheidbarkeit der Massen von Primärteilchen der kosmischen Strahlung mit detektorunabhängigen Simulationen. Wir stellen fest, dass die Massenunterscheidbarkeit für Detektionsschwellwerte von einigen GeV wächst, obwohl die Anzahl der detektierten Myonen abnimmt. Eine gute Kompositionssensitivität wird jedoch nur für große Detektionsflächen erreicht oder wenn die Tiefe des Schauermaximums zusätzlich aus den Messungen abgeleitet werden kann. Diese Ergebnisse berücksichtigend hat Auger entschieden,

Szintillatoren mit einer Fläche von $3.8\,\mathrm{m}^2$ auf den bereits existieren Wasser-Cherenkov-Detektoren anzubringen.

Um eine auf den Messungen der AMIGA Myonzählern basierende unverzerrte Schätzung der Myondichte zu gewährleisten, optimieren und erweitern wir die bestehende Rekonstruktionsmethode. In diesem Zusammenhang entwickeln wir ein geometrisches Korrekturverfahren für Myonen, die aufgrund ihres schrägen Einfalls ein Signal in mehreren Detektorstreifen hinterlassen. Außerdem schlagen wir eine neue unverzerrte Parametrisierung der lateralen Dichtefunktion der Myonen vor und stellen sicher, dass der optimale Abstand für ihre Auswertung unverändert bleibt.

Das Prototyparray für AMIGA, bestehend aus einem Hexagon aus sieben Myondetektoren, ist seit Februar 2015 in Betrieb. Wir wählen die kalibrierten Daten eines Jahres aus und entwickeln eine Methode um Perioden auszuschließen, während derer bestimmte AMIGA-Module nicht funktionsfähig waren, um eine hohe Qualität der Daten zu gewährleisten. Zudem schließen wir fehlerhafte Module aus und korrigieren für die flächenabhängigen Effizienzen der Detektormodule. Weiterhin definieren wir einen zenithwinkelunabhängigen Schätzer ρ_{35} der Myondichte, indem wir die Abschwächung des Myonsignals durch die Atmosphäre und die Erdschicht oberhalb der vergrabenen Myondetektoren parametrisieren.

Die grössten systematischen Unsicherheiten für AMIGA entstehen durch die modulflächenspezifische Effizienzkorrektur, das Setzen des Diskriminatorschwellwerts der einzelnen Szintillatorkanäle, die Dichte des Bodens, die Parametrisierung der lateralen Dichtefunktion der Myonen und die Abschwächungskorrektur. Wir schätzen die einzelnen Beiträge ab und erhalten eine systematische Gesamtunsicherheit von ungefähr 14% von ρ_{35}.

Mehrere Experimente haben einen "Myonüberschuss" in ihren Daten beobachtet. Unsere Analyse von AMIGA-Daten bestätigt diesen Unterschied im Myonanteil zwischen Simulationen und Daten bei etwas anderen Energien. Indem wir X_{max}-Messungen von Auger als Schätzer der mittleren logarithmischen Masse

in Daten verwenden finden wir, dass der Myonanteil in Simulationen um 38% bis 53%, abhängig vom hadronischen Wechselwirkungsmodell, erhöht werden müsste um mit den AMIGA-Ergebnissen übereinzustimmen.

Basierend auf den Myondichtemessungen des AMIGA Prototyparrays analysieren wir die Entwicklung der Massenkomposition indem wir die korrigierten Myondichten ρ_{35} mit einer Potenzgesetzparametrisierung als Funktion der Energie fitten. Zusätzlich berechnen wir die energieabhägige mittlere logarithmische Masse. In Übereinstimmung mit vorherigen X_{max}-Messungen des Pierre-Auger-Observatoriums weisen die Ergebnisse auf ein Leichterwerden der Massenkomposition im Energiebereich von $10^{17.4}$ eV bis $10^{18.3}$ eV hin.

AMIGA wird Ende 2019 vervollständigt sein und bis 2025 Daten nehmen. Obwohl das endgültige Detektordesign im Vergleich zum Prototyparray leicht verändert sein wird, da die Photomultiplier durch Silicon-Photomultiplier ersetzt werden, sind die meisten der in dieser Arbeit entwickelten Verbesserungen der Rekonstruktion anwendbar. Die vorgestellte erste systematische Analyse von Daten des AMIGA Prototyparrays zeigt, dass AMIGA auf dem Weg ist Kompositionsmessungen durchzuführen, die dabei helfen werden astrophysikalische Modelle des Ursprungs und der Propagation ultra-hochenergetischer kosmischer Strahlung einzuschränken.

RESUMEN

Los detalles del origen, la aceleración y la propagación de los rayos cósmicos de alta energía aún no han sido resueltos. Para discriminar entre diferentes escenarios astrofísicos es de vital importancia la medición precisa de la composición química de los rayos cósmicos desde la región de la transición de fuentes galácticas a extragalácticas hasta las energías más altas.

El número de muones en las lluvias extendidas de partículas secundarias es un observable crucial para discernir entre grupos de rayos cósmicos con diferentes masas. Por esta razón, el Observatorio Pierre Auger está siendo mejorado mediante la instalación de nuevos detectores que permitirán medir la componente muónica de la lluvia evento por evento. Como parte de esta actualización, la extensión denominada AMIGA, consistente en contadores de centelleo segmentados subterráneos, proporcionará una medición directa de la densidad de muones. Además, se utilizará para validar las mediciones indirectas de muones obtenidas con los principales detectores de la actualización.

Para definir las características específicas de los detectores de la actualización ya instalados, estudiamos el impacto del umbral de detección de energía de los muones en la separabilidad de los rayos cósmicos primarios de masas diferentes con simulaciones independientes del detector. Usando sólo el número de muones como observable sensible a la composición, encontramos que la capacidad de discriminación aumenta considerando umbrales de detección de pocos GeV a pesar que el número de muones detectados disminuye. Sin embargo, una buena sensibilidad a la composición sólo se consigue para grandes áreas de detección de muones, o si la profundidad atmosférica del máximo de la lluvia puede inferirse adicionalmente de las mediciones. Considerando estos resultados, Auger decidió desplegar centelladores con un

área de $3.8\,\mathrm{m}^2$ en la parte superior de los detectores Cherenkov ya existentes.

Con el fin de garantizar una estimación no sesgada de la densidad de muones basada en las medidas de los contadores de AMIGA, optimizamos y ampliamos el proceso de reconstrucción. En este contexto, desarrollamos una corrección geométrica para aquellos muones con incidencia inclinada que impactan en más de una barra del detector. Además, derivamos una nueva parametrización no sesgada de la distribución lateral de muones y nos aseguramos de que la distancia óptima para su evaluación permaneciera constante.

El arreglo prototipo del sistema de detección de muones de AMIGA, consistente de siete detectores de muones de $30\,\mathrm{m}^2$ desplegados en un hexágono, está en funcionamiento desde febrero de 2015. Seleccionamos una muestra de un año de datos calibrados tomados con el arreglo prototipo y, para garantizar una alta calidad del conjunto de datos, desarrollamos un método para rechazar períodos durante los cuales ciertos módulos presentaban signos de mal funcionamiento, excluimos módulos defectuosos y corregimos por las eficiencias dependiente de su área. Parametrizando para simulaciones y datos la atenuación de la señal muónica debida a la atmósfera y a la capa de suelo sobre los detectores de muones enterrados, obtuvimos un estimador de la densidad de muones ρ_{35} independiente del ángulo cenital.

Las incertezas sistemáticas principales por AMIGA surgen de la correción de eficiencia dependiente del área del modulo de detector, la configuración de los umbrales de discriminación de los canales individuales de los centelladores, la densidad del suelo, la parametrización de la distribución lateral de muones y la corrección por atenuación. Estimamos las contribuciones individuales y obtenemos una incertidumbre sistemática total de alrededor de 14 % de ρ_{35}.

Un "exceso de muones" en los datos ha sido observado por varios experimentos. Nuestros resultados con los datos de AMIGA confirman este desacuerdo del contenido de muones entre las

simulaciones y los datos a las energías bajo estudio. Usando las mediciones del Observatorio Auger la profundidad atmosférica del máximo de la lluvia como estimador de la masa logarítmica media en los datos, encontramos que, dependiendo del modelo de interacción hadrónica, el contenido de muones en las simulaciones tendría que ser incrementado en un 38 % a un 53 % para que coincida con los mediciones de AMIGA.

Analizamos la evolución de la composición primaria en base a las mediciones de las densidades de muones medidas por el arreglo prototipo de AMIGA, ajustando las densidades de muones corregidas ρ_{35} con una parametrización tipo ley de potencia en función de la energía. Además, computamos la masa media logarítmica dependiente de la energía. De acuerdo con las mediciones previas de la profundidad atmosférica del máximo de la lluvia del Observatorio Pierre Auger, los resultados indican una tendencia hacia composición liviana de los núcleos en el rango de energía de $10^{17.4}$ eV a $10^{18.3}$ eV.

AMIGA estará completamente terminado a finales de 2019 y registrará datos hasta 2025. Aunque el diseño final del detector se modificará ligeramente en comparación con el arreglo prototipo, reemplazando sus tubos fotomultiplicadores por fotomultiplicadores de silicio, la mayoría de las mejoras de reconstrucción desarrolladas en esta tesis son aplicables. El primer análisis sistemático de los datos del arreglo prototipo presentado muestra que AMIGA está en camino para realizar mediciones de composición que ayudarán a restringir los modelos astrofísicos del origen y de la propagación de los rayos cósmicos de alta energía.

ACKNOWLEDGMENTS

I would like to thank my supervisors Markus Roth and Federico Sanchez for their guidance, valuable advise, and many fruitful discussions during my PhD. I would also like to thank Prof. Johannes Blümer and Prof. Alberto Etchegoyen for reviewing my thesis and especially for giving me the opportunity to take part in the Double Doctoral degree in Astrophysics program between the Karlsruhe Institute of Technology and the Universidad Nacional de San Martín in Buenos Aires.

Within the DDAp, I had the opportunity to work on-site with the experts on the AMIGA muon detectors which greatly facilitated our scientific discourse. My two stays in Argentina also gave me the chance to get to know the language and culture of this wonderful country. For their warm welcome at the ITeDA institute in Buenos Aires and our cross-atlantic friendship, I would like to thank especially Nico, Ana, Belén, Matías, Johan, Federico, Diego, Juan, and Brian.

For the establishment of the DDAp program and their support in all kind of organizational issues I would further like to thank Frank Schröder, Marie-Christine Mundt, and the helpful staff at ITeDA.

Furthermore, I would like to thank my colleagues Daniela, Ariel, Alex, David, Darko, Tanguy, Nico, Ana, Diego, Juan, and Brian from both IKP and ITeDA for their support and many valuable discussions. For proof-reading my thesis and correcting my Spanish abstract I would like to thank Markus, Ewa, Nico, David, Belén, Ana-Laura, Ana, Isabel, and Alvaro.

In particular, I want to thank my parents for their steady support – most recently by providing an "all-inclusive" hotel service with child care in the stressful last weeks of finalizing my thesis. Above all, I would like to thank Hannes for not only helping

me with any technical issue and for proof-reading my thesis, but mainly for his steady nerves and his enduring commitment to juggle his job, my PhD thesis, and our new-born son Lars in these busy last months. Last but not least, I would like to thank Lars for being such a lovely little person and reminding me about the really important things in life.

CONTENTS

1 INTRODUCTION 1
1.1 Key contributions 6
1.2 Publications 7

2 COSMIC RAYS 9
2.1 Sources and propagation 10
2.2 Energy spectrum 19
2.3 Extensive air showers 28
2.4 Mass composition 33

3 THE PIERRE AUGER OBSERVATORY 43
3.1 Surface detector 43
3.2 Fluorescence detector 51
3.3 AugerPrime upgrade 54
3.4 AMIGA muon detector 56

4 IMPACT OF MUON DETECTION THRESHOLDS 71
4.1 Simulations and methods 72
4.2 $N_\mu - X_{\max}$ correlation dependence 75
4.3 Impact of statistical fluctuations 81
4.4 Geometrical interpretation 82
4.5 Effect of interaction models, energies, and zenith angles 86
4.6 Photonuclear interactions 91
4.7 Implications for the Auger upgrade 96

5 MD RECONSTRUCTION OPTIMIZATION 97
5.1 Simulation libraries 98
5.2 Muon counting strategy 104
5.3 Pile-up correction 107
5.4 Study of the inhibition window size 111
5.5 Corner-clipping correction 118

5.6 Muon lateral density function 130
5.7 Optimal distance 152
5.8 Composition sensitivity 159

6 DATA SELECTION AND SYSTEMATICS 169
6.1 Data selection and quality cuts 169
6.2 Bad period rejection 170
6.3 Module efficiency 176
6.4 Lateral trigger probability 182
6.5 Attenuation correction 191
6.6 Systematic uncertainties 212

7 ANALYSIS OF THE MEASURED MUON DENSITIES 227
7.1 Energy dependence of the muon density 228
7.2 Comparison with simulations 235
7.3 Muon content disagreement in simulations and data . 243
7.4 Mean logarithmic mass 250
7.5 Comparison with other muon measurements 252

8 CONCLUSION 273

ACRONYMS 281

BIBLIOGRAPHY 285

1

INTRODUCTION

Each second, the earth's atmosphere is hit by about ten thousand particles per square meter. Around 90% of these *cosmic rays (CRs)* arriving from space are protons, the rest are heavier ionized nuclei. Their energies cover a huge range from less than a GeV to more than 10^{20} eV, three orders of magnitude above the energies that can currently be reached with the Large Hadron Collider. There is good evidence that CRs up to energies of about 10^{17} eV stem from within our galaxy and are accelerated in supernova remnants. However, the situation is less clear for higher energies. While it is generally believed that ultra-high energy cosmic rays originate from outside our galaxy, their sources are still unknown and it is an open question at which energies the transition to extragalactic CRs takes place. Since theoretical models make distinct predictions of the elemental composition of CRs at the highest energies, precise composition measurements are needed to provide answers. In this thesis, we demonstrate the capability of composition analyses with the Auger Muons and Infill for the Ground Array (AMIGA), which will be installed as part of the current upgrade of the Pierre Auger Observatory, by analyzing one year of data taken by the AMIGA engineering array.

Up to energies of 10^{14} eV per particle, the flux and elemental composition of primary CRs has been measured by various balloon and satellite experiments. The energy spectra of different nuclei can be commonly described as a function of their rigidity ($\propto$ energy/charge) as expected for rigidity-dependent acceleration or propagation mechanisms. Since the CR flux decreases as a function of the energy according to a steeply falling power law $J(E) \propto E^{-2.7}$, direct detection of primary CRs is, however, unfeasible for energies above about 10^{14} eV. Instead, large air shower

arrays on the surface of the earth with areas up to thousands of square kilometers and exposure times of years have been built. They measure the secondary particles which are produced in a cascade of interactions following the initial interaction of the primary cosmic ray particle with a nucleus in the atmosphere. The detection of such extensive air showers (EASs), however, only yields indirect and limited information about the incident primary particle.

Important results on the origin of CRs with energies below 10^{17} eV have been obtained by the KArlsruhe Shower Core and Array DEtector (KASCADE) and KASCADE-Grande experiments. Measuring the electromagnetic and muonic shower components simultaneously, they established that the steepening of the CR all-particle flux at energies $2 - 5 \times 10^{15}$ eV, the so-called *knee*, corresponds to a drop-out of light elements while the *second knee* at 8×10^{16} eV is related to a decrease of the flux of heavy elements. These observations agree well with the expected rigidity-dependent drop-out of elements for particles that are accelerated by diffuse shock acceleration in galactic supernova remnants.

At $E \approx 10^{18.6}$ eV, a flattening of the flux has been observed by several air shower experiments. Two main classes of models exist to explain this *ankle* feature. The so-called *dip models* predict that extragalactic protons are already dominant below the ankle, but suppressed due to positron-electron pair production with photons from the cosmic microwave background. In contrast, *mixed-composition models* interpret the ankle as a result of the transition from galactic to extragalactic CRs at this energy. Additionally, different scenarios, as for instance the one of Unger et al. [1], which explains the observed spectral features by photo-disintegration effects in the source environment, have been proposed. Since these models differ in their predictions of the elemental composition, a precise measurement of the CR mass composition is of crucial importance to decide between theoretical scenarios and to elucidate the origin of the flux suppression at energies above 4×10^{19} eV.

In the energy region of the ankle and above, the Pierre Auger Observatory and the Telescope Array are the two leading air shower experiments. The Pierre Auger Observatory consists of a $3000\,\mathrm{km}^2$ grid of WCDs to measure the secondary particles that are produced in an EAS. Additionally, during clear moonless nights, fluorescence telescopes measure the fluorescence light that is generated in the atmosphere. From the longitudinal profile of the shower development, the atmospheric depth of maximum shower development X_{max}, where the number of produced particles reaches the maximum, can be inferred. Employing $\langle X_{\mathrm{max}} \rangle$ and $\sigma(X_{\mathrm{max}})$ as composition-sensitive observables, results indicating a lightening of the composition in the energy range between $10^{17.2}\,\mathrm{eV}$ and $10^{18.33}\,\mathrm{eV}$, followed by a development towards again heavier elements up to $10^{19.6}\,\mathrm{eV}$, have been obtained by the Pierre Auger Observatory.

However, due to the low duty cycle of $\sim$15% of the fluorescence telescopes, the number of events with X_{max} information is very small at the highest energies. The Pierre Auger Observatory is currently being upgraded to extend the mass composition sensitivity up to the flux suppression region. As a consequence of the higher muon content of EASs initiated by heavy nuclei, the number of muons that are produced in an EAS is a further mass sensitive parameter. The installation of scintillators on top of each WCD will enable the disentangling of the electromagnetic and muonic signal components by a combined analysis of the detector signals. In addition, 61 scintillation detectors with an area of $30\,\mathrm{m}^2$ each will be buried at a depth of 2.3 m next to the WCDs on the 750 m grid of the array. The AMIGA extension, instrumenting a total area of $23.5\,\mathrm{km}^2$, will provide the possibility of direct muon density measurements for energies above $10^{17.5}\,\mathrm{eV}$ and will further serve as a cross-check for the more indirect scintillator-based measurements.

In this thesis, we study the impact of the energy detection threshold of muons on the mass separability of primary cosmic rays with detector-independent CORSIKA simulations. The

outcome of the analysis has been ultimately used to define the specifics of the now deployed upgrade detectors. We show that the composition sensitivity, based on muon measurements only, is enhanced for increasing thresholds up to few GeV. However, a good separability of primary cosmic rays is only achieved for large detection areas, or if the depth of shower maximum, as a second mass-sensitive observable, can be inferred from the measurements.

In order to ensure unbiased and zenith-independent estimates of the muon densities, based on the measurements of the AMIGA muon counters, we optimize and extend the existing reconstruction procedure. Analyzing one year of calibrated data of the AMIGA engineering array, consisting of a hexagon of seven muon detectors of $30\,\mathrm{m}^2$ area each, we find that the muon content in simulations would need to be increased by 38% to 53%, depending on the hadronic interaction model, to match the AMIGA measurements. The energy evolution of the measured muon densities and the inferred mean logarithmic masses hint at a slight lightening of the composition in the energy range from $10^{17.4}\,\mathrm{eV}$ to $10^{18.3}\,\mathrm{eV}$ in agreement with X_{max} measurements of the Pierre Auger Observatory.

The thesis is structured as follows. In Chapter 2, we give a short introduction to the topic of CRs. After discussing astrophysical source, acceleration, and propagation scenarios, we describe the observed energy spectrum of CRs and possible interpretations of its features. Furthermore, we review recent measurements of the CR mass composition and their implications for models of the transition from galactic to extragalactic CRs and up to the highest energies.

We proceed with the presentation of the Pierre Auger Observatory in Chapter 3, starting with a description of the surface detector and the fluorescence detector. Subsequently, we discuss further extensions and the planned upgrade of the observatory. We describe the AMIGA extension in detail, including the detector layout, mechanical design, electronics, and event acquisition and

give a short outlook on the silicon photomultiplier and electronics upgrade.

In Chapter 4, we present the simulation study of the impact of the detection threshold of muons on the separation quality of primary cosmic rays in the energy region of the ankle. To explain the observed dependence of the separability of primaries on the detection threshold of muons, we analyze the correlation of the number of muons with the shower maximum as a function of the muon energy. Beyond the interpretation as a result of the underlying hadronic interactions and the shower geometry, we investigate the role of muons produced in a shower by photon-air interactions.

In Chapter 5, we turn to the AMIGA muon detectors and review the reconstruction procedure to derive the muon density ρ_{450} at the optimum core distance as an estimator of the muon content of EASs. Then, we present our improvements to avoid biases of ρ_{450}. In a first step, we determine the optimal length of the inhibition window in the muon counting strategy. Second, we introduce a geometrical correction procedure to correct for the bias that is induced by "corner-clipping muons" hitting multiple detector strips due to their inclined momentum. Furthermore, we derive a new unbiased parametrization of the muon lateral distribution function (MLDF) and determine the optimal distance for its evaluation. Finally, the effect of fixing the β slope parameter in the MLDF parametrization and the chosen evaluation core distance is analyzed for composition analyses.

In Chapter 6, we apply the improved reconstruction procedure to one year of calibrated data taken with the engineering array of AMIGA. To begin with, we construct a reliable data sample by developing a bad period rejection for AMIGA. We further exclude erroneous modules, and correct for the different efficiencies of small and large detector modules. As a first analysis, we study the lateral trigger probability that is obtained for the processed data sample and compare results with simulations. Next, we parametrize the attenuation of the muonic signal due to the

atmosphere and soil layer above the buried muon detectors for both data and simulations and define a zenith-independent estimator ρ_{35} of the muon density. Furthermore, we estimate the systematic uncertainties arising from the module area-dependent efficiency correction, the setting of the discriminator thresholds of the individual scintillator channels, the density of the soil, the parametrization of the MLDF, and the attenuation correction.

In Chapter 7, we use the corrected data set for analyses of the muon content of extensive air showers. For this purpose, we perform a power law fit of the energy dependence of the mean muon densities measured by AMIGA and compare the results with simulations. We further quantify the observed disagreement of the muon content between simulations and data with the help of Auger measurements of the mean depth of shower maximum X_{max}. Additionally, we qualitatively analyze the evolution of the logarithmic mass based on the AMIGA muon measurements. We conclude with a comparison of the obtained mean muon densities with muon measurements of other experiments and previous studies with a special focus on the comparison with the Auger analysis of highly inclined events. We summarize our results in Chapter 8.

1.1 KEY CONTRIBUTIONS

- Analyzing the impact of the detection threshold of muons and the role of muons produced in a shower by photon-air interactions on the separation quality of different primary cosmic rays in the energy region of the ankle.
- Improving the reconstruction procedure for AMIGA to derive an unbiased estimate of the muon density at the optimum core distance. Main contributions: determining the optimal inhibition window size, developing a geometrical correction procedure for "corner-clipping muons", and deriving a new unbiased parametrization of the muon lateral distribution function.

- Selecting a reliable data sample of one year taken with the engineering array, developing a bad period rejection for AMIGA, excluding faulty modules, and correcting for the different efficiencies of small and large detector modules.
- Applying the improved reconstruction procedure to the data set, studying the muon lateral trigger probability, and parametrizing the attenuation of the muonic signal due to the atmosphere and soil layer above the buried muon detectors to define a zenith-independent estimator ρ_{35} of the muon density.
- Estimating the systematic uncertainties arising from the module area-dependent efficiency correction, the setting of the discriminator thresholds of the individual scintillator channels, the soil density, the parametrization of the MLDF, and the attenuation correction.
- Analyzing the muon content of extensive air showers with the corrected data set: fitting the energy dependence of the mean muon densities measured by AMIGA by a power law parametrization, quantifying the observed disagreement of the muon content between simulations and data with the help of Auger X_{max} measurements, qualitatively analyzing the evolution of the logarithmic mass based on the AMIGA muon measurements, and comparing results with other experiments and previous Auger muon studies.

1.2 PUBLICATIONS

Some ideas and figures of this thesis have appeared previously or will appear shortly in the following publications.

Short author list papers & conference proceedings:

S. Müller and M. Roth, "A CORSIKA Study on the Influence of Muon Detector Thresholds on the Separability of Primary Cosmic Rays at Highest Energies", *Proc. 34th Int. Cosmic Ray Conf.* PoS(ICRC2015)419, The Hague, The Netherlands (2015)

S. Müller et al., "Impact of Muon Detection Thresholds on the Separability of Primary Cosmic Rays", *Proc. 35th Int. Cosmic Ray Conf.* PoS(ICRC2017)311, Busan, Korea (2017)

S. Müller et al., *Impact of Muon Detection Thresholds on the Separability of Primary Cosmic Rays*, Astropart. Phys. **97** (2018) 174–185

FULL COLLABORATION PAPERS & CONFERENCE PROCEEDINGS:

B. Wundheiler for the Pierre Auger Collaboration, "The AMIGA Muon Counters of the Pierre Auger Observatory: Performance and Studies of the Lateral Distribution Function", *Proc. 34th Int. Cosmic Ray Conf.* PoS(ICRC2015)324, The Hague, The Netherlands (2015)

J. Figueira for the Pierre Auger Collaboration, "An Improved Reconstruction Method for the AMIGA Detectors", *Proc. 35th Int. Cosmic Ray Conf.* PoS(ICRC2017)396, Busan, Korea (2017)

S. Müller for the Pierre Auger Collaboration, "Direct Measurement of the Muon Density in Air Showers with the Pierre Auger Observatory", *Proc. Ultra High Energy Cosmic Rays 2018*, UHECR2018, Paris, France (2018)

Pierre Auger Collaboration, *The AMIGA Engineering Array at the Pierre Auger Observatory*, Nucl. Instrum. Methods Phys. Res. A (in preparation) (2018)

2 COSMIC RAYS

Cosmic rays (CRs) cover a huge range in energy from less than a GeV to more than 10^{20} eV. These mainly charged particles are produced in astrophysical sources and arrive on earth after propagation through the interstellar medium. Around 90% are protons, 10% helium and the rest heavier ionized nuclei [9]. There is experimental evidence that CRs up to energies of about 10^{17} eV are accelerated in supernova remnants within our galaxy [10]. In contrast, the sources of ultra-high energy cosmic rays (UHECRs) are still unknown.

In Section 2.1, we discuss possible acceleration mechanisms of CRs in astrophysical sources and give an overview over propagation effects as deflection in interstellar magnetic fields and energy losses of protons and nuclei. We present the measured energy-dependent CR flux and interpretations of the spectral features of the *knee* and the *second knee*, the *ankle*, and the flux suppression at the highest energies in Section 2.2. The discrepancy in the astrophysical interpretations of the energy spectrum demonstrates the need for additional mass composition measurements. At energies above 10^{14} eV, primary CRs can, however, only be indirectly detected by the measurements of secondary particles produced in extensive air showers with large air shower arrays. In Section 2.3, we give an overview over the physics of extensive air showers and mass-sensitive shower observables that can be employed for composition analyses. We summarize the composition results of various air shower experiments in Section 2.4 and discuss the implications of the Auger measurements of the depth of shower maximum for astrophysical models in the energy range of the transition from galactic to extragalactic CRs up to the flux suppression region.

2.1 SOURCES AND PROPAGATION

Potential sources of CRs must fulfill certain requirements to be able to accelerate particles to the observed energies. According to the Hillas criterion [11], the energy-dependent Larmor radius

$$r_L(E) = \frac{1.1}{Z}\left(\frac{E}{10^{18}\,\mathrm{eV}}\right)\left(\frac{B}{\mu\mathrm{G}}\right)^{-1}\mathrm{kpc} \tag{2.1}$$

of a particle with charge Ze within a magnetic field with strength B must not exceed the size of the source R_{source}. This sets a limit on the maximal energy

$$E_{\mathrm{max}} = Z\left(\frac{B}{\mu\mathrm{G}}\right)\left(\frac{R_{\mathrm{source}}}{\mathrm{kpc}}\right)\times 10^{18}\,\mathrm{eV} \tag{2.2}$$

a particle can reach being trapped within the accelerating region [12].

An adapted version of the so-called *Hillas plot* from Ref. [13] is shown in Fig. 2.1. It places candidate sources of CRs in a plane of the magnetic field B versus their characteristic size R. The yellow dashed lines show the lower limits for the acceleration of protons to characteristic energies where features in the CR flux are observed. Due to the higher electric charge, nuclei with charge Ze can be accelerated to Z times higher energies than protons within the same sources.

According to the Hillas criterion, supernova remnants (SNRs) are possible source candidates for CRs with energies below the knee. For multiple reasons, discussed later in this chapter, it is generally accepted that galactic CRs are accelerated in SNRs by the mechanism of diffusive shock acceleration. Possible sources for protons at ultra-high energies above the ankle are radio galaxy lobes and clusters of galaxies as well as jets from active galactic nuclei (AGNs) and gamma-ray bursts (GRBs) [13].

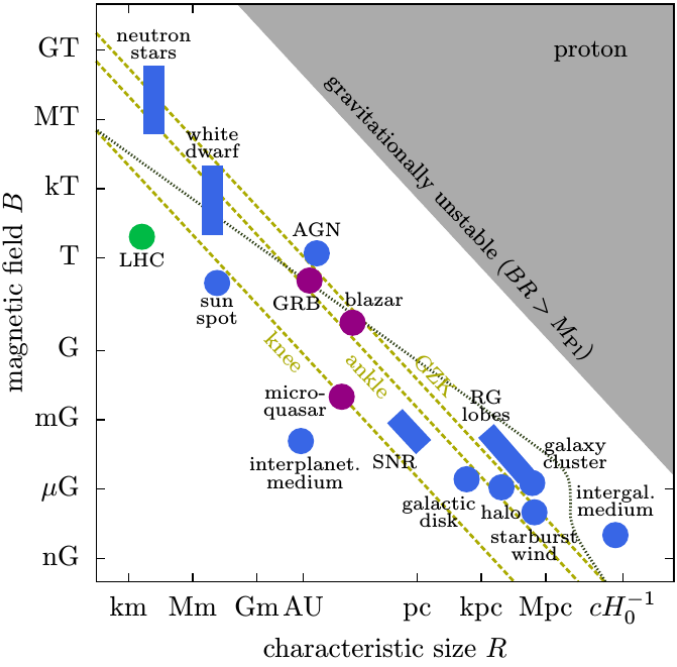

Figure 2.1: Adapted version of the Hillas plot from Ref. [13] which places candidate sources of CRs in a plane of the magnetic field B versus their characteristic size R. Yellow dashed lines show the lower limits for the acceleration of protons to characteristic energies where features in the CR flux are observed: the *knee* at $\sim 10^{15.5}$ eV, the *ankle* at $\sim 10^{18.5}$ eV, and the Greisen-Zatsepin-Kuzmin (GZK) suppression at $\sim 10^{19.6}$ eV.

2.1.1 *Acceleration mechanisms*

There are two different types of mechanisms which are capable to accelerate particles up to ultra-high energies and, at the same time, yield a power law injection spectrum. One is the direct acceleration of particles by an extended electric field as for unipolar inductors in relativistic magnetic rotators or black holes with magnetized disks losing rotational energy in jets. However, despite being in principle very efficient, plasmas in the astrophysical environments typically destroy such large scale electric fields and high energy densities provide opportunities for energy losses. Furthermore, this mechanism predicts a hard injection spectrum which does not match the slope of the measured flux of UHECRs [13].

The second acceleration mechanism is based on the energy transfer from a macroscopic object to microscopic particles through repeated interactions. A standard example is diffusive shock acceleration, also called "first-order Fermi acceleration", in supernova remnants, where the diffusion of charged particles in the moving magnetized plasmas leads to repeated crossings of the shock front resulting in a net energy gain.

Shock waves are typically produced when ejected material from an astrophysical object encounters the surrounding medium with supersonic motion. As mentioned previously, this is the case for expanding supernova remnants where the ejected material from the supernova explosion produces a shock wave ahead of the expanding supernova remnant. Further shock regions are gamma-ray bursts, jets and hot-spots in active galactic nuclei or large scale accretion shocks in galaxy clusters [12].

The acceleration of particles by diffusive shock acceleration at a plane shock front is illustrated in Fig. 2.2. In the rest frame of the shock front, the unshocked gas ("upstream") moves towards the shock with a velocity $\vec{\mathbf{u_1}}$, while the shocked gas ("downstream") moves away with a velocity $\vec{\mathbf{u_2}}$ and $|u_2| < |u_1|$. Hence, in the lab frame, the plasmas of both the upstream and the downstream

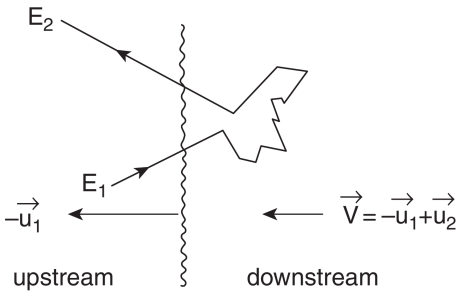

Figure 2.2: Illustration of first-order Fermi acceleration at a plane shock front from [14]. In the rest frame of the shock front, the unshocked gas ("upstream") moves towards the shock with a velocity $\vec{\mathbf{u_1}}$, while the shocked gas ("downstream") moves away with a velocity $\vec{\mathbf{u_2}}$. Hence, in the lab frame, the plasmas of both the upstream and the downstream region move towards the left with velocities of $-\vec{\mathbf{u_1}}$ and $\vec{\mathbf{V}} = -\vec{\mathbf{u_1}} + \vec{\mathbf{u_2}}$, respectively. The average fractional energy gain per crossing back and forth across the shock is $\Delta E/E \sim \frac{4}{3}(u_1 - u_2)/c$.

region move towards the left with velocities of $-\vec{\mathbf{u_1}}$ and $\vec{\mathbf{V}} = -\vec{\mathbf{u_1}} + \vec{\mathbf{u_2}}$, respectively [14].

Particles starting on the upstream side of the shock diffuse in the plasma by collisionless "scattering" on magnetic turbulences. The diffusion process creates an isotropic angular distribution of the particles in the rest frame of the upstream plasma. After interacting elastically with the upstream plasma, which moves with a speed of $-\vec{\mathbf{u_1}}$ in the lab frame towards them, the particles eventually cross the shock front. On the downstream side of the shock, moving with velocity $\vec{\mathbf{V}} = -\vec{\mathbf{u_1}} + \vec{\mathbf{u_2}}$ towards the particles, the particle distribution gets in turn isotropized by collisions with magnetic turbulences. As a result, some of the particles cross the shock front back to the upstream region [15].

Crossing back and forth across the shock plane always results in an energy gain. On average, the fractional gain is $\Delta E/E \sim 4/3\,\beta$, where $\beta = V/c$ is the relative velocity of the shocked plasma in units of c [14]. Since the acceleration process is first-order in shock

velocity, particles need to perform many shock crossing cycles to achieve high energies.

According to a derivation by Lagage and Cesarsky [16], the maximum energy that can be achieved by diffusive shock acceleration in a supernova remnant can be formulated, in analogy to the Hillas criterion of Eq. (2.2), as

$$E_{\max} = \text{const} \times \beta ZeBR \tag{2.3}$$

where $R = u_1 \times T_A$ is the radius at the time when the supernova remnant expansion begins to slow down [14]. Estimating the magnetic field of the interstellar medium (ISM) as $B_{\text{ISM}} \sim 3\,\mu\text{G}$ gives the charge-dependent maximum energy

$$E_{\max} \leq Z \times 3 \times 10^4\,\text{GeV}. \tag{2.4}$$

However, recently there has been both theoretical and observational evidence indicating that the magnetic fields in supernova shocks may be significantly higher in than in the interstellar medium. As a consequence, $E_{\max}$ gets close to the energy region about 1 PeV where the spectrum steepens at the knee [14], which is discussed in Section 2.2.

Diffusive shock acceleration gives rise to a power law particle spectrum $N(p) \propto p^{-\gamma_p}$ in momentum with a universal slope γ_p which is ≈ 4 for strong shocks. For relativistic particles, γ_p is equivalent to a slope in energy γ_e which can be calculated using the fact that $E^{-\gamma_e}\mathrm{d}E = 4\pi p^2 p^{-\gamma_p}\mathrm{d}p$. The resulting spectral index $\gamma_e \approx 2$ corresponds to the one required to explain the CR spectrum at energies below the knee, if propagation effects lead to a steepening by ~ 0.7 [17].

2.1.2 *Propagation*

During propagation from the accelerating source to the observer, CR particles experience two kinds of processes. While cosmic magnetic fields alter the direction and travel time of charged CRs,

their energy and elemental composition remains unaffected. On the contrary, interactions with cosmic background photons lead to energy losses and changes in the elemental composition but do not change the direction of propagation [18].

The deflection of charged particles by magnetic fields in the environment of the accelerating source, in the intergalactic medium, and in the galaxy is visualized in Fig. 2.3. The galactic magnetic field follows the spiral-shaped distribution of matter of the galaxy. Its intensity depends on the distance from the galactic center and has an average value of $B \sim 4\,\mu\text{G}$. According to Eq. (2.1), particles with energies below $10^{18}\,\text{eV}$ consequently have Larmor radii $r_L < 300\,\text{pc}$ and are thus strongly confined inside the galaxy. However, the galactic magnetic field only has little impact for energies above $10^{19}\,\text{eV}$. The non-observation of a clear anisotropy in the flux at these energies, which would be produced by a galactic source, motivates the search for extragalactic sources of UHECRs [19]. Recent studies conclude that the deflection for particles of charge Z and energy E in the galactic magnetic field should be smaller than $10^\circ Z \left(4\times10^{19}\,\text{eV}/E\right)$. The deflection process can distort the angular images of the CR sources such that the flux may appear dispersed or globally translated in the sky with a small dispersion [18].

The extragalactic magnetic fields beyond the galactic disk are much less known. Measurements of Faraday rotation and synchrotron radiation halos have been used to estimate the magnetic fields in a few clusters of galaxies, yielding somewhat different field strengths of $B \sim 0.1 - 1\,\mu\text{G}$ and $B \sim 1 - 10\,\mu\text{G}$, respectively. Outside of these regions, which enclose a fraction of less than 10^{-6} of the universe, only an upper limit of $B < 10^{-9}\,\text{G}$ exists [19]. Due to the much lower magnetic field intensities in comparison to the galaxy, the Larmor radius of UHECRs becomes extremely large. For protons with energy $E > 10^{20}\,\text{eV}$, deflections from less than a degree [20] to $10 - 20^\circ$ [21] are predicted.

During propagation in the intergalactic medium, UHECRs interact with background photons from the cosmic microwave

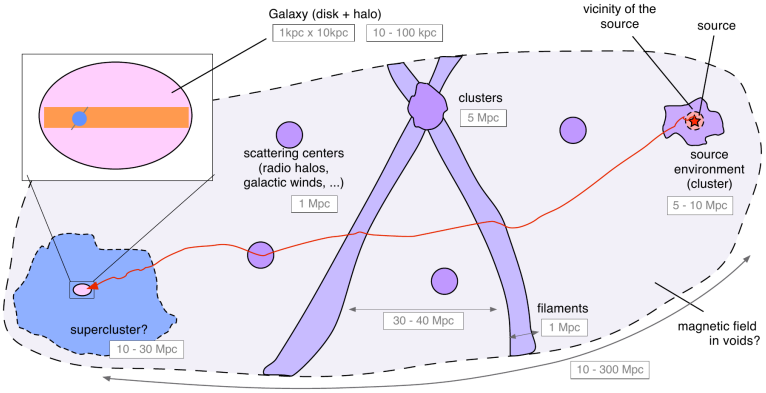

Figure 2.3: Schematic representation of magnetized regions intervening in UHECR propagation. From [18].

background and the extragalactic background light. While interactions with the cosmic microwave background primarily take place at the highest energies, interactions with the extragalactic background light, ranging from infrared to ultraviolet, predominate at slightly lower energies [18]. The main energy loss processes are photo-pion production, pair production, photodisintegration (in the case of nuclei) and the adiabatic expansion of the universe.

Photo-pion production occurs when a nucleon (free or bound to a nucleus) interacts with a background photon such that nucleons and pions are produced. The main interaction channels are [22]

$$p + \gamma \to \Delta^+ \to \begin{cases} p + \pi^0 \\ n + \pi^+. \end{cases} \tag{2.5}$$

The charged pions, in turn, produce neutrinos and electrons

$$\pi^+ \to \mu^+ + \nu_\mu, \quad \mu^+ \to e^+ + \nu_e \bar{\nu}_\mu \tag{2.6}$$

while neutral pions produce gamma rays

$$\pi_0 \to \gamma\gamma. \tag{2.7}$$

The energy threshold for photo-pion production is $\sim 3 \times 10^{19} A(\mathrm{meV}/\epsilon)\,\mathrm{eV}$, where ϵ is the photon energy and A the mass number of the nucleus. The interaction of protons with photons from the cosmic microwave background ($\epsilon \approx 0.7\,\mathrm{meV}$) causes a cutoff in the UHECR spectrum, starting from energies around $3 \times 10^{19}\,\mathrm{eV}$ which is known as the Greisen-Zatsepin-Kuzmin (GZK) effect. It implies that the sources of almost all protons reaching earth with energy greater than $10^{20}\,\mathrm{eV}$ must be located within about 100 Mpc [23].

Electron-positron pair production

$${}^{A}_{Z}\mathrm{X} + \gamma \to {}^{A}_{Z}\mathrm{X} + e^+ + e^- \tag{2.8}$$

is caused by the interaction of ultra-high energy nuclei with background photons. Due to the relatively short mean free path and the very small fractional energy loss it can be well approximated as a continuous energy loss process. The energy threshold is $\sim 5 \times 10^{17} A(\mathrm{meV}/\epsilon)\mathrm{eV}$ and the energy loss length scales as $l^{-1}_{\mathrm{nuclei}} = l^{-1}_{\mathrm{protons}} Z^2/A$ for nuclei with mass number A and charge Z.

Another important energy loss process for nuclei is photodisintegration, where a nucleus is split into smaller parts due to interactions with photons

$${}^{A}_{Z}\mathrm{X} + \gamma \to \begin{cases} {}^{A-1}_{Z}\mathrm{X} + n \\ {}^{A-1}_{Z-1}\mathrm{X} + p. \end{cases} \tag{2.9}$$

The two main types of processes, contributing at increasing energy ranges, are the giant dipole resonance for photons with energies $\epsilon' \leq 30\,\mathrm{MeV}$), and the quasi-deuteron process for $30\,\mathrm{MeV} < \epsilon' < 150\,\mathrm{MeV}$. For higher energies, photodisintegration cross sections rapidly decrease and pion production dominates [23].

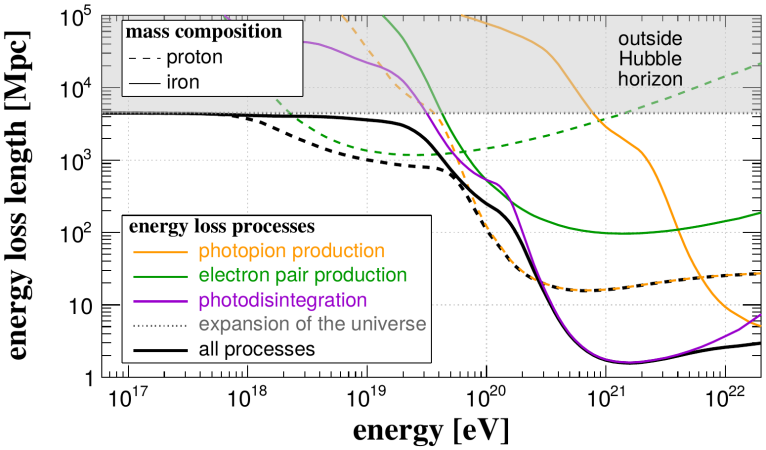

Figure 2.4: Energy loss lengths for different processes: photo-pion production (orange), electron pair production (green), photodisintegration (purple), adiabatic expansion of the universe (gray) and total (black). Solid lines are for iron nuclei, and dashed lines for protons. From [22].

The expansion of the universe itself leads do adiabatic energy losses

$$E = \frac{E_0}{1+z} \tag{2.10}$$

where z is the redshift and E_0 the initial energy of the nucleus [22].

Another relevant process is nuclear decay of the unstable products of photodisintegration and photo-pion interactions. The most relevant processes for this energy range are α and $\beta^{\pm}$ decays, and nuclear dripping [23]. The energy loss lengths for the discussed processes of photo-pion production, photodisintegration, pair production and adiabatic expansion of the universe are illustrated in Fig. 2.4 for the case of iron and proton primaries.

There exist several standard, simplified models to describe propagation within the galaxy. These differ in their assumptions

about the source distribution and the treatment of diffusion and convection [14]. In the *leaky box model*, the galaxy is described as a cylinder of radius $R_d \approx 15\,\text{kpc}$ and height $H \approx 15\,\text{kpc}$ within which CRs propagate freely for a time $\tau_{\text{esc}} = {}^{H^2}/_{D(E)}$, where $D(E) = D_0 E^{\delta}$ is the diffusion coefficient in the galaxy [17]. The slope δ can be derived from measurements of the boron to carbon ratio as will be discussed in the next section.

2.2 ENERGY SPECTRUM

The energy spectrum of CRs arriving at earth corresponds to the injection spectrum of the source which is modified by propagation effects. In the simplified leaky box model of diffusion in the galaxy, the spectrum of primary CRs at earth will be $N(E) \propto E^{-\gamma_{\text{inj}}-\delta}$ for a source spectrum $N_s(E) \propto E^{-\gamma_{\text{inj}}}$. On the other hand, the spectrum of secondaries, resulting from spallation processes during propagation, will be given by $N_{\text{SEC}}(E) \approx N(E)\mathcal{R}_{\text{spall}} \propto E^{-\gamma_{\text{inj}}-2\delta}$ where $\mathcal{R}_{\text{spall}}$ is the rate of spallation reactions. Consequently, the ratio ${}^{N_{\text{SEC}}(E)}/_{N(E)} \propto E^{-\delta}$ between the flux of secondaries and primaries , for instance boron and carbon (B/C), probes the energy dependence of the galactic diffusion coefficient and allows to infer the injection spectrum of the sources [17]. Recent measurements of the B/C flux ratio by AMS-02 have obtained a spectral index of $\delta \approx 0.33$ above a rigidity of 65 GV in agreement with the Kolmogorov theory of turbulence which predicts $\delta = {}^1/_3$ asymptotically [24].

Up to primary energies of about 10^{14} eV, the flux of different primary CR species can be directly measured by satellite or space-born experiments. However, as a consequence of the steeply falling flux spectrum, only an indirect detection with large air shower arrays on the surface of the earth is possible for higher energies. The all-particle flux, shown in Fig. 2.5, follows a power law $\propto E^{-\gamma}$ with $\gamma \approx 2.7$ up to PeV energies where a steepening to $\gamma \approx 3.1$, the so-called *knee*, appears. Mass composition measurements indicate that the steepening is caused by a sequential drop-

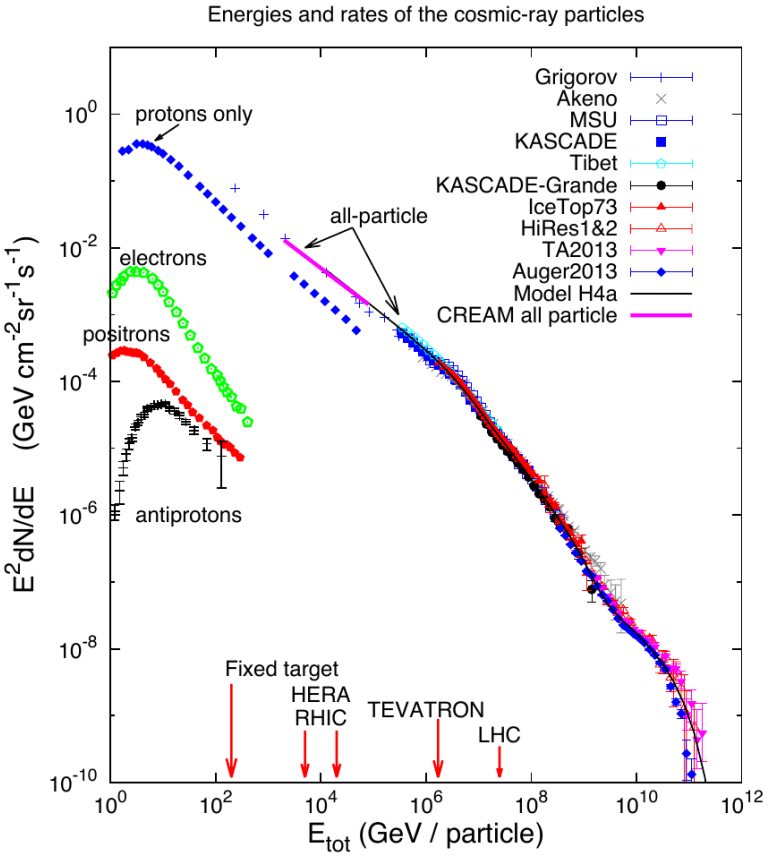

Figure 2.5: Overview of the energy spectrum of primary CRs. Up to primary energies of about 10^{14} eV, primary CRs can be directly detected by satellite or space-born experiments. For higher energies, only an indirect measurement of the (mostly all-particle) flux with large air shower arrays on ground is possible as a consequence of the steeply falling flux spectrum. From [25], originally from [14].

out of elements. It can be interpreted by a rigidity-dependent acceleration mechanism of CRs, where protons can reach a maximum energy of $\sim 5 \times 10^{15}$ eV. At the so-called *ankle* at around 10^{18} eV, the spectrum flattens again back to $\gamma \approx 2.7$, which might be related to a transition from particles of galactic to particles of extra-galactic origin. Finally, around $10^{19.6}$ eV, a strong suppression of the flux is observed. In the following, we discuss the different energy regions and interpretations of the spectral features.

2.2.1 *Up to the knees*

Until recently, the paradigm was that the energy spectrum of primary CRs was a feature-less power law between a few GeV per nucleon and the knee at around 3×10^{15} eV [26]. However, direct precision measurements of first the PAMELA satellite experiment [27] and now the AMS-02 experiment [28] on the International Space Station show that the proton spectrum is distinctly softer than that of helium. In contrast, an identical rigidity dependence has been observed for He, C, and O above 60 GV. For all detected primary CR species, p, He, C, and O, AMS-02 measured a hardening of their spectra above 200 GV/nucleon [29, 30]. These results, in combination with the rigidity-dependence of the fluxes of the secondary CR particles, lithium, beryllium, and boron, measured by AMS-02 [30], need to be accommodated for in current source and propagation models.

The energy region of the knee has been studied by multiple extensive air shower experiments which all show a bending of the all-particle flux corresponding to the knee of the spectrum [31]. However, only a few were able to separate individual mass groups of primary CRs. Measuring the electromagnetic and muonic shower components simultaneously, the KASCADE established that the steepening of the CR all-particle flux at energies $2 - 5 \times 10^{15}$ eV corresponds to a drop-out of light elements followed by an increasing dominance of heavy primaries towards higher energies [32, 33]. The KASCADE data are not in disagree-

ment with a constant rigidity of the knee position for the different considered light primaries (p, He, C) [34]. Similar results for three mass groups of primary CRs were obtained by EAS-TOP measurements [35].

The successor experiment KASCADE-Grande extended the accessible energy range up to 2×10^{18} eV. By the combined analysis of the charged particle, the electron, and the muon components measured by the detector arrays of Grande and KASCADE, it allowed for an event-by-event separation between light, medium, and heavy primaries. At about 8×10^{16} eV, a knee-like feature was identified in the spectrum of the heavy component, while an ankle-like feature was observed at an energy of $10^{17.08 \pm 0.08}$ eV for the light component [36].

The all-particle energy spectrum and spectra of individual mass groups obtained with KASCADE and KASCADE-Grande is shown in Fig. 2.6. The observations of a sharp decline of the contribution of light elements at the knee, followed by a suppression of the flux of heavy elements at the second knee, could be interpreted by a rigidity-dependent acceleration mechanism as diffusive shock acceleration in galactic SNRs which has been discussed in Section 2.1.1. According to the charge-dependent maximum energy $E_{\max}$ of Eq. (2.4), iron nuclei could reach a 26 times larger energy than protons, and the knee would result as the superposition of the cutoffs of different elemental species [17].

2.2.2 *Acceleration in galactic supernova remnants?*

Diffusive shock acceleration in supernova remnants has been a favored candidate for the origin of galactic CRs since the late '70s for mainly two reasons. Supernovas could easily supply the measured energy density of CRs if 10% of the explosion energy were transferred into accelerated particles. Beyond that, diffusive shock acceleration produces approximately the right energy spectrum with a spectral index of $\gamma \approx 2$ as discussed in Section 2.1.1.

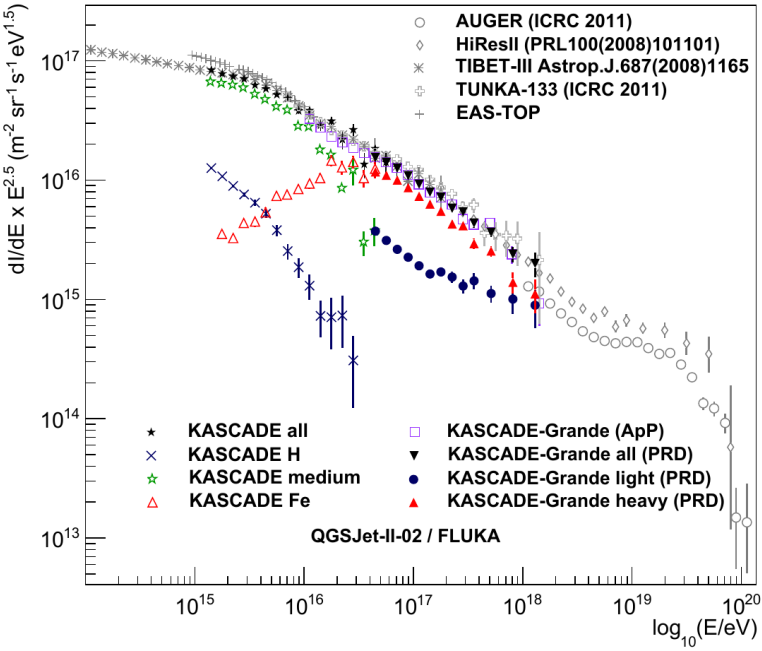

Figure 2.6: The all-particle energy spectrum and spectra of individual mass groups obtained with KASCADE and KASCADE-Grande. From [36].

However, in order to be able to accelerate particles up to the energies of the knee, the magnetic fields in the vicinity of supernova shocks must be largely amplified compared to the interstellar medium. A possible mechanism is provided by the theory of non-linear diffusive shock acceleration, which has been developed in the last decade. Indeed, evidence for the presence of amplified magnetic fields has been provided by X-ray telescopes looking at SNRs. In addition to further experimental indications for the efficient acceleration of hadrons, γ-ray observations have recently provided direct evidence of the presence of mildly rela-

tivistic protons in supernova remnants interacting with molecular clouds [17].

A remaining theoretical difficulty comes from the evidence from γ-ray emitting supernova remnants that the source spectra are systematically steeper than the prediction of $\propto E^{-2}$ from diffusive shock acceleration. Calculations of the modification of the source spectrum by propagation effects from measurements of the B/C flux ratio support the conclusion of a relatively steep particle spectrum $\gamma_{\mathrm{inj}} \approx 2.3 - 2.4$ [24]. While, presently, these observations can only be accommodated in a phenomenological way, further progress in simulations could provide the necessary missing information on the properties of the relevant magnetic turbulence and the process of particle injection within the nonlinear diffusive shock acceleration theory.

Another puzzle are the observations of a spectral hardening above 200 GV/nucleon for both primary and secondary CRs and of a softer proton spectrum compared to helium by AMS-02. While the stronger hardening of the secondaries above 200 GV suggests a relation to the propagation properties in the galaxy, the difference between the rigidity spectral indices of protons and helium might be explained by selective acceleration mechanisms in supernova shocks as proposed by Hanusch et al. [37].

2.2.3 *Ankle and flux suppression*

According to the explanation that the knee and the second knee result from the charge-dependent maximum energies that can be reached by the acceleration in galactic supernova remnants, the second knee marks the end of the galactic CR spectrum [38]. At an energy of about 5×10^{18} eV, a flattening of the energy spectrum, dubbed the *ankle*, has been observed by multiple air shower experiments. The ankle feature is commonly assumed to be related to the transition between galactic and extragalactic CRs. However, distinct astrophysical explanations exist that can in large part be classified by the so-called *ankle*, *dip* and *mixed composition mod-*

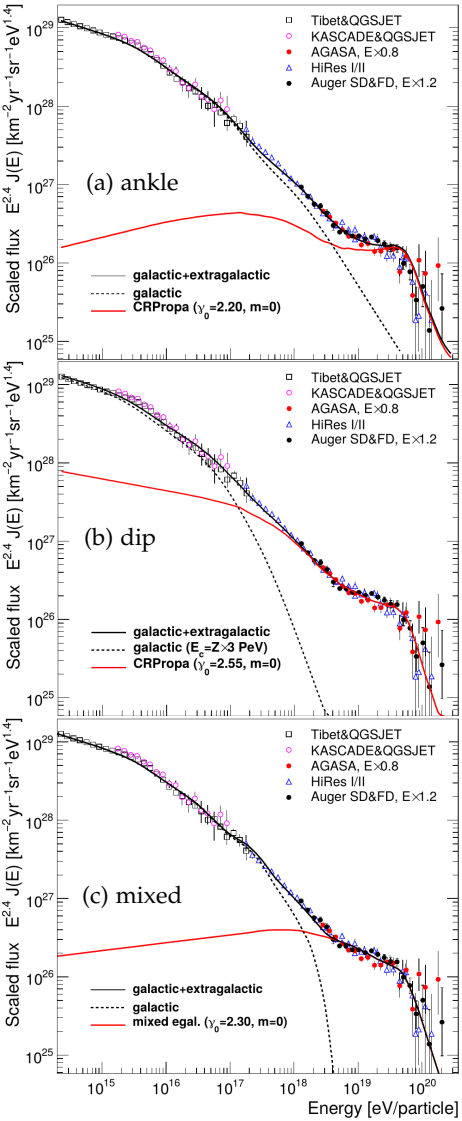

Figure 2.7: Illustration of (a) *ankle*, (b) *dip*, and (c) *mixed composition models*. From [38].

els. Although all three models assume the intersection of a steep galactic component with a flatter extragalactic one, they differ in their predictions of the transition energy and the CR mass composition [39].

In the traditional *ankle model*, the transition occurs at the ankle which is modeled as the intersection of a steep iron-dominated galactic component with a flat proton-dominated extragalactic component as illustrated in Fig. 2.7a. The assumption of a new high-energy galactic component with a maximum energy that is at least $30 - 40$ times higher than in the standard model of diffusive shock acceleration in supernova remnants, would however require a significant modification of the rigidity model of the knee [38, 39].

The *dip model*, shown in Fig. 2.7b, predicts an almost pure proton composition of the extragalactic component. It could originate from active galactic nuclei with a neutron mechanism for particle escape, providing a pure proton spectrum, or from the enhancement in the proton fraction in relativistic shock acceleration [39]. The transition from heavy galactic to light extragalactic CRs begins at the second knee at $(4 - 7) \times 10^{17}$ eV. It is completed at the beginning of the e^+e^- pair-production dip at $E \sim 1\,\mathrm{EeV}$ that is caused by the energy losses of protons through the Bethe-Heitler process. The ankle appears automatically as a part of the dip whose observed shape allows an admixture of not more than 15% of light nuclei. In addition, the so-called GZK cutoff is predicted as a consequence of large energy losses due to resonant photo-pion production at energies above $10^{19.5}$ eV [38].

In *mixed composition models*, extragalactic CRs are assumed to be composed of nuclei of various types based on the argument that any acceleration mechanism operating in gas involves different nuclei [39]. The transition from the galactic component to the extragalactic component, which is much softer than in the dip model as illustrated in Fig. 2.7c, occurs in the vicinity of the ankle. Due to the about a factor 10 higher transition energy, mixed composition models need galactic sources with a higher maxi-

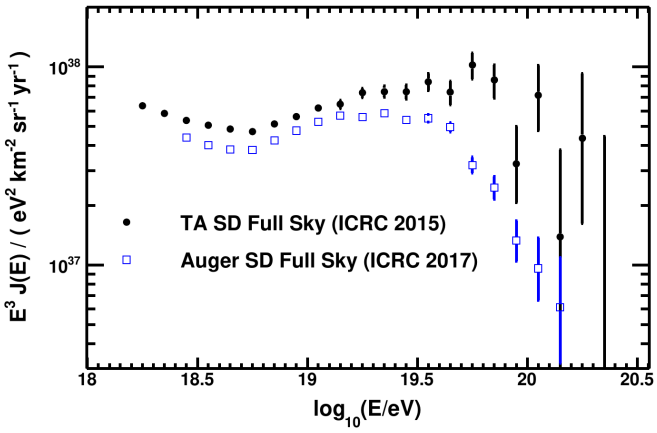

Figure 2.8: Comparison of the energy spectra measured by TA and Auger presented at the ICRC 2017. From [40].

mum acceleration energy than in the dip model. In the energy region of the transition the mass composition changes from a iron-dominated galactic component to a lighter extragalactic one. The individual spectra of nuclei with mass A are subsequently suppressed at energies above approximately $A \cdot 10^{18}$ eV as a result of the Lorentz-factor dependence of the energy losses [38].

The described models of the transition from galactic to extragalactic CRs can be partly constrained by measurements of the energy spectrum. The position of the ankle agrees remarkably well between the two currently largest extensive air shower experiments with the Telescope Array (TA) measuring only a 8% larger energy than the Pierre Auger Observatory. However, their spectra differ significantly in the region of the flux suppression as shown in Fig. 2.8.

While TA reports $E_{1/2} = (6 \pm 0.7\,(\text{stat.})) \times 10^{19}$ eV, Auger finds $E_{1/2} = (2.26 \pm 0.08\,(\text{stat.}) \pm 0.4\,(\text{syst.})) \times 10^{19}$ eV as the position of the observed cutoff [41], which is defined as the energy at which

the integral spectrum drops by a factor of two below what would be expected with no cutoff [42].

This discrepancy is reflected in the differing interpretations of the ankle and cutoff region by TA and Auger. Fitting the spectrum with a model in which the primaries are protons, TA interprets the ankle with the dip model and the cutoff by the GZK effect [42]. In contrast, the energy $E_{1/2} \sim 2.26 \times 10^{19}$ eV of the cutoff reported by Auger is at considerable odds with the prediction of $E_{1/2} = 5.3 \times 10^{19}$ eV for the GZK suppression energy [43]. Taking into account mass composition measurements, which will be discussed in Section 2.4, Auger favors mixed composition models for the description of the transition from galactic to extragalactic cosmic rays.

2.3 EXTENSIVE AIR SHOWERS

The discrepancy in the astrophysical interpretations of the energy spectrum of cosmic rays by TA and Auger shows that additional mass composition measurements are needed to conclude about the origins of the observed spectral features. However, at energies above 10^{14} eV, direct measurements of primary masses are not feasible. Instead, large air shower arrays on the surface of the earth can only indirectly detect primary CRs by measuring the shower of secondary particles that is produced as a result of the initial interaction of a CR primary with a nucleus from the air at a typical height of 15 to 35 km [44]. Mass composition analyses consequently rely on the comparison of mass-sensitive air shower observables with simulations. These are subject to uncertainties as hadronic interaction models cannot yet be probed by particle accelerators at these high energies [45]. In the following, we will give an overview over the physics of air showers and derive mass-sensitive observables which will be used in the composition measurements that are presented in Section 2.4.

Although extensive air showers develop in a complex way and detailed numerical simulations are necessary to infer the prop-

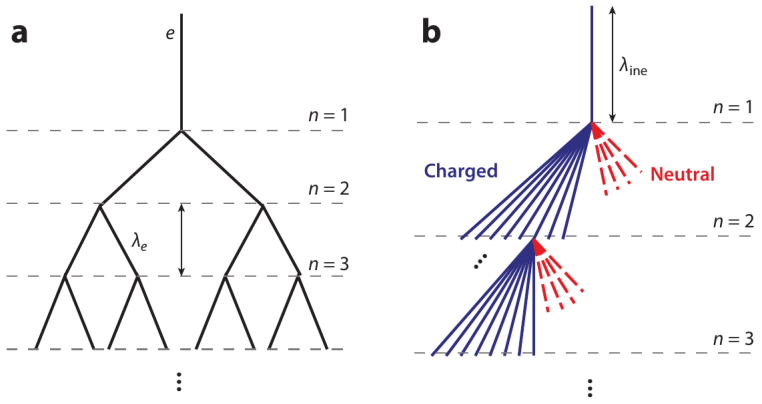

Figure 2.9: Simplified cascade model of an air shower. (a) An electromagnetic shower. (b) The hadronic component of a hadron-induced shower; dashed lines represent neutral particles (π^0), and solid lines represent charged particles ($\pi^{\pm}$). Only one charged hadron interaction is shown for each generation. From [44].

erties of the initial CR particle, the basic features of electromagnetic (EM) showers can be understood with a simple model derived by Heitler [46]. The principles of this model are illustrated in Fig. 2.9a. After traversing a fixed distance λ_e, an electromagnetically interacting primary particle (electron, positron, or photon) with energy E_0 undergoes a two-body splitting. In the case of photons, e^+e^- pairs are produced, while electrons and positrons radiate bremsstrahlung [47]. The particle-multiplication process stops after n splittings when the individual energy of a single particle $E_0/2^n$ drops below the critical energy E_c where ionization-energy losses dominate over radiative losses [44].

In this simplified model, the corresponding atmospheric depth X_{max}, where the maximum number of particles $N_{\text{max}} = 2^n = E_0/E_c$ is reached, can be calculated as [47]

$$X_{\text{max}}^{\text{EM}}(E_0) \sim \lambda_e \ln\left(\frac{E_0}{E_c}\right). \tag{2.11}$$

The predictions of the Heitler model that $N_{\max}$ is proportional to E_0 and $X_{\max}$ depends logarithmically on the primary energy E_0 are confirmed by cascade theory and detailed numerical simulations [44].

The Heitler model has been generalized to hadronic showers by Matthews [47]. Although the "Heitler-Matthews model" constitutes a strong simplification of the complex hadronic multiparticle productions and particle decays, it provides insights into the features of hadronic showers.

The hadronic shower development is schematically visualized in Fig. 2.9b. The primary hadron with energy E produces a number of n_{tot} new particles of which one third are neutral pions, decaying promptly into two photons ($\pi_0 \to 2\gamma$), and two thirds charged pions. As long as their energy is greater than the typical decay energy E_{dec}, the charged pions interact again with air nuclei after traveling the mean interaction length λ_{ine}. If the energy falls below E_{dec}, the pions decay weakly ($\pi^+ \to \mu^+\nu_\mu$ or $\pi^- \to \mu^-\overline{\nu}_\mu$) such that one muon is produced per hadron. The total number of muons

$$N_\mu = n_{\text{ch}}^n = \left(\frac{E_0}{E_{\text{dec}}}\right)^\alpha, \tag{2.12}$$

where $\alpha = \frac{\ln n_{\text{ch}}}{\ln n_{\text{tot}}} \approx 0.82 \ldots 0.94$ and $E_{\text{dec}} = {}^{E_0}/_{n_{\text{tot}}^n}$, is hence given by the number of charged hadrons. The Heitler-Matthews model yields the important result that N_μ has a power-law dependence on the energy of the primary particle. However, the exact parameters need to be determined through detailed simulations.

Since one-third of the energy is transferred via π_0 decay to the EM shower component in each hadronic interaction, approximately 90% of the primary energy is carried by EM particles after

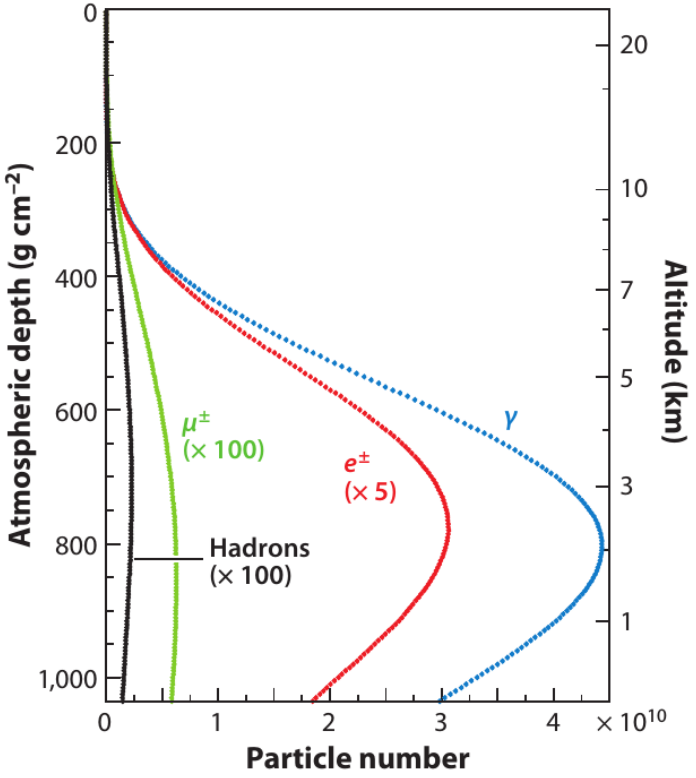

Figure 2.10: Average longitudinal particle profiles for simulated vertical, proton-induced showers at 10^{19} eV at the atmospheric depth of the Pierre Auger Observatory. From [44].

$n \approx 6$ generations. Correspondingly, the depth of the shower maximum of a hadronic shower

$$X_{\max}^{\text{had}}(E_0) \approx \lambda_{\text{inel}} + X_{\max}^{\text{EM}}\left[E_0/(2n_{\text{tot}})\right] \tag{2.13}$$

$$\sim \lambda_{\text{inel}} + X_0 \ln\left(\frac{E_0}{2n_{\text{tot}}E_c}\right), \tag{2.14}$$

where λ_{inel} is the hadronic interaction length, is determined by the outnumbering EM particles [44]. For illustration, the mean longitudinal particle profiles of the EM, muonic, and hadronic shower components are shown in Fig. 2.10 for proton showers simulated with CORSIKA at an energy of 10^{19} eV.

In the Heitler-Matthews model, a nucleus with atomic number A and total energy E_0 is considered as A independent single nucleons with reduced energy E_0/A. This superposition model leads to the predictions

$$N_{\text{EM,max}}^{A}(E_0) = A \cdot N_{\text{EM,max}}^{p}(E_0/A) \approx N_{\text{EM,max}}^{p}(E_0), \tag{2.15}$$

$$X_{\max}^{A}(E_0) = X_{\max}^{p}(E_0/A), \quad \text{and} \tag{2.16}$$

$$N_{\mu}^{A} = A \cdot \left(\frac{E_0/A}{E_{\text{dec}}}\right) = A^{1-\alpha} \cdot N_{\mu}^{p}(E_0), \tag{2.17}$$

where the labels p and A denote the particle numbers and the depth of the shower maximum of proton- and nucleus-induced showers, respectively [44].

Since the sub-showers with reduced energies penetrate less deeply in the atmosphere, the depth of shower maximum for iron showers is $80 - 100\,\text{gcm}^{-2}$ higher than for proton showers. Furthermore, as a consequence of the less-than-linear growth of the muon number with energy, nuclear showers with the same total primary energy have more muons (approximately 40% for iron) than proton showers [44, 47]. Both the depth of shower maximum $X_{\max}$ and the number of muons N_{μ} in a shower are hence mass-sensitive observables which can be used for analyses of the composition of cosmic rays.

2.4 MASS COMPOSITION

The depth of shower maximum $X_{\max}$ can be directly inferred from the observation of the fluorescence and Cherenkov light that is emitted by an extensive air shower as a function of height in the atmosphere [38]. While the identification of the primary particle that initiates an extensive air shower is currently not possible on an individual shower level, the distribution of $X_{\max}$ can be used to study the mass composition of primary CRs. Most commonly, the first two moments, the mean value $\langle X_{\max} \rangle$ and the dispersion $\sigma(X_{\max})$ are employed for this purpose.

Fig. 2.11 shows the distributions of the depth of shower maximum, obtained from simulations, for proton and iron primary particles versus the *calorimetric energy*, which corresponds to the energy in the electromagnetic shower component that can be inferred from fluorescence measurements of the longitudinal shower profile. As expected from the Heitler-Matthews model, the depth of shower maximum increases with the logarithm of energy and, on average, penetrates deeper in the atmosphere for light primaries (proton) than for heavy primaries (iron) [48].

2.4.1 *Distribution of X_{max}*

Even for extreme compositions of pure proton together with pure iron, shower-to-shower fluctuations lead, however, to considerable overlaps of the $X_{\max}$ distributions. As a consequence of the smaller interaction length of iron nuclei in air compared to protons, the width of the $X_{\max}$ distribution of iron showers is about a factor three smaller than that for proton (about 20 and 60 $\mathrm{g\,cm^{-2}}$ at 10^{18} eV respectively) [38, 44]. In addition to the mean value $\langle X_{\max} \rangle$, the dispersion $\sigma(X_{\max})$ is hence sensitive to the primary particle types [48].

Furthermore, it carries information on the "mixedness" of the composition. The variance of the combined $X_{\max}$-distribution for a mixed composition with fractions f_i of nuclei of mass A_i with

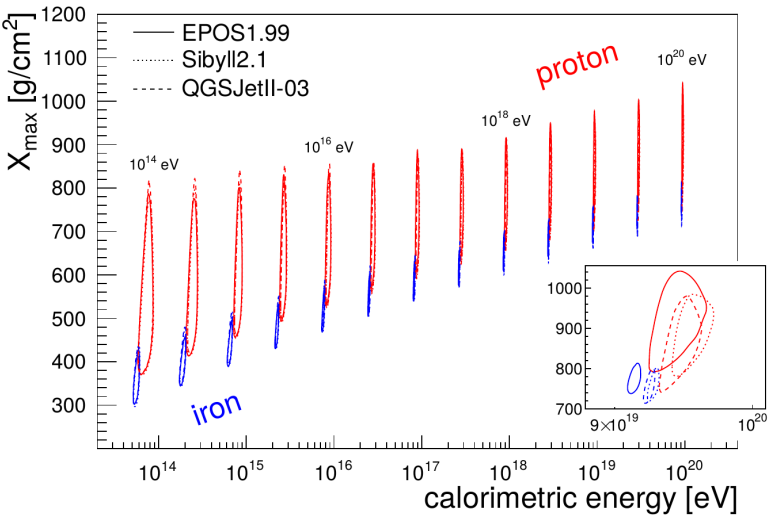

Figure 2.11: Air shower simulation of the shower maximum vs. calorimetric energy. Contour lines illustrate the regions which include 90% of the showers and the inset shows a detailed view at 10^{20} eV. From [48].

average shower maxima of $\langle X_{\max}\rangle_i$ and width σ_i, respectively, corresponds to

$$\sigma^2(X_{\max}) = \langle\sigma_i\rangle^2 + \left(\left\langle\langle X_{\max}\rangle_i^2\right\rangle - \langle X_{\max}\rangle^2\right), \tag{2.18}$$

where $\langle X_{\max}\rangle = \langle\langle X_{\max}\rangle_i\rangle$ is the mean of the combined distribution. In the case of two components only, this reduces to

$$\sigma^2(X_{\max}) = f\sigma_1^2 + (1-f)\,\sigma_2^2 + f\,(1-f)\,(\Delta\langle X_{\max}\rangle)^2. \tag{2.19}$$

Since the separation of the individual distributions adds to the total width, the combined distribution can hence, depending on the component fraction f and the separation $\Delta\langle X_{\max}\rangle$ of the means, be broader than the individual distributions [48].

2.4.2 *Elongation rate*

A robust indicator of a change of the CR composition with energy is the *elongation rate*

$$D = \frac{\mathrm{d}\langle X_{\mathrm{max}}\rangle}{\mathrm{d}\ln(E)} \tag{2.20}$$

which measures the change of the shower maximum per logarithm of energy. Within a *semi-superposition model*, which complements the approximation of the Heitler-Matthews model that a primary nucleus of mass A and energy E can be treated as a superposition of A nucleons of energy $E' = E/A$ by more realistic assumptions, the mean depth of maximum for a nucleus of mass A can be expressed as

$$\langle X^A_{\mathrm{max}}\rangle = \langle X^p_{\mathrm{max}}\left(E' = E/A\right)\rangle = c + D_p \ln\left(E/A\right), \tag{2.21}$$

where c and D_p, the elongation rate for protons, depend on the characteristics of hadronic interactions [48]. It follows from Eq. (2.21) that a nearly constant elongation rate $D_A \approx D_p$ is expected for a pure composition for all nuclei. Air shower simulations confirm the independence from the primary mass and the used hadronic interaction model and predict a value around 60 g/cm2/decade [43]. Changes of the elongation rate consequently strongly suggest a change in the primary mass composition.

2.4.3 *Logarithmic mass*

The mean value $\langle X_{\mathrm{max}}\rangle$ of the depth of shower maximum and its dispersion $\sigma(X_{\mathrm{max}})$ can be converted to the first two moments $\langle \ln A\rangle$ and $\sigma^2(\ln A)$ of the log-mass distribution. Refining the

method originally proposed in [49], the mean and dispersion of $X_{\max}$ for a mixed composition have been related by

$$\langle X_{\max} \rangle = \langle X_{\max} \rangle_p + f_E \langle \ln A \rangle \quad \text{and} \tag{2.22}$$

$$\sigma^2(X_{\max}) = \langle \sigma^2_{\text{sh}} \rangle + f_E^2 \, \sigma^2(\ln A) \tag{2.23}$$

to the mean logarithmic mass $\langle \ln A \rangle$ in [50]. Here, $\langle X_{\max} \rangle_p$ is the mean depth of shower maximum for protons, f_E an energy-dependent parameter, and $\langle \sigma^2_{\text{sh}} \rangle$ contains the shower-to-shower fluctuations. Inverting Eqs. (2.22) and (2.23), the first two moments of $\ln A$ are obtained as

$$\langle \ln A \rangle = \frac{\langle X_{\max} \rangle - \langle X_{\max} \rangle_p}{f_E} \tag{2.24}$$

and

$$\sigma^2(\ln A) = \frac{\sigma^2(X_{\max}) - \sigma^2_{\text{sh}}(\langle \ln A \rangle)}{b\sigma_p^2 + f_E^2}, \tag{2.25}$$

where b is a hadronic interaction model specific parameter that is used in the parametrization of σ^2_{sh} as a polynomial in $\ln A$ [51].

A compilation of the average logarithmic mass of cosmic rays derived from the measurements of various experiments until 2013 is shown in Fig. 2.12. The turning points of changes in the composition coincide with the breaks in the energy spectrum which have been discussed in Section 2.2. Above the knee at about 10^{15} eV, the mean logarithmic mass becomes increasingly heavier and reaches a maximum near the second knee around 10^{17} eV. During the next decade until the ankle, a transition towards a lighter composition followed by a trend towards a heavier composition at the highest energies is observed [45, 48].

2.4.4 *Auger X_{max} measurements*

In the energy range above the second knee up to the highest energies, the distribution of the depth of maximum as a function

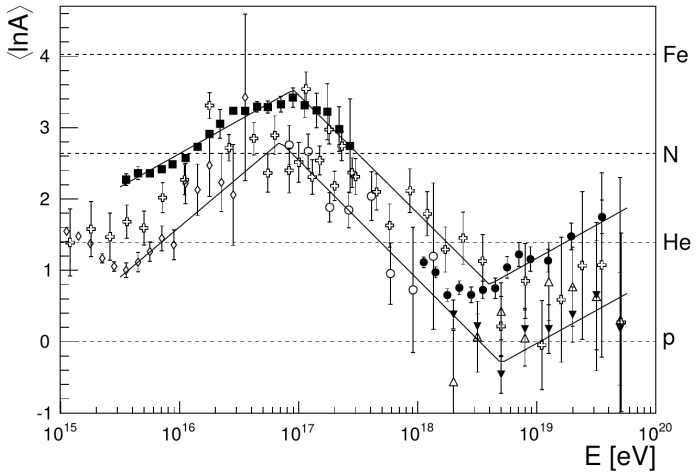

Figure 2.12: Average logarithmic mass of cosmic rays as a function of energy derived from X_{max} measurements with optical detectors for the QGSJETII [52] hadronic interaction model. Lines are estimates on the experimental systematics, i.e. upper and lower boundaries of the data presented. From [48].

of energy has been measured by the modern CR experiments of TA and Auger. Although the mass composition that is inferred by TA differs from the one obtained by Auger, the TA results on $\langle X_{max} \rangle$ are consistent with the ones of Auger within the uncertainties stated by the two experiments [42].

The means and standard deviations of the X_{max} distributions measured by the Pierre Auger Observatory with its fluorescence detector are shown as a function of energy in Fig. 2.13. Since detector effects, such as the detector resolution and the inhomogeneous X_{max} acceptance within the tails of the X_{max} distributions, have been removed, they can be compared directly with predictions of air shower simulations [53]. Additionally, the evolution of the mean logarithmic mass and its dispersion that is in-

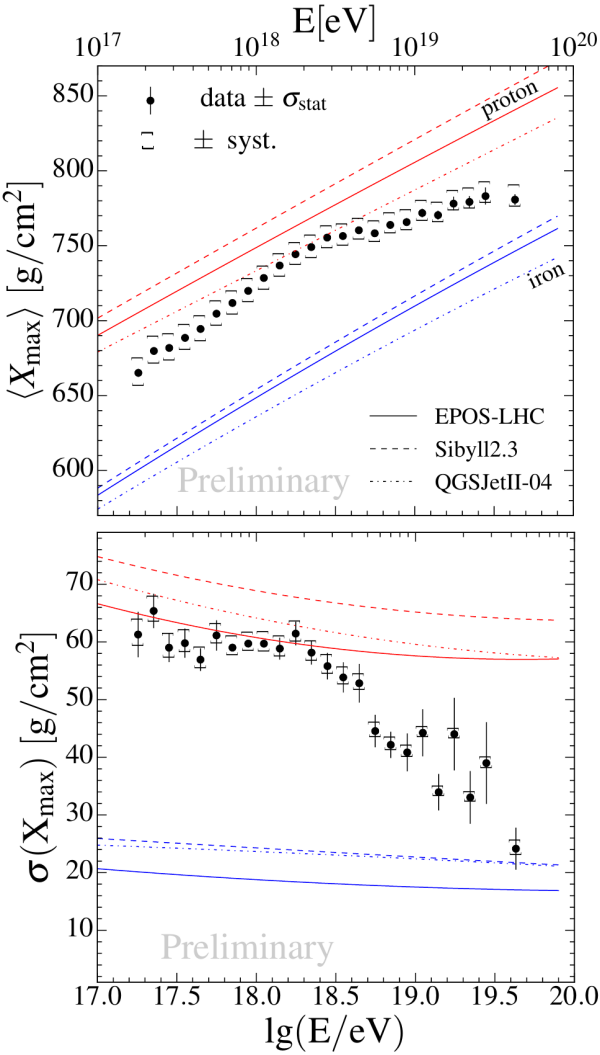

Figure 2.13: The mean (top) and the standard deviation (bottom) of the measured X_{max} distributions as a function of energy compared to air-shower simulations for proton and iron primaries. From [53].

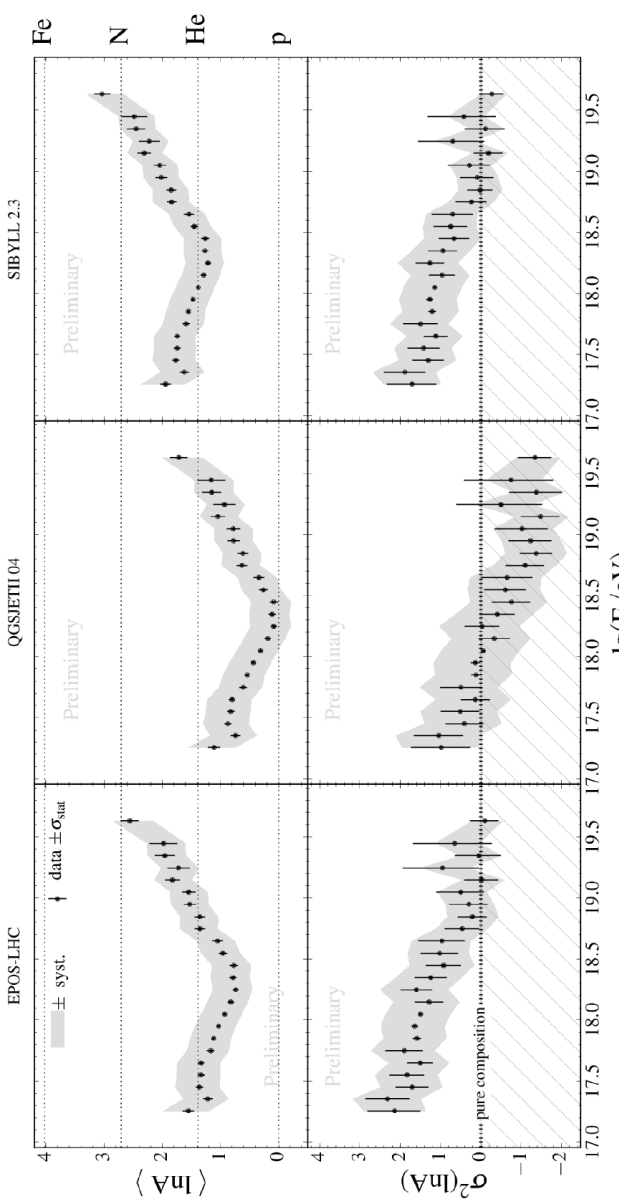

Figure 2.14: The mean (top) and the variance (bottom) of ln A estimated from data with the EPOS-LHC [54] (left), QGSJETII-04 [52] (middle), and SIBYLL2.3 [55] (right) hadronic interaction models. From [53].

ferred from the $\langle X_{\mathrm{max}} \rangle$ and $\sigma(X_{\mathrm{max}})$ values measured by Auger for three hadronic interaction models is displayed in Fig. 2.14.

Both the comparison of the mean $\langle X_{\mathrm{max}} \rangle$ values with model expectations and the derived mean logarithmic masses $\langle \ln A \rangle$ indicate that the composition evolves towards a very light composition between $10^{17.2}$ eV and $10^{18.33}$ eV. The data on the dispersion of the X_{max} distributions are compatible with both a light and a mixed composition at low energies. Being larger than the expectation of approximately 60 g/cm2/decade, the observed elongation rate of 79 ± 1 g/cm2/decade provides a model-independent confirmation that the mean primary mass is becoming lighter until a break at at $10^{18.33 \pm 0.02}$ eV. The evolution of the average logarithmic mass and the significantly smaller elongation rate of about 26 ± 2 g/cm2/decade indicate that the composition becomes again heavier towards higher energies. Furthermore, the decrease of $\sigma(X_{\mathrm{max}})$ and $\sigma(\ln A)$ above $10^{18.33}$ eV indicate a rather pure and heavy composition with a decreasing relative fraction of protons [53].

2.4.5 *Implications for astrophysical models*

The evolution of the average mass of cosmic rays towards a lighter composition between $10^{17.2}$ eV and $10^{18.33}$ eV is qualitatively consistent with a transition from a heavy galactic component to a light extragalactic component which gets increasingly heavy for energies above the break at $10^{18.33}$ eV [43].

These observations disfavor both the ankle model and the dip model, discussed in Section 2.2.3, to explain the transition from galactic to extragalactic cosmic rays. While the ankle model predicts a heavy galactic component at the energy of the ankle, all experimental data show a light composition here [39]. The dip model, requiring a pure proton composition of the extragalactic cosmic rays, is in conflict with the increasingly heavy mass composition at the highest energies. In contrast, mixed composition

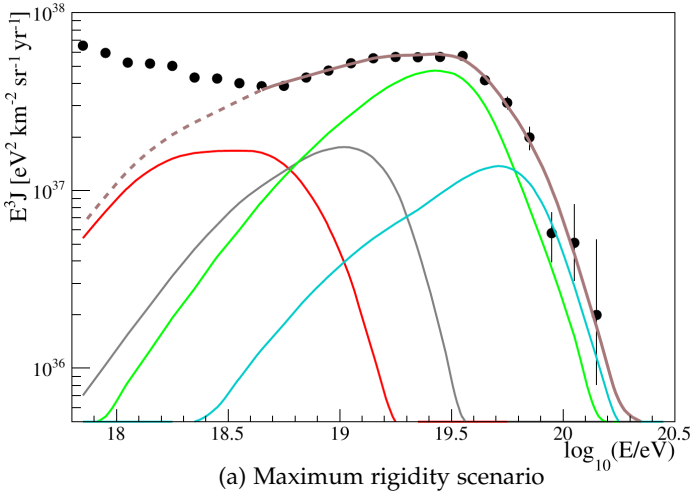

(a) Maximum rigidity scenario

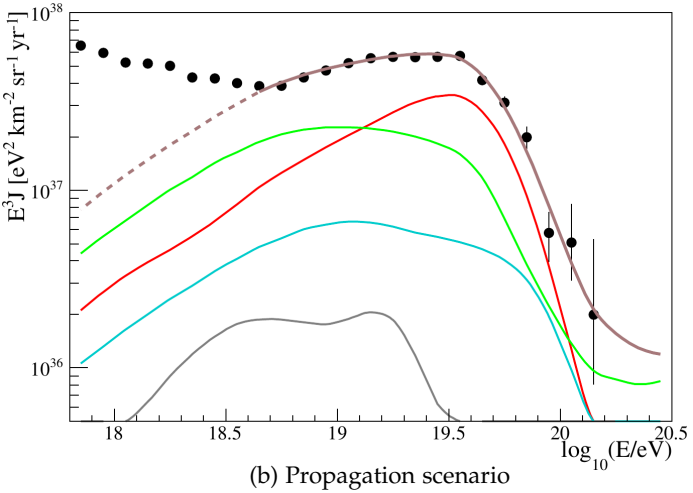

(b) Propagation scenario

Figure 2.15: Contributions of different mass groups (protons - red, helium - gray, nitrogen - green, iron - blue) to the energy spectrum measured by Auger within two distinct astrophysical scenarios: (a) maximum-rigidity scenario, (b) photo-disintegration scenario. From [56].

models can consistently describe the energy spectrum and X_{max} distributions that have been measured by Auger.

However, while estimations of the mean logarithmic mass are possible, the contribution of individual elements cannot be inferred unambiguously from the data. A combined fit to both the energy spectrum and mass composition data measured by the Pierre Auger Observatory with an astrophysical model of sources of UHECRs at energies above the ankle demonstrates that both a photo-disintegration scenario and a maximum-rigidity scenario can provide a good description of the data [56].

The distinct energy evolution of the mass composition for both models, consisting of a mix of p, He, N and Si, is displayed in Fig. 2.15. While in the model of Fig. 2.15a photo-disintegration effects are assumed to cause the flux suppression, the maximum-rigidity model (Fig. 2.15a) explains the observed cutoff by both the maximum acceleration energies and the energy losses during extragalactic propagation [43].

Within the energy range up to $10^{19.2}$ eV that is well covered by fluorescence measurements, the predictions of $\langle X_{\mathrm{max}} \rangle$, $\sigma(X_{\mathrm{max}})$ and the muonic shower content are very similar for both models. However, the extrapolations to higher energies into the flux suppression region are significantly different [57]. The installation of additional muon-sensitive detectors within the upgrade of the Pierre Auger Observatory, discussed in Chapter 3, will provide the possibility of mass composition studies with an enhanced sensitivity and constrain different astrophysical models in the energy region from the ankle up to the highest energies.

3 THE PIERRE AUGER OBSERVATORY

The Pierre Auger Observatory, being in operation since 2004, is the world's largest cosmic rays observatory. It is located in the province of Mendoza (Argentina) in a vast high plain with a mean altitude of 1400 m. The objectives of the observatory are to probe the origin and characteristics of ultra-high energy cosmic rays by performing precise measurements of the flux, composition and anisotropy for primary energies above 10^{17} eV. A key feature is its hybrid construction, combining a large surface detector and a fluorescence detector, which allows to observe air showers simultaneously by two complementary techniques.

In Section 3.1, we give an overview of the surface detector including the trigger system, the shower geometry reconstruction, and the estimation of the primary energy. We continue with the fluorescence detector in Section 3.2 and discuss the upgrade of the Pierre Auger Observatory in Section 3.3. The AMIGA extension, being a part of the upgrade, is reviewed in Section 3.4.

3.1 SURFACE DETECTOR

The surface detector (SD) is composed of a 3000 km^2 triangular grid, comprising 1660 water-Cherenkov detectors (WCDs) with a mutual spacing of 1500 m and a smaller array of 23.5 km^2 with 61 stations that are separated by 750 m each. It is overlooked by 27 fluorescence telescopes that are located at four sites on its periphery. The hybrid design of the Pierre Auger Observatory is illustrated in Fig. 3.1.

An SD station consists of a water tank with an area of 10 m^2 and a height of 1.2 m. Twelve tons of ultra-pure water are contained within a sealed liner with a reflective inner surface. Three

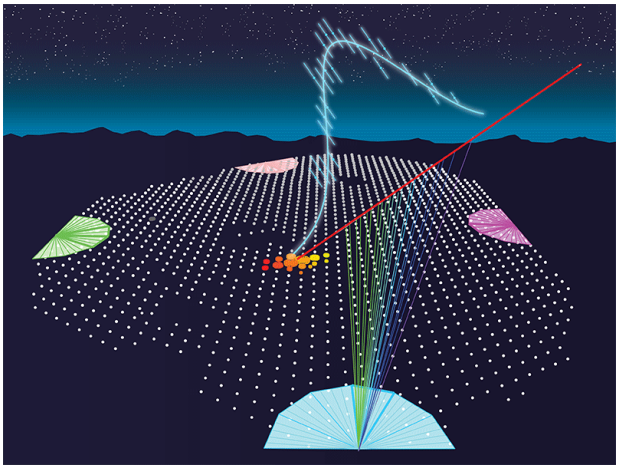

Figure 3.1: Visualization of the hybrid design of the Pierre Auger Observatory, comprising a large SD array on the surface and 27 fluorescence telescopes located at four sites on its periphery. While the SD detects secondary particles that are produced during the shower development, the FD overlooks the array and measures the longitudinal shower profile in the atmosphere. From [58] (APS/Carin Cain).

photomultiplier tubes (PMTs) that are symmetrically mounted on the surface of the liner record the Cherenkov light which is produced by relativistic charged particles in the water or by high energy photons converting into electron-positron pairs in the water volume. Each station is self-contained with a solar power system supplying the PMTs and the station electronics. A schematic view of a WCD with its main components is shown in Fig. 3.2.

At energies above 10^{19} eV, the footprint of an air shower on the ground extends over more than 25 km^2. A trigger system ensures to distinguish real showers that are well contained within the array from background signals from low energy air showers. Subsequently, the geometry of the shower and the energy of the primary CR particle can be reconstructed from the distribution of the signals and their timing information over the array [59].

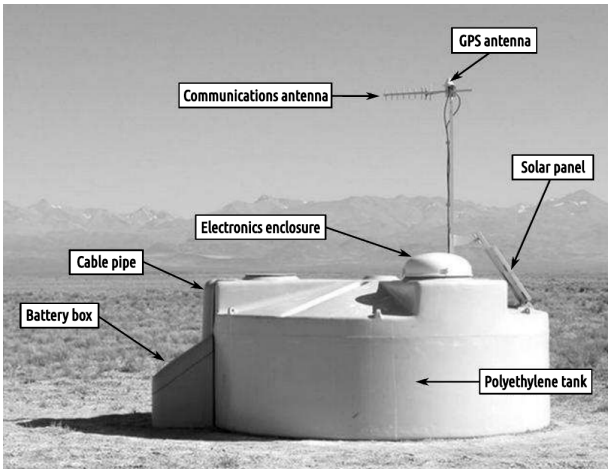

Figure 3.2: A schematic view of a surface detector station in the field, showing its main components. From [59].

TRIGGER SYSTEM The hierarchical trigger system for the SD array starts at a single station level where two kinds of triggers are formed. The *T1* trigger either requires the coincidence of all three PMTs above a certain threshold (simple threshold trigger *TH*) or the coincidence of two PMTs above a lower threshold but with a signal extending above a defined minimum time span (time-over-threshold trigger *ToT*). All ToT-T1 triggers are promoted to the next higher *T2* level, whereas TH-T1 triggers are requested to pass a further higher threshold in coincidence among the three PMTs.

The T3 trigger is formed at the central data acquisition system (CDAS) by combining the spatial and temporal information of the T2 triggers and initiates the data acquisition from the array. It requires the coincidence of at least three detectors that have passed the ToT condition or at least four detectors with any T2 that meet the requirement of a minimum of compactness on the triangular grid.

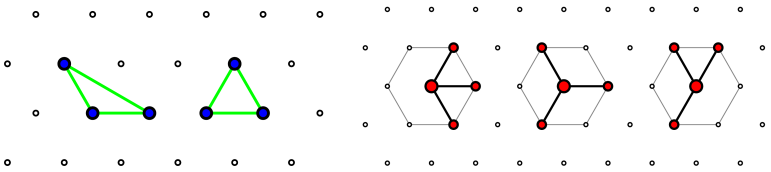

(a) 3TOT configurations (b) Minimal 4C1 configurations

Figure 3.3: The possible configurations of the T4 physics trigger. All symmetry transformations of the triangular grid are additional valid T4 configurations. From [60].

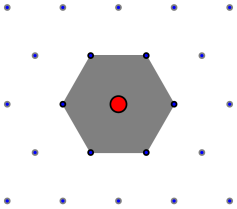

Figure 3.4: The T5 fiducial trigger configuration. The central station (red) with the largest signal is surrounded by six functioning stations. From [60].

Two additional offline triggers ensure a good data quality for physics analyses. The T4 trigger distinguishes real showers from background signals from low energy air showers within the stored T3 data. The possible configurations of the T4 trigger are illustrated in Fig. 3.3. The 3ToT criterion (Fig. 3.3a) requires three nearby T2-ToT triggered stations in a triangular pattern while the 4C1 condition (Fig. 3.3b) requires four nearby stations with T2 triggers of any kind. In both cases, the timing information of the stations need to fit to a plane shower front moving at the speed of the light.

The fiducial T5 trigger (also referred to as 6T5) requires that the station with the highest signal is surrounded by a working hexagon as shown in Fig. 3.4. Thereby, it guarantees the selection

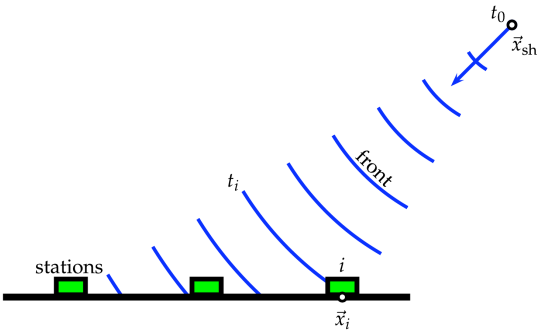

Figure 3.5: Reconstruction of the shower geometry: schematic representation of the evolution of the shower front. From [59].

of events that are well contained within the array, assuring the accurate reconstruction of the impact point on the ground [61].

SHOWER GEOMETRY The arrival direction of the shower is approximated by fitting the start times of the signals of the individual SD stations to a plane front or, in case of a sufficient number of triggered stations, to a more detailed model of a sphere inflating with the speed of light

$$c\,(t_i - t_0) = |\vec{x}_{\mathrm{sh}} - \vec{x}_i| \tag{3.1}$$

where $\vec{x}_i$ are the station positions. and $\vec{x}_{\mathrm{sh}}$ and t_0 are the virtual origin and start-time of the shower development as illustrated in Fig. 3.5.

The impact point $\vec{x}_{\mathrm{gr}}$ of the air shower on the ground, the so-called *shower core*, is calculated by fitting a Nishimura-Kamata-Greisen lateral distribution function (LDF) [62, 63]

$$S(r) = S(r_{\mathrm{opt}}) \left(\frac{r}{r_{\mathrm{opt}}}\right)^{\beta} \left(\frac{r + r_1}{r_{\mathrm{opt}} + r_1}\right)^{\beta+\gamma} \tag{3.2}$$

to the signals of the SD stations at ground. Here, r_{opt} (equals 1000 m for the SD-1500 and 450 m for the SD-750 array) is the *optimum distance*, $r_1 = 700$ m, and $S(r_{\mathrm{opt}})$ corresponds to the *shower*

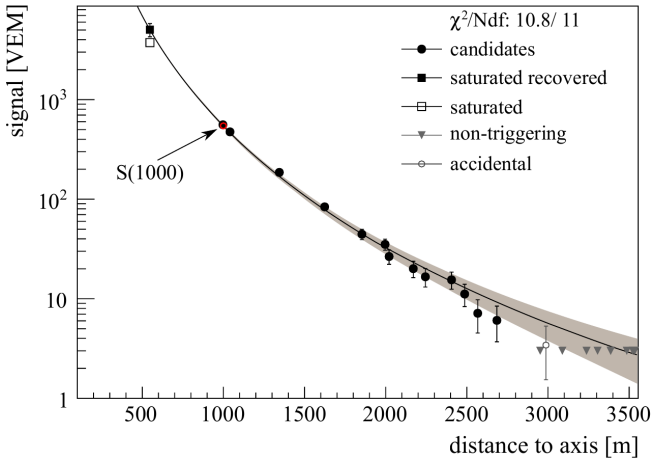

Figure 3.6: Fit of the lateral distribution function to the signals of the SD stations at ground for an example event. From [59].

size which is used for the estimation of the primary energy. For events with only three stations, β and γ are fixed to parametrized values; otherwise they are left as free fit parameters. In addition to SD stations with signals, the maximum likelihood fit of the LDF takes into account stations that did not trigger and stations close to the shower core with saturated signal traces as illustrated in Fig. 3.6.

The shower axis

$$\hat{a} = \frac{\vec{x}_{\mathrm{sh}} - \vec{x}_{\mathrm{gr}}}{\left|\vec{x}_{\mathrm{sh}} - \vec{x}_{\mathrm{gr}}\right|} \tag{3.3}$$

is calculated from the virtual shower origin $\vec{x}_{\mathrm{sh}}$ and the shower impact point on the ground $\vec{x}_{\mathrm{gr}}$. For events with more than three stations, the angular resolution is better than 1.6°, and better than 0.9° for events with more than six stations [59].

ENERGY CALIBRATION After correcting for its zenith angle dependence, the shower size $S(1000)$ is employed to estimate the

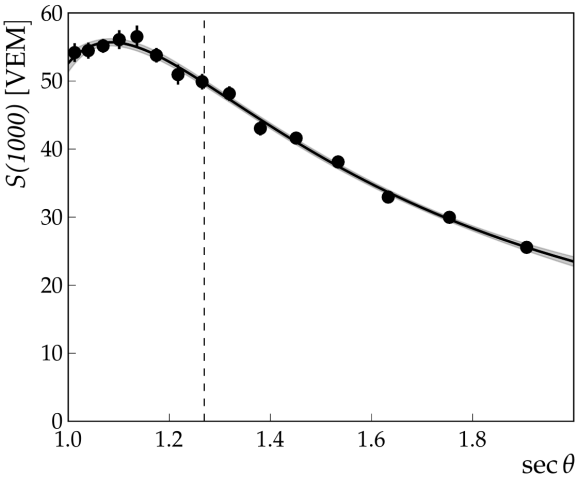

Figure 3.7: Attenuation curve described by a third degree polynomial in $x = \cos^2\theta - \cos^2\theta_{\text{ref}}$ with $\theta_{\text{ref}} = 38^\circ$ (dashed vertical line). Example for a CIC cut value of $S_{38} \sim 50$ VEM which corresponds to an energy of about 10.5 EeV. From [59].

shower energy by the calibration with FD measurements of the calorimetric energy. The decrease of $S(1000)$ as a function of the zenith angle θ, caused by the attenuation of the shower particles in the atmosphere, is shown in Fig. 3.7. By means of the constant intensity cut (CIC) method [64], the attenuation can be fitted with a third degree polynomial

$$f_{\text{CIC}}(\theta) = 1 + ax + bx^2 + cx^3 \tag{3.4}$$

in $x = \cos^2\theta - \cos^2\theta_{\text{ref}}$. In this way, the zenith angle dependence of the shower size can be removed by converting $S(1000)$ to

$$S_{38} \equiv {}^{S(1000)}/_{f_{\text{CIC}}(\theta)}, \tag{3.5}$$

corresponding to the signal the shower would have produced had it arrived at the median angle $\theta_{\text{ref}} = 38^\circ$ of the zenith angle range $0^\circ \leq \theta \leq 60^\circ$. In the case of the SD-750 array, the shower size

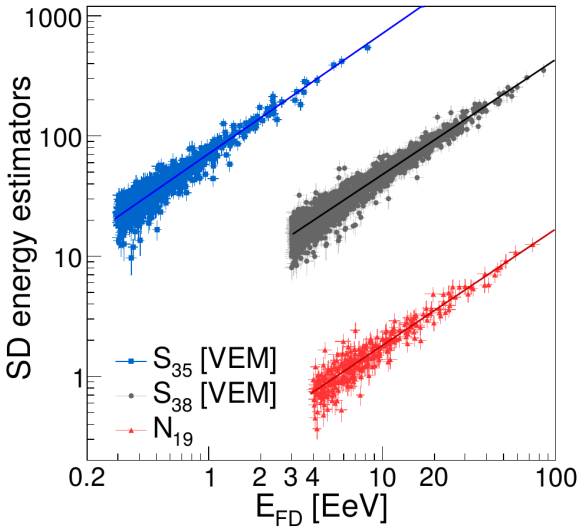

Figure 3.8: Correlation between the SD energy estimators S_{38}, S_{35}, N_{19} and the FD energy. From [43].

$S(450)$ at the optimum distance of 450 m is converted into S_{35} at the median angle of $\theta_{\text{ref}} = 35^\circ$ for the smaller zenith angle range $0^\circ \leq \theta \leq 55^\circ$. For showers with large zenith angles $62^\circ \leq \theta \leq 80^\circ$, the relative muon content N_{19} with respect to a simulated proton shower with energy 10^{19} eV is employed to estimate the shower energy [65].

The shower size obtained from the SD is related to the almost calorimetric measurement of the shower energy from the FD with the hybrid detection of showers by both the FD and the SD. To ensure the high quality of the events, strict quality and field of view cuts for the FD are employed (for details see [59]). The calibration fits

$$E_{\text{FD}} = A \left(S_{38}/\text{VEM}\right)^B , \tag{3.6}$$

relating S_{38} (SD-1500) and S_{35} (SD-750) to the energy E_{FD} measured by the FD, are shown in Fig. 3.8. Here, one vertical-equivalent

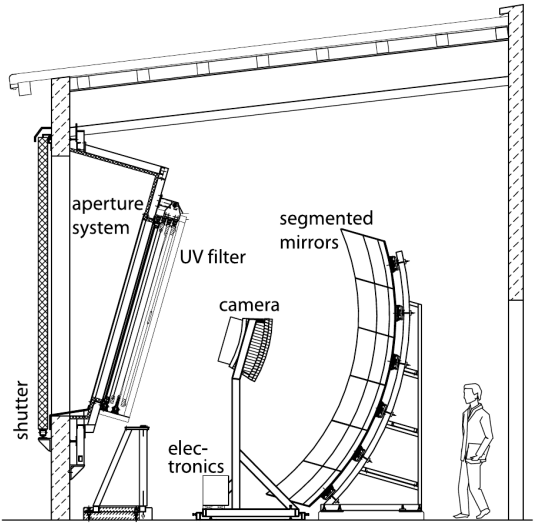

Figure 3.9: Schematic view of a fluorescence telescope with a description of its main components. From [59].

muon (VEM) corresponds to the charge deposited in the WCD by a vertical and central throughgoing muon. The SD energy estimator

$$E_{\mathrm{SD}} = A \left(S_{1000}/f_{\mathrm{CIC}}/\mathrm{VEM}\right)^{B} \tag{3.7}$$

is used for the energy estimation of events that are detected by the SD but not by the FD, exhibiting a low duty cycle of 15% only. The relative systematic uncertainty $\sigma_{E_{\mathrm{SD}}}/E_{\mathrm{SD}}$, is about 14% [43, 59].

3.2 FLUORESCENCE DETECTOR

The fluorescence detector (FD) measures the longitudinal development of air showers by detecting the ultra-violet fluorescence light that is induced by the energy deposit of charged particles in the atmosphere. The SD array is overlooked by 24 fluorescence telescopes from four sites at its periphery as shown in Fig. 3.10.

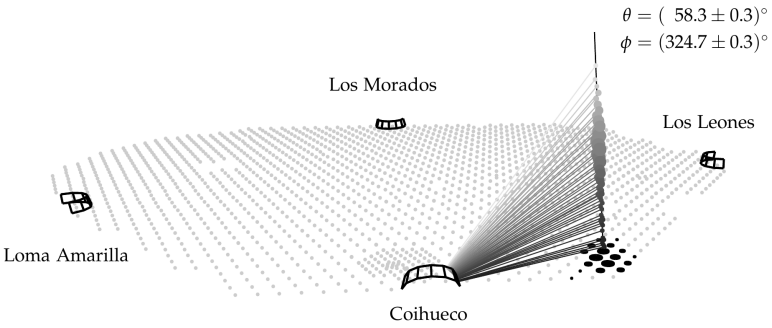

Figure 3.10: Event geometry. Pixel viewing angles are shown as shaded lines and the shower light and SD signals are illustrated by markers of different size in logarithmic scale. From [66].

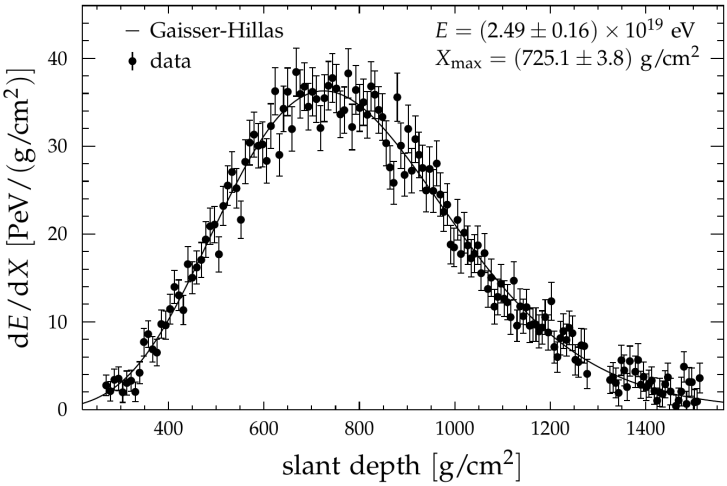

Figure 3.11: Longitudinal profile (dots) and Gaisser-Hillas function (line). From [66].

At each site, six independent telescopes collect the fluorescence light of air showers over an aperture of $3.8\,\mathrm{m}^2$ each. A schematic view of a fluorescence telescope is given in Fig. 3.9. A segmented spherical mirror with a surface of $13\,\mathrm{m}^2$ focuses the light onto a PMT camera. Spherical aberrations of the shower image on the camera are minimized by corrector lenses. The camera covers 30° in azimuth and elevations from 1.5° to 30° above the horizon. Since the FD operates only during dark nights and under good meteorological conditions, which are continuously monitored, the duty cycle is only about 15%.

The arrival direction of a shower is reconstructed with a precision of about 0.6° from the arrival times of the shower light as a function of the viewing angle and from the SD measurements of the arrival time of the shower front at ground level. The time-dependent PMT signals of the telescope cameras are then projected to the shower axis and, given the distance to the shower, the light emitted by the air-shower particles along the shower axis is calculated.

The shower maximum and the total energy are obtained from a log-likelihood fit using the Gaisser-Hillas function [67]

$$f_{\mathrm{GH}} = \left(\frac{\mathrm{d}E}{\mathrm{d}X}\right)_{\mathrm{max}} \left(\frac{X - X_0}{X_{\mathrm{max}} - X_0}\right)^{\frac{X_{\mathrm{max}} - X_0}{\lambda}} e^{\frac{X_{\mathrm{max}} - X}{\lambda}} \tag{3.8}$$

for the description of the dependence of the energy deposit on the slant depth as illustrated in Fig. 3.11. The total shower energy is obtained by the integration of f_{GH} and the subsequent correction for the "invisible" energy of 10 to 15% that is carried away by neutrinos and muons.

In addition to the standard FD telescopes with a field of view up to 30° in elevation, three fluorescence telescopes covering the elevation range from 30° to 58° were built in front of the FD site at Coihueco (see Fig. 3.10). Enabling an unbiased detection of nearby low-energy showers in combination with the SD-750 array, the High Elevation Auger Telescopes (HEAT) have extended the

energy range of high quality hybrid air shower measurements down to 10^{17} eV [59].

3.3 AUGERPRIME UPGRADE

In order to provide additional measurements of mass composition-sensitive observables up to energies of the flux suppression region, an upgrade of the Pierre Auger Observatory, named AugerPrime, is currently carried out. Its main goal is to constrain astrophysical models in the energy region of the ankle and to elucidate the origin of the flux suppression.

The key part of the upgrade is the installation of a new plastic scintillation detector, named the surface scintillator detector (SSD), above each of the existing WCDs of the full 3000 km^2 array of the SD. Due to the different responses of the WCD and the SSD to muons and electromagnetic particles, the sampling of the secondary shower particles with both detectors allows for the reconstruction of the electromagnetic and muonic shower component.

An SSD consists of two scintillator modules with a total area of 3.8 m^2. The light produced in the 1 cm thick scintillator segments of both modules is guided by wavelength-shifting (WLS) fibers to a PMT. A schematic view of an SSD and a station of the AugerPrime engineering array are shown in Fig. 3.12. The Auger upgrade comprises the upgrade of the SD stations with new electronics that process both the WCD and SSD signals. Together with an additional small PMT inserted in the WCD, the dynamic range of the WCD is enhanced by a factor of 32 [68].

In addition to the installation of SSDs, a network of underground muon detectors is deployed in the SD-750 array as part of the AMIGA extension. It will provide direct measurements of the muon content of a sub-sample of extensive air showers falling into the SD-750 array and serve for the verification and fine-tuning of the methods used to extract muon information from the combined SSD and WCD signals. Moreover, the availability of muon information on an event-by-event basis will allow to study the fea-

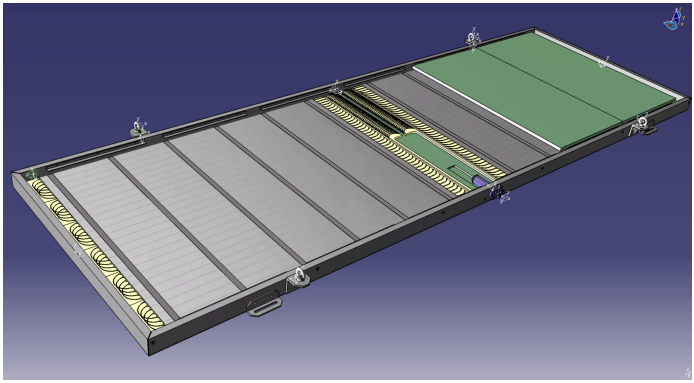

(a) Layout of the surface scintillator detector (SSD)

(b) One station of the AugerPrime engineering array

Figure 3.12: An SSD upgrade detector consists of two scintillator modules with a total area of 3.8 m^2 that are mounted on top of a WCD. From [68].

tures of hadronic interactions. The AMIGA extension is discussed in detail in Section 3.4.

The upgrade of the Auger Engineering Radio Array (AERA) enhancement of the Pierre Auger Observatory will be a further part of AugerPrime. With more than 150 autonomous antenna stations, covering an area of about $17\,\mathrm{m}^2$, AERA is currently the largest antenna array for air-shower detection [69]. The radio upgrade of AugerPrime foresees to equip each SD station of the full Auger array with an antenna. The reconstruction of shower parameters as the direction, energy, and, especially, the depth of shower maximum will increase the composition sensitivity for large zenith angles, for which the scintillator upgrade is not effective.

To demonstrate the potential of AugerPrime, two astrophysical benchmark models have been chosen as representations of a maximum-rigidity scenario and of a photo-disintegration scenario. In Section 2.4.5, we discussed that although both scenarios approximately reproduce the spectrum and the $\langle X_{\mathrm{max}} \rangle$ and $\sigma(X_{\mathrm{max}})$ measured by the Pierre Auger Observatory so far, their energy-dependent mass composition is very different. The discrimination power of the additional information that will be provided by AugerPrime is illustrated in Fig. 3.13. While the mean depth of shower maximum $\langle X_{\mathrm{max}} \rangle$, its fluctuations $\sigma(X_{\mathrm{max}})$, and the relative muon number R_μ are very similar in the energy range up to $10^{19.2}\,\mathrm{eV}$, which is well covered by FD measurements, the two scenarios can be distinguished with high significance and statistics in the energy region of the flux suppression [57].

3.4 AMIGA MUON DETECTOR

As part of the upgrade of the Pierre Auger Observatory, scintillation detectors with an area of $30\,\mathrm{m}^2$ will be buried next to each of the 61 WCDs of the SD-750 array. The Auger Muons and Infill for the Ground Array (AMIGA) enhancement will provide direct measurements of the shower muon content and its time structure

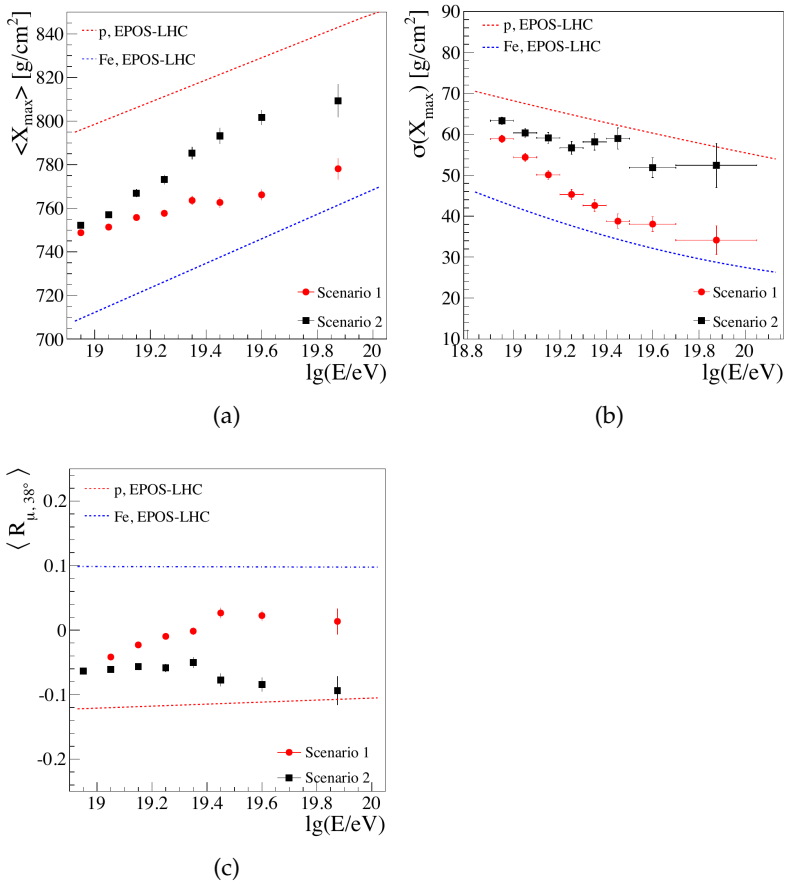

Figure 3.13: Reconstructed mean depth of shower maximum $\langle X_{\mathrm{max}} \rangle$ (a) and its fluctuations (b), and the mean relative number of muons at 38° (c) using only SD data. Shown are the two scenarios: (1) maximum-rigidity model, (2) photo-disintegration model. The number of muons is given relative to that expected for an equal mix of p-He-CNO-Fe as primary particles. From [57].

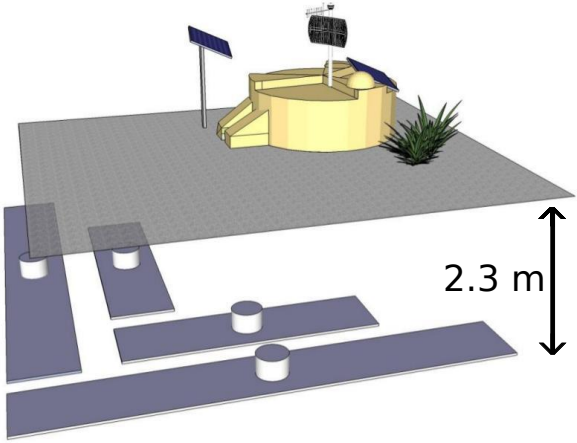

Figure 3.14: Scheme of an AMIGA muon counter composed by two $5\,m^2$ and two $10\,m^2$ plastic scintillator modules buried at a depth of 2.3 m next to a WCD at the surface.

for showers that fall into the SD-750 array. After its completion in 2019, AMIGA will record data until 2025 [57].

A schematic view of an AMIGA detector is shown in Fig. 3.14. The total detection area of $30\,m^2$ is segmented into plastic scintillator modules of $5\,m^2$ and $10\,m^2$ that are arranged in a perpendicular layout. The scintillators are buried underground at a depth of 2.3 m to absorb the electromagnetic shower component and let only pass muons. The soil shielding causes an energy detection threshold of $1\,\mathrm{GeV}/\cos(\theta)$ for muons with zenith angle θ.

Since the end of 2014, the AMIGA engineering array, sketched in Fig. 3.15, is fully operational. It consists of seven muon detectors that are arranged in a hexagonal layout around the SD station with ID 1622 (dubbed Phil Collins). In addition to five $30\,m^2$ muon counters, two twin counters of double size were installed to assess the muon counting accuracy. At the central counter (PC), two additional modules of $10\,m^2$ size were buried at a smaller depth of 1.3 m to study the effect of the soil shielding [5].

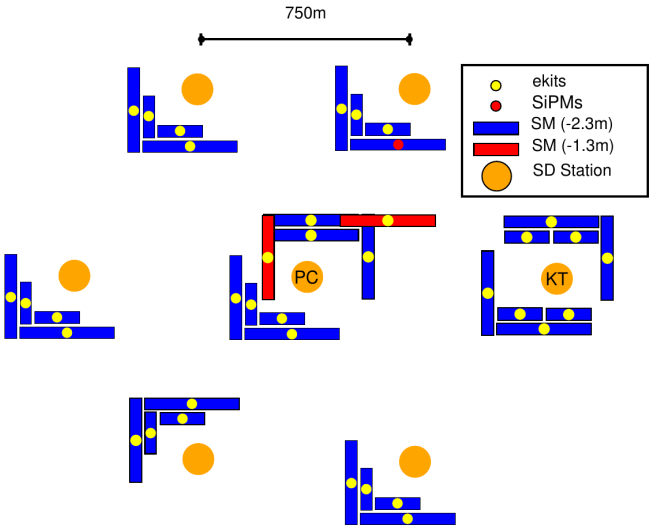

Figure 3.15: The AMIGA engineering array as of 2015, consisting of five 30 m^2 muon counters buried 2.3 m underground and two twin counters of double size. Two additional 10 m^2 modules (red) are buried at 1.3 m depth to study soil shielding effects. From [5].

While the detectors of the engineering array have been equipped with photomultiplier tubes (PMTs), the final design of AMIGA foresees to replace PMTs by silicon photomultipliers (SIPMs). This change is motivated by the lower costs, longer lifetime, better sturdiness, and higher photon detection efficiency compared to PMTs as well as the absence of optical cross-talk between neighboring channels. However, SIPMs exhibit a higher noise rate and temperature dependence [70].

Since we analyze data recorded by the AMIGA engineering array with its original PMT design in this thesis, we focus on the description of the PMT electronics setup in Section 3.4.2. Details on the proposed electronics and calibration method for SIPMs can be found in [70]. The mechanical design of the detectors and the

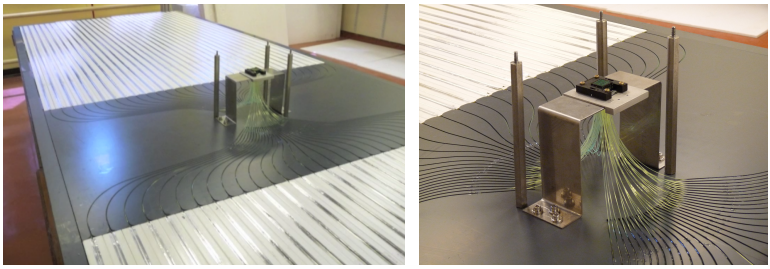

Figure 3.16: 10 m^2 AMIGA scintillator module (without casing). The module is segmented into 2 $\times$ 32 scintillator bars on both sides of the central PMT. Wavelength-shifting fibers that are glued lengthwise into a groove of each bar transport the scintillation light to the PMT.

event acquisition procedure remain unchanged by the installation of SIPMs.

3.4.1 *Mechanical design*

The AMIGA modules are segmented into 64 scintillator bars that are 4 cm wide, 1 cm thick, and 2 m (4 m) long for the 5 m^2 (10 m^2) modules. On each side of the electronics setup, mounted at the module center as shown in Fig. 3.16, 32 bars are arranged. They are made out of extruded Dow Styron 663W polystyrene doped by weight with 1% PPO (2,5-diphenyloxazole) and 0.03% POPOP (1,4-bis(5-phenyloxazole-2-yl)benzene). Since the attenuation length of the scintillators is 55 ± 5 mm for the fast component and $\sim$24 cm for the slow component, the scintillation light is transported by wavelength-shifting (WLS) optical fibers to the central 64 multi-pixel PMT. The WLS fibers of 1.2 m diameter are glued lengthwise into a groove of each bar with an optical cement that matches the refractive index of the fiber and the scintillator. Except for the 2 mm groove, the scintillator bars are completely coated with TiO2 as an outer layer for reflectivity [71].

The detection principle of a muon hitting the scintillator is illustrated in Fig. 3.17. The muon deposits energy in the base of the plastic scintillator (polystyrene) which is dominantly transferred to the primary PPO fluor via resonant dipole-dipole interactions strongly coupling the base and the fluor. The primary fluor re-radiates the observed energy at wavelengths where the base is more transparent. Additionally, it shortens the decay time and increases the total light yield [72]. The attenuation length in the scintillator is further increased when the emitted light is absorbed by the second fluor POPOP whose absorption spectrum is adjusted to the emission spectrum of the emitting primary fluor. Acting as a wavelength shifter with an emission maximum at around 420 nm, the emitted light is finally absorbed and transported to the PMT by the WLS optical fibers [71].

3.4.2 *Electronics*

The AMIGA muon detectors are designed to count individual muons in synchronization with the associated SD station. The electronics therefore consists of two parts: the underground electronics installed in each buried module, and the surface electronics at the SD station which is common to all muon counter modules and serves as an interface with the SD electronics. It handles both the communication with the underground modules of the muon counter and the central data acquisition system (CDAS) of the observatory.

The underground electronics at the center of each scintillator model includes the PMT, an analog board to digitize the analog pulses from the PMT, a digital board with an field-programmable gate array (FPGA) and memory, as well as a micro-controller board for interface, data transmission and slow control [71].

DIGITIZATION OF ANALOG PULSES The analog board accommodates 64 pre-amplifiers and adjustable-threshold discriminators to convert the analog pulses of each PMT pixel to continuous

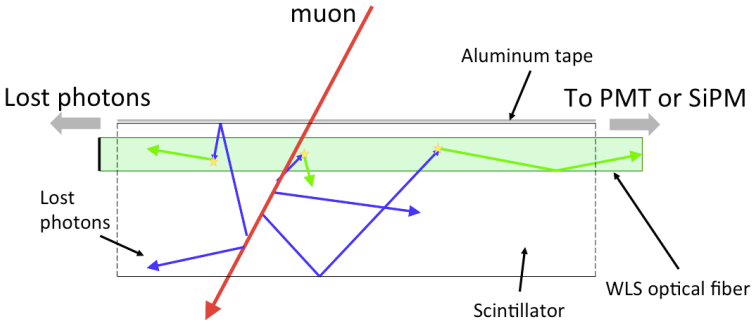

(a) Muon detection principle

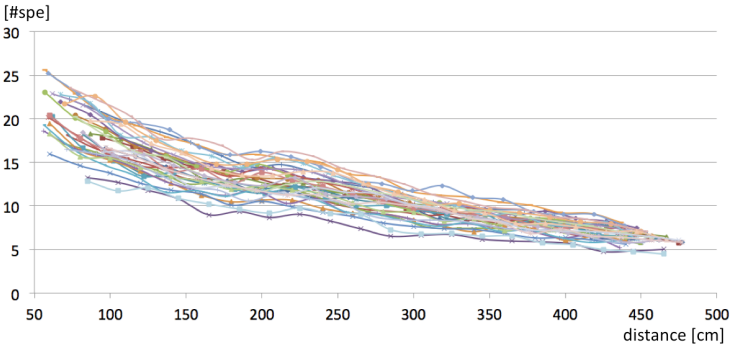

(b) Light attenuation curves

Figure 3.17: (a) Illustration of the detection principle of a muon hitting the scintillator. The emitted scintillation light (blue) is transported to the PMT/SIPM by WLS fibers (green). (b) Light attenuation curves for 32 WLS fibers as a function of the distance to the PMT for a module that was scanned with a radioactive source. From [71].

binary signals. Since the average single photo-electron (SPE) amplitude V_{SPE} can differ up to a factor of 2^{12} between the different PMT pixels, the threshold voltages of the discriminators are individually set to a predefined percentage of V_{SPE} for each pixel.

The FPGA located at the digital board acquires the data from the analog board with a frequency of 320 MHz corresponding to a sampling interval of $1/320\,\mathrm{MHz} = 3.125\,\mathrm{ns}$. Per time bin, one bit per channel is saved in the front-end memory which consists of two circular buffers that can store up to 6.4 µs of data ($2048 \times 3.125\,\mathrm{ns}$). Upon request from the CDAS, the binary traces are recovered and transmitted [73].

The thresholds of the 64 discriminators at the analog board need to be adjusted such that an SPE is represented by a single 1 or two consecutive 1s in the sampled binary trace. Due to the longer analog pulse lengths, muons can be efficiently distinguished from isolated SPEs, which are produced by background or side effects like cross-talk between neighboring channels, by a match of the patterns 101 or 111 in three consecutive time bins [5, 74].

The effect of different discriminator thresholds is illustrated in Fig. 3.18 for the case of stand-alone SPE pulses. Setting the threshold too low might produce two or three adjacent time bins above threshold (1s). On the other hand, too high thresholds cause a loss of counting efficiency since the discriminator digital output might be too short for the FPGA sampling period. Simulations have shown that a discriminator threshold at the level of 30% (red dashed line) of the mean SPE peak amplitude is optimal for the representation of SPEs as a 010 pattern for a sampling period of 3.125 ns.

CHANNEL CALIBRATION Since the AMIGA underground muon detectors are deployed over a large area and will be operated continuously for years, an automated calibration procedure is implemented locally in the field. In the following, we

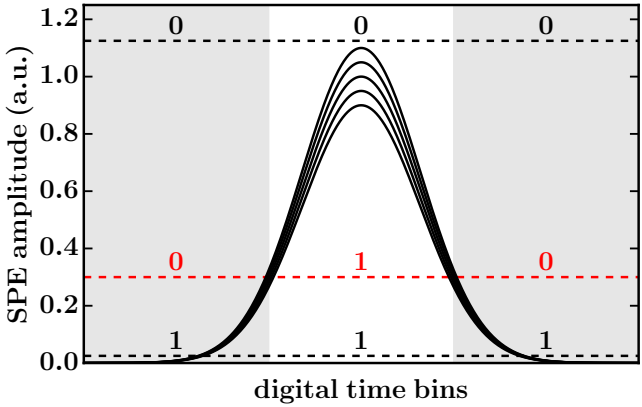

Figure 3.18: Visualization of the effect of different discriminator thresholds on the digitization for the case of stand-alone SPE pulses. A too small threshold (lower dashed line) might produce multiple 1s, too high thresholds (upper dashed line) cause a loss of counting efficiency. Simulations show that a threshold of $\sim 30\% V_{\mathrm{SPE}}$ (red dashed line) is optimal to represent an SPE by a single 1 or two consecutive 1s for a sampling period of 3.125 ns.

describe the calibration for PMTs, details on the strategy for SIPMs can be found in [70].

As motivated in the preceding, the individual discriminator thresholds for each scintillator channel should be set to 30% of the channel-dependent mean single photo-electron amplitude V_{SPE}. However, since V_{SPE} cannot be measured directly, it is inferred from measurements of the background radiation caused by terrestrial radiation, background muons, and PMT dark rate.

Within a period of two hours, the rate of a selected binary pattern, corresponding to a single 1 in a 25 ns time window of eight bins, is measured as a function of the discriminator voltage V_{Thr} for each channel. An example calibration curve for one individual channel is shown in Fig. 3.19a. The threshold voltage V_{010}^{Bck}, for which the rate of the chosen 00001000 pattern (plus permuta-

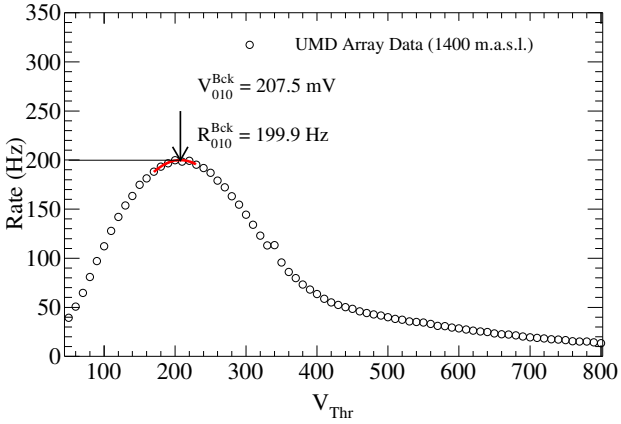

(a) Rate of 010 pattern for one channel

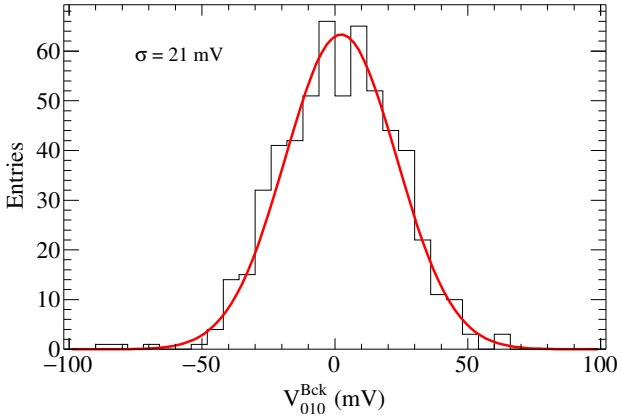

(b) Distribution of V_{010}^{Bck} for all channels

Figure 3.19: Calibration procedure applied in the AMIGA engineering array. (a) Rate curve based on the 010 pattern of an individual scintillator channel. (b) Distribution of V_{010}^{Bck} for the whole engineering array. To superimpose data from all stations, the front-end-dependent mean values have been subtracted from the distributions for each detector module. From [8].

tions) is maximal, corresponds to the peak amplitude of the most probable pulses due to background radiation in the field [8].

The dispersion of the distribution of V_{010}^{Bck} in all channels of the engineering array is shown in Fig. 3.19b. In order to get rid of differences in the photo-multiplier gain as a result of different biases of the PMT high-voltages, the front-end-dependent mean values have been subtracted from the distributions for each detector module. The spread of $\sim$21 mV, which corresponds to $\sim$10% of the mean peak amplitude $\langle V_{010}^{\text{Bck}} \rangle$ of all channels, is mainly a result of the typical gain differences in each PMT pixel [8]. In Section 6.6, we use this dispersion to analyze the systematic uncertainty caused by variations in the calibration of the discriminator threshold.

Laboratory measurements have shown that the channel-specific mean amplitude V_{SPE} can be related to V_{010}^{Bck} by $V_{\text{SPE}} \sim 0.8 \times V_{010}^{\text{Bck}}$. From the scan of the background rates and the determination of V_{010}^{Bck}, the individual discriminator thresholds can hence be set to a predefined percentage of the mean single photo-electron amplitude V_{SPE}. During the data taking period from Oct. 2015 to Oct. 2016 considered in this thesis, the thresholds have been set to 30% of the single photo-electron amplitude V_{SPE}, corresponding to $\sim 0.3 \times 0.8 \times V_{010}^{\text{Bck}}$.

3.4.3 *Event acquisition*

To avoid data loss, the AMIGA counters continuously acquire data, independently of the SD. At any moment, a circular buffer scheme stores the past acquired 2048 bins equal to 6.4 µs of data in each module. However, the data is only transmitted to the CDAS upon triggers from the SD.

If a T1 condition is fulfilled for the associated SD station, a local time stamp (LTS) is generated in the internal FPGA of the local surface station and the trigger signal is, together with the LTS, transmitted to the underground electronics of the muon detector (MD) scintillator modules ((1) to (3) in Fig. 3.20). The event acqui-

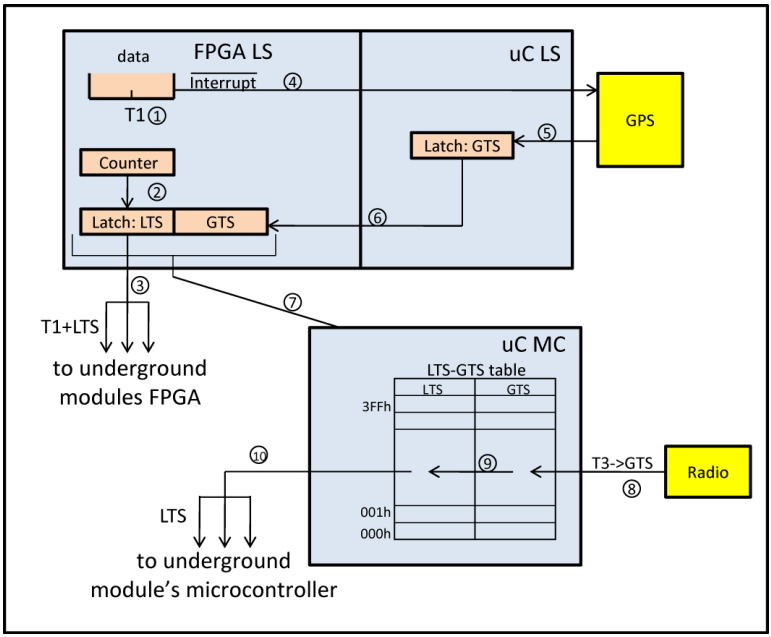

Figure 3.20: Surface electronics synchronization scheme. From event acquisition (1) to (7) to data request (8) to (10). From [73].

sition buffer data of the underground MD modules is then moved to an external random-access memory memory bank which can store up to 2048 events. The associated LTS of the T1 trigger is saved together with the event data.

After the event ending, a second timestamp, the GPS timestamp (GTS), is generated to identify the corresponding SD event and transmitted to the local station FPGA ((4) to (6)). The LTS-GTS pair of the two timestamps is then sent to the MD microcontroller and stored in a look-up table (7).

If an event fulfills the SD high-level T3 condition, a data request is sent to all triggered SD stations. The GTS that is received by the surface-station radio is looked up in the LTS-GTS table of the mi-

crocontroller and, on a match, the corresponding LTS is sent to the MD underground electronics through the ethernet link ((8) to (10)). If the LTS is found in the external memories of the single modules, the data is retrieved and sent to the CDAS of the observatory [73].

In each event, statuses are assigned to the participating MD modules. A module is flagged as *rejected* if some error occurred (detailed in the following), *silent* if the partner SD station is silent and no MD error occurred, and *candidate* in all other cases.

If, on T3 data request, the GTS is not found in the LTS-GTS table of the MD microcontroller (see (8), (9) in Fig. 3.20), the MD modules can be either silent or rejected. All associated MD modules are marked as silent, if the partner SD station is flagged as silent, i.e. did not pass a T1 trigger condition. In contrast, if the SD station is a candidate (but the GTS is no found in the MD table of LTS-GTS timestamps, i.e. some error occurred), all MD modules are rejected.

If, on the contrary, the GTS is found in the LTS-GTS table on T3 data request, the LTS is searched for in the external memories of the underground modules. If the LTS is not found in the random-access memory of a module, it is flagged as rejected. Otherwise, if the LTS is found, the module is considered as candidate if the partner SD station is as well a candidate. If this is not the case, i.e. the LTS is found in the module but the partner SD station is silent or has some error, the MD module is rejected due to the inconsistency between SD and MD.

For candidate modules, an additional module reconstruction status is assigned during the MD reconstruction which is based on the binary time traces. If all channel traces are entirely filled with 0s (not a single 1), the module is flagged as *empty*. On the contrary, a module is considered as *saturated* if in at least one *global* time window (see Section 5.3.2) all channels have a signal. If the module is neither silent nor saturated, it is flagged as *good*.

In the fit of the muon lateral distribution function in Section 5.6, saturated, candidate, and silent modules are distinguished. In

this context, saturated modules refer to candidate modules with a saturated reconstruction status, and candidate modules to non-saturated candidate modules.

4

IMPACT OF MUON DETECTION THRESHOLDS ON THE SEPARABILITY OF PRIMARY COSMIC RAYS

The number of muons in an extensive air shower is a crucial mass-related observable since heavier cosmic ray particles produce a significantly larger muon content. Currently, the Pierre Auger Observatory is carrying out a major upgrade by installing muon-sensitive detectors of different types, as has been discussed in Chapter 3.

As a prerequisite to define the specifics of the upgrade detectors, we analyzed the impact of the muon detection threshold in the range from 0.1 to 10 GeV on the mass separability of extensive air showers. Although larger detection thresholds of muons imply reduced statistics, it is not clear a priori if low-energy muons help to better discriminate between air showers from different primary particles.

In this study, we focus on the energy region where the transition from galactic to extragalactic cosmic rays and a corresponding change in the composition is expected and take $E = 3.16 \times 10^{18}$ eV as a representative primary energy. To explain the observed dependence of the separability of primaries on the detection threshold of muons, we analyze the correlation of N_μ with $X_{\max}$ for different detection thresholds of muons and distances to the shower core.

We do not attempt to do a detailed detector-specific study, but describe general results that are purely based on the underlying physics of air showers. Instead of simulating experiment specific detector responses, we model typical statistical fluctuations in N_μ and $X_{\max}$ since we do not expect large contributions from detector resolution effects [5]. As an outcome of this study, the

decision to deploy simple and cheap scintillation detectors for the upgrade of Auger has been made.

4.1 SIMULATIONS AND METHODS

We used the CORSIKA software package [75] to perform full simulations of extensive air showers without applying a thinning algorithm (i.e. sampling of representative particles) to avoid artificial fluctuations potentially affecting our analysis [76, 77]. For primary protons and iron nuclei, 115 showers with a primary energy of 3.16×10^{18} eV were simulated each. Hadronic interactions at lower energies were modeled with FLUKA [78], and at high energies the EPOS-LHC model [79, 80] was chosen. The zenith angles of the primary particles were fixed to $\theta = 38°$, which corresponds to the median of the zenith angle distribution for showers in a typical range from 0° to 60°. The azimuthal angles φ were generated randomly for each air shower. Due to limited computational resources, we only recorded muons stemming from hadronic interactions with energy $\geq 0.1\,\mathrm{GeV}$ and applied a distance cut w.r.t. the core position of $r_{\mathrm{cut}} = 200\,\mathrm{m}$.

To analyze the dependence of the composition sensitivity on the detection threshold of muons for muon detectors of different sizes, we first determine the "true" muon density in the shower plane. The coordinates where a muon hits the ground are hence projected onto the plane perpendicular to the momentum of the primary cosmic ray particle. For each simulated shower and each detection threshold of muons, we calculate the radius-dependent muon density

$$\rho_\mu = \frac{N_{\mathrm{ring}}}{\pi \left((r + \delta r)^2 - r^2 \right)}, \tag{4.1}$$

where N_{ring} denotes the total number of muons with projected coordinates inside the ring with inner and outer radii r and $r + \delta r$, respectively. Since we simulate the showers without any particle

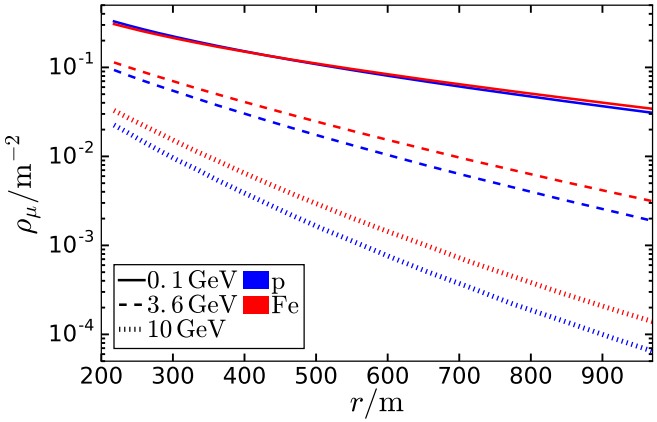

Figure 4.1: Mean lateral muon densities for proton (blue) and iron (red) showers for detection thresholds of muons of $E_{\mathrm{th}} = 0.1, 3.6$ and 10 GeV.

thinning, we fully account for physical shower-to-shower fluctuations in the muon density. We assume no significant azimuthal asymmetries are present.

The number of muons measured by a detector with limited detection area is dominated by a Poissonian probability distribution [5]. We therefore account for fluctuations in the number of muons falling inside the detection area A by sampling from a Poissonian distribution

$$P_\lambda(k) = \frac{\lambda^k}{k!} e^{-\lambda} \quad \text{with} \quad \lambda = \rho_\mu A \tag{4.2}$$

for each radial distance to the shower core and detection threshold of muons. By using unthinned showers, we avoid unphysical fluctuations of the muon density [76]. The obtained muon densities as a function of the radial distance from the shower core are shown in Fig. 4.1 for proton and iron showers and detection thresholds of $E_{\mathrm{th}} = 0.1$, 3.6 and 10 GeV.

We quantify the impact of the detection threshold of muons on the separability between extensive air showers of proton and iron primary cosmic rays, based on the number of muons only, by the figure of merit

$$f_N = \frac{\overline{N}_{\mathrm{Fe}} - \overline{N}_{\mathrm{p}}}{\sqrt{\sigma^2_{N,\mathrm{p}} + \sigma^2_{N,\mathrm{Fe}}}} \tag{4.3}$$

Means $\overline{N}_{\mathrm{p}}$ ($\overline{N}_{\mathrm{Fe}}$) and uncertainties $\sigma_{N,\mathrm{p}}$ ($\sigma_{N,\mathrm{Fe}}$), originating from both the finite detector size and the stochastic nature of the first interaction and subsequent shower development, are determined for each detection threshold of muons, radial distance to the shower core, and detection area.

Additionally, we analyze the dependence of the composition sensitivity on the detection threshold of muons for a bivariate composition analysis using both the N_μ and X_{max} information. The Fisher discriminant ratio

$$f(\vec{\omega}, \vec{\mu}_{\mathrm{p}}, \vec{\mu}_{\mathrm{Fe}}, \hat{\Sigma}_{\mathrm{p}}, \hat{\Sigma}_{\mathrm{Fe}}) = \frac{\left(\vec{\omega}^\top (\vec{\mu}_{\mathrm{p}} - \vec{\mu}_{\mathrm{Fe}})\right)^2}{\vec{\omega}^\top (\hat{\Sigma}_{\mathrm{p}} + \hat{\Sigma}_{\mathrm{Fe}}) \vec{\omega}} \tag{4.4}$$

quantifies the separation between the proton and iron primary classes separated by the linear discriminant $\vec{\omega}$. Here, $\vec{\mu}_{\mathrm{p}} = \left(\overline{N}_{\mathrm{p}}, X^{\mathrm{p}}_{\mathrm{max}}\right)^\top$ ($\vec{\mu}_{\mathrm{Fe}}$) and $\hat{\Sigma}_{\mathrm{p}}$ ($\hat{\Sigma}_{\mathrm{Fe}}$) are the vectors of the means and the covariance matrices of the two classes. This measure is maximized for the discriminant

$$\vec{\omega}^{\mathrm{max}} = \left(\hat{\Sigma}_{\mathrm{p}} + \hat{\Sigma}_{\mathrm{Fe}}\right)^{-1} \left(\vec{\mu}_{\mathrm{p}} - \vec{\mu}_{\mathrm{Fe}}\right). \tag{4.5}$$

We employ the square-root of the maximal Fisher discriminant ratio

$$f_{N-X} \equiv \sqrt{\max_{\vec{\omega} \neq 0} f} = \sqrt{\left(\vec{\mu}_{\mathrm{p}} - \vec{\mu}_{\mathrm{Fe}}\right)^\top \left(\hat{\Sigma}_{\mathrm{p}} + \hat{\Sigma}_{\mathrm{Fe}}\right)^{-1} \left(\vec{\mu}_{\mathrm{p}} - \vec{\mu}_{\mathrm{Fe}}\right)^\top} \tag{4.6}$$

to quantify the separation between the proton and iron primary classes separated by $\vec{\omega}^{\max}$.

We account for statistical fluctuations in $X_{\max}$ by assuming Gaussian distributions around the true $X_{\max}$ values (from CORSIKA) with standard deviation $\sigma(X_{\max}) = 20\,\mathrm{g/cm^2}$, which corresponds approximately to the reconstruction resolution of the fluorescence detectors of the Pierre Auger Observatory [66] at the considered primary energy. Analogous to the procedure for N_μ, we generate the set of 115 reconstructed $X_{\max}$ values (for each primary) according to this probability distribution.

4.2 DEPENDENCE OF THE COMPOSITION SENSITIVITY ON THE $N_\mu - X_{\max}$ CORRELATION

The dependence of the composition sensitivity on the detection threshold of muons, based on the number of muons only, is shown in Fig. 4.2a for an example detection area of $A = 10\,\mathrm{m^2}$ and different radial distances to the shower core. It is surprising that the optimum separation power for f_N, based on the number of muons only, is not found for the lowest energy threshold for which the number of detected muons is largest and correspondingly the detection fluctuations are smallest. Instead, the best separation of primaries for a detection area of $10\,\mathrm{m^2}$ is obtained for thresholds of about 4.2 GeV for a small core distance of $r = 210\,\mathrm{m}$.

As expected, the composition sensitivity is much higher if a second observable, the depth of shower maximum $X_{\max}$, is used in addition to the muon content of an extensive air shower (Fig. 4.2b). Even for a distance of $r = 960\,\mathrm{m}$, f_{N-X} is of the order of the maximally achieved f_N values based on the number of muons only. For a detection area of $10\,\mathrm{m^2}$, smallest possible detection thresholds are favored for all core distances.

In order to explain the dependence of f_N and f_{N-X} on the detection threshold of muons, we first consider the correlation of the true N_μ and $X_{\max}$ values and later evaluate the impact

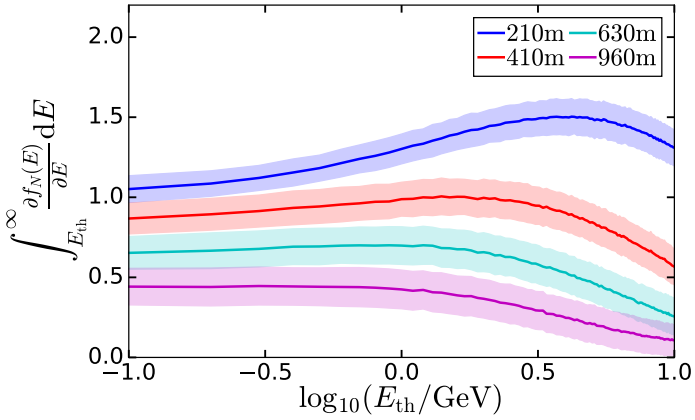

(a) Figure of merit f_N

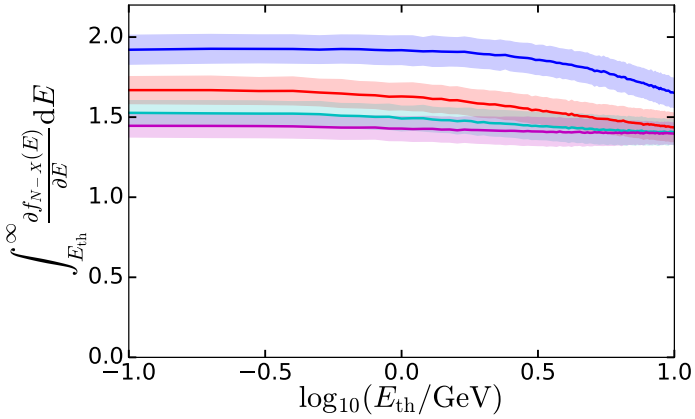

(b) Fisher discriminant ratio f_{N-X}

Figure 4.2: (a) Figure of merit f_N based on the measured number of muons N_μ as a function of the detection threshold E_{th} for a detection area of $A = 10\,\mathrm{m}^2$. (b) Fisher discriminant ratio f_{N-X} making use of the information of the shower maximum X_{max} in addition to N_μ. Results are displayed for different radial distances from the shower core, shaded bands denote the 1σ uncertainties of f_N and f_{N-X}.

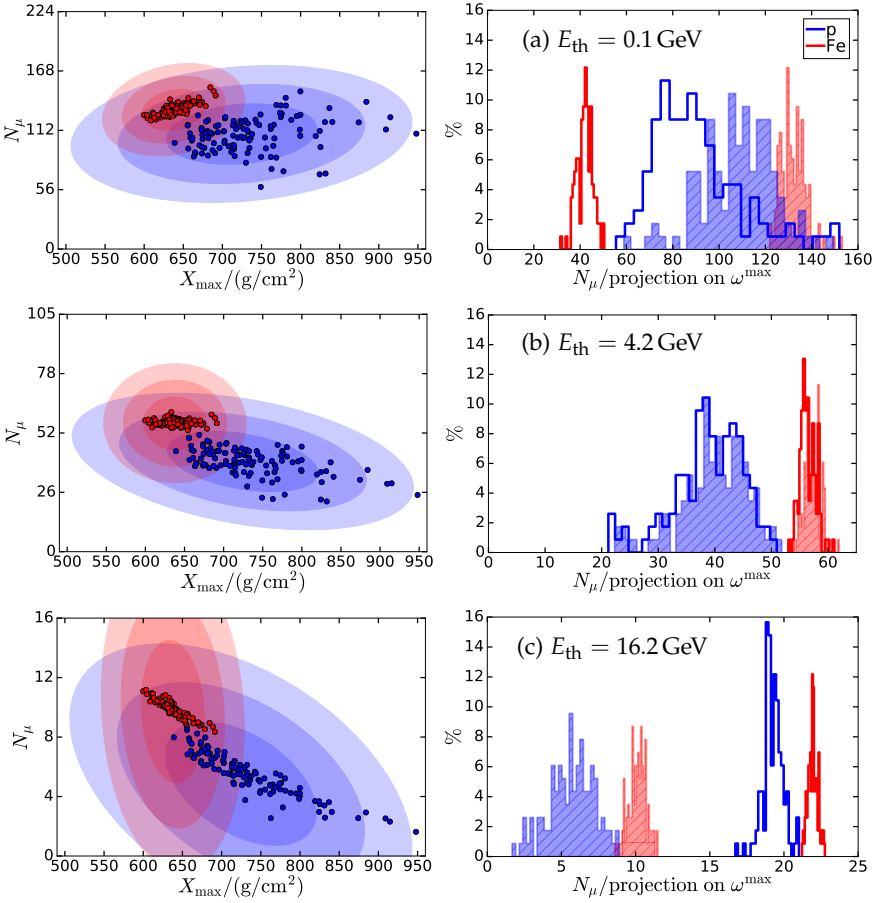

Figure 4.3: Left: $N_\mu - X_{\max}$ distributions for a core distance of $r = 210\,\text{m}$ and different detection thresholds of muons E_{th}. Right: projections of the true $N_\mu - X_{\max}$ distributions (points on the left hand side) on the N_μ-axis (shaded histograms) and the optimal Fisher discriminants (solid histogram lines). Note that the flip in ordering of the projected proton and iron distributions is due to the changing orientation of the Fisher discriminant.

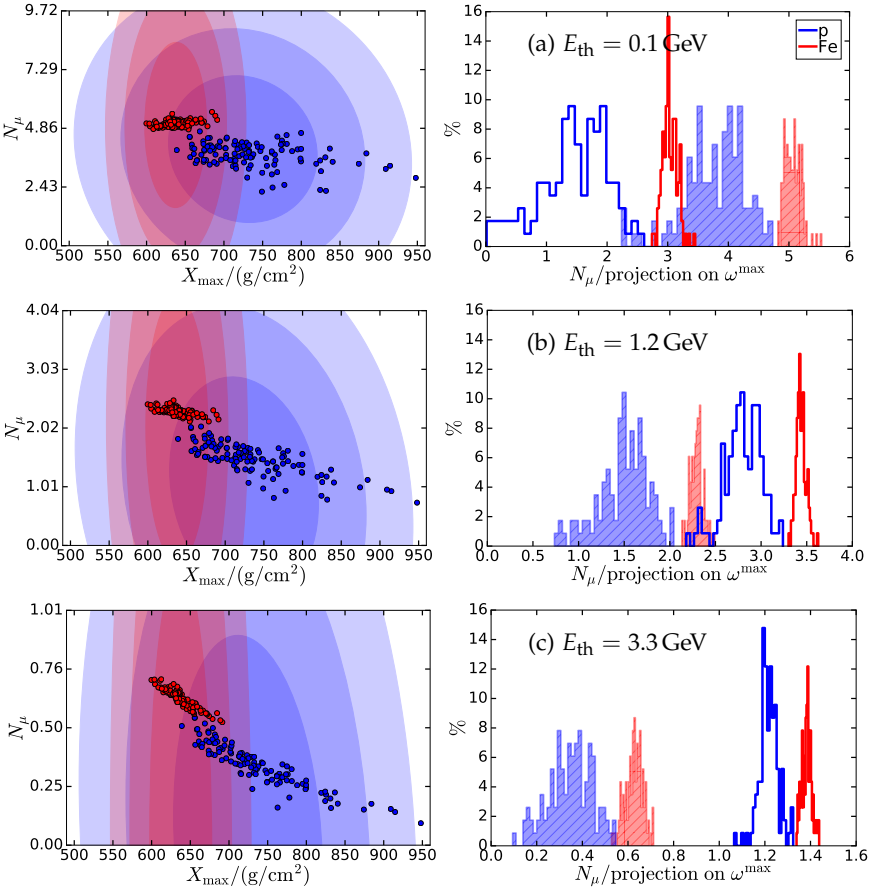

Figure 4.4: Left: $N_\mu - X_{\mathrm{max}}$ distributions for a core distance of $r = 960\,\mathrm{m}$ and different detection thresholds of muons E_{th}. Right: projections of the true $N_\mu - X_{\mathrm{max}}$ distributions (points on the left hand side) on the N_μ-axis (shaded histograms) and the optimal Fisher discriminants (solid histogram lines).

of statistical fluctuations. For a small detection threshold of $E_{\text{th}} = 0.1\,\text{GeV}$ at a radial distance of $r = 210\,\text{m}$ (Fig. 4.3a), the number of muons and the shower maximum are positively correlated for both iron and proton showers. Since proton showers generally have larger $X_{\max}$ values than iron showers, the positive correlation causes an almost complete overlap of the muon number distributions of the two primaries. This leads to a reduced separability based on the number of muons for small detection thresholds (see Fig. 4.6, solid lines).

For increasing thresholds, the correlation ellipses are rotated and the correlation changes from positive to negative. This leads to an increase in the composition sensitivity due to the smaller overlap of the proton and iron muon number distributions. Optimal composition sensitivity, based on ideal muon densities, is obtained for a threshold of 7.7 GeV where both proton and iron showers have a negative $N_\mu - X_{\max}$ correlation and can be clearly separated. For higher thresholds, the increasing negative correlation for both primaries causes again an overlap of muon numbers for shallow proton showers and deep iron showers and hence a reduction of the composition sensitivity. The Pearson correlation coefficients $r_{N,X} = \frac{\text{cov}(N_\mu, X_{\max})}{\sigma_{N_\mu}\,\sigma_{X_{\max}}}$ of the true $N_\mu - X_{\max}$ distributions are shown as a function of the detection threshold of muons in Fig. 4.5. in Figs. 4.5a and 4.5b.

For a large core distance of $r = 960\,\text{m}$, N_μ and $X_{\max}$ are already negatively correlated for proton showers at the smallest threshold of 0.1 GeV (see Fig. 4.4 and Fig. 4.5b). Hence, the true muon number distributions (without any statistical fluctuations accounted for) do not overlap. This leads to a better separability at a large distance of 960 m compared to 210 m based on true N_μ values. Moreover, the increase of separation power as a function of the detection threshold of muons is much smaller then for $r = 210\,\text{m}$. Thresholds of around $E_{\text{th}} = 1.2\,\text{GeV}$ yield optimum composition sensitivity for true muon densities.

Bivariate Fisher discriminant analyses, based on both N_μ and $X_{\max}$, are virtually not affected by the overlapping muon number

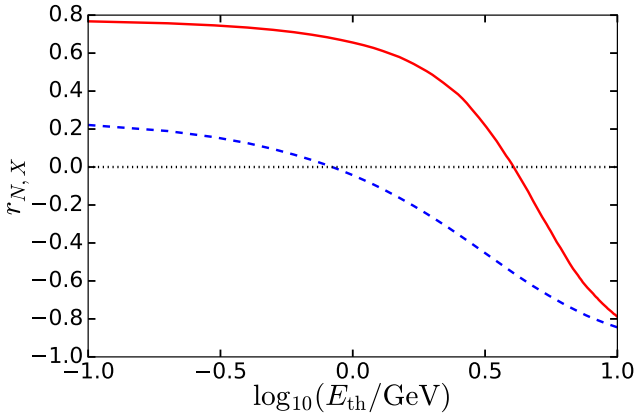

(a) $r = 210\,\mathrm{m}$

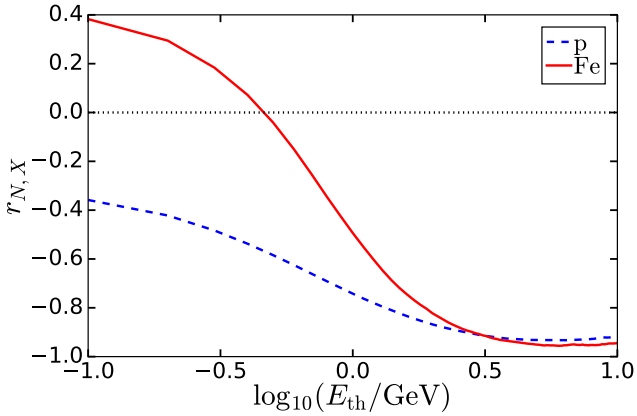

(b) $r = 960\,\mathrm{m}$

Figure 4.5: Pearson product-moment correlation coefficient $r_{N,X}$ measuring the correlation between the number of muons and the electromagnetic shower maximum as a function of the detection threshold of muons E_{th} for proton and iron showers and core distances of $r = 210\,\mathrm{m}$ (a) and $r = 960\,\mathrm{m}$ (b).

distributions for small detection thresholds of muons, since the optimal Fisher discriminant axis is chosen such that the separation between the projected distributions is maximized. The best separation in terms of f_{N-X} is obtained when the ratio of the distance of distribution means and the averaged width of the distributions is maximal. Since the increasing negative $N_\mu - X_{\max}$ correlation for both proton and iron showers causes a reduction of the distribution widths, maximum separability is obtained for a very high detection threshold of about 16.2 GeV for $r = 210\,\mathrm{m}$. The same line of reasoning holds for a large core distance of 960 m. However, maximum separability is obtained for a smaller detection threshold of 3.3 GeV due to the reduced $N_\mu - X_{\max}$ correlation w.r.t. $r = 210\,\mathrm{m}$.

4.3 IMPACT OF STATISTICAL FLUCTUATIONS OF N_μ & $X_{\max}$

For muon detectors of limited size, statistical fluctuations in the detected number of muons increase with decreasing muon densities. As a consequence, the separability of primaries, based on the number of muons only, is worse for $r = 960\,\mathrm{m}$ than for $r = 210\,\mathrm{m}$ for all considered detection areas $\leq 60\,\mathrm{m}^2$ (see Fig. 4.6b left). Furthermore, there is no improvement of f_N for higher detection thresholds at large core distances such that lowest detection thresholds are favored. However, for small core distances, the functional dependence of f_N on the detection threshold of muons remains very similar for all considered detection areas (see Fig. 4.6a left). Even though the separability is decreased for smaller areas, the feature of a strong reduction of separability for smallest thresholds and a preference for thresholds of $3.6 - 5.1\,\mathrm{GeV}$ (for $5 - 60\,\mathrm{m}^2$) persists. This shows that the composition separability at lowest thresholds, based on the number of muons only, is mainly determined by the overlapping muon number distributions as a result of the positive $N_\mu - X_{\max}$ correlation for proton showers.

In a bivariate analysis of true N_μ and $X_{\max}$ values, maximum separability is obtained for detection thresholds of about 16.2 GeV for $r = 210\,\mathrm{m}$ and 3.3 GeV for 960 m. However, for detectors of limited size, Poissonian fluctuations in N_μ lead to a strong reduction of the separability for high detection thresholds. A small increase of f_{N-X} for higher detection threshold of muons can only be observed for small core distances ($r = 210\,\mathrm{m}$, Fig. 4.6a right) and a detection area of at least $30\,\mathrm{m}^2$. In all other cases, lowest possible detection thresholds yield equally good composition sensitivity. At a large distance of $r = 960\,\mathrm{m}$ (Fig. 4.6b right), the information on N_μ becomes even negligible for high detection thresholds and f_{N-X} approaches

$$f_X = \frac{\overline{X}_{\mathrm{max,Fe}} - \overline{X}_{\mathrm{max,p}}}{\sqrt{\sigma^2_{X,\mathrm{p}} + \sigma^2_{X,\mathrm{Fe}}}} \approx 1.39 \tag{4.7}$$

based on $X_{\max}$ only. However, even though bivariate analyses yield much better separability far from the shower core, the maximum values for f_N and f_{N-X} are very similar for small core distances. Close to the shower core and for optimal detection thresholds, the separation power based on the number of muons only is hence as good as the separation based on both N_μ and $X_{\max}$.

4.4 GEOMETRICAL INTERPRETATION OF THE $N_\mu - X_{\max}$ CORRELATION

The observed dependence of the $N_\mu - X_{\max}$ correlation on the detection threshold of muons and distance to the shower core can be qualitatively explained by the distribution in transverse momentum of muons that are produced in hadronic interactions during the shower development. The differential muon number distribution in momentum space can be estimated from hadronic interaction models by

$$\frac{\mathrm{d}^2 N_\mu}{\mathrm{d}^2 \vec{p}_\perp} = \frac{\mathrm{d}^2 N_\mu}{\mathrm{d}\varphi p_\perp \mathrm{d}p_\perp} = \frac{N_\mu^{\mathrm{tot}}}{2\pi p_{\perp_0}} e^{-\frac{p_\perp}{p_{\perp_0}}}, \tag{4.8}$$

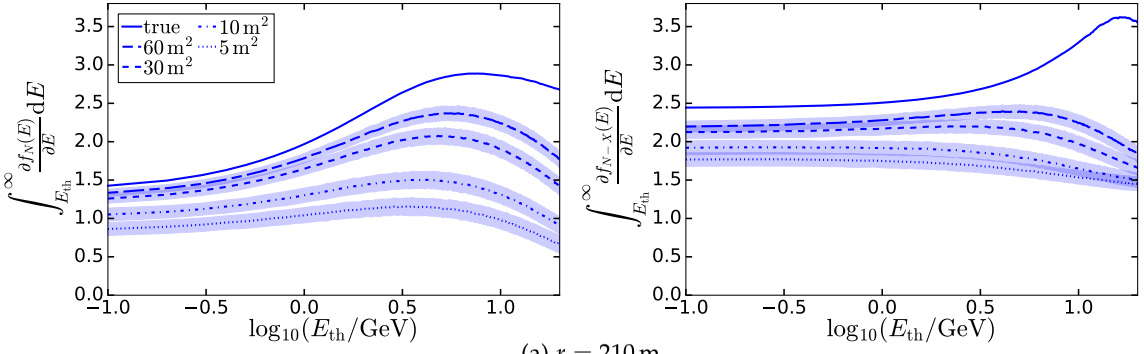

(a) $r = 210\,\mathrm{m}$

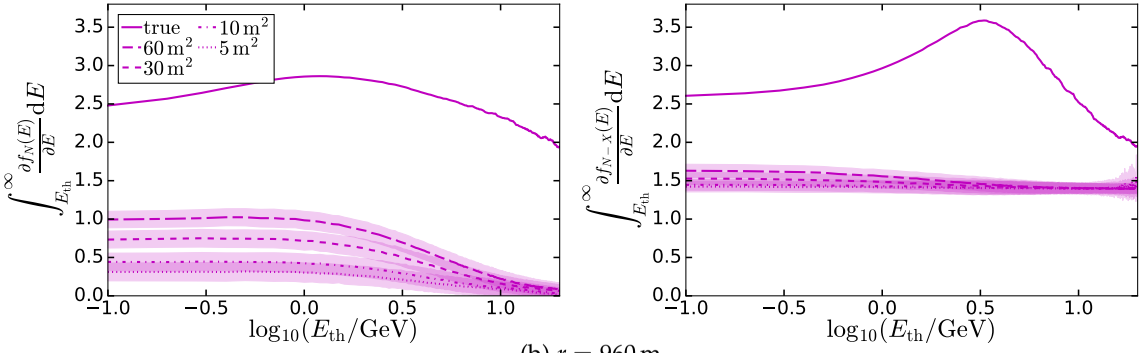

(b) $r = 960\,\mathrm{m}$

Figure 4.6: Figure of merit f_N (left) and Fisher discriminant ratio f_{N-X} (right) for core distances $r = 210\,\mathrm{m}$ (top) and 960 m (bottom) as a function of the detection threshold of muons E_{th} for different muon detector sizes of $A = 5, 10, 30\,\mathrm{m}^2$ and $60\,\mathrm{m}^2$ compared to results for "true" N_μ and X_{max} values.

where $\vec{p}_\perp$ ($p_\perp = |\vec{p}_\perp|$) designates the transverse momentum w.r.t. the shower axis, $p_{\perp_0} = \langle p_\perp \rangle \approx 350 - 400\,\mathrm{MeV}$ the average transverse momentum [44, 81], and N_μ^{tot} the total number of muons. The atmospheric slant depth $X_{\mu_{\max}}^{\mathrm{prod}}$, where the production of muons is maximal, is related to the slant depth of the electromagnetic shower maximum by $X_{\mu_{\max}}^{\mathrm{prod}} \approx X_{\max}^{\mathrm{em}} - \Delta$ with $\Delta \approx 200\,\mathrm{g\,cm^{-2}}$ [82]. For a muon produced at slant depth $X_{\mu_{\max}}^{\mathrm{prod}}$ and hitting the ground at core distance r without any intermediate interactions (i.e. following a straight line), the transverse muon momentum $p_\perp$ can be related to the total momentum p_μ, the distance to the shower core r in the shower plane and the geometrical distance R along the shower axis from the point of production to the intersection of the shower axis and the ground plane by

$$p_\perp = p_\mu \frac{r}{R}. \tag{4.9}$$

Here, the geometrical relations $\tan\theta_\mu = \frac{r}{R} \approx \theta_\mu$ and $\sin\theta_\mu = \frac{p_\perp}{p_\mu} \approx \theta_\mu$ for the angle θ_μ between the muon momentum and the shower axis and $r \ll R$ and $p_\perp \ll p_\mu$ have been used. Employing Eqs. (4.8) and (4.9), the muon number density in the shower plane can be expressed by

$$\frac{\mathrm{d}^2 N_\mu}{\mathrm{d}^2\vec{r}} = \frac{\mathrm{d}^2 N_\mu}{\mathrm{d}^2\vec{p}_\perp}\frac{\mathrm{d}^2\vec{p}_\perp}{\mathrm{d}^2\vec{r}} = N_\mu^{\mathrm{tot}} \frac{p_\mu^2}{2\pi p_{\perp_0} R^2} e^{-\frac{p_\mu}{p_{\perp_0} R} r}. \tag{4.10}$$

In Fig. 4.7, lateral distribution functions are plotted for different detection thresholds of muons and different ranges of electromagnetic shower maximum. From Eq. (4.10) it follows that they steepen with increasing muon energy and decreasing distance R. Since R is inversely related to the maximum muon production depth $X_{\mu_{\max}}^{\mathrm{prod}} \approx X_{\max}^{\mathrm{em}} - \Delta$, a steepening is hence expected for larger depths of electromagnetic shower maximum. Consequently, there is a crossing of lateral distribution functions for showers of different $X_{\max}$ values at some radial distance to the

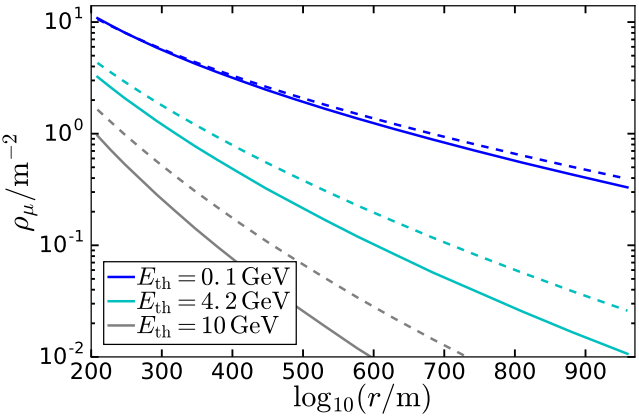

(a) proton

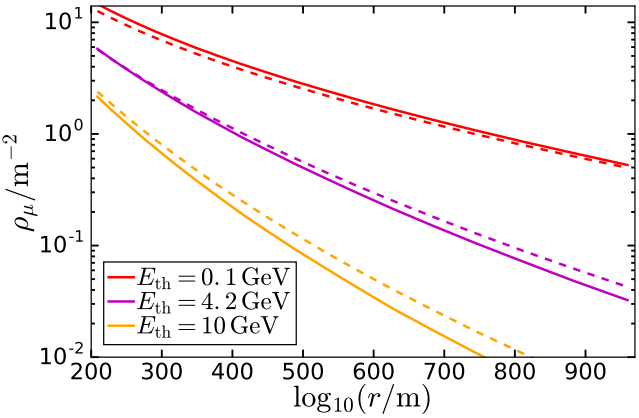

(b) iron

Figure 4.7: Lateral distribution functions for muon detection thresholds of 0.1, 4.2, and 10 GeV for (a) proton and (b) iron showers. Results are shown for different bins in electromagnetic shower maximum. Proton: $675\,\mathrm{g/cm^2} \leq X_{\mathrm{max}} \leq 700\,\mathrm{g/cm^2}$ (dashed), $825\,\mathrm{g/cm^2} \leq X_{\mathrm{max}} \leq 850\,\mathrm{g/cm^2}$ (solid); iron: $600 \leq X_{\mathrm{max}} \leq 625$ (dashed), and $675\,\mathrm{g/cm^2} \leq X_{\mathrm{max}} \leq 700\,\mathrm{g/cm^2}$ (solid).

shower core which depends on the detection threshold of muons. At the intersection point r_{cross}, the number of muons is uncorrelated w.r.t. the position of the shower maximum. For core distances $r > r_{\text{cross}}$, the $N_\mu - X_{\text{max}}$ correlation is negative, while it is positive for $r < r_{\text{cross}}$. For iron showers, the $N_\mu - X_{\text{max}}$ correlation for the lowest threshold of $E_{\text{th}} = 0.1\,\text{GeV}$ is positive over the whole considered radial range $r \leq 1000\,\text{m}$ due to the intersection of lateral distribution functions at a larger core distance. For a muon detection threshold of $E_{\text{th}} = 4.2\,\text{GeV}$, the lateral distribution functions intersect at around $r_{\text{cross}} = 210\,\text{m}$ leading to the zero correlation shown in Figs. 4.3b and 4.5a. Proton lateral distribution functions cross at a larger core distance of about $r_{\text{cross}} = 250\,\text{m}$ for $E_{\text{th}} = 0.1\,\text{GeV}$ such that the $N_\mu - X_{\text{max}}$ correlation is positive for a core distance of $r_{\text{cross}} = 210\,\text{m}$ (Fig. 4.3a) and negative for $r_{\text{cross}} = 960\,\text{m}$. Since intersection points are shifted towards smaller distances (below the inner radius cut in simulations) for higher detection thresholds of muons, N_μ and X_{max} are negatively correlated for all other detection thresholds of muons shown in Fig. 4.7. For a fixed radial distance r, it can be derived from Eq. (4.10) that the $N_\mu - X_{\text{max}}$ correlation decreases with increasing muon energy as shown in Figs. 4.5a, 4.5b and 4.7.

4.5 EFFECT OF DIFFERENT INTERACTION MODELS, ENERGIES, ZENITH ANGLES, AND PARTICLE THINNING

The described results have been obtained for showers with zenith angle $\theta = 38^\circ$ and energy $3.16 \times 10^{18}\,\text{eV}$ for the EPOS-LHC high-energy interaction model. We demonstrate their general validity for different hadronic interaction models, primary energies and zenith angles in the following. All plots of this section have been produced with a library of thinned CORSIKA showers with a thinning level of 10^{-6}. The library of fixed energy, described in detail in Section 5.1.2, comprises simulations for the hadronic interaction models EPOS-LHC and QGSJETII-04, proton and iron primaries,

and different fixed energies and shower zenith angles. For each configuration, 120 CORSIKA showers are available.

The impact of the hadronic high energy interaction model is illustrated exemplarily in Fig. 4.8 for a primary energy of $10^{18.5}$ eV and zenith angle $\theta = 38^{\circ}$. Despite small differences in the numerical values, the functional dependence of the figure of merit f_N on the detection threshold of muons is very similar for both considered interaction models EPOS-LHC and QGSJETII-04.

The effect of different zenith angles and primary energies on the figure of merit is shown in Fig. 4.9 for the EPOS-LHC high energy interaction model. Both a change in zenith angle and in energy is reflected in a modification of the distance R along the shower axis between the muon production point and the intersection of the shower axis with the ground plane. The smaller the primary energy, the higher up in the atmosphere muons are produced and hence the larger is R. Similarly, a larger shower zenith angle θ leads to a higher production point and, additionally, a longer travel distance R through the atmosphere. As a consequence of the increase of R, the muon detection thresholds where maximum separation is obtained are shifted towards higher values for increasing zenith angles in Figs. 4.9a and 4.9c. The same effect is visible for a decreasing primary energy in Figs. 4.9b and 4.9d.

For an additional comparison of the effect of hadronic interaction models, Fig. 4.10 displays the figure of merit for showers simulated with the QGSJETII-04 high energy interaction model [52, 83]. The good agreement between the results for EPOS-LHC and QGSJETII-04 confirms that our conclusions are independent of the employed high energy hadronic interaction model.

Fig. 4.11 shows that the use of thinned simulations leads to a bias of the figure of merit for thinned simulations w.r.t. the figure of merit for unthinned simulations of the order of 5% which increases for higher detection thresholds of muons. To avoid any additional sources of uncertainties, we have therefore based the main part of our analysis on unthinned showers. However, we

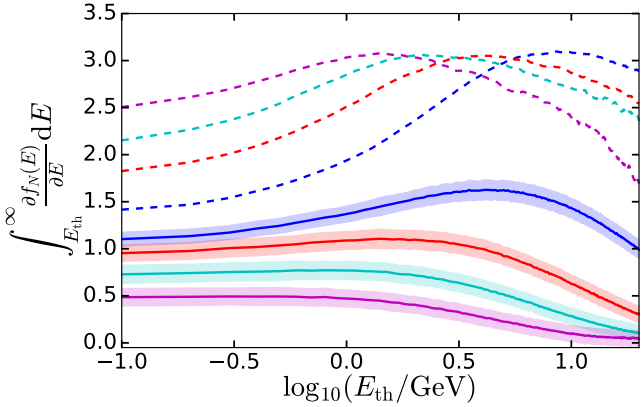

(a) EPOS-LHC

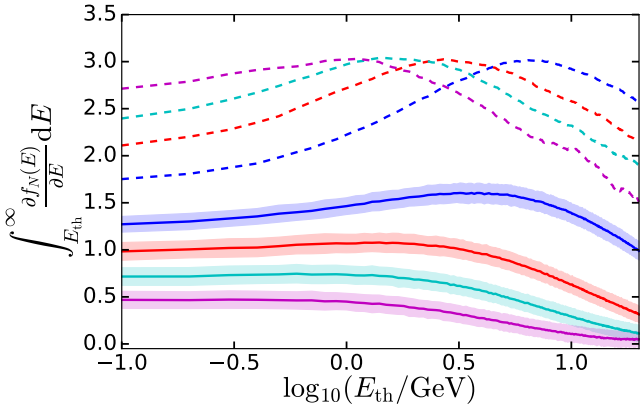

(b) QGSJETII-04

Figure 4.8: Figure of merit $f_N(E_{\rm th})$ for simulations with the EPOS-LHC (a) and QGSJETII-04 (b) high energy interaction models for a primary energy of $10^{18.5}$ eV and shower zenith angle $\theta = 38°$. Dashed lines: f_N based on the "true" muon densities; solid lines: f_N for a detector with area 10 m^2 and corresponding Poissonian fluctuations. Results are displayed for different radial distances from the shower core; shaded bands denote the 1σ uncertainties of f_N.

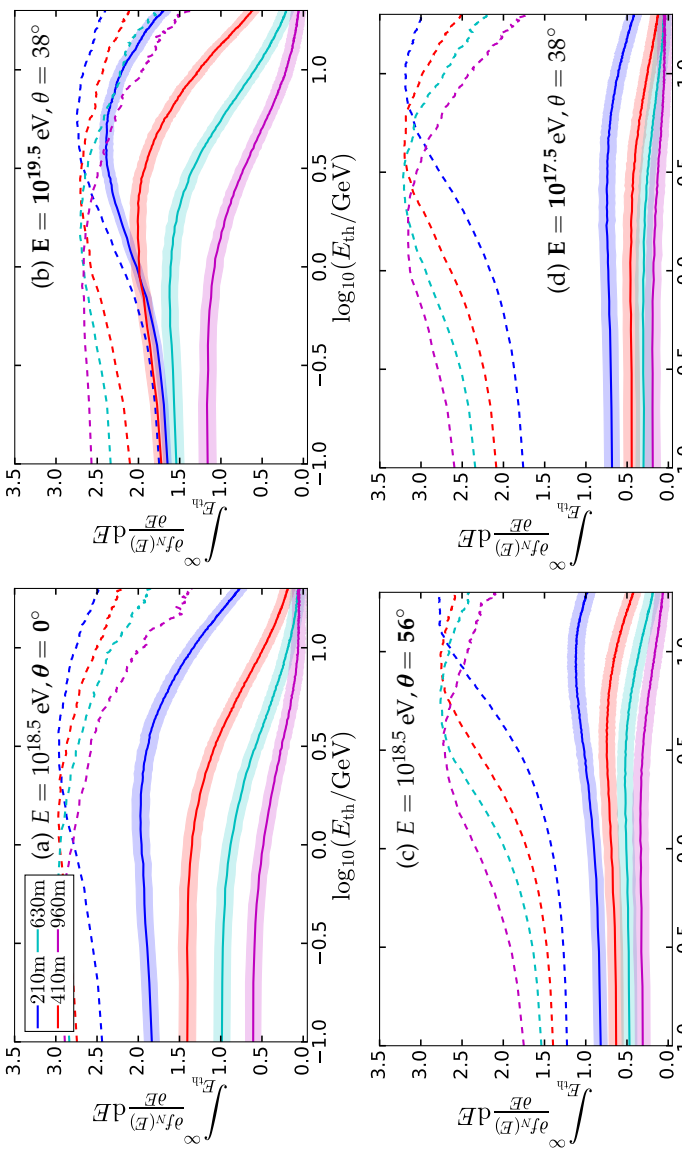

Figure 4.9: Figure of merit $f_N(E_{th})$ for simulations with the EPOS-LHC high energy interaction model. The effect of different zenith angles is visualized in (a) and (c) for $\theta = 0°, 56°$ and $E = 10^{18.5}$ eV. The impact of E is shown in (b) and (d) for energies of $10^{19.5}$ eV and $10^{17.5}$ eV and $\theta = 38°$. Dashed lines: f_N based on "true" muon densities; solid lines: f_N for a detector with area 10 m^2 and corresponding Poissonian fluctuations.

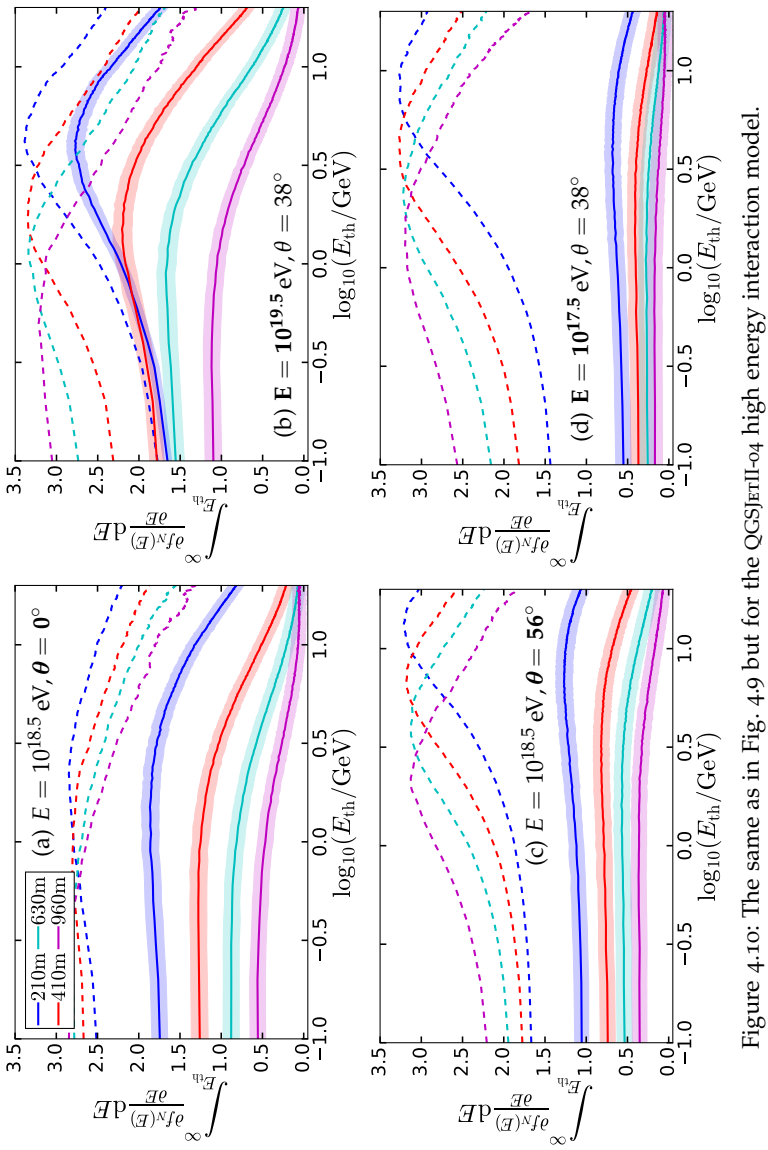

Figure 4.10: The same as in Fig. 4.9 but for the QGSJetII-04 high energy interaction model.

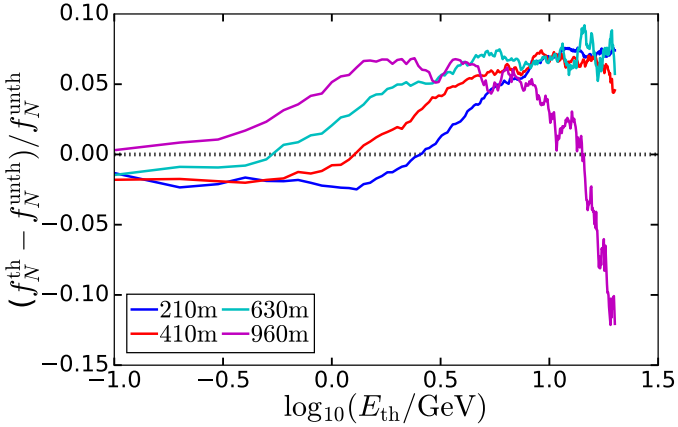

Figure 4.11: Bias $(f_{\mathrm{N}}^{\mathrm{th}} - f_{\mathrm{N}}^{\mathrm{unth}})/f_{\mathrm{N}}^{\mathrm{unth}}$ of the figure of merit for thinned simulations (thinning level 10^{-6}) w.r.t. the figure of merit for unthinned simulations for a primary energy of 3.16×10^{18} eV, zenith angle of $\theta = 38°$, and hadronic high-interaction model EPOS-LHC. The shown bias is based on the "true" muon densities that have been obtained by averaging over rings in the shower plane.

have additionally used thinned showers here to describe the impact of different energies, zenith angles, and hadronic interaction models in a qualitative way.

4.6 PHOTONUCLEAR INTERACTIONS

Extensive air showers initiated by a nucleus with atomic number A can be considered as a superposition of air showers induced by A nucleons with energy E/A. Since the primary energy of each of these subshowers is reduced, less interaction generations and consequently less energy loss in electromagnetic interactions is predicted. At the same time, more muons from the hadronic part of the shower are expected for primaries with large A compared to proton induced showers [47]. On the other hand,

less electromagnetic interactions could lead to a reduction in the number of muons produced by electromagnetic $\mu^+\mu^-$ pair creation processes

$$\gamma + \text{air} \rightarrow \mu^+\mu^-$$

or hadronic photon-air interactions (photo-production) of the type

$$\gamma + \text{air} \rightarrow \text{hadron/meson} + X$$

with subsequent decay of the hadron or meson into a muon. We distinguish muons from photonuclear precursor reactions from muons produced by other hadronic interactions by increasing the "hadronic generation counter" (defined for the EHISTORY option [84] in CORSIKA) by a unique value every time a photonuclear reaction takes place in the preceding interaction chain.

The muon energy distribution for muons stemming from preceding photonuclear interactions is shown in Fig. 4.12 for $r = 210\,\text{m}$ where the separation power between primary particles based on the number of muons is maximal in the considered radial range. Up to muon energies of about 10 GeV, the number of muons resulting from photonuclear processes is larger for proton than for iron primaries. The distribution for muons without any preceding photonuclear interactions is plotted for comparison. Here, the number of muons is largest for iron primaries over the whole energy range. For proton, the percentage of muons from photonuclear interaction drops from approximately 11% at $E_{\text{th}} = 0.1\,\text{GeV}$ to 4% at highest energy thresholds. As expected from the Heitler-Matthews model, the ratios are generally smaller for iron primaries; here the percentage of muons from photonuclear interactions is between 5% and 2%.

We display the impact of muons from photonuclear reactions on both the figure of merit f_N and on the Fisher discriminant ratio f_{N-X} in Fig. 4.13. The f_N and f_{N-X} values which would be obtained if muons from photonuclear reactions could be excluded are shown by dashed lines for comparison. The largest difference

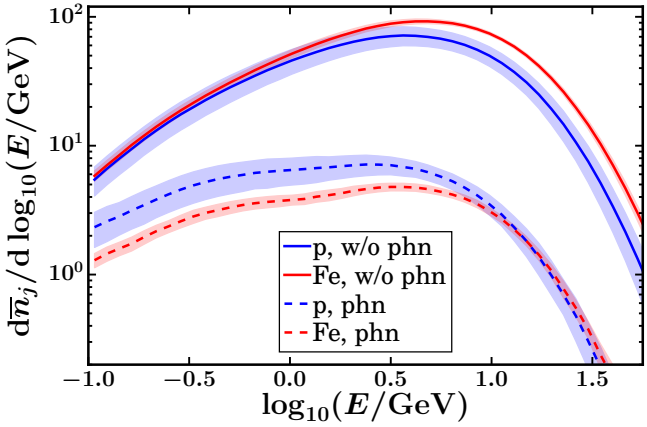

Figure 4.12: Muon energy distribution for iron and proton primaries at $r = 210\,\mathrm{m}$ from the shower core and a detection area of $A = 10\,\mathrm{m}^2$. Shaded bands denote one standard deviation due to shower-to-shower fluctuations. Results are shown for muons with only (dashed) and without (solid) preceding photonuclear reactions.

can be seen for the lowest detection threshold of $E_{\mathrm{th}} = 0.1\,\mathrm{GeV}$ at distance $r = 210\,\mathrm{m}$ from the shower core. Here, the figure of merit rises from $f = 1.04 \pm 0.08$ to $f_{\mathrm{w/o\ phn}} = 1.24 \pm 0.08$ if muons resulting from preceding photonuclear interactions are omitted. For higher thresholds, the impact of muons from photonuclear reactions becomes less important. Likewise, the figures of merit f and $f_{\mathrm{w/o\ phn}}$ approach each other for increasing distances to the shower core. The Fisher discriminant ratio f_{N-X} improves less by omitting muons from photonuclear reactions than the figure of merit f_N. It is shifted up by a constant offset for small detection thresholds of muons; for high thresholds, where Poissonian uncertainties lead to a reduction of the separability, the influence of muons from photonuclear reactions vanishes.

To quantify the relative increase of f_N in the absence of muons from photonuclear interactions ("w/o phn"), we show the en-

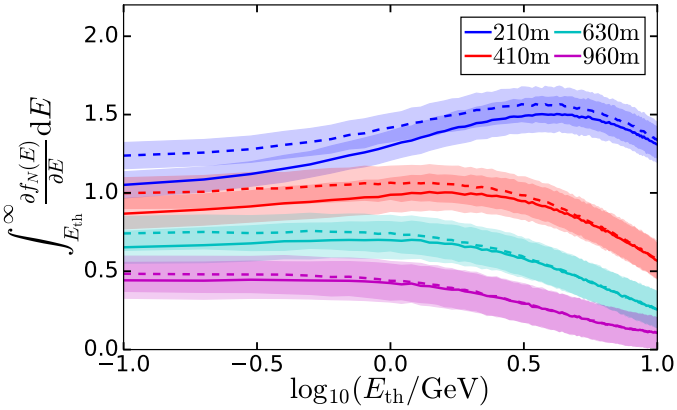

(a) Figure of merit f_N

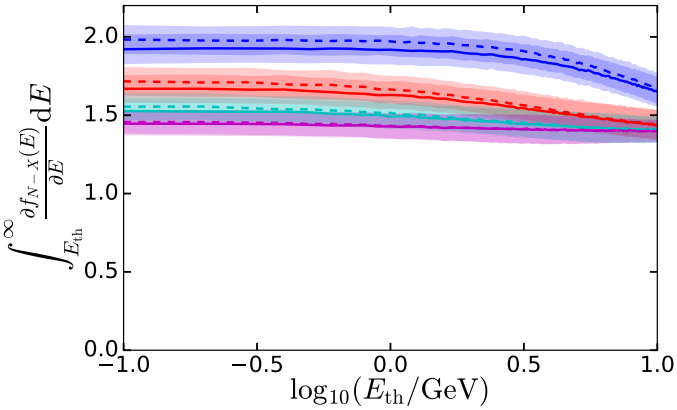

(b) Fisher discriminant ratio f_{N-X}

Figure 4.13: (a) Figure of merit f_N based on the measured number of muons N_μ and (b) Fisher discriminant ratio f_{N-X} making use of the information of the shower maximum X_{max} in addition to N_μ for a muon detection area of $10\,\mathrm{m}^2$ as a function of detection threshold E_{th} if all muons are taken into account (solid lines) and if only muons without any preceding photonuclear interactions are considered (dashed). Uncertainties are displayed by shaded bands.

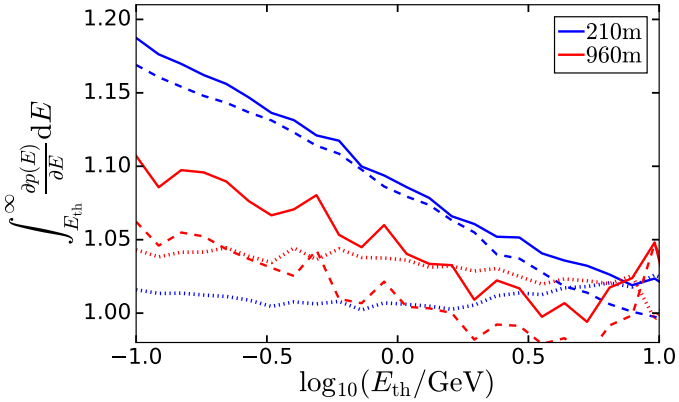

Figure 4.14: Enhancement factors $\int_{E_{\mathrm{th}}}^{\infty} \frac{\partial p(E)}{\partial E} \mathrm{d}E$ as a function of detection threshold for $p = p_f$ (solid lines), $p = p_{\Delta N}$ (dashed), and $p = p_\sigma^{-1}$ (dotted); see text for definitions.

hancement factor $p_f = \frac{f_{\text{w/o phn}}}{f} = \frac{p_{\Delta N}}{p_\sigma}$ (solid) with $p_{\Delta N} = \frac{\left(\overline{N}_{\text{Fe, w/o phn}} - \overline{N}_{\text{p, w/o phn}}\right)}{\left(\overline{N}_{\text{Fe}} - \overline{N}_{\text{p}}\right)}$ (dashed) and $p_\sigma = \frac{\sigma_{\text{w/o phn}}}{\sigma}$ (dotted: p_σ^{-1}) in Fig. 4.14 as a function of the detection threshold of muons. For a threshold of 0.1 GeV, the figure of merit would increase by about 11% to 18%, depending on the distance to the shower core, if muons from photonuclear reactions could be excluded. With increasing detection threshold, the effect becomes less pronounced. The ratio of nominators $p_{\Delta N}$ impacts most to the change in p_f. The effect of muons from photonuclear reactions on ΔN can be illustrated by splitting the total muon number difference

$$\begin{aligned} \Delta N = \overline{N}_{\text{Fe}} - \overline{N}_{\text{p}} = &\left(\overline{N}_{\text{Fe, w/o phn}} - \overline{N}_{\text{p, w/o phn}}\right) \\ &+ \left(\overline{N}_{\text{Fe, phn}} - \overline{N}_{\text{p, phn}}\right) \end{aligned} \tag{4.11}$$

into a sum of contributions from muons produced by photonuclear processes and muons without preceding photonuclear inter-

actions. Since $\overline{N}_{\mathrm{Fe,\,phn}} < \overline{N}_{\mathrm{p,\,phn}}$ up to radius dependent muon energies (c.f. Fig. 4.12), ΔN is lowered by muons stemming from photonuclear processes. Uncertainties due to shower-to-shower fluctuations and Poissonian uncertainties are much less altered by muons from preceding photonuclear reactions since they constitute only a small part of the total number of muons in an extensive air shower (c.f. Fig. 4.12 right). Nevertheless, neglecting muons from photonuclear reactions leads to a small reduction of the total uncertainties and therefore to a further enlargement of the figure of merit.

4.7 IMPLICATIONS FOR THE AUGER UPGRADE

In the study presented in this chapter, we showed that the composition sensitivity, based on the number of muons only, is enhanced for increasing thresholds up to few GeV. However, a good separability of distinct mass groups of cosmic rays is only achieved if the detection areas are very large, or if the depth of shower maximum, as a second mass-sensitive observable, can be inferred from the measurements. Taking into account these results, the Pierre Auger Observatory decided for the installation of plastic scintillation detectors, covering an area of $3.8\,\mathrm{m}^2$ above the existing water-Cherenkov detectors, as the main part of the planned upgrade [57]. The combination of the signals of the two detector types will provide an indirect measurement of the number of muons, while the information on the timing of the signals will be used to estimate the depth of shower maximum. Additionally, direct muon number measurements will be performed for verification with buried scintillators of $30\,\mathrm{m}^2$ area at a depth of 2.3 m underground by the AMIGA part of the upgrade.

5 MD RECONSTRUCTION OPTIMIZATION

The AMIGA extension of the Pierre Auger Observatory is designed for the direct measurement of the muon content of extensive air showers. The layout and detection principle of the muon detectors have been discussed in Section 3.4. In this chapter, we review the MD reconstruction procedure to derive the muon density $\rho_{r_{\text{opt}}}$ at an optimal distance of $r_{\text{opt}} = 450\,\text{m}$ as an estimator of the muon content on an event-by-event level and present extensions and improvements.

The simulation libraries that have been employed for the analysis and enhancement of the MD reconstruction are described in Section 5.1. The reconstruction procedure is divided into two steps: First, the muon densities are estimated for each module of the AMIGA counters that are part of the event. Then, using the information on their distance to the shower axis, $\rho_{r_{\text{opt}}}$ is determined by a fit of the muon lateral distribution function (MLDF). We introduce the muon counting strategy that is based on the identification of characteristic patterns within time windows in the binary time traces of each scintillator strip in Section 5.2. As a result of the detector segmentation, the obtained muon numbers need to be corrected for pile-up as will be discussed in Section 5.3.

Cross-checking the muon counting strategy in Section 5.4, we find that an inhibition window size of seven bins is preferable to the former default setting of eight bins. Further, we analyze the bias that is induced by *corner-clipping muons* which hit multiple detector strips due to their inclined momentum direction and present a geometrical correction procedure in Section 5.5.

Since we find that the former parametrization of the MLDF causes significant biases of the muon density estimates, especially for proton primaries, we derive a new parametrization of the

MLDF in Section 5.6. Based on the radius-dependent systematic uncertainties, we verify in Section 5.7 that $r_{\text{opt}} = 450\,\text{m}$ is, as for the former MLDF, the optimal distance to evaluate the new MLDF. Finally, in Section 5.8, we study the effects of the radial distance and of fixing the β parameter in the MLDF parametrization for composition analyses.

5.1 SIMULATION LIBRARIES

Simulations of extensive air showers and the corresponding detector responses are a crucial tool to develop and verify reconstruction methods of physical shower quantities from the observed detector signals. Moreover, they provide the theoretical expectations that experimental results need to be compared with. In this thesis, we make use of two libraries of extensive air shower simulations, calculated with the COsmic Ray SImulations for KAscade (CORSIKA) program. The common simulation settings are discussed in Section 5.1.1. A library with fixed primary energies and zenith angles, described in Section 5.1.2, is used for the verification and improvement of the MD reconstruction. A second library with a continuous distribution of primary energies is described in Section 5.1.3. It is mainly used for the comparison with data in Chapter 6.

5.1.1 *CORSIKA settings*

Given certain input parameters as the energy of the primary particle and its zenith and azimuth angle, the physical processes of the extensive air shower development were simulated with the CORSIKA program [75]. Hadronic interactions were modeled with the high-energy hadronic interaction models QGSJETII-04 [85] and EPOS-LHC [79, 80] for interaction energies above 100 GeV (in the laboratory frame). For lower energies, the FLUKA [78] interaction model was used. To reduce computational costs, cut-off energies of 100 MeV for hadrons, 10 MeV for muons, and 10 eV for elec-

trons and photons were defined (ECUT option, see [86]). If the kinetic energy of a particle falls below these cut-off values, it is not further tracked in the simulation. In addition, the particle thinning algorithm [76, 87] (i.e. sampling of representative particles) with a thinning level of $t = 10^{-6}$ was employed. The observation level was set to the mean altitude of the Pierre Auger Observatory surface array of 1452 m above sea level, corresponding to an atmospheric depth of $869.96\,\mathrm{g/cm^2}$.

5.1.2 *Library of fixed energy*

The library of fixed energy was produced for proton and iron primaries and for both the EPOS-LHC and the QGSJETII-04 hadronic high-energy interaction models. For energies of $10^{17.5}$ eV, 10^{18} eV, $10^{18.5}$ eV, and 10^{19} eV, 120 showers were simulated for each primary for different shower zenith angles of $0^\circ, 12^\circ, 22^\circ, 32^\circ, 38^\circ, 48^\circ$, and 56°. The season dependent variations in the atmosphere are accounted for by using twelve different monthly models [88] in CORSIKA, i.e. ten showers were produced for each atmosphere model for a given hadronic interaction model, primary, energy and zenith angle configuration. The azimuth angles of the showers were generated randomly from a uniform distribution between 0° and 360°.

5.1.3 *Library of continuous energy*

In addition to the fixed library, a library of continuous energy was produced for the QGSJETII-04 hadronic interaction model. For the primary energy intervals $10^{17}\,\mathrm{eV} - 10^{18}\,\mathrm{eV}$, $10^{18}\,\mathrm{eV} - 10^{19}\,\mathrm{eV}$, and $10^{19}\,\mathrm{eV} - 10^{20}\,\mathrm{eV}$, 1000 extensive air showers were simulated for proton and iron primaries each. The distribution of showers is flat in energy and follows a $\sin^2\theta$ distribution in the zenith angle θ within the range from 0° to 70°. The azimuth angles were generated randomly from a uniform distribution between 0° and 360°. All monthly atmosphere models have been employed, al-

though not with exactly the same frequencies. The atmospheric models for January and February have been used 100 times each, all other monthly models 80 times.

5.1.4 *Offline simulation and reconstruction*

For the simulated air showers, the detector responses of the SD and MD are simulated with the Offline data analysis software framework [89, 90]. We use the v3r3 version of the official branch as of revision number r29804. To gain sufficient statistics, each shower is placed five times inside an array of SD stations, which are distributed on a regular grid with a 750 m spacing, within a rectangular region around the central WCD. Next to each WCD, a $30\,\mathrm{m}^2$ AMIGA detector, consisting of three $10\,\mathrm{m}^2$ modules arranged in an L-shape, is buried at a soil depth of 2.3 m.

The secondary particles arriving at ground have weights due to the thinning algorithm that is applied in the CORSIKA simulations. A fair representation of the particles entering the detector is obtained by a method referred to as *resampling* or *unthinning* [77]. The number of particles impacting the detector is randomly generated according to a Poissonian probability distribution whose mean corresponds to the resampled weight $w_r = w \cdot A_\mathrm{d}/A_\mathrm{sr}$, where w is the particle weight, A_d the area of the detector, and A_sr the area of the sampling region. If the resampled weight is smaller than one, the particle is kept with a probability w_r; otherwise, it may generate several clones. The resulting regenerated particles are randomly distributed over the detector area with the same momentum directions as the incident weighted particle.

It has been shown for the SD that the thinning procedure with subsequent resampling in Offline does not introduce significant biases or fluctuations in important observables for the standard thinning level of 10^{-6} [91]. The cut-off energies defined in CORSIKA are properly taken into account in the particle generation routine (the CachedXShowerRegenerator module in Offline,

see [86] on ECUTS) by choosing particle energy thresholds that are less or equal to the cut-off energies from CORSIKA.

The resampled particles are injected into the WCDs and, in parallel, in a larger circular patch on ground containing the MD modules. The soil propagation and the subsequent detector simulation are performed with GEANT4 [92]. The complete chain of processes is simulated; for AMIGA this includes the energy deposit in the scintillators, the light propagation through the WLS fibers, the PMT response, and the discrimination and digitization as described in Section 3.4. However, no inefficiencies of the $10\,\mathrm{m}^2$ modules is accounted for in simulations.

In the subsequent reconstruction procedure, the shower observables such as the primary energy and geometry of the shower (core position, zenith and azimuth angle) are reconstructed with $\overline{\text{Off}}\underline{\text{line}}$ from the simulated SD detector responses as explained in Section 3.1. For the MD, the main observable of interest is the muon density at an optimal distance from the shower core. The detailed MD reconstruction procedure is described in Section 5.2.

5.1.5 *Reweighting of the continuous shower library*

The flat distribution in primary energy of the continuous shower library differs fundamentally from the steeply falling energy spectrum observed in data. The number of reconstructed showers is displayed as a function of the logarithmic energy in Fig. 5.1a for both simulations and AMIGA data. For simulations, the energy corresponds to the Monte Carlo energy, for data, the SD-reconstructed energy is employed. While the measured number of AMIGA events decreases linearly in log-log scale, the number of simulated showers increases between 10^{17} eV and 10^{18} eV, then falls abruptly to a smaller number of events and rises again up to the energy of 10^{19} eV afterwards. This event distribution in log-log scale is a consequence of the flat energy distribution of the continuous shower library with an equal number of showers N_{sim} in the two energy ranges $10^{17}\,\text{eV} - 10^{18}\,\text{eV}$ and $10^{18}\,\text{eV} - 10^{19}\,\text{eV}$.

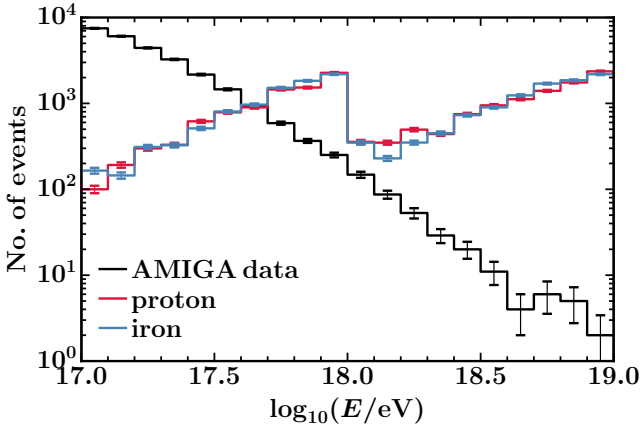

(a) Original spectra for simulations and data

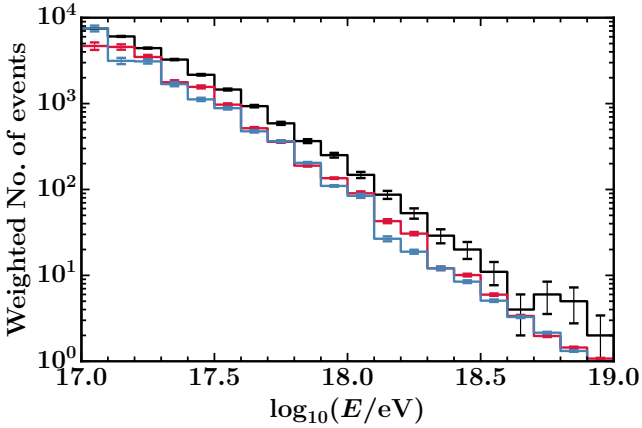

(b) Spectra after reweighting of simulations

Figure 5.1: The flat distribution in primary energy of the continuous shower library (proton, iron in Fig. 5.1a) differs fundamentally from the steeply falling energy spectrum observed in data (AMIGA data). We mimic the event distribution in data by weighting the simulated showers according to the Auger energy spectrum (Fig. 5.1b). Error bars denote the Poissonian uncertainties in each energy bin.

For the comparison of the energy evolution of the muon densities measured by the AMIGA engineering with simulations in Chapter 7, we weight the showers according to the Auger energy spectrum that has been published at the ICRC 2017 [41]. The flux of CRs has been fitted with the function

$$J(E) = \begin{cases} J_0 \left(\frac{E}{E_{\text{ankle}}}\right)^{-\gamma_1} & ; E \leq E_{\text{ankle}} \\ J_0 \left(\frac{E}{E_{\text{ankle}}}\right)^{-\gamma_2} \left[1 + \left(\frac{E_{\text{ankle}}}{E_{\text{s}}}\right)^{\Delta\gamma}\right] \left[1 + \left(\frac{E}{E_{\text{s}}}\right)^{\Delta\gamma}\right]^{-1} & ; E > E_{\text{ankle}} \end{cases}$$

where $E_{\text{ankle}} = 5.08 \times 10^{18}\,\text{eV}$ corresponds to the ankle, $E_{\text{s}} = 3.9 \times 10^{19}\,\text{eV}$ the suppression energy, and $\gamma_1 = 3.293$, $\gamma_2 = 2.53$, and $\Delta\gamma = 2.5$ to the spectral indexes. We employ the parametrization of the spectrum to assign a weight

$$w(E) = \begin{cases} 0.1 \cdot \left(\frac{E}{E_{\text{ankle}}}\right)^{-\gamma_1} & ; 10^{17}\,\text{eV} \leq E \leq 10^{18}\,\text{eV} \\ 1 \cdot \left(\frac{E}{E_{\text{ankle}}}\right)^{-\gamma_1} & ; 10^{18}\,\text{eV} \leq E \leq E_{\text{ankle}} \\ 1 \cdot \left(\frac{E}{E_{\text{ankle}}}\right)^{-\gamma_2} \left[1 + \left(\frac{E_{\text{ankle}}}{E_{\text{s}}}\right)^{\Delta\gamma}\right] \left[1 + \left(\frac{E}{E_{\text{s}}}\right)^{\Delta\gamma}\right]^{-1} & ; \\ & E_{\text{ankle}} \leq E \leq 10^{19}\,\text{eV} \end{cases} \tag{5.1}$$

to each simulated shower as a function of its energy. Since the event density $N_{\text{sim}}/(10^{18}-10^{17})\text{eV}$ in energy is by a factor of 10 larger than $N_{\text{sim}}/(10^{19}-10^{18})\text{eV}$, the multiplication with a factor of 0.1 for showers between $10^{17}\,\text{eV}$ and $10^{18}\,\text{eV}$ is necessary to achieve a smooth transition at $10^{18}\,\text{eV}$ between the two sets of simulated showers. As the total number of showers should remain unchanged by the weighting procedure, we normalize the weights w_i according to

$$\hat{w}_i = w(E_i) \frac{N}{\sum_{n=1}^{N} w(E_n)} \tag{5.2}$$

such that the total number of events

$$\sum_{i=1}^{N} \hat{w}_i = N \tag{5.3}$$

is preserved. The obtained weighted simulation spectra are shown in Fig. 5.1b together with the observed spectrum for AMIGA data.

5.2 MUON COUNTING STRATEGY

The MD muon counting strategy is based on the identification of patterns in the binary time traces for each scintillator bar within time windows of fixed length [5, 74]. The pattern definition needs to be strict enough to reject any background effects as cross-talk between neighboring PMT pixels or thermal single photo-electrons (SPEs). On the same time, it has to be loose enough to identify muons with different signal lengths and time structures. These are subject to variations due to the convolution of several effects as the energy deposit by the muon, the light attenuation in the wavelength-shifting (WLS) fibers, the quantum efficiency of the PMT, and the subsequent digitization of the analog pulses [93].

5.2.1 *Muon identification pattern*

The digitization of analog PMT pulses is performed by means of adjustable threshold discriminators and subsequent FPGA sampling at a frequency of 320 MHz (see Section 3.4). The discriminator thresholds are calibrated individually for each channel by a background calibration method to $\approx$ 30% of the mean channel specific single photo-electron (SPE) amplitude $\langle V_{\mathrm{SPE}} \rangle$. For this threshold value, the binary pattern of an SPE is restricted to one or two consecutive digital ones.

In contrast, muon pulses are in general much wider with a mean pulse width of 27.71 ± 0.23 ns corresponding to ≈ 9 SPE pulse widths above a threshold of $30\% \langle V_{\mathrm{SPE}} \rangle$ [94]. As a result of

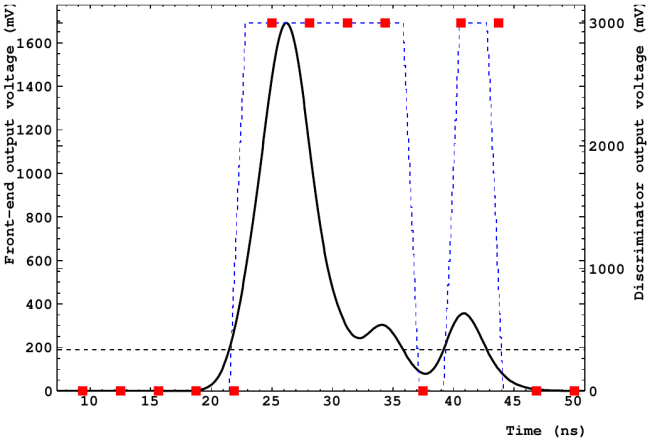

Figure 5.2: Example of a simulated analog muon pulse (solid black curve) that is digitized by the comparison with a threshold voltage (grey dashed line, discriminator output blue dashed line) and sampled in intervals of 3.125 ns (red squares). From [94].

the convolution of exponential decay processes in the light emission of the scintillators and WLS fibers [71], their time structures can be quite complex. A simulated example muon pulse is shown in Fig. 5.2. The discrimination of the analog pulse above a defined threshold (grey dashed line) and the subsequent electronic sampling produces a binary 1111011 pattern (red squares) of length $7 \times 3.125\,\text{ns} \approx 22\,\text{ns}$.

In the standard counting strategy, muons are identified by a match of the patterns 101 or 111 in three consecutive time bins [5, 74]. It is referred to as $1x1$ or gap strategy as the middle bin (x) can be either a one or zero. Hence, isolated SPE pulses, produced by background effects like cross-talk between neighboring PMT pixels or thermal fluctuations, are efficiently rejected due to their short length of one or maximally two consecutive positive bins for the chosen discriminator threshold. On the contrary, muons are successfully identified since most muon pulses extend over

at least three time bins. The intermediate x bin accounts for the fact that muon traces can be disconnected with null samples in between.

5.2.2 *Inhibition time window*

The possibility of null samples (0s) within a binary muon trace requires the application of time windows

$$\ldots \underbrace{1\,x\,1\,x\,x\,x\,x}_{w} \ldots \rightarrow 1\mu$$

starting from the first identified pattern match ($1x1$), over which the muon search process is stopped [6]. Without such "inhibition" windows, a disconnected muon trace (including one or more zeros) could be interpreted as stemming from two or more muons. The window has to be chosen long enough to ensure that the majority of muon traces does not extend over more than one window length. Otherwise, the last bins of a single muon pulse could be interpreted as the first muon pattern match of a second time window which would lead to over-counting.

At the same time, the window size must not be too large since multiple muons hitting the same scintillator strip within the same window would not be resolved. This so-called pile-up effect was taken into account in the detector design by choosing a high segmentation of 64 scintillator strips per module. However, undercounting due to pile-up is still encountered in case of very high muon densities that can occur close to the shower core or for high-energy events. It is hence necessary, given the constraints from the mean muon pulse widths to avoid over-counting, to choose the window size as small as possible.

The effect of over-counting for different inhibition window sizes has been first analyzed in a simulation study where 1000 muons were injected at a distance of 1 m from the central PMT [71]. Within a time span of 200 ns, muons where identified within window time spans that were varied in steps of 5 ns. The per-

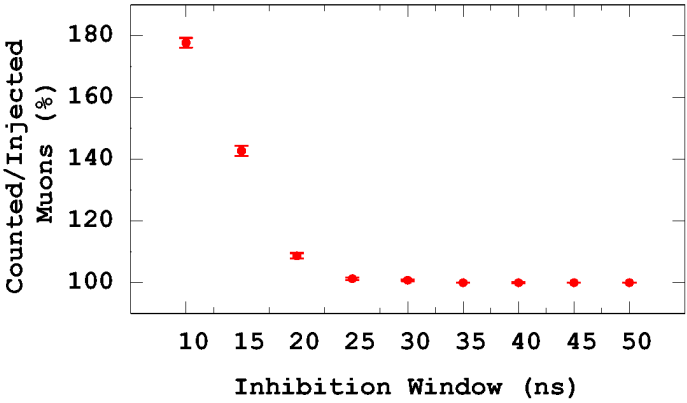

Figure 5.3: Percentage of muon over-counting as a function of the inhibition window size obtained from simulations. 1000 muons were injected at a distance of 1 m from the PMT over a time span of a 200 ns; muons were identified with the $1x1$ gap strategy. From [71].

centage of over-counting is shown in Fig. 5.3: a 10 ns window leads to 80% over-counting, 20 ns to 9%, and 25 ns to only 1.3% over-counting. For larger inhibition windows, virtually no over-counting is observed. Based on these results, the inhibition time window has been originally set to 25 ns, corresponding to eight bins of 3.125 ns by default. We show with extended studies that a window size of seven bins (22 ns) is however preferable, as will be discussed in Section 5.4.

5.3 PILE-UP CORRECTION

As a result of counting muons within extended time windows, muons which cross the same scintillator bar within the same window cannot be resolved individually. The sum of scintillator bars with signal for a fixed time window consequently tends to underestimate the true muon density. Nevertheless, it can be used to

estimate the most likely muon density by means of a Poissonian likelihood approach [95].

In Section 5.3.1, we focus on the theoretical derivation of the likelihood that describes the probability of measuring k muons within a single time window for a detector with n segments. The most probable muon density can then be estimated by the corresponding maximum likelihood estimator. The technical aspects of the muon counting algorithm, such as how to divide the time traces of the different channels into common time windows, are discussed in Section 5.3.2.

5.3.1 *Likelihood of a single time bin*

The probability of observing k muons for an unsegmented detector is given by the Poisson probability mass function

$$P_1(k;\mu) = e^{-\mu}\frac{\mu^k}{k!} \tag{5.4}$$

where the parameter μ corresponds to the average (*true*) number of muons. However, for a segmented detector, the probability of being hit by one or more muons (*on*) or being not hit (*off*) must be considered individually for each segment. The probability of a detector segment of $1/n$ of the total area being *off* is

$$P_1(k=0;\mu/n) = e^{-\mu/n} \equiv q \tag{5.5}$$

according to Eq. (5.4) with $k = 0$ and mean number of muons μ/n. In turn,

$$P_1(k\geq 1;\mu/n) = \left(1-e^{-\mu/n}\right) \equiv p = 1-q \tag{5.6}$$

is the complementary probability of ≥ 1 hits in one detector segment. Since the segment states are independent from each other, the probability of k segments being *on* follows the binomial distribution

$$P_n(k;\mu) = \binom{n}{k}p^k q^{n-k} = \binom{n}{k}e^{-\mu}\left(e^{-\mu/n}-1\right)^k \tag{5.7}$$

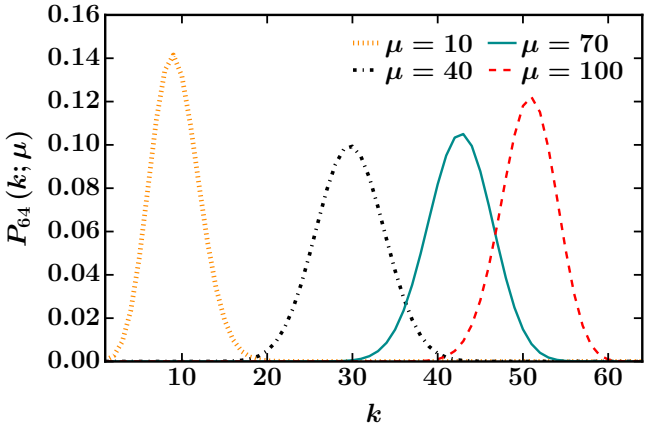

Figure 5.4: Probability of k segments with a reconstructed signal in a detector with $n = 64$ segments for different values of the true muon number μ.

which takes into account the number of combinations $\binom{n}{k}$ of k out of n scintillator strips with signal [95]. For illustration, the probabilities of k segments with signal in a detector divided into $n = 64$ segments are shown in Fig. 5.4 for different values of the true number of muons μ.

At the same time, Eq. (5.7) is the likelihood $L(\mu; k; n)$ of μ muons when k strips out of n are on. If $k < n$, the maximum likelihood estimator $\hat{\mu}$ is

$$\hat{\mu} = -n \ln\left(1 - \frac{k}{n}\right). \tag{5.8}$$

The functional dependence of $\hat{\mu}$ on k is shown in Fig. 5.5. For $k \to n$, the likelihood approaches unity for increasing μ and $\hat{\mu}$ tends to infinity. In the case of $k = n$, the module state is labeled as saturated (see Section 5.6) and the number of strips with signal k sets a lower bound to the number of muons in the fit of the muon lateral distribution function (MLDF).

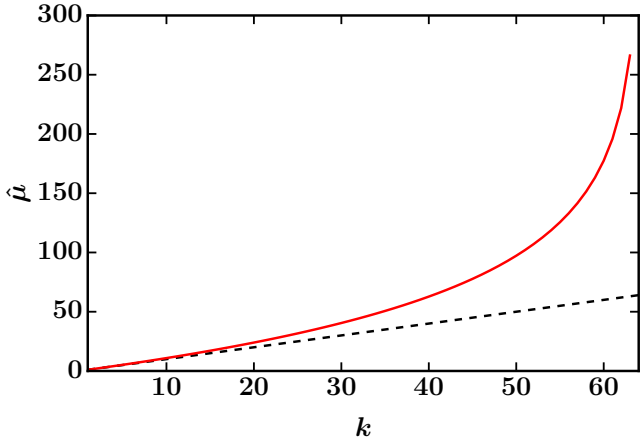

Figure 5.5: Number of muons $\hat{\mu}$ estimated from the number of pattern matches k for a detector divided into $n = 64$ segments (red solid line). The deviation of the corrected muon number estimate $\hat{\mu}$ from k (black dashed line, $\hat{\mu} = k$) increases with k.

5.3.2 *Muon number estimation for multiple time bins*

The muons produced in extensive air showers are spread in time such that the described muon number estimation for a single time bin needs to be generalized to multiple time bins. The muon number reconstruction algorithm consists of the following steps: First, muon pattern matches are individually searched in the binary trace (1024 bins of 3.125 ns each) of each scintillator strip. If such a $1x1$ pattern is found, an inhibition window is applied and the start time t_i of the window is stored. After the iteration over all 64 channels, a list of window start times is available for each channel. In order to be able to apply the likelihood approach from Section 5.3.1 for a single time window, the total event time is then split into N windows with length of the chosen inhibition window size. For each window w_i, the number of channels k_i

with a muon pattern match window starting within w_i is counted and the true number of muons is estimated by

$$\hat{\mu}_i = -n \ln\left(1 - \frac{k_i}{n}\right) . \tag{5.9}$$

The total number of muons

$$\hat{\mu} = -n \sum_{i=1}^{N} \ln\left(1 - \frac{k_i}{n}\right) \tag{5.10}$$

is then obtained by summing over all N time windows.

The described procedure is illustrated for a fictional event in Table 5.1. The binary traces are shown for seven channels within the time bins $551 - 562$ out of 1024 total time bins. Identified $1x1$ muon patterns within an inhibition window of seven bins are displayed by grey shaded columns, the starting 1s are highlighted in red. The subsequent splitting of the traces into "global" windows of seven bins is visually marked by horizontal red dashed lines, forming the boundaries of window number 70. The number of muon pattern matches k_i which start in the corresponding window (in window 70 three starting muon traces are visible) is then used to estimate the true number of muons within this time window. According to Eq. (5.10), the total number of muons is obtained by summing over all $N = {}^{1024}/_{7}$ windows.

5.4 STUDY OF THE INHIBITION WINDOW SIZE

In a first simulation study of the effect of the inhibition window size [71], described in Section 5.2.2, the percentage of over-counting was analyzed with a simplified scenario where 1000 muons were injected at a distance of 1 m to the PMT. However, in real extensive air showers, under-counting is an equally important effect that needs to be considered. Over-counting occurs if the chosen inhibition window size is smaller than the average muon pulse width. In this case, one muon can leave a signal in

		Channel Number							
Time Bin	Window Nb	1	2	3	4	5	6	⋯	64
⋮	⋮	⋮	⋮	⋮	⋮	⋮	⋮	⋮	⋮
551	69	1	0	0	0	x	0	⋯	0
552	69	x	0	0	0	0	0	⋯	0
553	70	1	0	0	0	0	0	⋯	1
554	70	x	0	0	0	0	0	⋯	x
555	70	x	0	1	0	0	1	⋯	1
556	70	x	0	x	0	0	1	⋯	x
557	70	x	0	1	0	0	0	⋯	x
558	70	0	0	x	0	0	0	⋯	x
559	70	0	0	x	1	0	0	⋯	x
560	70	0	0	x	x	0	0	⋯	1
561	71	1	1	x	1	1	0	⋯	1
562	71	x	1	0	x	0	1	⋯	0
⋮	⋮	⋮	⋮	⋮	⋮	⋮	⋮	⋮	⋮

Table 5.1: Fictional event to illustrate the muon number estimation based on the number of pattern matches in windows of seven bins. The boundaries of the global window with number 70 are visually marked by two red dashed lines. The number of pattern matches k_i in the ith global window corresponds to the number of muon pattern match windows (grey shaded columns of seven bins) starting in this window. The true number of muons $\hat{\mu}_i$ for the ith global window, accounting for the Poissonian probability of hitting k_i out of n segments, is estimated with Eq. (5.9). The sum over the estimated muon numbers of all global windows yields the total muon number estimate $\hat{\mu} = \sum_{i=1}^{N} \hat{\mu}_i$.

two consecutive time windows. On the contrary, small inhibition time windows are of advantage for high muon densities with a narrow spread of muon arrival times. This situation occurs especially near to the shower core and for high-energy events. Here, small inhibition time windows reduce the probability that a second muon arrives within the inhibition window of a previously identified muon and hence cannot be resolved.

The inhibition window size must be chosen such that it provides a good balance between over- and under-counting. For a realistic scenario, we study the impact of the window size on the reconstruction bias with simulations of extensive air showers. The employed CORSIKA library of fixed energy and the subsequent simulation of the detector responses for both SD and MD with Offline have been described in Sections 5.1.2 and 5.1.4. To avoid any effects from corner-clipping muons, that are discussed in Section 5.5, we restrict the analysis of the window size to vertical showers with zenith angle $\theta = 0°$. Analyzing the muon number reconstruction accuracy based on these simulations, we account for the effect of different muon number distributions and timings for different primary particles, energies, hadronic interaction models, and distances to the shower core. Furthermore, muons can hit the scintillator modules over their complete surface instead of an injection point at a fixed distance. Thereby, the effect of light attenuation within the optical fibers is taken into account.

We compare results for reconstructions that have been carried out for different inhibition window sizes of six, seven, and eight bins of 3.125 ns corresponding to approximately 19, 22, and 25 ns. For every AMIGA module, the number of muons N_{Rec} is calculated by Eq. (5.10) based on the number of channels with pattern matches in each time window. The reconstructed muon numbers N_{Rec} are then compared to the number of simulated muons N_{MC}

that truly hit the scintillator module surface after propagation through the soil. We quantify the reconstruction bias by

$$b_{\mathrm{Rec}} = \frac{N_{\mathrm{Rec}} - N_{\mathrm{MC}}}{\sqrt{N_{\mathrm{MC}}}} \tag{5.11}$$

which measures the relative bias of the muon number reconstruction w.r.t. the standard deviation $\sqrt{N_{\mathrm{MC}}}$ of a Poissonian distribution with mean N_{MC}.

The mean counting bias for inhibition windows of six, seven, and eight bins is shown in Figs. 5.6 and 5.7 for extensive air showers with primary energies of 10^{18} eV and 10^{19} eV simulated with the QGSJETII-04 high-energy interaction model. The bias b_{Rec} is displayed as a function of the radial distance from the shower core (top) and as a function of N_{MC} (bottom). Error bars correspond to the standard error of the mean within the bins in r or N_{MC}, respectively.

In Fig. 5.7, the lower muon number limit

$$\hat{\mu}_{\mathrm{sat}} = \sum_{i=1}^{N} k_i \tag{5.12}$$

for saturated modules (i.e. modules with 64 channels with signal in at least one global time window) is displayed by filled markers in addition to the muon number estimate for "candidate" modules (unfilled markers) that are neither "saturated" nor "silent" (see Section 3.4 for the definition of the module statuses). We only observe saturation for a simulated energy of 10^{19} eV, which is almost out of the accessible range for AMIGA. For smaller energies $E \leq 10^{18.5}$ eV no saturated counters occur in simulations. The lower muon limit $\hat{\mu}_{\mathrm{sat}}$ under-estimates the true muon density by not applying the correction Eq. (5.8) but summing over the number of channels with signals only. This is however accounted for by the Poissonian likelihood defined in Eq. (5.34) which treats $\hat{\mu}_{\mathrm{sat}}$ as a lower limit in the MLDF fit (see Section 5.6).

According to Figs. 5.6 and 5.7, a window of seven bins is preferable to windows of six or eight bins for both considered primary

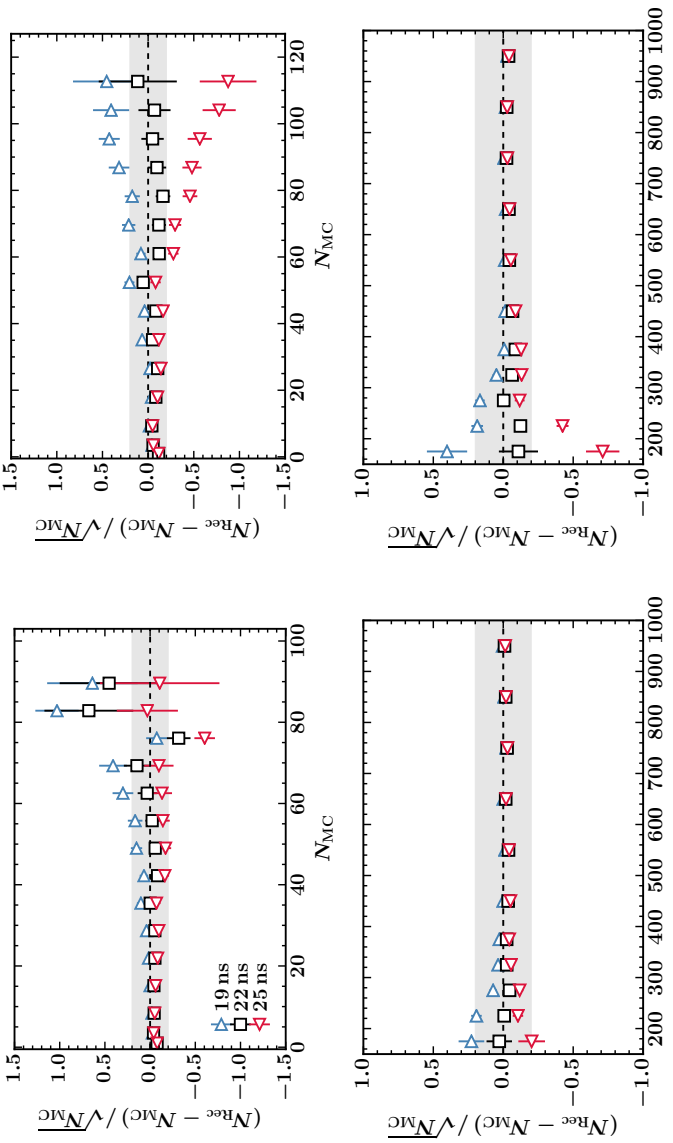

Figure 5.6: Reconstruction bias as a function of N_{MC} (top) and the core distance r (bottom) for showers with energy $E = 10^{18}$ eV simulated with the QGSJetII-04 high-energy model. Results are displayed for different inhibition windows of 19, 22, and 25 ns.

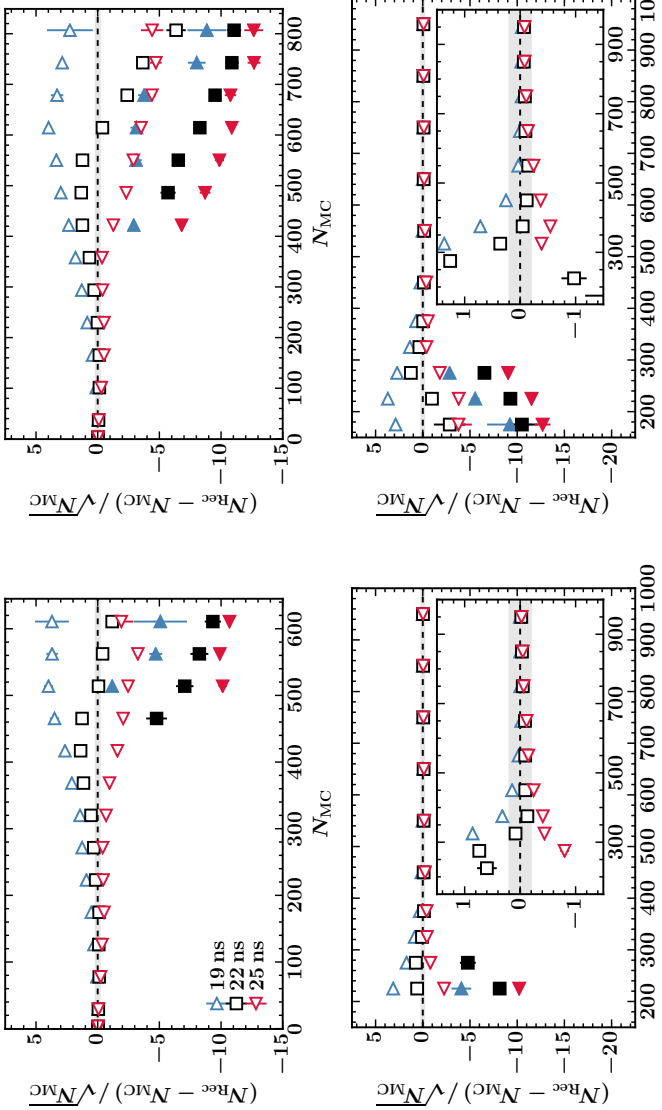

(a) Proton (b) Iron

Figure 5.7: The same as in Fig. 5.6 for showers with energy $E = 10^{19}$ eV simulated with the QGSJetII-04 high-energy model. Unfilled markers denote muon number estimates from candidate modules, filled markers the lower muon number limit for saturated modules. Inset plots show a zoomed version to intermediate distance.

energies. Close to the shower core, over-counting is observed for six bin windows, while eight bins lead to under-counting. At an intermediate energy for AMIGA of 10^{18} eV, over-counting can be as large as 40% of the Poissonian error $\sqrt{N_{\mathrm{MC}}}$ for a window of eight bins and an iron primary particle. At the same time, under-counting of up to 70% occurs for a window of six bins. For a high primary energy of 10^{19} eV, which is at the upper reachable limit for AMIGA, both over- and under-counting can be even as large as $\pm 4\sqrt{N_{\mathrm{MC}}}$ for windows of six and eight bins, respectively.

In contrast, for a window of seven time bins, the reconstruction bias is well contained within 20% of the Poissonian error for all radial distances and primary energies $\leq 10^{18.5}$ eV. In comparison to windows of six and eight bins, b_{Rec} is generally smaller and flatter as a function of the radial distance r or the injected number of muons N_{MC}. Even for a high primary energy of 10^{19} eV, the bias is flat and smaller than 20% of the Poissonian error for radial distances $\geq$ 350 m. For smaller core distances, the bias rises (over-counting) and then decreases again (under-counting) for very close core distances and iron primaries.

Both effects can be explained by the high muon densities near to the shower core shown in the top plot of Fig. 5.7. The estimated number of muons $\hat{\mu}(k)$, as a function of the pattern matches k within one time bin, deviates strongly from linearity for approximately $k \geq 40$ as displayed in Fig. 5.5. In this regime, which is encountered for high muon densities, small changes in k have a large impact on the estimator $\hat{\mu}(k)$ and can lead to over-counting as observed in Fig. 5.7. However, for very small core distances, the effect of muon pile-up, leading to under-counting as a consequence of the high muon densities and the narrow spread of the muon arrival times, outweighs the over-estimation of $\hat{\mu}(k)$.

Except for this extreme case of close core distances $\leq$ 350 m for a very high energy of 10^{19} eV and iron primaries, the reconstruction bias for a window of seven bins is $\leq$ 20% of $\sqrt{N_{\mathrm{MC}}}$ for all considered energies, primaries, and hadronic interaction models. Although inhibition windows of six and eight bins tend to pro-

duce over- and under-counting, respectively, for increasing muon densities, the biases of all three considered window sizes are very similar for core distances that are larger than about 450 m and energies $\leq 10^{18.5}$ eV as shown in Fig. 5.8.

5.5 CORNER-CLIPPING CORRECTION

In addition to the pile-up correction (Section 5.3), taking into account the Poissonian muon hit probabilities for a segmented detector, and the choice of an appropriate muon counting time window (Section 5.4), further possible counting biases need to be considered. A source of over-counting is the effect of corner-clipping muons that has been briefly discussed in Section 3.4. These are muons that arrive from an inclined, non-vertical, direction w.r.t. the surface of a scintillator module such that a signal is deposited in two or more neighboring scintillator bars as illustrated in Fig. 5.9.

Besides the muon inclination angle θ w.r.t. the upwards pointing z-axis, the difference in azimuth $\Delta\varphi_m = \varphi - \varphi_m$ between the momentum direction of the muon and the orientation of the module in the ground plane is of crucial importance. A muon can only hit two neighboring bars if both θ and $\Delta\varphi_m$ are distinct from zero as illustrated in Fig. 5.10. Maximal over-counting occurs for $\Delta\varphi_m = 90°$, when the muon momentum is perpendicular to the orientation of the scintillator bars and increases with θ.

We parametrize the counting bias stemming from corner-clipping muons with the library of fixed energy of EAS simulations that has been described in Sections 5.1.2 and 5.1.4. The percentage of over-counting due to corner-clipping muons is quantified for each candidate AMIGA module by the relative bias

$$b_{\text{clip}} = \frac{N_{\text{Rec}} - N_{\text{MC}}}{N_{\text{MC}}} \tag{5.13}$$

where N_{MC} is the number of simulated muons that truly hit the module and N_{Rec} the reconstructed number of muons. Owing to

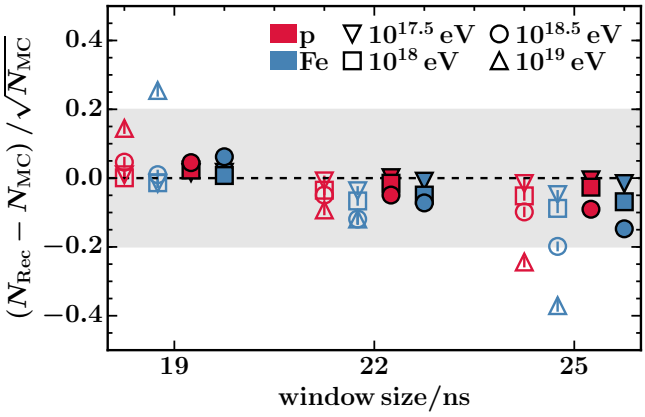

(a) 400 m $\leq r \leq$ 500 m

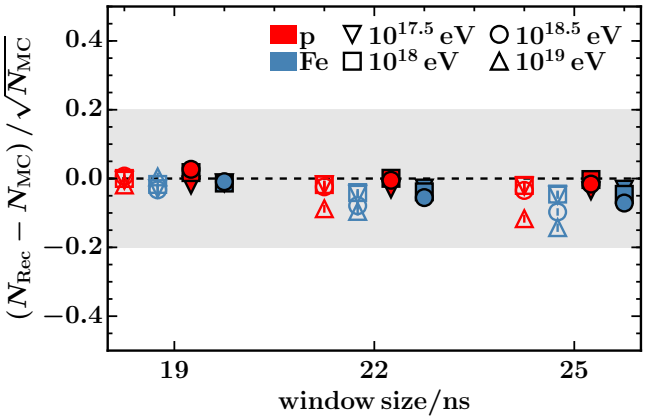

(b) 600 m $\leq r \leq$ 700 m

Figure 5.8: Comparison of the reconstruction bias for window sizes of six (19 ns), seven (22 ns), and eight (25 ns) bins within radial ranges of (a) 400 m $\leq r \leq$ 500 m and (b) 600 m $\leq r \leq$ 700 m for different primary energies (marker symbols), primary particles (color), and hadronic interaction models (QGSJETII-04: unfilled, EPOS-LHC: filled).

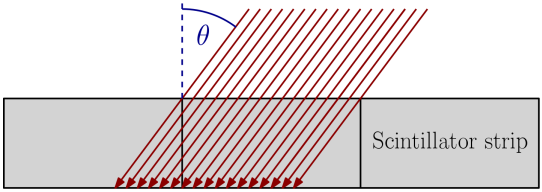

Figure 5.9: Illustration of the corner-clipping effect. An inclined muon can hit two neighboring scintillator strips which leads to an overestimation of the muon density if no correction is applied.

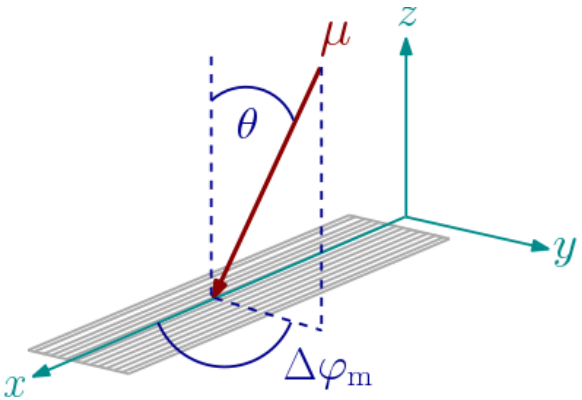

Figure 5.10: The probability of over-counting due to corner-clipping muons depends both on the zenith and the azimuth angle of the impinging muon w.r.t. the orientation of the detector module. Maximal over-counting occurs for $\Delta\varphi_{\mathrm{m}} = 90^{\circ}$ and increases with θ.

the fact that the momentum direction of the impinging muons cannot be reconstructed with the AMIGA detectors, we approximate the mean muon zenith and azimuth angles by the angles θ_{SD} and φ_{SD} of the shower axis that were reconstructed by the SD as described in Section 3.1.

We determine the average percentage of over-counting per module for different shower zenith angles of 0°, 12°, 22°, 32°, 38°, 48°, and 56° with simulations of the library of fixed energy described in Section 5.1.2. In order to reduce the dependency on the energy, primaries, and hadronic interaction models, we include simulations with primary energies of 10^{18} eV and $10^{18.5}$ eV, proton and iron primaries, and EPOS-LHC and QGSJETII-04 as hadronic high-energy interaction models. All n AMIGA modules within this set of simulations with distances 200 m $\leq r \leq$ 1000 m to the shower axis and at least one impinging muon ($N_{\mathrm{MC}} \geq 1$) are taken into account to calculate the weighted average percentage of over-counting

$$\overline{b}_{\mathrm{clip}} = \frac{\sum_{i=1}^{n} b^i_{\mathrm{clip}} / (\sigma^i_{\mathrm{clip}})^2}{\sum_{i=1}^{n} 1/(\sigma^i_{\mathrm{clip}})^2} \tag{5.14}$$

where we assume a Poissonian uncertainty $\sigma^i_{\mathrm{clip}} = 1/\sqrt{N^i_{\mathrm{MC}}}$. In Fig. 5.11, $\overline{b}_{\mathrm{clip}}$ is shown in bins of the approximated azimuth difference $\Delta\varphi_{\mathrm{m}} \approx \varphi_{\mathrm{SD}} - \varphi_{\mathrm{m}}$ between the mean muon momentum direction and the orientation of the module for the different shower zenith angles. The results of our parametrization of Eq. (5.15), that will be discussed in the following, are displayed by solid curves for each zenith angle $\theta \approx \theta_{\mathrm{SD}}$.

Since the corner-clipping effect is minimal for $\Delta\varphi_{\mathrm{m}} = 0°$ and 180° (the projection of the muon momentum in the ground plane is parallel to the module orientation) and maximal for $\Delta\varphi_{\mathrm{m}} =$ 90° and 270° (the momentum projection is perpendicular to the module orientation), the mean percentage of over-counting can be expressed by the parametrization

$$f_{\mathrm{clip}}(\theta, \Delta\varphi_{\mathrm{m}}) = a(\theta) + b(\theta) \cdot |\sin \Delta\varphi_{\mathrm{m}}| \tag{5.15}$$

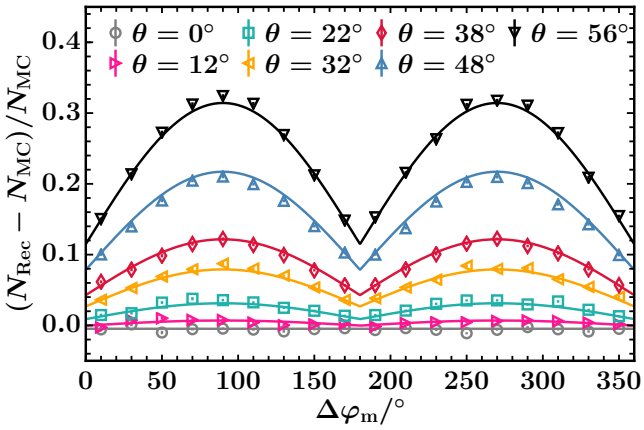

Figure 5.11: Dependence of over-counting due to corner-clipping muons as a function of the azimuth difference $\Delta\varphi_\mathrm{m}$. Markers show the weighted average percentage of over-counting, error bars the weighted standard deviation in bins of 20°. In addition, the results of the parametrization of Eq. (5.15) are shown by solid curves for each zenith angle $\theta \approx \theta_\mathrm{SD}$.

with $\theta \approx \theta_\mathrm{SD}$ and $\Delta\varphi_\mathrm{m} \approx \varphi_\mathrm{SD} - \varphi_\mathrm{m}$. Both the offset $a(\theta)$ and the amplitude $b(\theta)$ increase as a function of the zenith angle θ. We have parametrized the dependencies phenomenologically by

$$a(\theta) = a_0 + a_1\,(1 + a_2 \cos\theta)\sin\theta \quad \text{and} \tag{5.16}$$

$$b(\theta) = b_0\,(1 + b_1 \cos\theta)\sin\theta \tag{5.17}$$

and performed a global least squares (LS) minimization of

$$\begin{aligned}\chi^2 &= \mathrm{LS}\,(a_0, a_1, a_2, b_0, b_1) \\ &= \sum_{i=1}^{N} \left(\frac{b^i_\mathrm{clip} - f_\mathrm{clip}\,\left(\theta^i, \Delta\varphi^i_\mathrm{m}; a_0, a_1, a_2, b_0, b_1\right)}{\sigma^i_\mathrm{clip}} \right)^2\end{aligned} \tag{5.18}$$

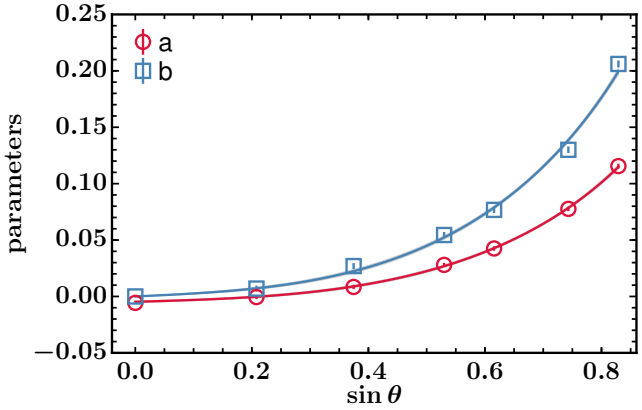

Figure 5.12: Functions $a(\theta)$ and $b(\theta)$ of Eq. (5.15) describing the dependence of muon over-counting on the zenith angle as a function of $\sin\theta$. Markers show the best-fit parameters of a and b with their corresponding standard deviations (error bars) that have been obtained with χ^2 fits for each zenith angle. Solid curves display the global-fit solution taking into account all zenith angels; the very small statistical uncertainties are indicated by shaded bands (hardly visible).

over the sum of all N modules. The relative bias is calculated as $b^i_{\text{clip}} = (N^i_{\text{Rec}} - N^i_{\text{MC}})/N^i_{\text{MC}}$. We employ Gaussian error propagation to calculate the uncertainties

$$\sigma^i_{\text{clip}} = \sqrt{\frac{1}{{N^i_{\text{MC}}}^2}{\sigma^i_{\text{Rec}}}^2 + \frac{{N^i_{\text{Rec}}}^2}{{N^i_{\text{MC}}}^4}{\sigma^i_{\text{MC}}}^2} \tag{5.19}$$

of the relative biases b^i_{clip}. Since we extract the number of injected muons N_{MC} directly from the CORSIKA simulations, we set the corresponding error σ_{MC} to zero. For the reconstructed number of muons N_{Rec}, we assume a Poissonian uncertainty $\sigma_{\text{Rec}} = \sqrt{N_{\text{MC}}}$

based on the injected number of muons. The uncertainties of the bias is therefore calculated as

$$\sigma^i_{\text{clip}} = \frac{1}{\sqrt{N^i_{\text{MC}}}} \tag{5.20}$$

for each of the modules. The LS minimization of Eq. (5.18) yields the best fit values

$$\begin{aligned} a_0 &= -0.005 \pm 0.001 & 0.515 &\pm 0.011 \\ a_1 &= 0.308 \pm 0.008 & -0.953 &\pm 0.010 \\ a_2 &= -0.951 \pm 0.014 \end{aligned} \tag{5.21}$$

with a reduced χ^2 value of $\chi^2_{\text{red}} = \chi^2/n_{\text{dof}} = 0.61$. The resulting parametrizations of $a(\theta)$ and $b(\theta)$ are plotted as a function of $\sin\theta$ in Fig. 5.12. The best-fit parameters that have been obtained for χ^2 fits for each zenith angle

We use the obtained parametrization of f_{clip} to correct the number of reconstructed muons by

$$N^{\text{corr}}_{\text{Rec}}\left(\theta, \Delta\varphi_{\text{m}}\right) = \frac{N_{\text{Rec}}}{1 + f_{\text{clip}}\left(\theta, \Delta\varphi_{\text{m}}\right)} \tag{5.22}$$

for each AMIGA module based on the geometry of the EAS and the azimuthal orientation of the module. The effect of the correction is illustrated in Fig. 5.13 for the example of proton simulations with primary energy $10^{18.5}$ eV, zenith angle 38° and QGSJETII-04 as high-energy hadronic interaction model. Without applying the correction of Eq. (5.22), the mean relative muon counting bias is of the order of 9% for all radial distances to the shower core. Furthermore, as expected, the bias depends on the considered range in azimuth difference $\Delta\varphi_{\text{m}}$. For the azimuth bin of $\Delta\varphi_{\text{m}} = 90° \pm 15°$, the mean bias is approximately 11% while it is only 5% in the azimuth bin of $\Delta\varphi_{\text{m}} = 0° \pm 15°$. After correcting N_{Rec} by Eq. (5.22) for the corner-clipping effect, the splitting for different azimuth bins is removed. The overall mean bias is

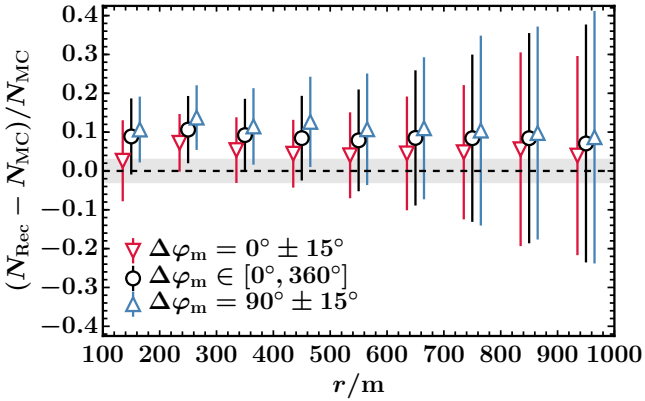

(a) Uncorrected

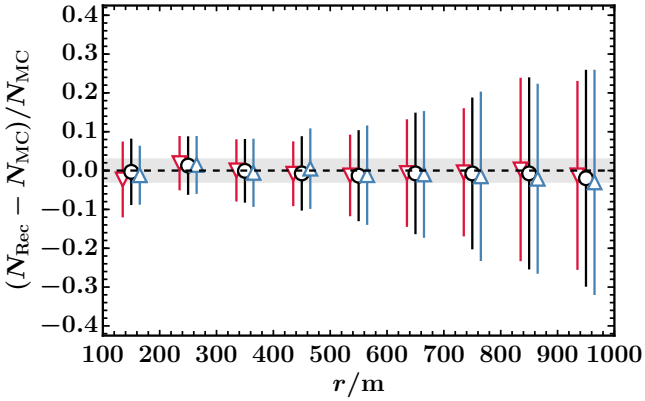

(b) Corrected

Figure 5.13: Relative muon counting bias in bins of radial distance for proton simulations with primary energy $10^{18.5}$ eV, zenith angle 38° and QGSJETII-04 as high-energy hadronic interaction model without applying the corner-clipping correction (a) and after correcting N_{Rec} by Eq. (5.22) (b). Markers denote the mean counting bias, error bars the standard deviation within each radial bin.

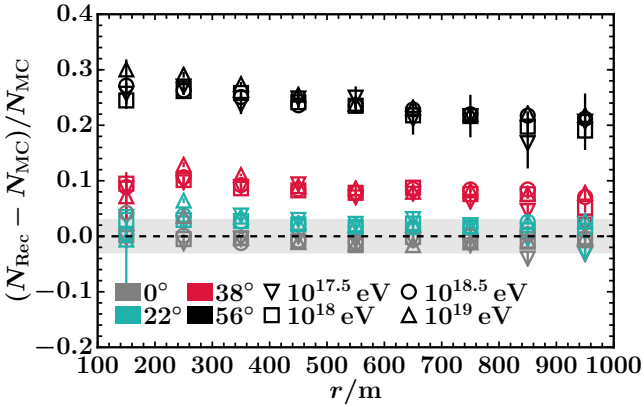

(a) Uncorrected

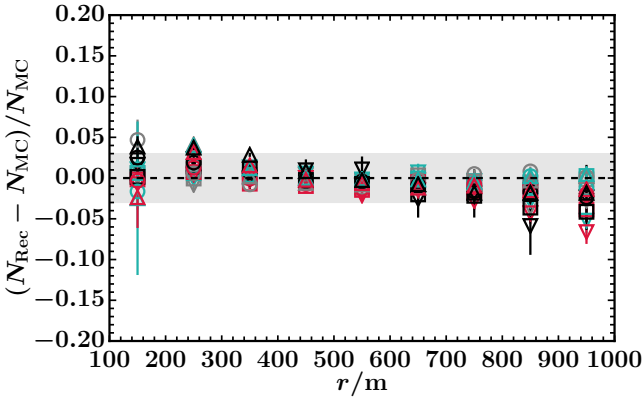

(b) Corrected

Figure 5.14: Relative muon counting bias in bins of radial distance for proton simulations with QGSJETII-04 as high-energy hadronic interaction model and different primary energies (marker symbols) and zenith angles (colors) without applying the corner-clipping correction (a) and after correcting N_{Rec} by Eq. (5.22) (b). Markers denote the mean counting bias, error bars the standard error of the mean within each radial bin.

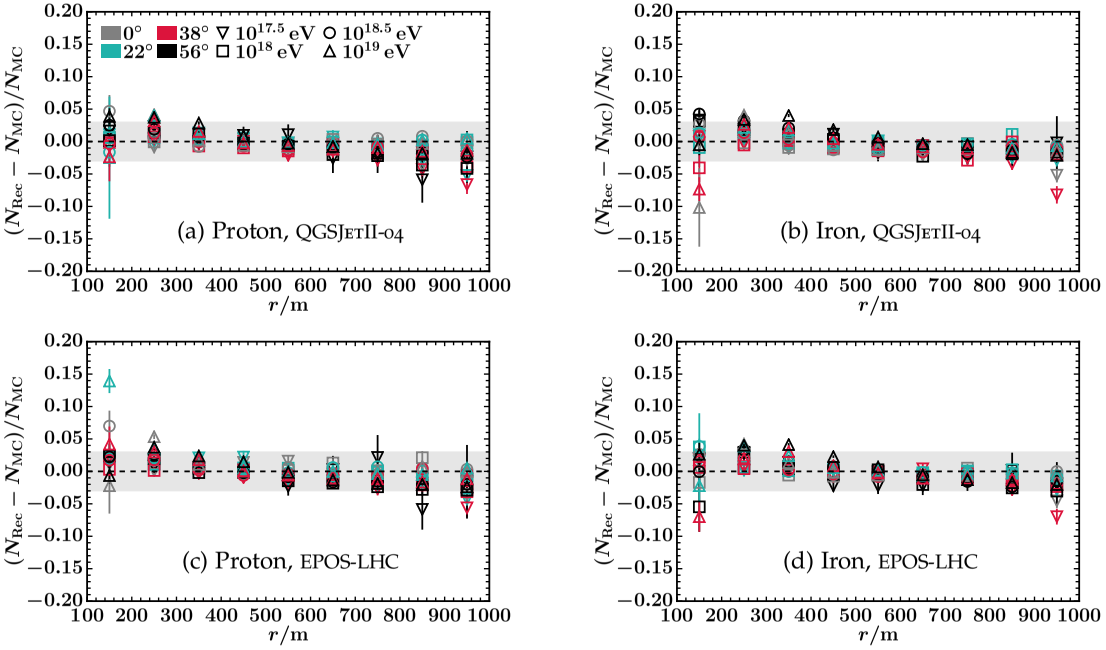

Figure 5.15: Relative muon counting bias in bins of radial distance for simulations with different primary particles and hadronic interaction models after applying the corner-clipping correction Eq. (5.22). Markers denote the mean counting bias, error bars the standard error of the mean within each radial bin.

smaller than 1% and, over the whole considered radial range, well contained within $\pm 3\%$ (shaded band).

The correction equally works well for other primary energies and shower zenith angles as illustrated in Fig. 5.14 for proton showers simulated with the QGSJETII-04 high-energy hadronic interaction model. Even the large bias of approximately $20 - 30\%$, depending on the distance to the shower core, for $\theta = 56^\circ$ is reduced to $\pm 6\%$. Fig. 5.15 shows that this holds for all primary energies and zenith angles for both proton and iron primaries and for both considered hadronic interaction models.

The previous results have been obtained on the level of single modules. However, in the MD reconstruction of events, an MLDF is fitted to the lateral distribution of the reconstructed muon densities of the individual modules to obtain the muon density ρ_{450} at the optimal distance of $r = 450\,\mathrm{m}$. The MLDF fitting procedure will be discussed in detail in Section 5.6. In Fig. 5.16 top, the mean relative bias $\left(\rho_{r_{\mathrm{opt}}} - \rho^{\mathrm{MC}}_{r_{\mathrm{opt}}}\right)/\rho^{\mathrm{MC}}_{r_{\mathrm{opt}}}$ of the fitted $\rho_{r_{\mathrm{opt}}}$ values for $r_{\mathrm{opt}} = 450\,\mathrm{m}$ is shown before (Fig. 5.16a) and after (Fig. 5.16b) the corner-clipping correction for MLDF fits with fixed β parameter. The reference values $\rho^{\mathrm{MC}}_{r_{\mathrm{opt}}}$ have been obtained by an MLDF fit to the number of truly injected muons N_{MC} in each module. The MLDF parameters β were in both cases fixed by Eq. (5.37) with $b_0 = 4.4$ and $b_1 = -1.1$ (see Eq. (5.46)). Applying the corner-clipping correction, the increase of the density bias as a function of the zenith angle up to 25% for $\theta = 56^\circ$ is virtually removed for all primaries, energies and hadronic interaction models. The bias is well contained within $\pm 3\%$ which shows the successful functioning of the developed correction method. The standard deviation σ of the relative bias remains approximately constant for $\theta \leq 32^\circ$ and is slightly reduced for higher zenith angles as shown in the bottom plots of Fig. 5.16.

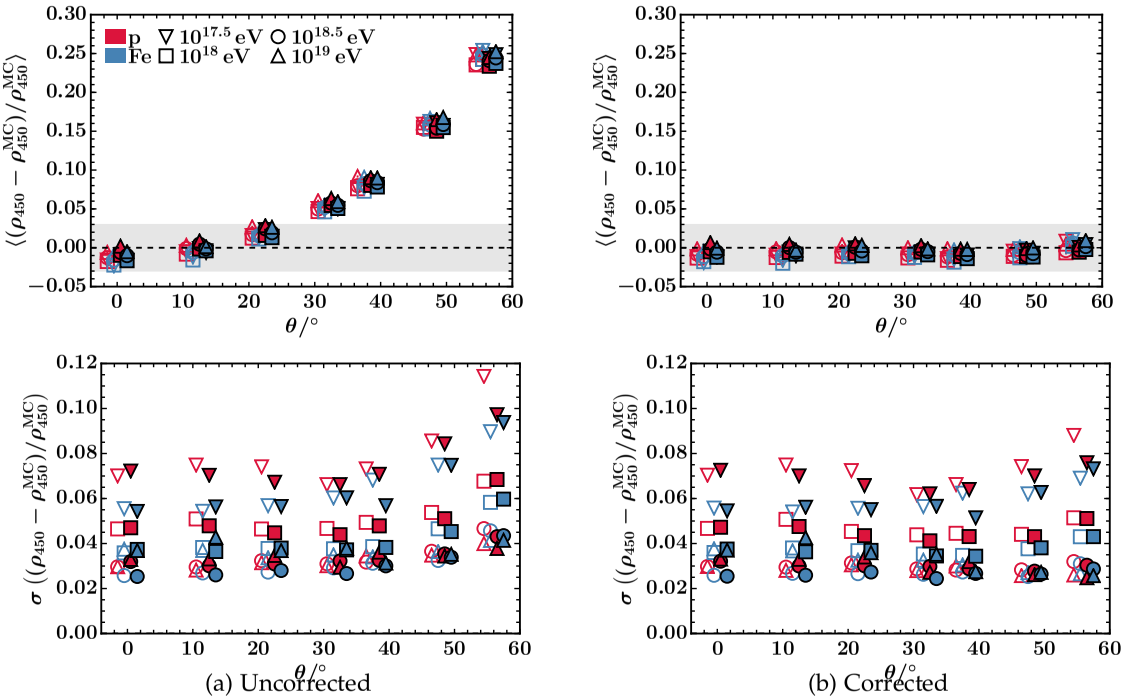

Figure 5.16: Mean (top) and standard deviation (bottom) of the relative bias $\left(\rho_{r_{opt}} - \rho_{r_{opt}}^{MC}\right)/\rho_{r_{opt}}^{MC}$ as a function of θ for MLDF fits with fixed β parameter. (a) Without applying the corner-clipping correction, (b) after correcting N_{Rec} by Eq. (5.22). Different energies are distinguished by marker symbols, primary particles by colors. Results for simulations with the EPOS-LHC (QGSJETII-04) interaction model are shown by filled (unfilled) markers.

5.6 MUON LATERAL DENSITY FUNCTION

The muon content in extensive air showers is a composition sensitive observable. It depends on the type of the primary cosmic ray particle such that heavy particles produce more secondary muons in the shower development than light primaries [44, 47]. In air shower experiments, only a part of the shower is sampled by detectors that are placed in a grid in the ground plane. However, the particle density at a certain reference distance from the shower core can be used as a proxy for the muon content of the shower. To this end, the muon lateral distribution function (MLDF) for AMIGA is parametrized by a KASCADE-Grande-like function [96]

$$\rho_\mu(r) = A_\mu \cdot \frac{f_\mu(r)}{f_\mu(r_{\text{opt}})} \quad \text{with} \tag{5.23}$$

$$f_\mu(r) = \left(\frac{r}{r^*}\right)^{-\alpha} \left(1 + \frac{r}{r^*}\right)^{-\beta} \left(1 + \left(\frac{r}{10r^*}\right)^2\right)^{-\gamma}. \tag{5.24}$$

The reference distance r_{opt} is usually chosen as the distance to the shower core where the functional form and slope of the LDF parametrization have the least impact on the fitted density, i.e. where the fluctuations of the LDF are minimal. It mainly depends on the detector spacing [97]; for an array with 750 m spacing an optimal distance of $r_{\text{opt}} = 450\,\text{m}$ has been found for both SD [98] and MD [99]. The muon density $A_\mu \equiv \rho_\mu(r_{\text{opt}})$ at the reference distance and the slope β of the MLDF are free parameters that are determined on an event-by-event level if certain conditions are met (see Section 5.6.2).

5.6.1 *Log-likelihood minimization*

We fit the parameters $\vec{p} = (A_\mu, \beta)$ with a log-likelihood minimization procedure. For a given *true* muon density ρ_μ, the expected

number of muons for a detector of area A and a shower zenith angle θ is

$$\mu = \rho_\mu \underbrace{A \cos\theta}_{A_{\text{eff}}}. \tag{5.25}$$

However, the actual number of muons that hit the detector in an event fluctuates according to a Poissonian probability distribution [99]

$$P(k;\mu) = e^{-\mu} \frac{\mu^k}{k!}. \tag{5.26}$$

Therefore, omitting *saturated* or *silent* modules for the moment (see Section 3.4 for the status definitions), the *candidate* likelihood

$$\mathcal{L}_{\text{cand}}(\vec{p}) = \prod_{i=1}^{N_{\text{cand}}} e^{-\mu(r_i;\vec{p})} \frac{\mu(r_i;\vec{p})^{n_i^{\text{corr}}}}{n_i^{\text{corr}}!} \tag{5.27}$$

needs to be maximized to derive the most likely parameters $\vec{p} = (A_\mu, \beta)$ of the MLDF defined in Eq. (5.23). In practice, for reasons of numerical stability, the negative log-likelihood function $-\log(\mathcal{L}_{\text{cand}}(\vec{p}))$ is minimized w.r.t. $\vec{p}$. Here, N_{cand} denotes the number of candidate modules in the event, r_i the core distance of the i-th module, and n_i^{corr} the estimated number of muons after applying both the pile-up and corner-clipping correction described in Sections 5.3 and 5.5.

This likelihood can only be employed for non-saturated candidate modules, i.e. modules without any errors in data acquisition (not *rejected*) and with a corresponding WCD that was flagged as a candidate station. Further, the module reconstruction status must not be *saturated*, that is the number of channels with signal k must be smaller than the total number of channels n for all time windows.

For saturated modules, the sum of the number of segments with signal over all time bins n^{sat} (Eq. (5.12)), is used as a lower limit in the LDF fit. The corresponding likelihood

$$\mathcal{L}_{\text{sat}}(\vec{p}) = \prod_{i=1}^{N_{\text{sat}}} \frac{1}{2}\left[1 - \text{Erf}\left(\frac{n_i^{\text{sat}} - \mu(r_i;\vec{p})}{\sqrt{2\mu(r_i;\vec{p})}}\right)\right] \tag{5.28}$$

is based on the fact that a Poisson distribution with mean value μ can be approximated by a Gaussian distribution

$$P(n;\mu) \approx e^{(n-\mu)^2/2\mu}\sqrt{2\pi\mu} \tag{5.29}$$

with mean value μ and standard deviation $\sigma = \sqrt{\mu}$. The probability that the actual number of muons n be greater than a given lower limit n_0 is then

$$P(n \geq n_0) = \frac{1}{\sqrt{2\pi\mu}} \int_{n_0}^{\infty} dn\, e^{-(n-\mu)^2/2\mu} \tag{5.30}$$

$$= \frac{1}{2}\left[1 - \text{Erf}\left(\frac{n_0 - \mu}{\sqrt{2\pi\mu}}\right)\right] \tag{5.31}$$

with the error function being

$$\text{Erf}(x) = \frac{2}{\sqrt{\pi}} \int_0^x \text{d}t e^{-t^2}. \tag{5.32}$$

An AMIGA muon counter (and all its modules) is flagged as *silent* when the SD partner tank is silent. For these modules, no muon data is available. Nevertheless, the likelihood

$$\mathcal{L}_{\text{sil}}(\vec{p}) = \prod_{i=1}^{N_{\text{sil}}} e^{-\mu(r_i;\vec{p})}\left(1 + \mu(r_i;\vec{p}) + \frac{1}{2}\mu(r_i;\vec{p})^2\right), \tag{5.33}$$

which corresponds to the probability of less or equal two muons in all N_{sil} modules is used to constrain the LDF fit at large distances to the shower core.

The product of the likelihood functions $\mathcal{L}_{\text{sat}}(\vec{p})$, $\mathcal{L}_{\text{cand}}(\vec{p})$, and $\mathcal{L}_{\text{sil}}(\vec{p})$ for the saturated, candidate, and silent modules forms the joined likelihood for any event

$$\begin{aligned}\mathcal{L}(\vec{p}) = &\prod_{i=1}^{N_{\text{sat}}} \frac{1}{2}\left[1 - \text{Erf}\left(\frac{n_i^C - \mu(r_i;\vec{p})}{\sqrt{2\mu(r_i;\vec{p})}}\right)\right] \\ &\times \prod_{i=1}^{N_{\text{cand}}} e^{-\mu(r_i;\vec{p})} \frac{\mu(r_i;\vec{p})^{n_i^{\text{corr}}}}{n_i^{\text{corr}}!} \\ &\times \prod_{i=1}^{N_{\text{sil}}} e^{-\mu(r_i;\vec{p})} \left(1 + \mu(r_i;\vec{p}) + \frac{1}{2}\mu(r_i;\vec{p})^2\right)\end{aligned} \tag{5.34}$$

that needs to be maximized ($-\log(\mathcal{L}(\vec{p}))$ minimized) in order to determine the most likely values of the MLDF parameters $\vec{p}$.

5.6.2 *Former MLDF parametrization*

The parameters r^* and α of the MLDF parametrization Eq. (5.23) are usually set to fixed values that are derived from simulations. There are multiple reasons for fixing the γ parameter as well [99]. At low energies, the number of triggered detectors does not suffice to fit γ. Furthermore, it only provides a correction for large distances to the shower core and is almost constant for different primary energies, zenith angles, and types of cosmic ray primaries [99, 100]. In the former Offline standard MD reconstruction, these parameters are fixed to

$$r^* = 150\,\text{m}, \quad \alpha = 1 \quad \text{and} \quad \gamma = 1.85. \tag{5.35}$$

Alternative values of

$$r^* = 320\,\text{m}, \quad \alpha = 0.75 \quad \text{and} \quad \gamma = 3 \tag{5.36}$$

were employed in recent CORSIKA simulation studies [95, 99]. They are based on modeling ideal detectors of the same size and energy detection threshold as the AMIGA detectors; however no full detector simulation with Offline was performed.

The parameter β depends on the shower zenith angle and is closely related to the slope of the MLDF. It is usually left as a free parameter unless there is not enough information for a reliable fit. This is the case if

- there are less than three candidate modules in the event
- or if there are no modules within the radial range from 250 m to 750 m.

Furthermore, β is fixed if none of the following conditions is met

- more than one module within the valid range with a mutual maximal distance larger than 250 m
- more than two modules within the valid range with a mutual maximal distance larger than 165 m
- more than three modules within the valid range with a mutual maximal distance larger than 125 m.

In the former standard MD reconstruction in $\overline{\text{Off}}\underline{\text{line}}$, β is then fixed to

$$\beta(\theta) = b_0 + b_1 \sec(\theta) \tag{5.37}$$

with $b_0 = 2.8$ and $b_1 = -1$. We have tested this parametrization with the library of fixed energy of EAS simulations, with a subsequent simulation and reconstruction of the AMIGA detector response, that has been described in Sections 5.1.2 and 5.1.4.

First, we fit the parameters $A_{\mu,i}$ and β_i for each event that allows for a free fit of β_i within the set of showers with energies $E \in \{10^{17.5}\,\text{eV}, 10^{18}\,\text{eV}, 10^{18.5}\,\text{eV}\}$, zenith angles $\theta \in \{0^\circ, 12^\circ, 22^\circ, 32^\circ, 38^\circ, 48^\circ, 56^\circ\}$, proton and iron primaries, and hadronic interaction models QGSJETII-04 and EPOS-LHC. For each of the four primary and hadronic interaction model combinations we then perform a LS minimization of

$$\begin{aligned} \chi^2 &= \text{LS}(b_0, b_1, b_2) \\ &= \sum_{i=1}^{N} \frac{(\beta_i - \beta(\theta_i, E_i; b_0, b_1, b_2))^2}{\sigma(\beta_i)^2} \end{aligned} \tag{5.38}$$

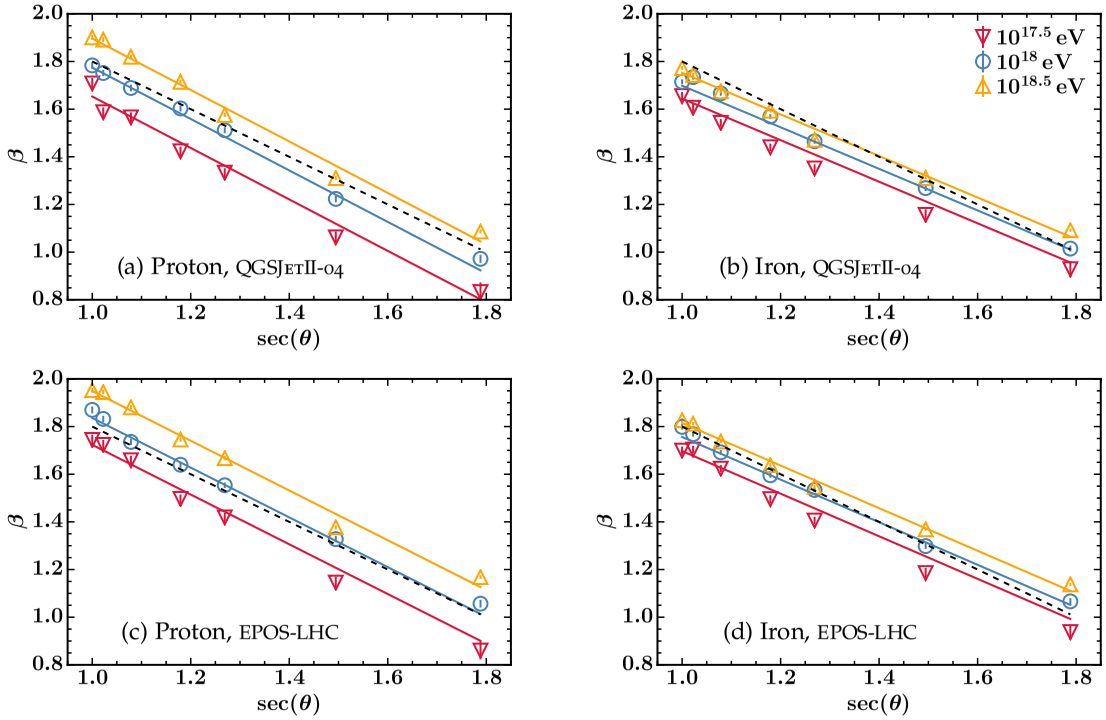

Figure 5.17: Weighted average of β (markers) for different energies as a function of $\sec\theta$ for the former standard MLDF parametrization Eq. (5.35) of r^*, α, and γ for different primaries and hadronic interaction models. The parametrizations of $\beta(\theta)$ that have been obtained by LS fits are shown by solid lines, the former standard parametrization from Offline is shown for comparison by a dashed black line.

Primary	Model	χ^2_{red}	Fit Parameters		
			b_0	b_1	b_2
p	QGSJETII-04	1.71	2.86±0.01	−1.08±0.01	0.24±0.01
	EPOS-LHC	1.73	2.88±0.01	−1.04±0.01	0.22±0.01
Fe	QGSJETII-04	1.73	2.58±0.01	−0.87±0.01	0.10±0.01
	EPOS-LHC	1.78	2.65±0.01	−0.89±0.01	0.11±0.01

Table 5.2: Best fit values with 1σ uncertainties for the parameters b_0, b_1, and b_2 describing the dependency of β on θ and E according to Eq. (5.39) that have been obtained with LS fits for each of the four primary - hadronic interaction model combinations.

summing over all events of the three fixed energies and seven fixed zenith angles. The dependency of β on the zenith angle θ and energy E is parametrized by

$$\beta(\theta, E; b_0, b_1, b_2) = b_0 + b_1 \sec\theta + b_2 \left(\log_{10}(E/\text{eV}) - 18\right) \tag{5.39}$$

where an additional energy-dependent term has been added to the former standard parametrization Eq. (5.37).

The best fit values for b_0, b_1, and b_2 and the corresponding reduced $\chi^2_{\text{red}} = \chi^2/n_{\text{dof}}$ values are given in Table 5.2. The dependency of β on $\sec\theta$ and the primary energy E is visualized for both proton and iron primaries and the hadronic interaction models EPOS-LHC and QGSJETII-04 in Fig. 5.17. The weighted averages

$$\overline{\beta} = \frac{\sum_{i=1}^{n} \beta_i/\sigma_i^2}{\sum_{i=1}^{n} 1/\sigma_i^2} \tag{5.40}$$

of β are displayed with markers for different primary energies, error bars corresponding to the standard deviation

$$\sigma[\overline{\beta}] = \frac{1}{n \sum_{i=1}^{n} 1/\sigma_i^2} \sum_{i=1}^{n} \left(\frac{\beta_i - \overline{\beta}}{\sigma_i} \right)^2 \tag{5.41}$$

are hardly visible due to their small values. Solid lines indicate the parametrizations that have been obtained by the LS fits.

For comparison, the former standard parametrization from Offline is shown by a dashed black line. Except for iron showers simulated with the QGSJETII-04 model, it matches well with the parametrizations that have been obtained for the mean energy of 10^{18} eV. However, we observe an additional energy splitting that is largest for proton showers which is not covered by the former standard MLDF parametrization of Eq. (5.37).

We test the accuracy of the former standard MLDF parametrization by calculating the mean relative difference

$$\frac{\rho - \rho_{\mathrm{Rec}}}{\rho} \tag{5.42}$$

between the reconstructed muon density ρ_{Rec} for each module and the density $\rho(r)$ at the respective distance $r \equiv r_{\mathrm{mod}}$ to the shower core that is obtained by single event fits of the MLDF. We distinguish the cases where β is left as a free fit parameter and where β is fixed according to the parametrization Eq. (5.37).

The mean relative density difference in bins of radial distance for MLDF fits with fixed β is shown in Figs. 5.18 to 5.20 for primary energies of $10^{17.5}$ eV, 10^{18} eV, and $10^{18.5}$ eV and different zenith angles, primaries, and hadronic interaction models. Error bars correspond to the standard error of the mean. The discrepancy between the parametrization Eq. (5.37) of β without an energy-dependent term and the one accounting for an energy splitting Eq. (5.39) is largest for proton showers with energy $10^{17.5}$ eV shown in Fig. 5.17 left. Although the energy splitting is reduced, the two parametrizations differ as well for iron showers

(more for the QGSJETII-04 than for the EPOS-LHC hadronic interaction model). The shortfall of the β parametrization for a primary energy of $10^{17.5}$ eV is reflected in the difference between the reconstructed muon densities and the parametrized MLDF with fixed β shown in Fig. 5.18. At radial distances up to approximately 350 m, the MLDF overshoots the reconstructed muon numbers. For larger radial distances, an undershooting up to the order of 20% occurs that decreases again with increasing distance to the shower core.

Even though less pronounced than for $10^{17.5}$ eV, the deficiency of the MLDF parametrization is equally visible for primary energies of 10^{18} eV (where the energy splitting matters the least) and $10^{18.5}$ eV in Figs. 5.19 and 5.20. Especially for proton showers, there is an obvious mismatch between the true shape and the parametrized functional form of the MLDF for both considered hadronic interaction models. This mismatch persists when β is left as a free fit parameter as shown in Fig. 5.21 for a primary energy of 10^{18} eV. This implies that the shape of the former standard MLDF that is defined by the parameters r^*, α, and γ (Eq. (5.35)) does not well describe the observed muon densities.

In addition, we have tested the alternative MLDF parametrization of Eq. (5.36). However, it yields very similar results as the examined former standard parametrization (see Fig. 5.22) and falls short in providing a consistent description of the shape of the lateral muon densities measured by AMIGA for both proton and iron primaries.

5.6.3 *Global fit of MLDF parameters*

We attempt to arrive at a better description of the lateral muon densities by performing a global fit of the parameters r^*, α, γ, and β that define the shape of the MLDF. By the term global we mean

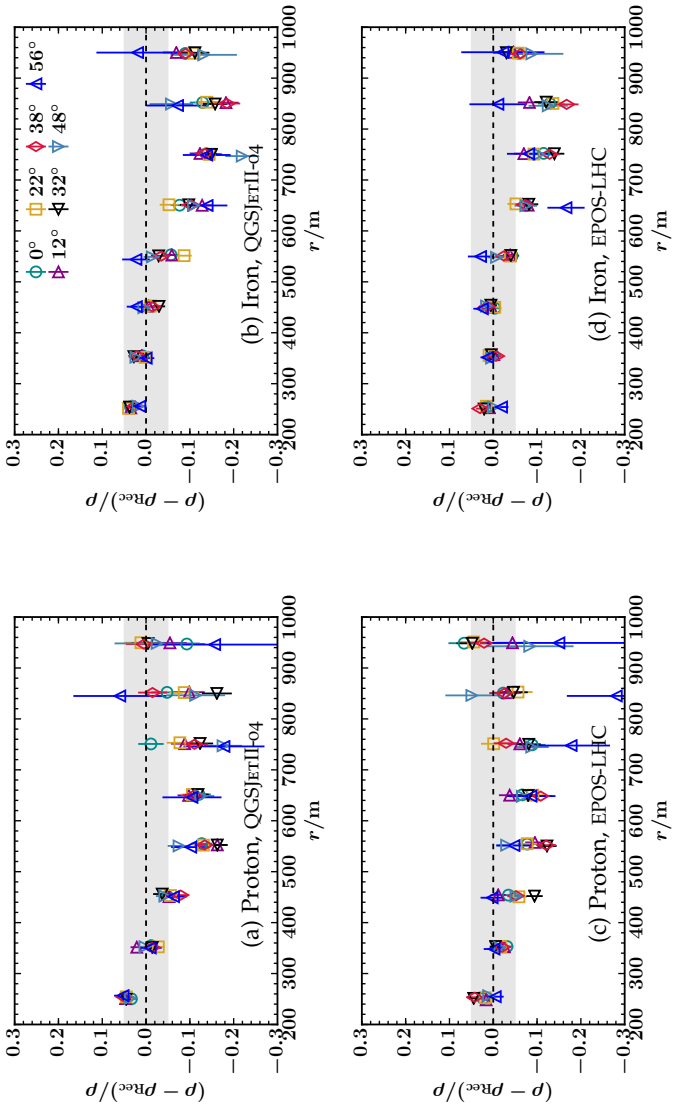

Figure 5.18: Mean relative difference of the densities ρ_{Rec} reconstructed on module level to the density $\rho(r)$ at the corresponding radial distance $r \equiv r_{\mathrm{mod}}$ that is obtained by MLDF fits of single events with fixed $\beta = \beta(\theta)$ according to the former standard MLDF parametrization Eq. (5.37) for a primary energy of $10^{17.5}$ eV.

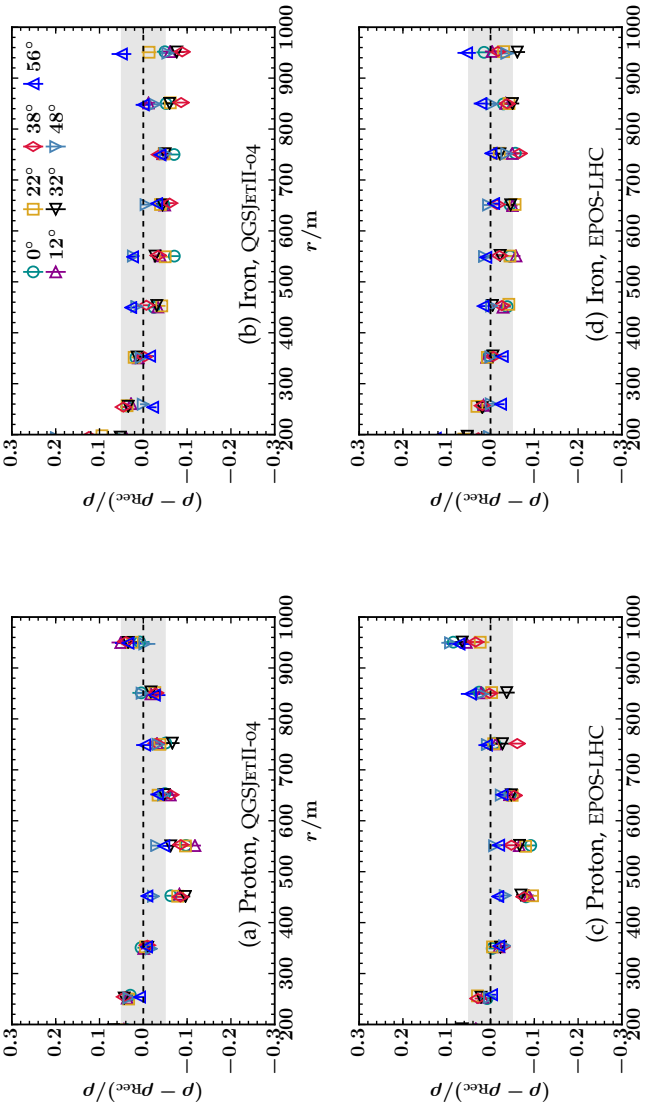

Figure 5.19: The same as in Fig. 5.18 (fixed β) for a primary energy of 10^{18} eV.

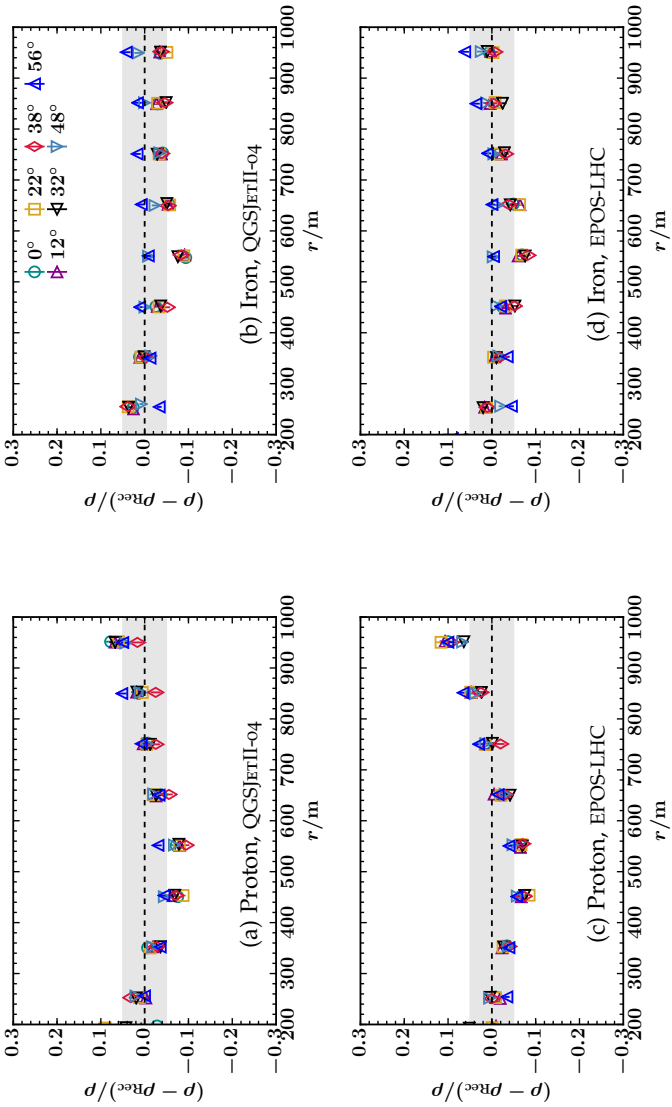

Figure 5.20: The same as in Fig. 5.18 (fixed β) for a primary energy of $10^{18.5}$ eV.

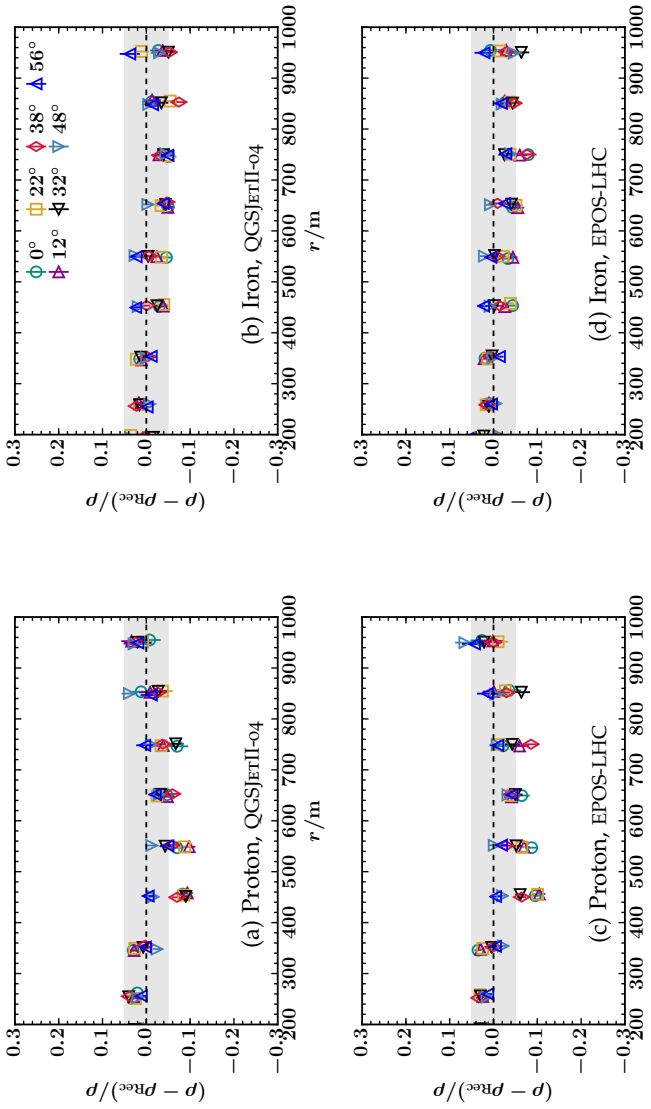

Figure 5.21: The same as in Fig. 5.18 for MLDF fits of single events with free β for a primary energy of 10^{18} eV.

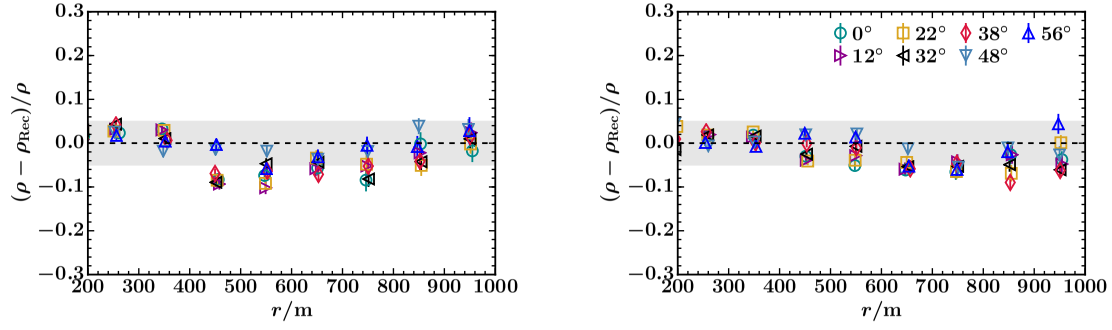

(a) Proton, QGSJETII-04

(b) Iron, QGSJETII-04

(c) Proton, EPOS-LHC

(d) Iron, EPOS-LHC

Figure 5.22: Mean relative difference of the reconstructed muon density ρ_{Rec} on module level to the density $\rho(r)$ at the corresponding radial distance $r \equiv r_{\mathrm{mod}}$ that is obtained by single event MLDF fits with free β using an alternative MLDF parametrization employed by [95, 100] for a primary energy of 10^{18} eV.

		Fit Parameters		
Primary	**Model**	r^*	α	γ
p	QGSJETII-04	283±11	0.21±0.04	5.20±0.29
	EPOS-LHC	278±11	0.20±0.04	4.83±0.26
Fe	QGSJETII-04	278±7	0.44±0.02	4.68±0.18
	EPOS-LHC	276±8	0.25±0.03	4.27±0.17
		b_0	b_1	b_2
p	QGSJETII-04	4.76±0.06	−1.27±0.02	0.10±0.01
	EPOS-LHC	4.80±0.06	−1.23±0.02	0.11±0.01
Fe	QGSJETII-04	3.95±0.04	−0.96±0.01	0.00±0.01
	EPOS-LHC	4.45±0.04	−1.03±0.01	0.00±0.01

Table 5.3: Best fit values of the MLDF parameters with 1σ uncertainties for global fits to simulations with primary energies of $10^{17.5}$ eV, 10^{18} eV, and $10^{18.5}$ eV and zenith angles of $0°, 12°, 22°, 32°, 38°, 48°, 56°$. Four fits were carried out for the combinations of the primaries proton and iron and the hadronic interaction models EPOS-LHC and QGSJETII-04.

that we do not fit the parameters for each event individually, but minimize a joined log-likelihood

$$\mathcal{L}_{\text{glob}} = \prod_{i=1}^{N_E} \prod_{j=1}^{N_\theta} \mathcal{L}\left(E_i, \theta_j, \vec{p}\right) \tag{5.43}$$

for each of the four combinations of primaries and hadronic interaction models. A single likelihood $\mathcal{L}\left(E_i, \theta_j, \vec{p}\right)$ is defined by Eq. (5.34) with $\mu(r; \vec{p})$ replaced by $\mu(r, E_i, \theta_j; \vec{p})$ (see below). The products run over $N_E = 3$ different primary energies $E_i \in \{10^{17.5}\,\text{eV}, 10^{18}\,\text{eV}, 10^{18.5}\,\text{eV}\}$, and $N_\theta = 7$ zenith angles $\theta_j \in \{0°, 12°, 22°, 32°, 38°, 48°, 56°\}$ each.

We assume constant, not zenith or energy-dependent, values of r^*, α, and γ as in the previous MLDF parametrization. The slope β is parametrized by Eq. (5.39) as a function of the zenith angle and the primary energy with fit parameters b_0, b_1, and b_2. In addition to these six parameters, we need $N_E \times N_\theta = 21$ different parameters $A_{\mu_{i,j}}$ to account for the different MLDF normalizations for different zenith angles and primary energies. We describe the lateral muon density for showers with primary energy E_i and zenith angle θ_j hence by

$$\rho_\mu\left(r, E_i, \theta_j; \vec{p}\right) = A_{\mu_{i,j}} \cdot \frac{f_\mu\left(r, E_i, \theta_j; \vec{p}\right)}{f_\mu\left(r_{\text{opt}}, E_i, \theta_j; \vec{p}\right)} \qquad \text{with} \tag{5.44}$$

$$f_\mu\left(r, E_i, \theta_j; \vec{p}\right) = \left(\frac{r}{r^*}\right)^{-\alpha} \left(1 + \frac{r}{r^*}\right)^{-\beta\left(E_i, \theta_j; \vec{b}\right)} \left(1 + \left(\frac{r}{10\, r^*}\right)^2\right)^{-\gamma}$$

where $\beta(E_i, \theta_j; \vec{b})$ with $\vec{b} = (b_0, b_1, b_2)$ is parametrized according to Eq. (5.39). The expected number of muons $\mu(r, E_i, \theta_j; \vec{p})$ is related to the muon density by $\mu(r, E_i, \theta_j; \vec{p}) = \rho_\mu(r, E_i, \theta_j; \vec{p}) A_{\text{eff}}$ (see Eq. (5.25)).

The minimization of the negative log-likelihood $-\log(\mathcal{L}_{\text{glob}})$ yields best fit values which are given in Table 5.3 together with their 1σ uncertainties. Here, we are only interested in the parameters $\vec{p} = (r^*, \alpha, \gamma, b_0, b_1, b_2)$ that describe the shape of the MLDF. The best fit values of the radial distance parameter r^* range from 275 m (iron, EPOS-LHC) to 284 m (proton, EPOS-LHC) and hence lie between the values of $r^* = 150$ m of the former standard MLDF parametrization of Eq. (5.35) and $r^* = 320$ m of the alternative parametrization of Eq. (5.36). In contrast, α is much smaller than in both previous parametrizations. It varies between 0.20 (proton, QGSJETII-04) and 0.44 (iron, QGSJETII-04) in comparison to $\alpha = 1$ and $\alpha = 0.75$ in the former standard and alternative MLDF parametrizations. The γ parameter is in turn significantly larger than in the two preceding MLDF parametrizations with values between 4.25 (iron, EPOS-LHC) and 5.13 (proton, QGSJETII-04) compared to $\gamma = 1.85$ and $\gamma = 3$, respectively. Equally, the b_0

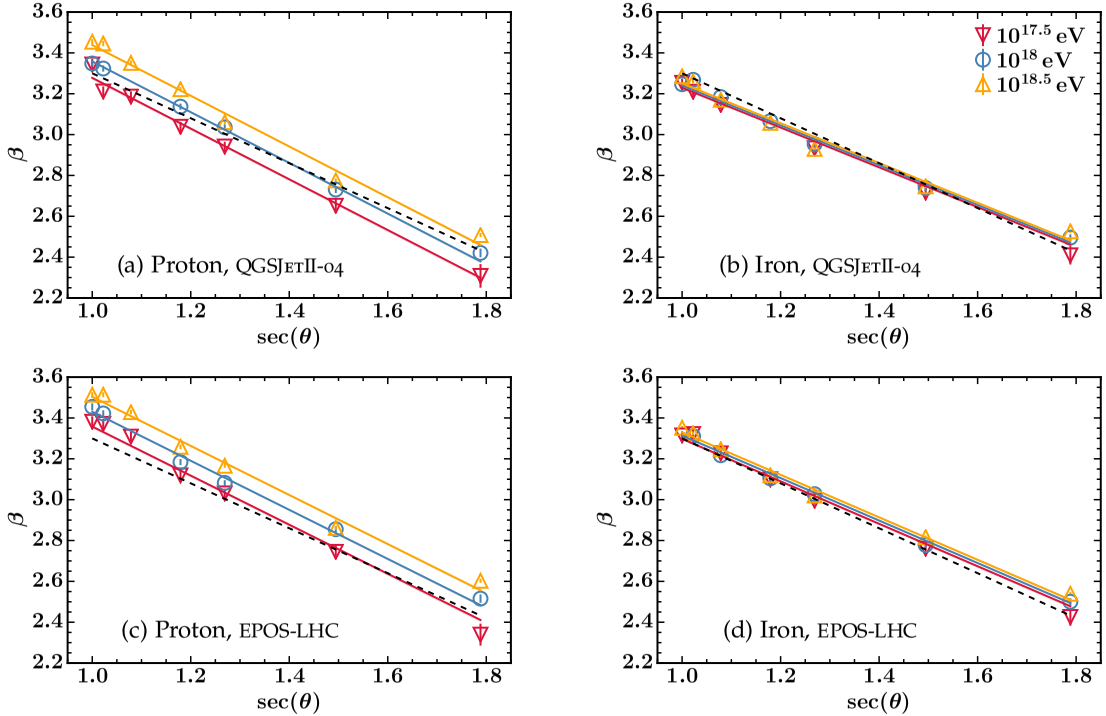

Figure 5.23: Weighted average of β (markers) for different energies as a function of $\sec\theta$ for the new MLDF parametrization Eq. (5.45) of r^*, α, and γ. The parametrizations of $\beta(\theta)$ that have been obtained by LS fits for a given primary - hadronic interaction model combination are shown by solid lines. The averaged solution $\beta(\sec\theta)$ is displayed by a dashed black line.

parameter lies with values between 3.94 and 4.82 well above the value of $b_0 = 2.8$ of the former standard MLDF parametrization. The dependency of β on $\sec\theta$ is quite similar with values of b_1 between -0.95 and -1.27 in comparison to $b_1 = -1$. Proton showers show a small energy dependence of β with $b_2 \approx 0.1$, while the energy dependence is negligible for iron showers. The corresponding parametrizations of β as a function of the zenith angle and primary energy are shown in Fig. 5.23 for the four combinations of primaries and hadronic interaction models.

The correlation matrices of the fit parameters are given in Fig. 5.24. The parameters r, α, and γ are highly correlated for all primaries and hadronic interaction models. On the contrary, the correlations of the β related parameters b_0 and b_2 to the remaining parameters differ for proton and iron primaries. For proton showers, b_0 and α are practically uncorrelated while they are negatively correlated for iron showers. In all cases, b_0 is positively correlated to γ and $r*$, and b_1 is negatively correlated to all other parameters with strongest correlations to $r*$ and γ. For iron showers, where no energy dependence is observed, b_2 is almost uncorrelated to all parameters. In contrast, there is a weak positive correlation of b_2 to r, α, and γ, a slightly negative correlation to b_1 and no correlation to b_0 for proton showers.

We propose a new parametrization of the MLDF based on the weighted averages of the best fit parameters for the four combinations of primaries and hadronic interaction models. We obtain

$$\begin{aligned} r^* &= 278 \pm 1.1\,\mathrm{m}, \quad \alpha = 0.3 \pm 0.05, \quad \gamma = 4.6 \pm 0.16 \quad \text{and} \\ b_0 &= 4.4 \pm 0.17, \quad b_1 = -1.05 \pm 0.06, \quad b_2 = 0.04 \pm 0.03 \end{aligned} \tag{5.45}$$

for the parameters defining the dependency of β on the zenith angle and primary energy. Following the convention of the previous parametrizations, we round these numbers to

$$\begin{aligned} r^* &= 280\,\mathrm{m}, \qquad \alpha = 0.3, \qquad \gamma = 4.6 \quad \text{and} \\ b_0 &= 4.4, \qquad b_1 = -1.1, \qquad b_2 = 0.0\,. \end{aligned} \tag{5.46}$$

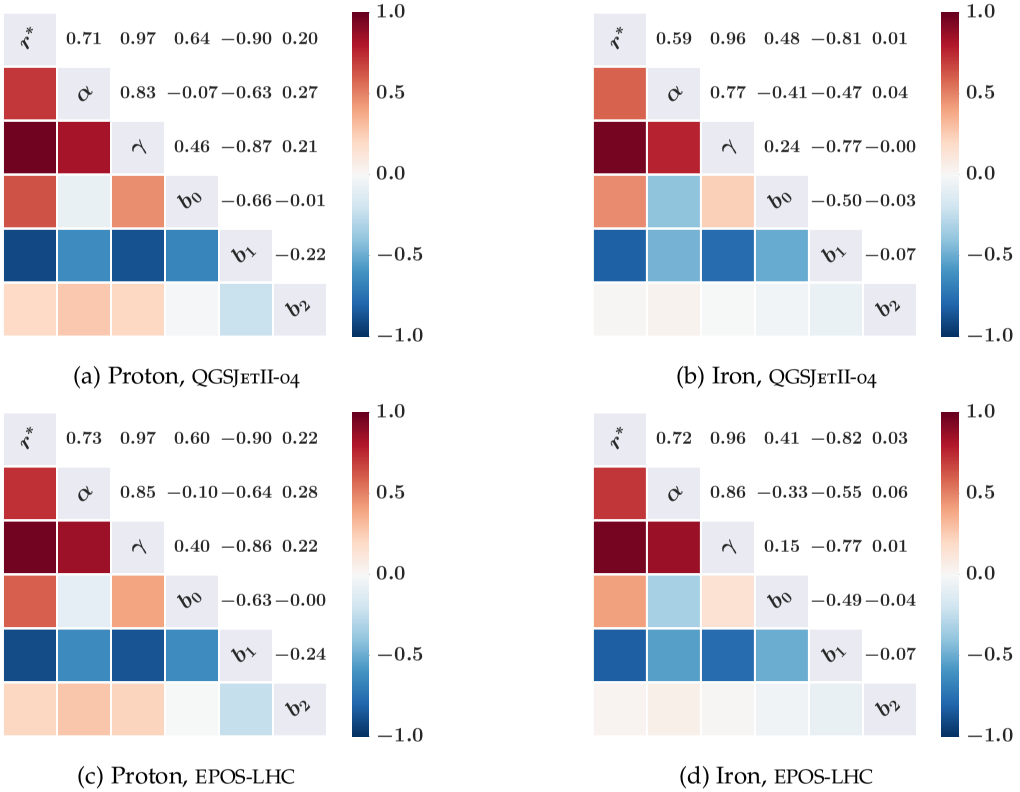

(a) Proton, QGSJETII-04

(b) Iron, QGSJETII-04

(c) Proton, EPOS-LHC

(d) Iron, EPOS-LHC

Figure 5.24: Correlation matrices for the parameters of the global MLDF fit given in Table 5.3.

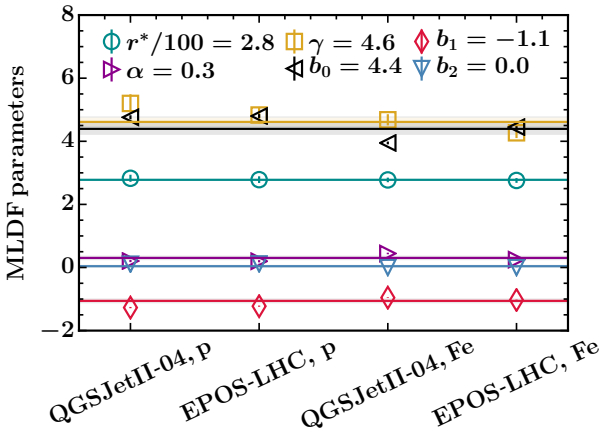

Figure 5.25: Visualization of the global MLDF parameters stated in Table 5.3. Solid lines correspond to the weighted parameter averages.

The slight energy dependence of the slope parameter β through b_2 is removed in this parametrization. The best fit values of the different primary and hadronic interaction combinations as well as the weighted averages of the parameters are visualized in Fig. 5.25.

The new MLDF parametrization describes the data better than the previous standard one as can be seen in Figs. 5.28 and 5.29. At a primary energy of 10^{18} eV, the mean relative muon density bias lies within $\pm 5\%$ over the whole radial range (except partly for the largest zenith angle of 56°). In particular, at intermediate distances between 400 and 600 m, the undershooting of the muon density by the MLDF for proton showers is strongly reduced for both fits with free and fixed β parameter.

For a primary energy of $10^{18.5}$ eV, shown in Fig. 5.26 for fixed $\beta = \beta(\theta)$, the shape of the new MLDF agrees as well significantly better than the old parametrization (Fig. 5.20) even though it still over-shoots the reconstructed muon densities for proton showers

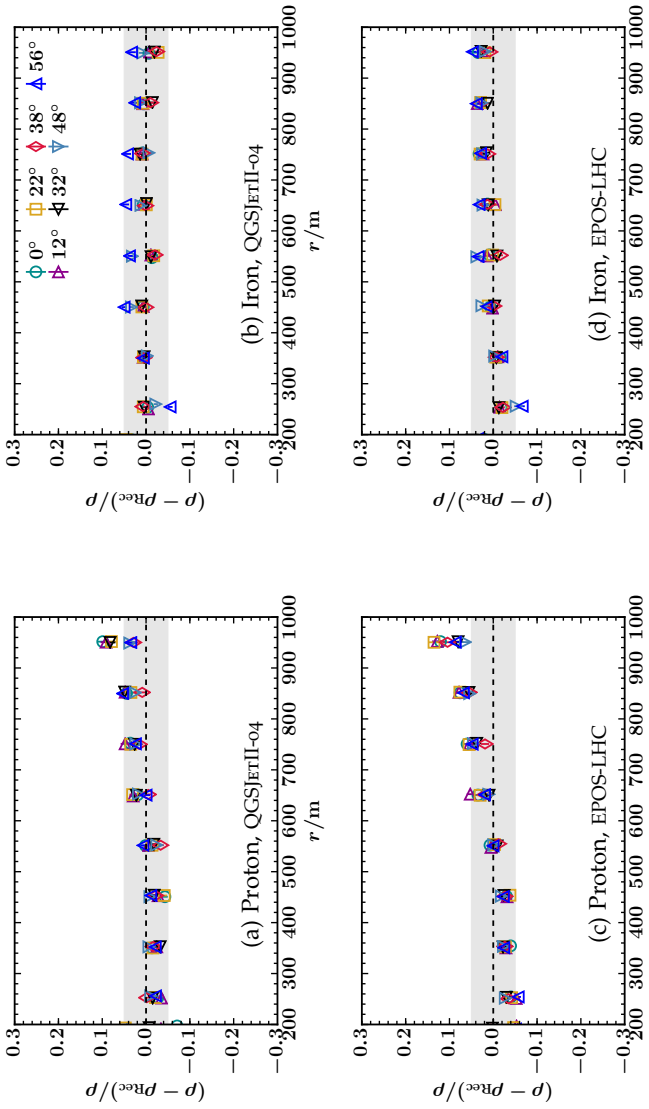

Figure 5.26: The same as in Fig. 5.28 (new MLDF parametrization) for single event fits with fixed $\beta = \beta(\theta)$ parametrized by Eq. (5.39) and a primary energy of $10^{18.5}$ eV.

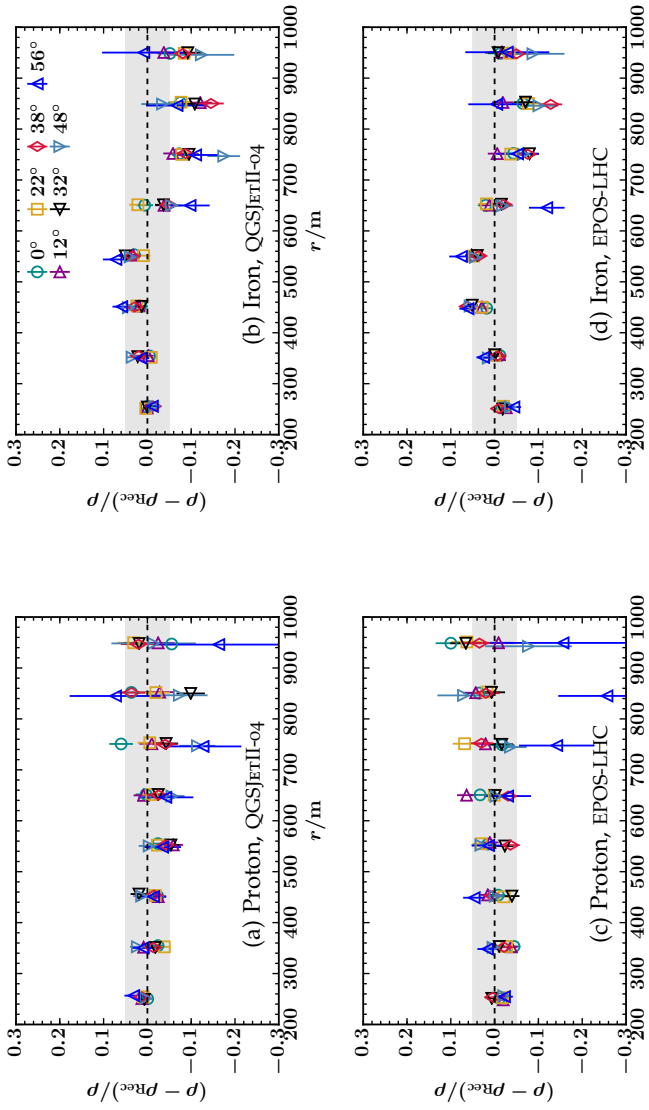

Figure 5.27: The same as in Fig. 5.28 (new MLDF parametrization) for single event fits with fixed $\beta = \beta(\theta)$ parametrized by Eq. (5.39) and a primary energy of $10^{17.5}$ eV.

at core distances above 600 m. Aside from the highest zenith angle of 56°, the MLDF description of iron showers with fixed β is essentially unbiased over the whole radial range in contrast to the previous parametrization displayed in Fig. 5.20 right. The improvement is equally noticeable for a primary energy of $10^{17.5}$ eV. While there is a strong under-shooting for proton showers with fixed β at core distances above 350 m when the former standard MLDF parametrization is employed, the bias is significantly reduced in the new parametrization shown in Fig. 5.27.

The relative biases of the MLDF parametrizations at the optimal core distance of $r = 450$ m (see Section 5.7) are displayed in Fig. 5.30 for both primaries and hadronic interaction models as well as all considered primary energies and shower zenith angles. The overall negative bias for both primaries (plots in left columns) up to -10% that is apparent for the previous MLDF parametrization is shifted upwards such that the bias is mostly contained within $\pm 6\%$.

5.7 OPTIMAL DISTANCE

The optimal distance r_{opt}, where the MLDF of Eq. (5.23) is evaluated, corresponds to the distance from the shower core where the systematic uncertainty of the expected signal is minimized. It mainly depends on the geometry of the detector array and only marginally on the energy, shower zenith angle or a specific choice of the LDF [97].

For AMIGA, an optimal distance of $r_{\text{opt}} = 450$ m has been found based on the MLDF parametrization of Eq. (5.36) [99]. As a consequence of the change of the MLDF parametrization according to Eq. (5.46), we need to redo the analysis and check if $r_{\text{opt}} = 450$ m still holds.

The optimal distance can be found for an individual event by fitting multiple MLDFs for different values of the slope parameter β. The range of the chosen β values should correspond to the uncertainty in β. The spread $\Delta\rho_\mu(r)$ in the signal at a core dis-

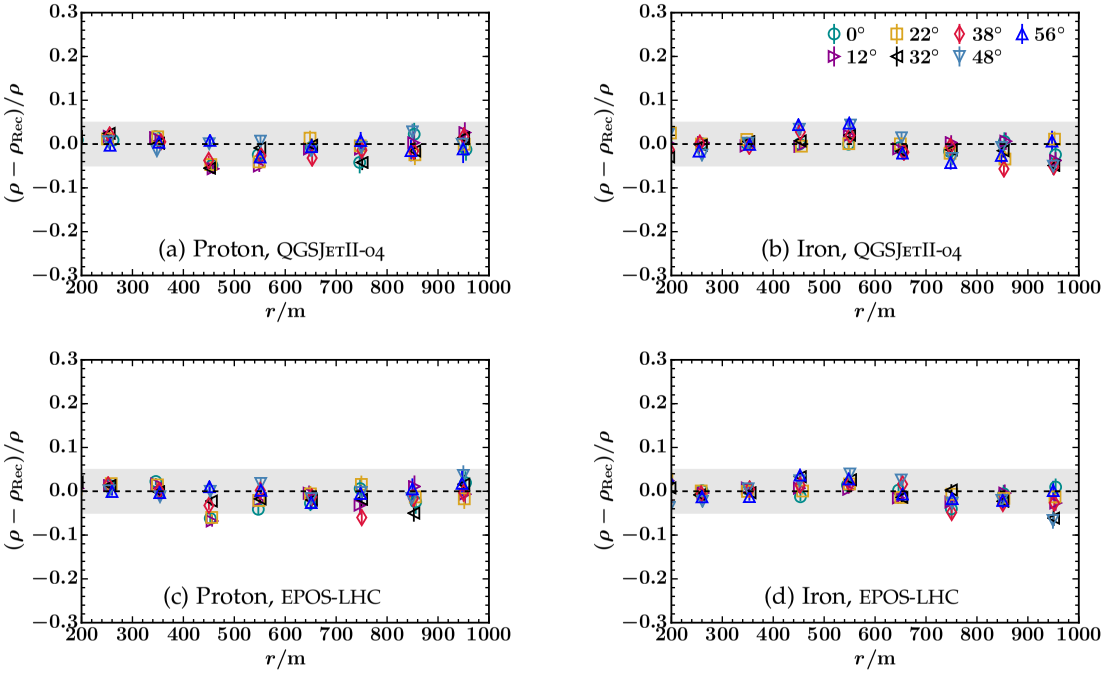

Figure 5.28: Mean relative difference of the reconstructed muon density ρ_{Rec} on module level to the density $\rho(r)$ at the corresponding radial distance $r \equiv r_{\mathrm{mod}}$ that is obtained by single event MLDF fits with free β using the new MLDF parametrization with $r^* = 280\,\mathrm{m}$, $\alpha = 0.3$, and $\gamma = 4.6$ for a primary energy of 10^{18} eV.

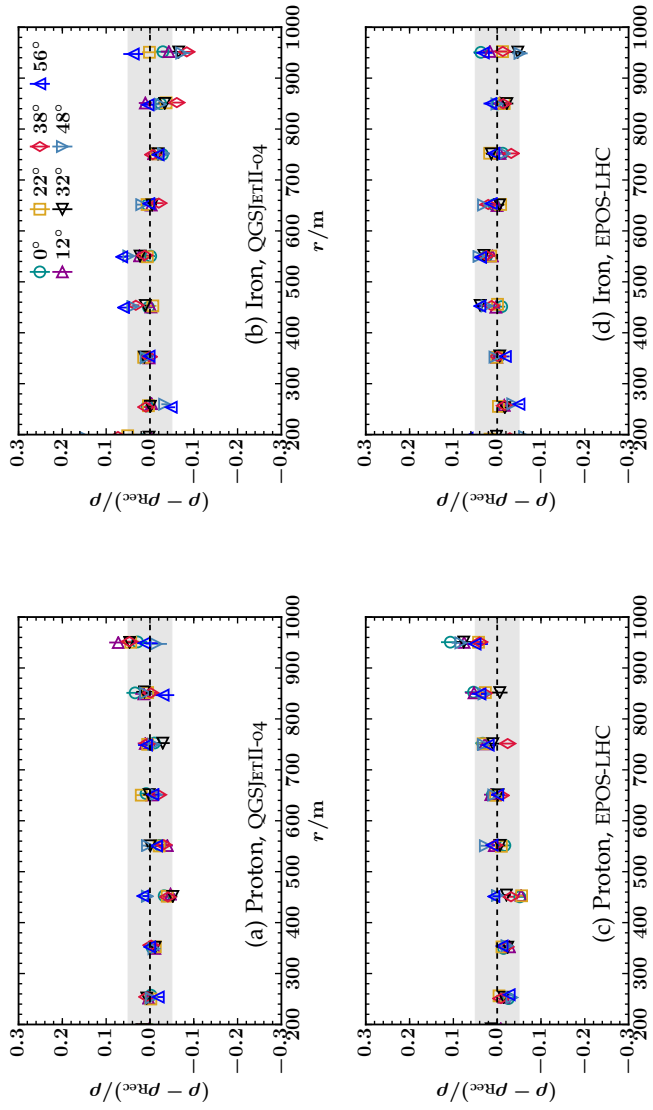

Figure 5.29: The same as in Fig. 5.28 (new MLDF parametrization, primary energy of 10^{18} eV) for single event fits with fixed $\beta = \beta(\theta)$ parametrized by Eq. (5.39).

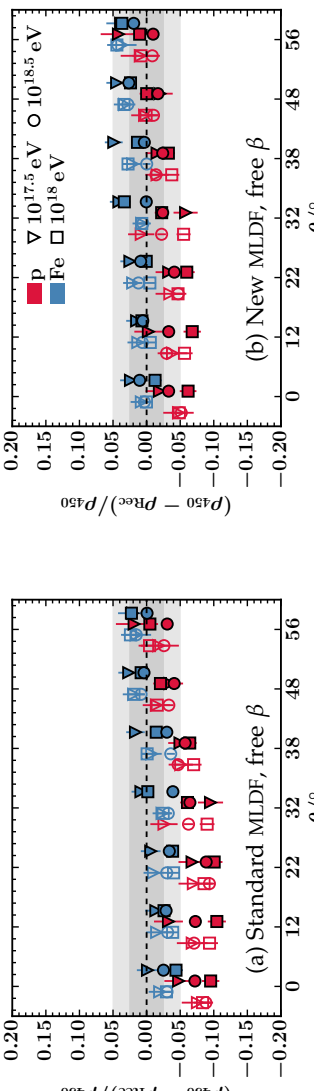

Figure 5.30: Relative bias of the MLDF with respect to the reconstructed muon densities at module level at a core distance of 450 m as a function of the shower zenith angle θ for the former standard (a, c) and the new MLDF parametrization (b, d). Primaries are distinguished by color (proton: red, iron: blue), energies by marker shape, and hadronic interaction models by the marker face color (QGSJetII-04: None, EPOS-LHC: color of primary).

tance r then corresponds to the systematic uncertainty in $\rho_\mu(r)$ due to the lack of knowledge of the true shape of the MLDF. Consequently, the optimal distance can be determined by minimizing the spread $\Delta\rho_\mu(r)$ [97].

In a first step, we analyze the mean relative systematic uncertainty in β by calculating the standard deviation

$$\langle \sigma_\beta^{\text{sys,rel}} \rangle = \sqrt{\frac{1}{N}\sum_{i=1}^{N}\left(\frac{\beta_i - \beta(\theta_i)}{\beta(\theta_i)}\right)^2} \tag{5.47}$$

of the relative difference of freely fitted parameters β_i (for events with sufficient detector information) to the parametrized slope $\beta(\theta_i)$ according to Eq. (5.39). Fig. 5.31a shows that $\langle \sigma_\beta^{\text{sys,rel}} \rangle$ depends mainly on the energy and type of the primary particle. The spread is largest for small energies and proton showers where the muon densities are smallest. In addition, the larger spread in X_{max} for proton showers leads to an increased variation of the MLDF slope β on an event-by-event level. The deviation of individual slopes β_i from the parametrization $\beta(\theta_i)$ is hence largely influenced by both physical shower-to-shower fluctuations and statistical uncertainties in the muon densities measured at single detector stations.

This conclusion is confirmed by a comparison with the relative statistical uncertainty $\langle \sigma_{\beta_i}^{\text{stat,rel}} \rangle$ of β. We calculate the statistical uncertainty individually for each event by drawing 50 balanced bootstraps [101, 102] of its MD data and performing an MLDF fit for each bootstrap sample. The standard deviation

$$\sigma_{\beta_i}^{\text{stat}} = \sqrt{\frac{1}{N}\sum_{k=1}^{N_b}\left(\beta_{i_k} - \beta_i\right)^2} \tag{5.48}$$

where $N_b = 50$ is the number of bootstraps, corresponds to the statistical error $\sigma_{\beta_i}^{\text{stat}}$ of the ith event. The mean relative statisti-

cal uncertainty, averaged over all N events with equal primary, energy, and zenith angle is hence given by

$$\langle \sigma_\beta^{\text{stat,rel}} \rangle = \frac{1}{N} \sum_{i=1}^{N} \frac{\sigma_{\beta_i}^{\text{stat}}}{\beta_i} \tag{5.49}$$

and is shown in Fig. 5.31b as a function of θ; error bars display the corresponding standard deviation.

The statistical uncertainties are very similar to the systematic uncertainties of β, which confirms that the systematic uncertainties are largely dominated by statistical effects. At a typical energy for AMIGA of 10^{18} eV, the relative systematic uncertainties are $\leq$ 13% for both primaries. We choose a 15% variation of β as a conservative estimate to calculate the resulting systematic uncertainty of $\rho_\mu(r)$ as a function of r. To this end, we fix the slopes of each event to $\beta(\theta_i) \pm 0.15 \cdot \beta(\theta_i)$ and perform MLDF fits to determine the muon density parameter A_μ of Eq. (5.23). The averaged muon density difference

$$\Delta\rho_{\mu,i}(r) = \sqrt{\big(\rho_\mu(r; 1.15\beta_i) - \rho_\mu(r;\beta_i)\big)^2 + \big(\rho_\mu(r; 0.85\beta_i) - \rho_\mu(r;\beta_i)\big)^2} \tag{5.50}$$

(with $\beta_i \equiv \beta(\theta_i)$) yields a conservative estimate of the systematic uncertainty in ρ_μ for a single event. The mean relative systematic uncertainty

$$\langle \sigma_{\rho_\mu}^{\text{sys,rel}}(r) \rangle = \frac{1}{N} \sum_{i=1}^{N} \frac{\Delta\rho_{\mu,i}(r)}{\rho_{\mu,i}} \tag{5.51}$$

is obtained by averaging over the normalized systematic muon density uncertainties of the individual events. Confirming the results of [99] for a different MLDF parametrization, Fig. 5.32 shows for a primary energy of 10^{18} eV that the systematic uncertainty is minimized at a core distance around $r_{\text{opt}} = 450\,\text{m}$.

The normalized mean relative systematic uncertainties $\langle \sigma_{\rho_{450}}^{\text{sys,rel}} \rangle = \langle \sigma_{\rho_\mu}^{\text{sys,rel}}(450\,\text{m}) \rangle$ at the optimal distance are plotted as a function of θ in Fig. 5.33 for all considered energies,

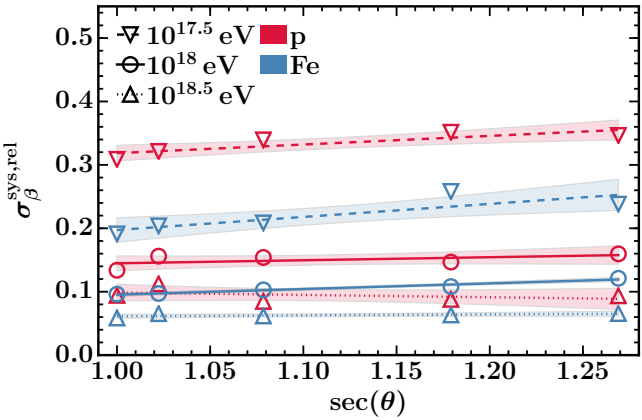

(a) Systematic uncertainty of β

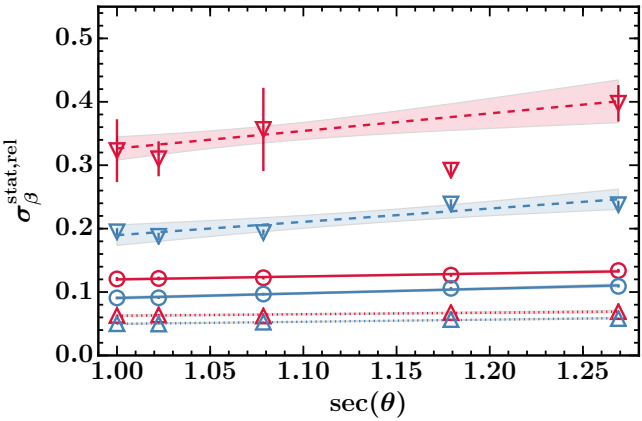

(b) Statistical uncertainty of β

Figure 5.31: Relative systematic (a) and statistical (b) uncertainty of β as a function of $\sec\theta$ for proton (red) and iron (blue) primaries and different primary energies (marker symbols).

primaries, and both high-energy hadronic interaction models QGSJETII-04 and EPOS-LHC. The relative systematic uncertainties vary between 7% ($\theta = 48^\circ$) and 10.4% ($\theta = 0^\circ$) of ρ_{450}.

5.8 COMPOSITION SENSITIVITY

The figure of merit, first introduced in Chapter 4, measures the separation quality of showers that are produced by proton and iron primary particles based on their muonic shower content. In practice, the muon density at the optimal distance r_{opt} is taken as a proxy for the total number of muons of a shower such that the figure of merit reads

$$f = \frac{\langle \rho_{\text{Fe}} \rangle - \langle \rho_{\text{p}} \rangle}{\sqrt{\sigma_{\text{p}}^2 + \sigma_{\text{Fe}}^2}} \tag{5.52}$$

where $\langle \rho_{\text{p/Fe}} \rangle$ are the means and $\sigma_{\text{p/Fe}}$ the standard deviations of the muon density distributions of the two primaries. A good composition sensitivity is obtained if the muon density difference between the primaries is large and the uncertainties of the densities within the set of showers for each primary are small.

In Fig. 5.34, mean muon lateral distribution functions for proton and iron showers with a primary energy of 10^{18} eV and zenith angle of $\theta = 22^\circ$ are shown. They have been obtained by first fitting individual MLDFs with fixed β parameter to the set of available showers. Then, the average (solid lines) and 1σ uncertainties (shaded bands) have been calculated as a function of the radial distance to the shower core. The distributions of the corresponding muon densities ρ_{450} at the optimal distance for proton and iron showers are shown in Fig. 5.35. The separation quality, quantified by the figure of merit (Eq. (5.52)), depends on the separation of the distribution means w.r.t. the widths of the distributions.

While we have found that $r = 450\,\text{m}$ is the optimal distance to reduce the systematic uncertainty of the estimated muon density to a minimum value, it is a priori not clear if it is as well the optimal distance for composition analyses. To answer this question,

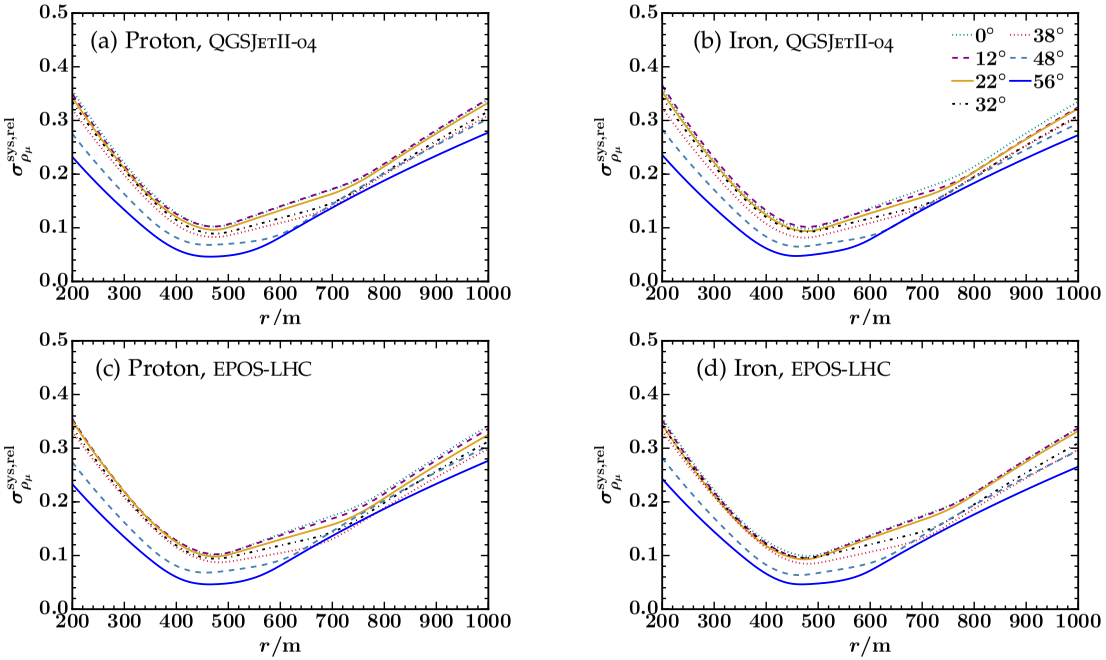

Figure 5.32: Mean systematic uncertainty of ρ_μ as a function of the distance to the shower core r for a primary energy of 10^{18} eV and different shower zenith angles. Results are shown for proton and iron primaries and both considered hadronic interaction models QGSJETII-04 and EPOS-LHC in (a)-(d).

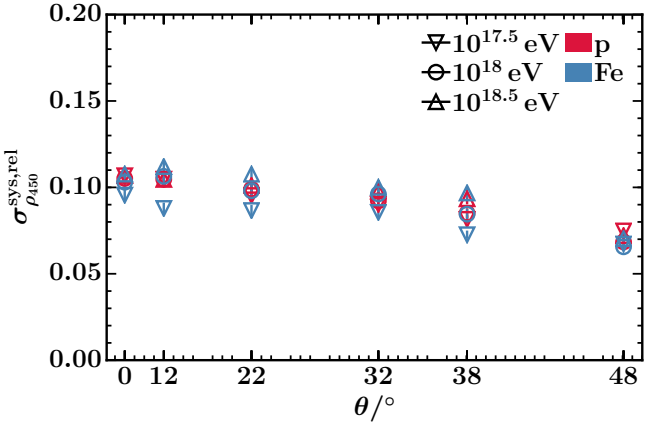

(a) QGSJETII-04

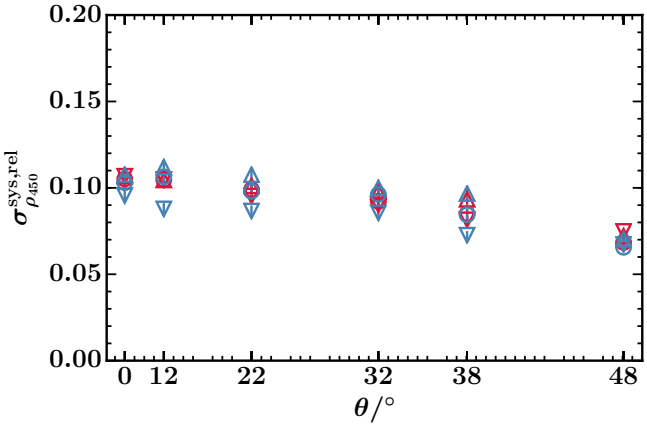

(b) EPOS-LHC

Figure 5.33: Normalized systematic uncertainties $\sigma^{\text{sys,rel}}_{\rho_{450}}$ of the muon density at $r_{\text{opt}} = 450\,\text{m}$ as a function of θ for simulations with the QGSJETII-04 (a) and the EPOS-LHC (b) hadronic high-energy interaction models, proton and iron primaries, and different primary energies. Markers show the mean systematic uncertainty, error bars denote the standard error of the mean.

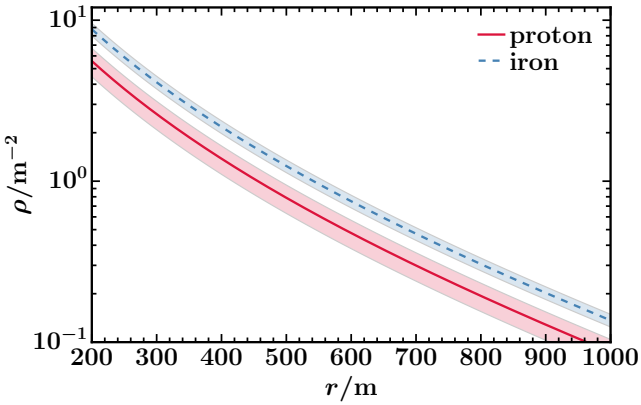

Figure 5.34: Mean muon lateral distributions for MLDF fits with fixed β parameter for proton and iron showers with primary energy of 10^{18} eV and zenith angle $\theta = 22^\circ$ that were simulated with the QGSJETII-04 hadronic interaction model. Shaded bands correspond to the standard deviation of the single event fits.

we analyze the figure of merit as a function of the radial distance to the shower core. We do this both for MLDF fits with free and with fixed β parameter to see the impact of fixing the MLDF slope to a parametrized value. The dependencies of the figure of merit on the core distance are shown in Figs. 5.36 and 5.37 for energies of $10^{17.5}$ eV and 10^{18} eV and different zenith angles.

For MLDF fits with free β parameter and a primary energy of $10^{17.5}$ eV, maximum separability is obtained at distances around 450 m for small zenith angles; however the functional dependence of the figure of merit on the radial distances varies largely between different angles. Higher primary energies lead to a shift of the radial distance with maximum separation power towards larger core distances as can be seen in Figs. 5.37 and 5.38 for energies of 10^{18} eV and $10^{18.5}$ eV. On the contrary, equal separation power for all distances is obtained for fits with fixed β parameter. The corresponding figures of merit are at least as large as the

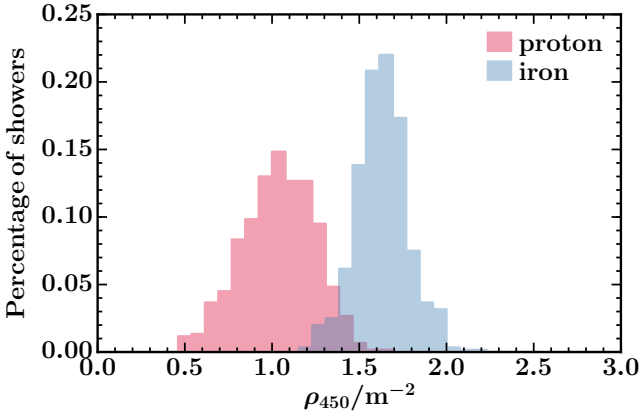

Figure 5.35: Distribution of muon densities ρ_{450} for proton and iron showers from MLDF fits with fixed β parameter at the optimal distance of $r = 450\,\mathrm{m}$ for showers with primary energy $10^{18}\,\mathrm{eV}$ and zenith angle 22° that were simulated with the QGSJETII-04 hadronic interaction model.

maximum figures of merit values for free β fits at the distance with largest separation power.

The dependence of the figure of merit on the radial distance for MLDF fits with free β parameter is a result of the radius dependent differences in the spread of the muon densities. The normalized standard deviations $\sigma(\rho)/\langle\rho\rangle$ of the muon density based on single event MLDF fits with free β parameter are shown as a function of the radial distance to the shower core in Figs. 5.39a and 5.39c for showers simulated with the QGSJETII-04 hadronic interaction model, primary energy of $10^{18}\,\mathrm{eV}$ and all available zenith angles. The uncertainties reach their minimum at distances around 500 to 600 m in agreement with the core distances where maximum separation power is achieved.

The strong increase of the standard deviation $\sigma(\rho)$ for small distances can be explained as a result of the small number of

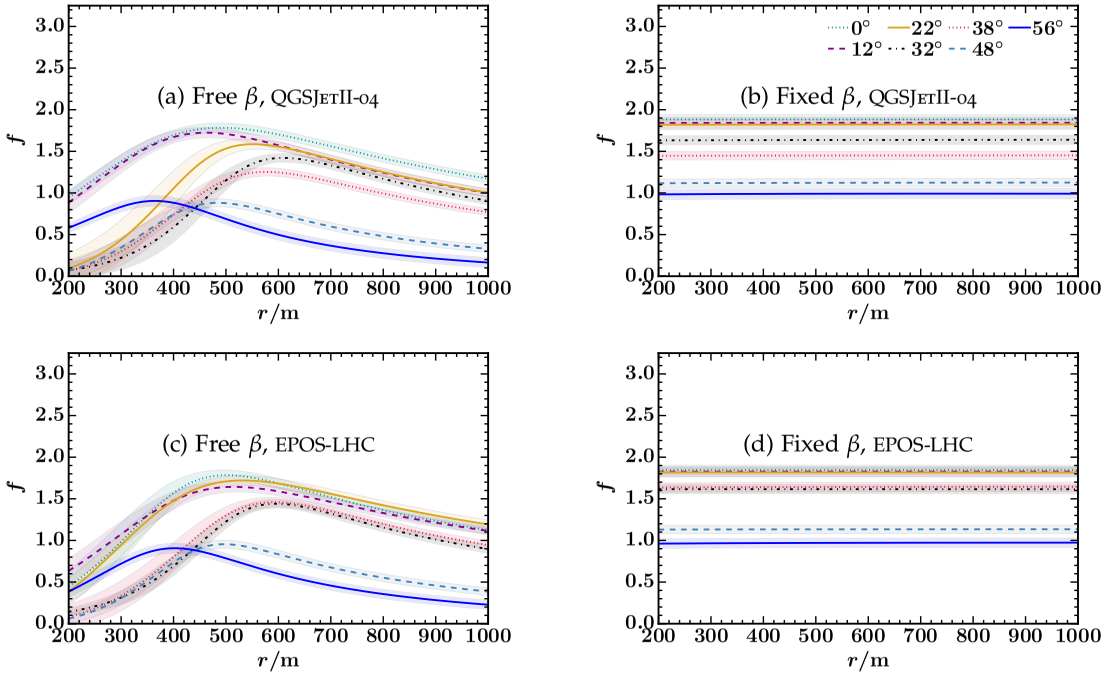

Figure 5.36: Figure of merit for a primary energy of $10^{17.5}$ eV and different zenith angles as a function of the radial distance to the shower core based on the densities that are obtained by single event MLDF fits. Left: the MLDF fits were carried out with β as a free parameter, right: β was fixed to the parametrized values of $\beta(\theta)$.

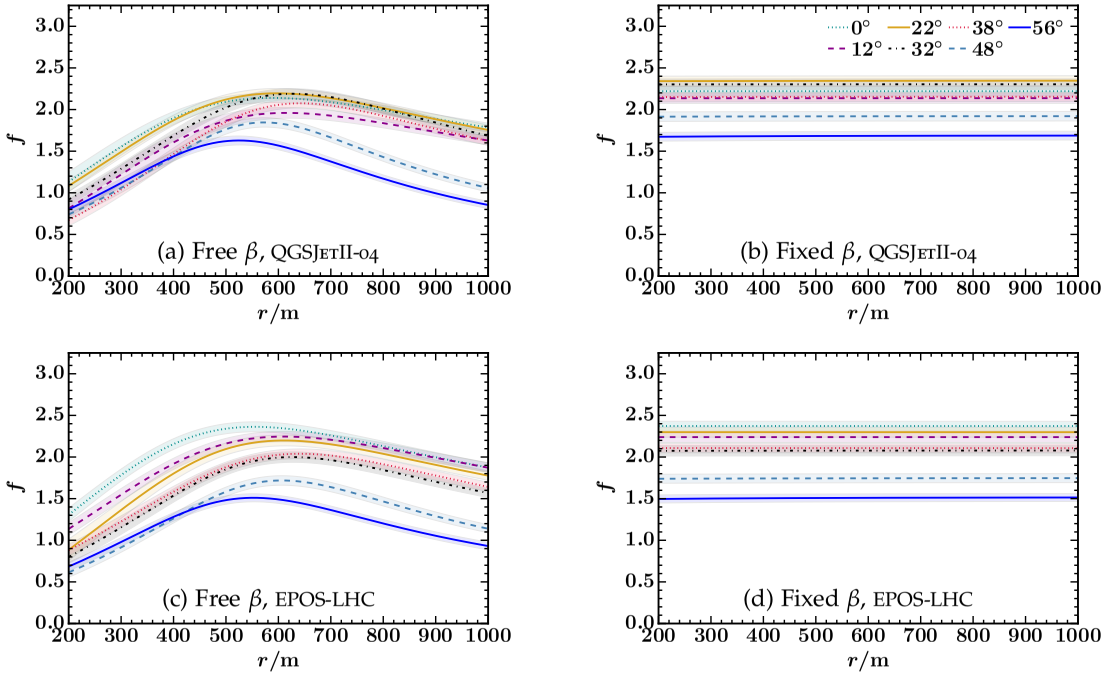

Figure 5.37: The same as in Fig. 5.36 for a primary energy of 10^{18} eV

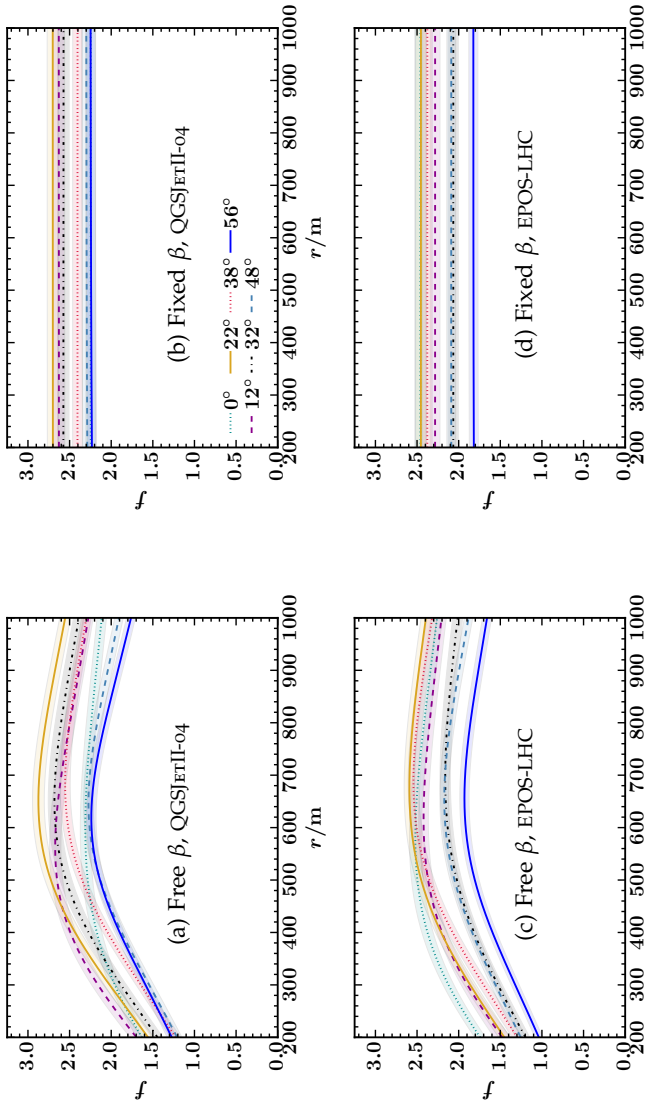

Figure 5.38: The same as in Fig. 5.36 for a primary energy of $10^{18.5}$ eV

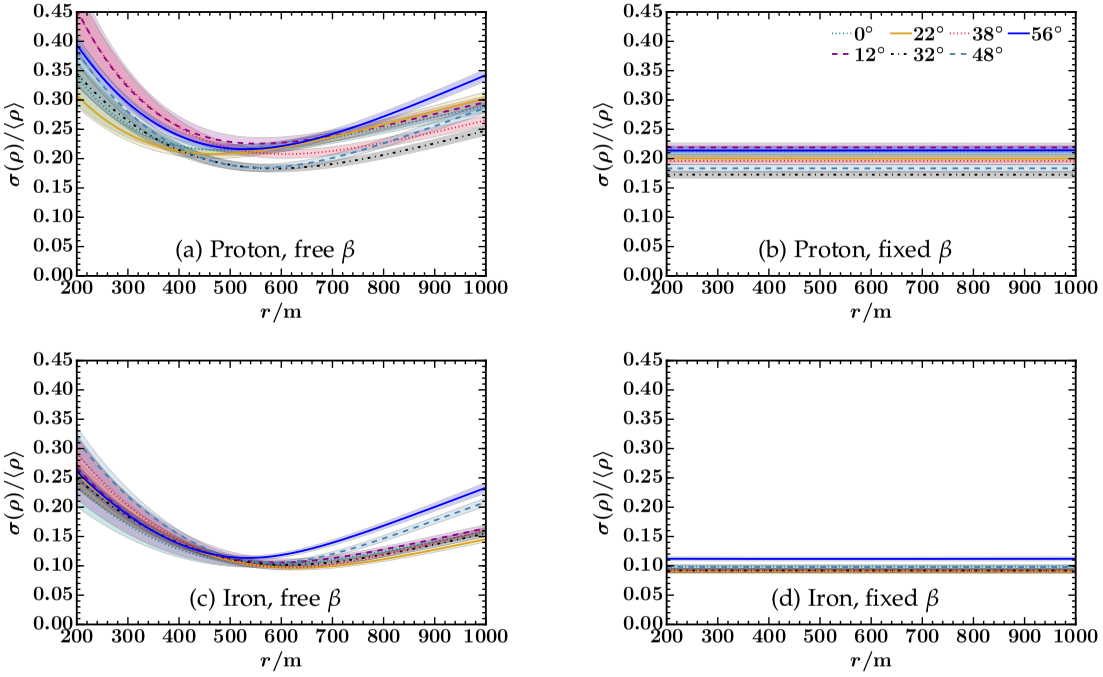

Figure 5.39: Relative uncertainty of the muon density based on single event MLDF fits as a function of the radial distance to the shower core for showers simulated with the QGSJETII-04 hadronic interaction model, primary energy of 10^{18} eV and different zenith angles. Left: the MLDF fits were carried out with β as a free parameter, right: β was fixed to the parametrized values of $\beta(\theta)$.

modules near to the shower core. The number of modules grows linearly as a function of the distance to the shower core for equal radial bin widths δr due to the linear increase

$$\begin{aligned} A(r;\delta r) &= \pi \left((r+\delta r)^2 - r^2 \right) \\ &= \pi \left(2r\delta r + \delta r^2 \right) \end{aligned} \tag{5.53}$$

of the ring areas $A(r;\delta r)$ in the shower plane with r. The sparse number of modules near to the core leads to looser constraints of the MLDF with decreasing core distance and consequently to increased fluctuations between the MLDF fits for different showers. At the same time, the larger muon densities for small core distances constrain the Poissonian likelihood stronger than the small densities at larger core distance. The overall uncertainties are hence a combination of these two effects and reach a minimum at intermediate energy-dependent distances.

In contrast to MLDF fits with free β, the uncertainties of the muon density for fixed β fits (Figs. 5.39b and 5.39d) are independent of the radial distance within showers of a fixed zenith angle θ. This is a consequence of the fixed slope $\beta = \beta(\theta)$, which is the same for all single event fits. Since only the normalization of the MLDF is fitted for each event, the additional uncertainty of the β slope parameter is removed and the uncertainties of the muon density are mainly dominated by shower-to-shower fluctuations. As a consequence, the uncertainties of the fixed β fits are even smaller than the minimum uncertainties of the MLDF fits with free β parameter at the respective optimal distance.

For composition analyses, it seems hence of advantage to parametrize β as a function of the zenith angle θ and then fix it for individual fits of single events. In this way, the shower-to-shower fluctuations of the muon density are drastically reduced and the separability of primaries is increased to more than the maximum value that can be reached for fits with free β. In order to guarantee a minimal bias of the estimated muon densities, the MLDFs should be evaluated at the optimal distance of $r_{\text{opt}} = 450\,\text{m}$.

6

DATA SELECTION AND ESTIMATION OF SYSTEMATIC UNCERTAINTIES

In order to apply the improved reconstruction procedure to AMIGA data, we need to construct a reliable data sample. To this end, we select a time period of one year starting from October 2015 where the 010 strategy was employed to calibrate the muon detectors. Furthermore, as detailed in Section 6.1, SD quality cuts are employed and malfunctioning AMIGA counters are excluded. Beyond that, we have developed a bad period rejection for the MD on an individual module level which is explained in Section 6.2. We describe how we correct for the different efficiencies of small and large AMIGA modules and remove those modules with strongly deviating mean muon measurements in Section 6.3. As a first analysis, we study the lateral trigger probability that is obtained for the chosen data sample and compare results with simulations in Section 6.4. Since the muonic signal that is detected by the AMIGA underground detectors gets attenuated as a function of the shower zenith angle, we parametrize the attenuation for both data and simulations and define a zenith-independent estimator of the muon density in Section 6.5. Furthermore, we estimate the systematic uncertainties arising from the uncertainties in the setting of the discriminator threshold, the density of the soil, the parametrization of the MLDF, and the attenuation correction in Section 6.6.

6.1 DATA SELECTION AND QUALITY CUTS

During the prototype phase of AMIGA, different calibration procedures have been tested. For a first analysis of MD data obtained with the original PMT design, we choose the calibration period

from October 15th, 2015 to October 21st, 2016. During this period, the high voltage of the PMTs was set to 1030 V and the "010" calibration strategy, which has been described in Section 3.4, was employed. A scheme of the AMIGA engineering array, consisting of a hexagon of seven counters, has been shown in Fig. 3.15. Since counter 93 was taken out of acquisition for testing purposes, only six out of seven counters where in operation during the considered time period. Additionally, module 4 (5 m^2) of counter 1570 is not considered in the data analysis due to a memory failure as well as module 2 (5 m^2) of counter 688 which has been equipped with a SIPM instead of a PMT. Beyond that, the two modules of the central counter 1622 that are buried at a shallower depth of 1.3 m are not taken into account. Analyzing the efficiencies of individual modules in Section 6.3, we further find that module 1 (5 m^2) of counter 1764 should be excluded in the analysis due to an observed muon over-counting compared to the other modules. Overall, muon data from six counters consisting of 17 modules with 10 m^2 area and 12 smaller 5 m^2 modules is available for the following analyses.

The SD reconstruction of the events with available MD data has been performed as described in Section 3.1. The same SD quality cuts were applied as for the official data reconstruction for the ICRC 2017. These are the requirements of a space-time coincidence of at least three neighboring triggering stations, the containment of the events into an active hexagon, and the successful reconstruction of the lateral distribution of the events. Furthermore, periods with problems in the communication systems and events in the vicinity of lightnings were excluded and weather corrections have been applied [41].

6.2 BAD PERIOD REJECTION

In addition to the bad period rejection of SD, we have developed a bad period rejection method for the MD on an individual module level to exclude time periods where certain AMIGA modules were

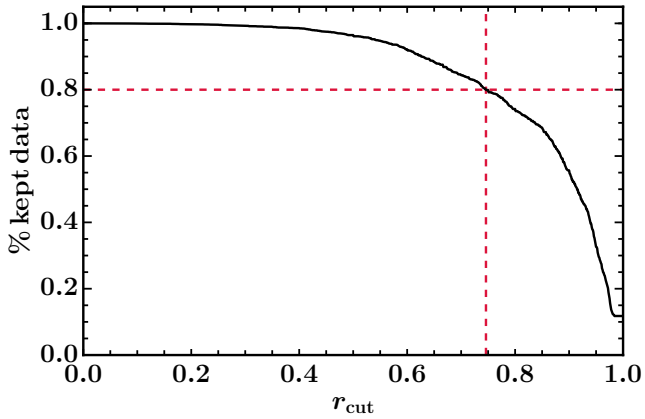

Figure 6.1: Percentage of kept data as a function of the cut in "efficiency" $\varepsilon = {}^{\#\mathrm{MD\,cand}}/_{\#\mathrm{SD\,cand}}$ that is applied on an individual module level.

malfunctioning. Since the MD is not self-triggering, but in "slave" mode of the SD (see Section 3.4), a muon counter (and all its modules) can only be a candidate if the corresponding SD partner station is a candidate. However, in the case of an SD candidate station, the associated AMIGA detector or some of its modules can be subject to a variety of errors. Therefore, we take the daily rate of MD candidates w.r.t. the number of SD candidates as a criterion for the successful operation of individual modules. If the partner SD station is a candidate, the corresponding muon detector and all its modules should be present in the stored event data with assigned statuses (candidate or rejected). However, we regularly observe "missing" counters and modules that are not present in the event; we consider these equally as error cases.

In Figs. 6.2 and 6.3, the daily ratio of MD to SD candidates is plotted for the complete data period for each counter (subplots) with all modules. We observe severe drops of the candidate ratios on certain days; in some cases (eg. counter 1570), an overall trend of a diminishing candidate ratio with time becomes apparent. We

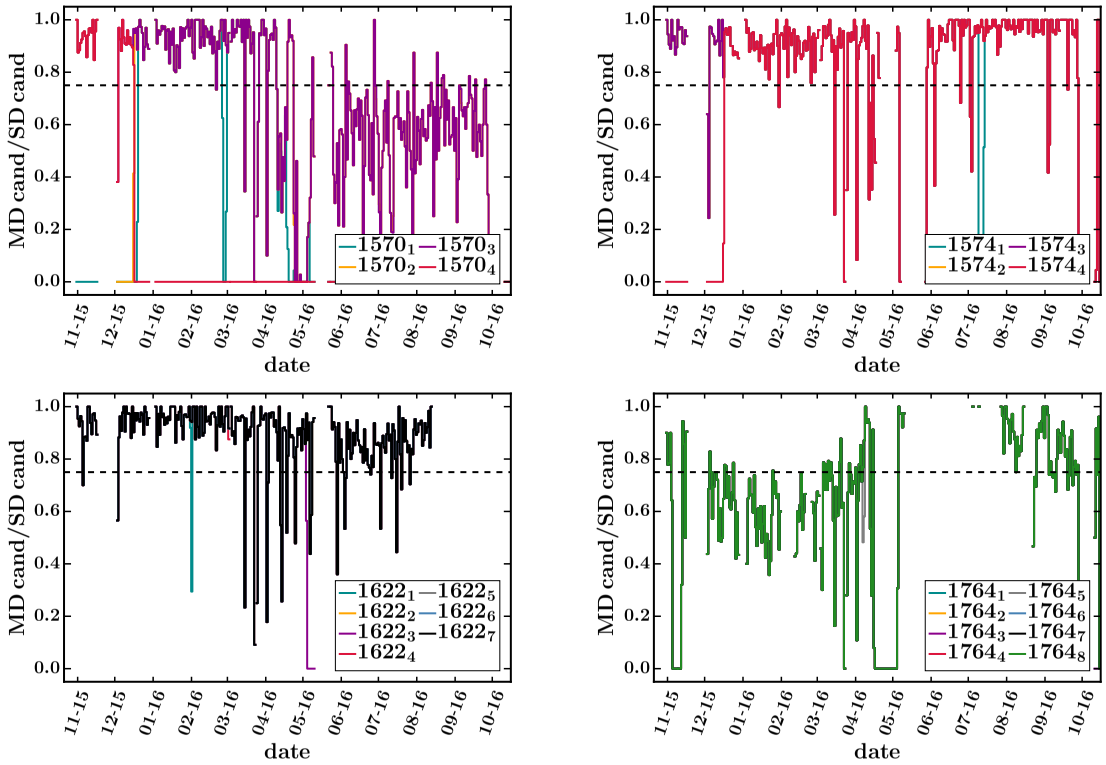

Figure 6.2: Percentage of MD candidate modules w.r.t. the number of SD candidate stations on an individual module basis for the MCs with IDs 1570, 1574, 1622, and 1764 in 1 day intervals. Label numbers indicate the MD counter number, indexes the module number. A rejection level of 75% is visualized by a black dashed line.

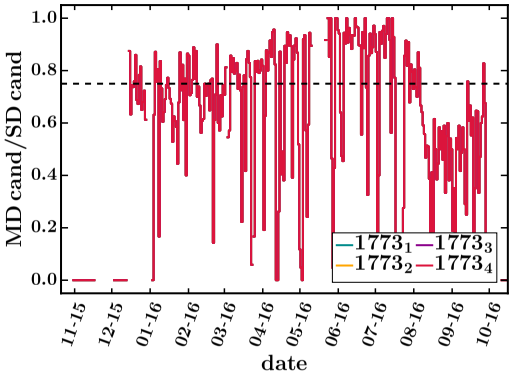

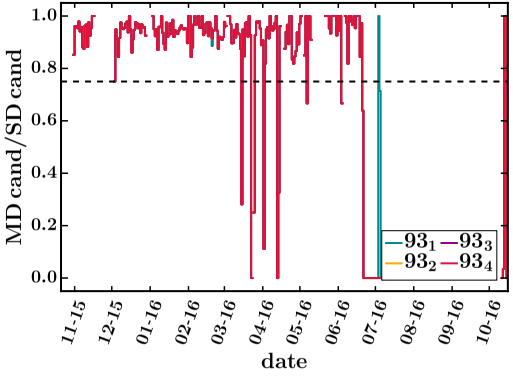

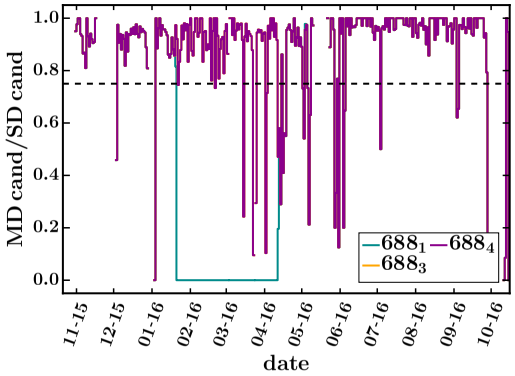

Percentage of MD candidate modules w.r.t. the ID of SD candidate stations on an individual module basis for the MD counters with IDs 1773, 688, and 93 in 1 day intervals. Label numbers indicate the MD counter number, indexes the module number. A rejection level of 75% is visualized by a black dashed line.

Figure 6.3

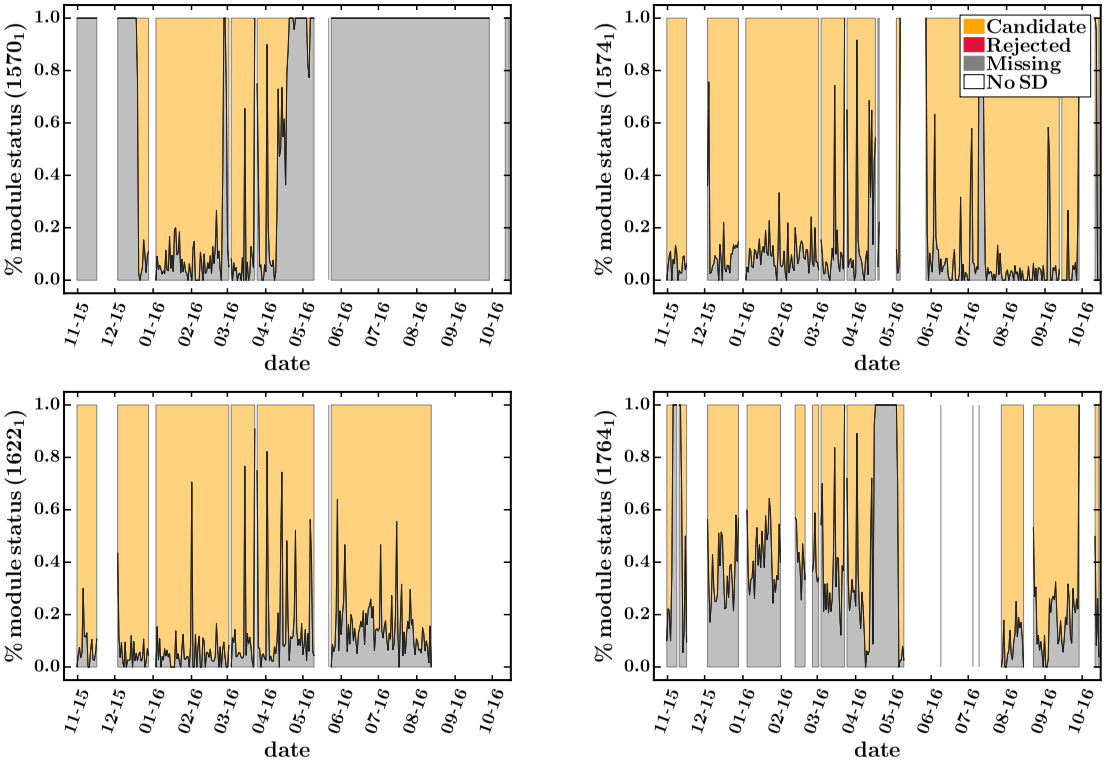

Figure 6.4: Stack plot of module statuses (candidate, rejected, missing) for MD modules with a candidate partner SD station as a function of time in bins of 1 day. Results are displayed for the modules with ID 1 of the MCs with IDs 1570, 1574, 1622, and 1764.

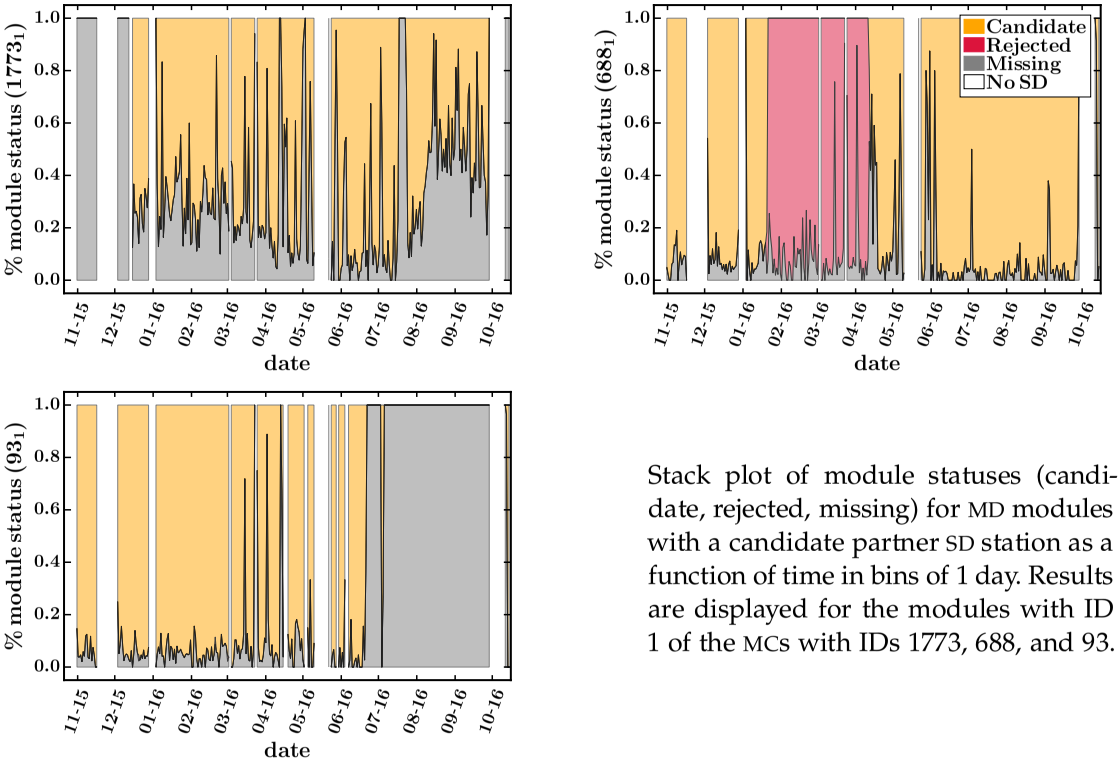

Stack plot of module statuses (candidate, rejected, missing) for MD modules with a candidate partner SD station as a function of time in bins of 1 day. Results are displayed for the modules with ID 1 of the MCs with IDs 1773, 688, and 93.

Figure 6.5

define a minimum MD to SD candidate ratio r_{cut} as a criterion to reject days for individual modules. The value of r_{cut} is obtained by requiring that at least 80% of the total data is kept. The percentage of kept data is plotted as a function of r_{cut} in Fig. 6.1. In order to reject not more than 20% of the total data, days with a candidate ratio above 75% need to be retained. Dashed lines indicate the cut value of $r_{\text{cut}} = 0.75$ in Figs. 6.2 and 6.3; days with an equal or higher candidate ratio are kept, those with lower ratios are rejected.

The rejection reasons are illustrated exemplarily in Figs. 6.4 and 6.5 for the modules with ID 1 of each counter. While modules with a valid *rejected* status make up a much smaller contribution, the main source of rejection are *missing* modules in the event which are most likely caused by failures of the AMIGA data broadcasting system.

6.3 MODULE EFFICIENCY

Laboratory measurements show that the $10\,\text{m}^2$ detector modules are less efficient ($\epsilon^{10\text{m}^2}_{\text{win7}} = 95\%$ for the $1x1$ counting strategy and a window of seven bins) than the $5\,\text{m}^2$ modules ($\epsilon^{5\text{m}^2}_{\text{win7}} = 104\%$) as a consequence of the light attenuation in the longer wavelength-shifting fibers. The efficiency above 100% of the $5\,\text{m}^2$ modules is caused by over-counting of muons as a result of after-pulsing of the PMT. These measurements and the related systematic uncertainty are discussed in Section 6.6.2.

The reduced muon counting efficiency of the larger $10\,\text{m}^2$ modules observed in the laboratory is confirmed with data from the engineering array. For the analysis, we apply cuts in energy ($10^{17.5}\,\text{eV} \leq E \leq 10^{18.5}\,\text{eV}$), zenith angle ($0^\circ \leq \theta \leq 45^\circ$), and radial distance ($200\,\text{m} \leq r \leq 750\,\text{m}$). For a specific counter, we select only events where at least one $10\,\text{m}^2$ and one $5\,\text{m}^2$ module are non-saturated candidates. We calculate the averaged muon

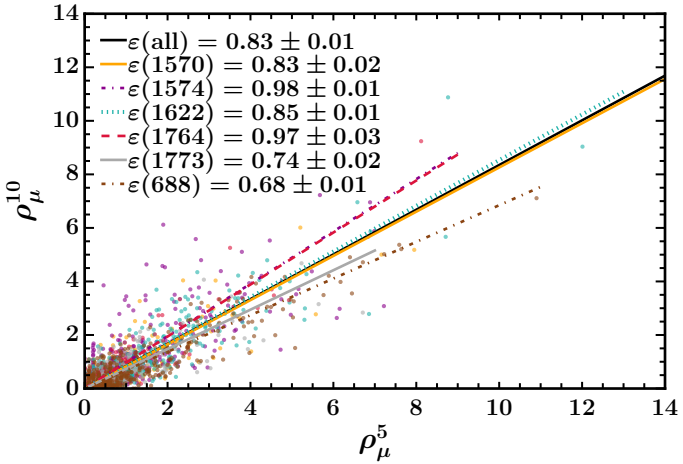

Figure 6.6: Averaged muon densities of $10\,\mathrm{m}^2$ modules as a function of the muon densities of the $5\,\mathrm{m}^2$ modules within individual counters (colors). Regression lines show the overall efficiency (black line) as well as the efficiencies for single counters.

densities ρ_μ^5 and ρ_μ^{10} for each event and fit the average efficiency ε of the $10\,\mathrm{m}^2$ w.r.t. the $5\,\mathrm{m}^2$ modules by minimizing

$$\chi^2 = \sum_{i=1}^{N} \left(\frac{\left(\varepsilon \cdot \rho_\mu^5 - \rho_\mu^{10}\right) A}{\sqrt{\rho_\mu^5 A}} \right)^2 \quad , \quad \rho_\mu^5 > 0 \tag{6.1}$$

with $A = 10\,\mathrm{m}^2$ where we assume Poissonian fluctuations $\sqrt{\rho_\mu^5 A}$ in the measured muon numbers.

The averaged muon densities of the $10\,\mathrm{m}^2$ modules as a function of the muon densities of the $5\,\mathrm{m}^2$ modules within individual counters are shown in Fig. 6.6. The corresponding efficiencies for single counters as well as the overall efficiency of the $10\,\mathrm{m}^2$ modules w.r.t. the $5\,\mathrm{m}^2$ modules are represented by regression lines. Although the laboratory result of a reduced efficiency of

the larger modules is generally confirmed, the efficiencies vary significantly between the counters.

Since the comparison of the muon densities measured by the individual modules of a counter on an event-by-event level only yields information on their relative performance, it is not possible to determine the absolute efficiency of a single module. For the analysis of data recorded by the AMIGA engineering array, we hence correct the estimated muon density for each module by the area-dependent efficiency according to $\rho_\mu^{\text{corr}} = \rho_\mu^{\text{corr}}/\epsilon$ with the efficiencies $\epsilon_{\text{win7}}^{5\text{m}^2}$ and $\epsilon_{\text{win7}}^{10\text{m}^2}$ derived from laboratory measurements.

However, to detect and reject faulty modules, we indirectly assess the performance of single modules by mutually comparing the mean muon densities that are measured by all modules of all counters. The disadvantage of this approach, compared to the event-by-event analysis of individual counters, is that different sets of events with distinct primary energies and core distances for each counter need to be compared to each other. It is hence necessary to normalize the measured muon densities taking into account the primary energy and the distance to the shower core.

We try to overcome the effect of differences in the radial distributions of individual modules by fitting MLDFs with fixed parametrized slope $\beta(\theta)$ to the muon density measured by a single module in an individual event (only one data point per event). We evaluate the MLDFs at the optimal distance $r_{\text{opt}} = 450\,\text{m}$ where the shape of the MLDF has the least impact on the resulting muon density as demonstrated in Section 5.7. We hereby restrict the considered radial range to $200\,\text{m} \leq r \leq 750\,\text{m}$ to limit the effect of Poissonian fluctuations at large core distances. Furthermore, we restrict the zenith angle range to $0^\circ \leq \theta \leq 45^\circ$ to avoid strong attenuation effects.

We account for the impact of the different primary energies by normalizing the muon densities ρ_{450} at the optimal distance by a factor of $\left(E/E_{\text{ref}}\right)^\alpha$ with $\alpha = 0.9$ based on the evolution of the total number of muons with energy in the Heitler-Matthews model [44, 47]. We choose a reference energy of $E_{\text{ref}} = 10^{18}\,\text{eV}$ as

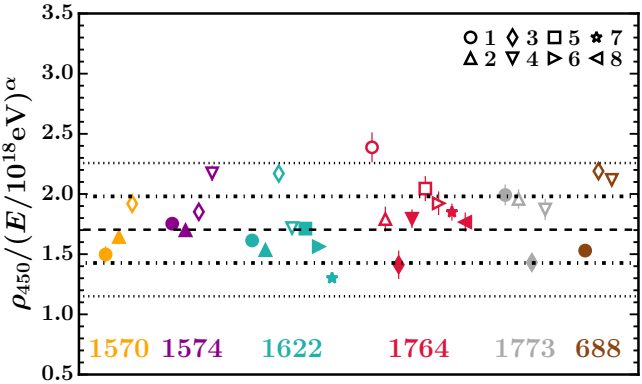

(a) Uncorrected

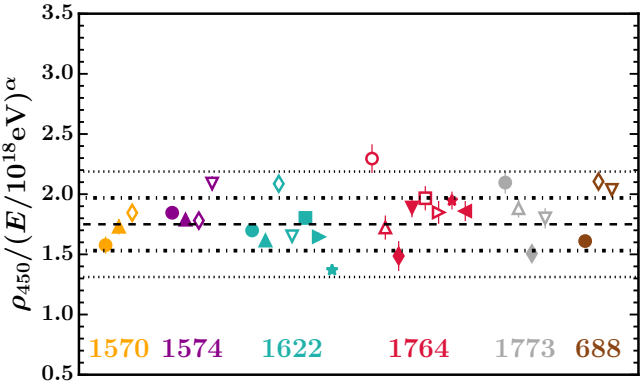

(b) Efficiency corrected

Figure 6.7: Normalized muon densities for individual modules within the energy range $10^{17.5}\,\mathrm{eV} - 10^{18.5}\,\mathrm{eV}$ without efficiency correction (a) and after correcting by global module area-dependent factors $1/\varepsilon$ ($\varepsilon = 1.04$ (0.95) for $5\,\mathrm{m}^2$ ($10\,\mathrm{m}^2$)) (b). Markers denote the median muon densities, error bars the standard error of the median. Colors indicate the specific counter, marker symbols the module number. $10\,\mathrm{m}^2$ ($5\,\mathrm{m}^2$) modules are represented by filled (empty) symbols. The weighted average of all module medians is shown by a dashed line, dashed-dotted lines indicate 1σ, dotted lines 2σ ranges.

Counter	Module	$\tilde{\rho}_{450}$	$(\tilde{\rho}_{450} - \langle\tilde{\rho}_{450}\rangle_w)/\sigma_w(\tilde{\rho}_{450})$	# Entries
1570	1	1.58 ± 0.07	-0.79 ± 0.33	126
	2	1.73 ± 0.06	-0.10 ± 0.29	190
	3	1.85 ± 0.07	0.43 ± 0.33	189
1574	1	1.85 ± 0.04	0.44 ± 0.19	472
	2	1.79 ± 0.04	0.17 ± 0.18	460
	3	1.78 ± 0.05	0.14 ± 0.24	402
	4	2.09 ± 0.06	1.55 ± 0.28	370
1622	1	1.70 ± 0.04	-0.23 ± 0.20	484
	2	1.61 ± 0.04	-0.62 ± 0.16	484
	3	2.09 ± 0.06	1.54 ± 0.28	437
	4	1.65 ± 0.05	-0.45 ± 0.21	429
	5	1.80 ± 0.04	0.24 ± 0.18	485
	6	1.65 ± 0.04	-0.48 ± 0.16	487
	7	1.37 ± 0.03	-1.74 ± 0.14	486
1764	**1**	$\mathbf{2.30 \pm 0.12}$	$\mathbf{2.49 \pm 0.54}$	**125**
	2	1.72 ± 0.10	-0.12 ± 0.46	121
	3	1.49 ± 0.12	-1.20 ± 0.57	56
	4	1.89 ± 0.08	0.64 ± 0.37	144
	5	1.97 ± 0.10	0.99 ± 0.46	122
	6	1.85 ± 0.09	0.45 ± 0.43	128
	7	1.95 ± 0.07	0.90 ± 0.34	141
	8	1.86 ± 0.08	0.50 ± 0.38	140
1773	1	2.10 ± 0.09	1.58 ± 0.42	210
	2	1.88 ± 0.08	0.61 ± 0.35	180
	3	1.51 ± 0.05	-1.11 ± 0.23	209
	4	1.80 ± 0.08	0.23 ± 0.38	190
688	1	1.61 ± 0.04	-0.64 ± 0.19	402
	3	2.11 ± 0.06	1.62 ± 0.26	520
	4	2.04 ± 0.05	1.31 ± 0.24	503

Table 6.1: Mean normalized muon densities $\tilde{\rho}_{450}$ for events with $10^{17.5}\,\text{eV} \leq E < 10^{18.5}\,\text{eV}$; uncertainties denote the standard error of the median. The deviation of the single $\tilde{\rho}_{450}$ values from the overall module mean $\langle\tilde{\rho}_{450}\rangle_w$ in units of $\sigma_w(\tilde{\rho}_{450})$ indicates the agreement of the muon measurements of a module compared to the overall average.

a characteristic energy for AMIGA. The energy normalized muon densities are shown for all modules of each counter in Fig. 6.7 for the energy range of $10^{17.5}$ eV to $10^{18.5}$ eV. In Fig. 6.7a, results are displayed without any efficiency correction, in Fig. 6.7b the muon densities have been corrected by module area-dependent factors $1/\varepsilon$ with $\varepsilon = 1.04$ for $5\,\mathrm{m}^2$ modules and $\varepsilon = 0.95$ for $10\,\mathrm{m}^2$ modules according to the results of the laboratory efficiency measurements. Markers denote the medians $\tilde{\rho}_{450_i}$ of the energy normalized muon densities for each module i, error bars the standard error of the median $\tilde{\sigma}_{450_i} = \mathrm{MAD}(\rho_{450_i}/(E/E_{\mathrm{ref}})^{\alpha})/\sqrt{N_i}$ which is defined as the median absolute deviation divided by the square root of the number of data points. Colors indicate the specific counter, marker symbols the module number. Furthermore, the module area is distinguished by the marker filling: $10\,\mathrm{m}^2$ modules are represented by filled symbols, $5\,\mathrm{m}^2$ by empty symbols. The weighted average

$$\langle \tilde{\rho}_{450} \rangle_w = \frac{\sum_{i=1}^{n} \tilde{\rho}_{450_i}/(\tilde{\sigma}_{450_i})^2}{\sum_{i=1}^{n} 1/(\tilde{\sigma}_{450_i})^2} \tag{6.2}$$

of all module medians $\tilde{\rho}^i_{450}$ is shown by a dashed line. Dashed-dotted lines indicate one weighted standard deviation

$$\sigma_w\left(\tilde{\rho}_{450}\right) = \sqrt{\frac{\sum_{i=1}^{n} \left(\tilde{\rho}_{450_i} - \langle \tilde{\rho}_{450} \rangle_w\right)^2 / \left(\tilde{\sigma}_{450_i}\right)^2}{n \sum_{i=1}^{n} 1/(\tilde{\sigma}_{450_i})^2}}, \tag{6.3}$$

dotted lines two weighted standard deviations.

Fig. 6.7a confirms that in general higher muon densities are measured by the $5\,\mathrm{m}^2$ than by the $10\,\mathrm{m}^2$ modules of a counter. However, this is not always the case, and the efficiency differences vary between individual modules and counters. The spread of the normalized muon densities is slightly reduced by correcting for the different efficiencies of small and large modules based on the laboratory measurements (Fig. 6.7a). The median values $\tilde{\rho}_{450_i}$ and their deviations from the overall weighted mean $\langle \tilde{\rho}_{450} \rangle_w$ in units of the weighted standard deviation $\sigma_w(\tilde{\rho}_{450})$ are stated

in Table 6.1. Due to the large spread between the modules, we only reject clear outliers which deviate more than 2σ from the overall mean. This is exclusively the case for module 1 of counter 1764, the remaining modules are kept in further data analyses.

6.4 LATERAL TRIGGER PROBABILITY

As a first analysis, we determine the muon lateral trigger probability (LTP) for AMIGA data and compare results with simulations. Formally, for self-triggering detector systems, the LTP is defined as the probability that a single detector is triggered by an extensive air shower as a function of the radial distance to the shower core. In addition to the core distance, the LTP depends on the primary energy as well as on the shower zenith angle due to attenuation effects.

Since AMIGA does not self-trigger but relies on the SD triggering system, the definition of an LTP for AMIGA needs to be adjusted. Instead of calculating the trigger probability (which depends only on the associated SD partner stations), we determine the probability of measuring at least one muon with modules with a total area of $10\,\mathrm{m}^2$. In bins of primary energy and radial distance, we define the LTP as the ratio

$$p_{\mathrm{LTP}} = \frac{N_{\mathrm{cand}}\,(\mu \geq 1)}{N_{\mathrm{cand}} + N_{\mathrm{sil}}} \tag{6.4}$$

of the number of candidate modules measuring at least one muon divided by the total sum of the number of candidate and silent modules. Silent modules, i.e. the modules of an AMIGA counter with associated silent SD station, are considered as measuring zero muons. The confidence interval of p_{LTP} is calculated as the binomial proportion confidence interval using the approximate score method of Wilson [103].

For data, all operating counter modules are considered in the analysis. We hereby consider both the large $10\,\mathrm{m}^2$ modules as well as the smaller $5\,\mathrm{m}^2$ modules which we join pairwise to form

joined $10\,\mathrm{m}^2$ modules. Single $5\,\mathrm{m}^2$ modules of a counter without a second candidate/silent $5\,\mathrm{m}^2$ module of the same counter to join are dropped in the analysis. In simulations, only $10\,\mathrm{m}^2$ modules are simulated which are not subject to inefficiencies as observed for real scintillator modules.

We parametrize the LTP as a Fermi function

$$f_{\mathrm{LTP}}(r, E) = \frac{1}{1 + \exp\left(\frac{r/100\,\mathrm{m} - a(E)}{b(E)}\right)} \tag{6.5}$$

with parameters

$$\begin{aligned} a(E) &= a_0 + a_1 \left(\log_{10}(E/\mathrm{eV}) - 17\right) \quad \text{and} \\ b(E) &= b_0 + b_1 \left(\log_{10}(E/\mathrm{eV}) - 17\right), \end{aligned} \tag{6.6}$$

which depends both on the radial core distance r and the primary energy E. To determine the free parameters $\vec{x_0} = (a_0, a_1, b_0, b_1)$, we divide the data (both for simulations and data) into N_E energy bins and N_r radial bins. Then, we maximize the likelihood

$$\mathcal{L} = \prod_{i=1}^{N_r} \prod_{j=1}^{N_E} p_{\mathrm{binom}}\left(k_{ij}, n_{ij}, f_{\mathrm{LTP}}\left(r_i, E_j; x_0\right)\right) \tag{6.7}$$

by numerically minimizing its negative logarithm $-\log \mathcal{L}$. Here, k_{ij} corresponds to the number of candidate modules $N_{\mathrm{cand}}\,(\mu \geq 1)$ measuring at least one muon within the ith radial and jth energy bin and n_{ij} to the total sum $N_{\mathrm{cand}} + N_{\mathrm{sil}}$ of candidate and silent modules within the bin. The probability mass function

$$p_{\mathrm{binom}}\,(k; n, p) = \binom{n}{k} p^k\,(1-p)^{n-k} \tag{6.8}$$

of the binomial distribution describes the probability of getting exactly k "successes", i.e. candidate modules measuring at least one muon, in n trials given the probability p measuring $N_\mu \geq 1$ for a single detector module.

6.4.1 *Simulations*

We employ the continuous CORSIKA simulation library described in Section 5.1.3 to determine the LTP based on simulations within the energy range $10^{17.5}\,\mathrm{eV} \leq E \leq 10^{18.2}\,\mathrm{eV}$. Assuming an isotrop distribution of CRs, we separately consider two angular bins $0^\circ \leq \theta \leq 30^\circ$ and $30^\circ \leq \theta \leq 45^\circ$ which are of equal size in bins of $\cos^2\theta$. The shower energy is binned logarithmically with bin edges $\log(E/\mathrm{eV}) = [17.5, 17.6, 17.8, 18.0, 18.2]$. The distribution of simulated showers is continuous in E and hence very different from the situation in data with a spectrum that is described by a steeply falling power law. To avoid a bias of the mean energy in the chosen energy bins when comparing simulations with data, we hence reweight the simulated showers as described in Section 5.1.5. The LTP defined in Eq. (6.4) is hence modified to

$$p_{\mathrm{LTP},w} = \frac{\sum_{i=1}^{N_{\mathrm{cand}}(\mu\geq 1)} \hat{w}_i}{\sum_{j=1}^{N_{\mathrm{cand}}} \hat{w}_j + \sum_{k=1}^{N_{\mathrm{sil}}} \hat{w}_k} \tag{6.9}$$

where $\hat{w}_i = w(E_i)^N / \sum_{n=1}^{N} w(E_n)$ are the energy-dependent normalized weights of single events.

The resulting measured and fitted LTPs are displayed in Fig. 6.8 for proton and iron primaries and both considered zenith angle ranges. The optimum fit parameters and their uncertainties are stated in Table 6.2. We calculate the parameter uncertainties and correlations by drawing 1000 balanced bootstraps [101, 102] of the considered data set and fitting the parameters $\vec{x_0}$ for each bootstrap sample. From these results, we calculate the covariance and correlation matrices which are visualized in Fig. 6.9. Both the parameters a_0 and a_1 as well as b_0 and b_1 are strongly anti-correlated. All distributions are well described by the parametrization of Eq. (6.5) as a function of the energy E and core distance r. As expected, the LTP increases for higher primary energies and decreases according to the Fermi function with increasing distance. The LTP is generally higher for iron than for

	$0^\circ \leq \theta \leq 30^\circ$		$30^\circ \leq \theta \leq 45^\circ$	
Parameters	Proton	Iron	Proton	Iron
a_0	4.60 ± 0.09	4.98 ± 0.08	3.62 ± 0.08	4.12 ± 0.08
a_1	4.58 ± 0.10	5.48 ± 0.10	5.03 ± 0.10	5.79 ± 0.10
b_0	1.07 ± 0.04	1.07 ± 0.05	0.91 ± 0.04	1.02 ± 0.04
b_1	0.34 ± 0.05	0.40 ± 0.05	0.44 ± 0.05	0.29 ± 0.05

Table 6.2: Parameters and uncertainties of the LTP parametrization Eq. (6.5) for proton and iron simulations with the QGSJETII-04 hadronic high-energy interaction model within the zenith angle ranges $0^\circ \leq \theta \leq 30^\circ$ and $30^\circ \leq \theta \leq 45^\circ$.

proton primaries due to the higher muon content in iron showers. Equally, the LTP is larger for the lower zenith angle bin as a consequence of the increased attenuation for larger shower zenith angles.

6.4.2 *Measured AMIGA data*

In addition to simulations, we parametrize the LTP for AMIGA measurements. We consider the same energy range and divide the showers in equal zenith angle ranges as for simulations. As mentioned previously, we join pairs of $5\,\mathrm{m}^2$ of the same counter to obtain larger modules with effective area of $10\,\mathrm{m}^2$ for the analysis.

The obtained LTP measurements and parametrizations are displayed in Fig. 6.10 for both considered zenith angle ranges as well as the correlation matrices of the fit parameters. The fit values and their uncertainties for both joined and individually considered module sizes are stated explicitly in Table 6.3. For illustration, the LTP at $r = 450\,\mathrm{m}$ is shown in Fig. 6.11 as a function of the primary energy for module combinations of $2 \times 5\,\mathrm{m}^2$, $1 \times 10\,\mathrm{m}^2$,

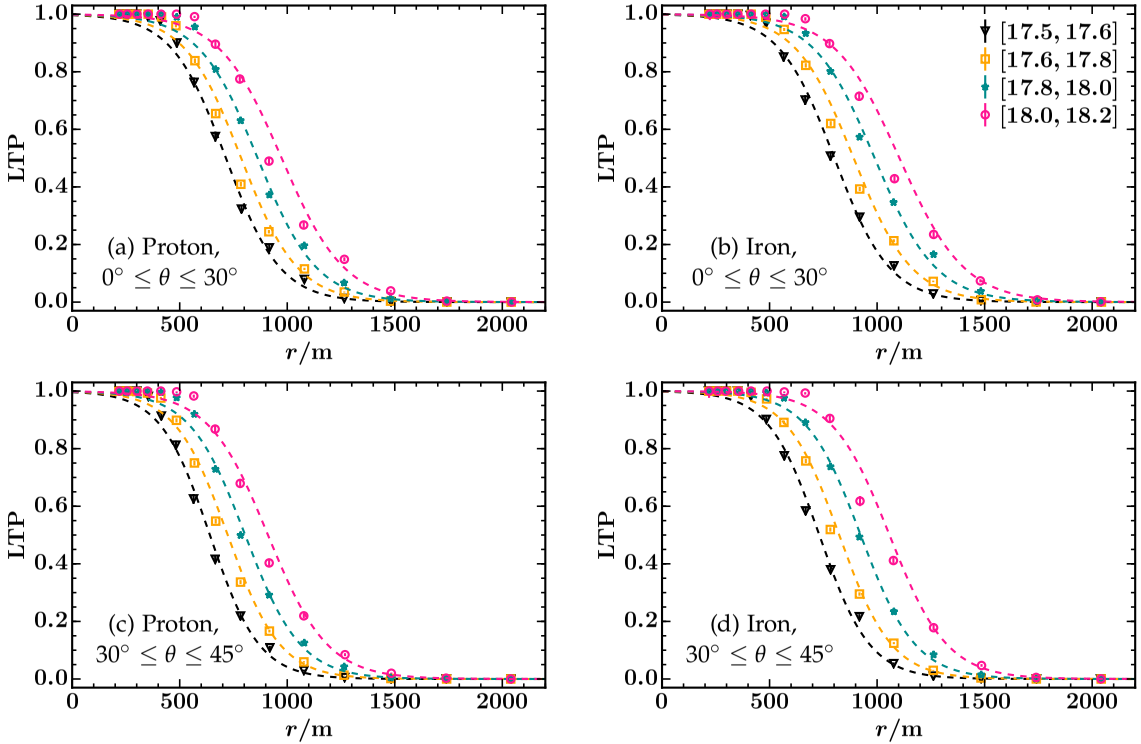

Figure 6.8: Lateral trigger probability for simulated extensive air showers with proton and iron primaries divided into zenith angle ranges $0° \leq \theta \leq 30°$ and $30° \leq \theta \leq 45°$ in bins of logarithmic energy. Markers denote the $p_{\mathrm{LTP},w}$ values in radial bins, error bars the corresponding binomial proportion confidence interval. Dashed curves display the global solution of the fitted Fermi function $f_{\mathrm{LTP}}(r, E)$ for different energy intervals.

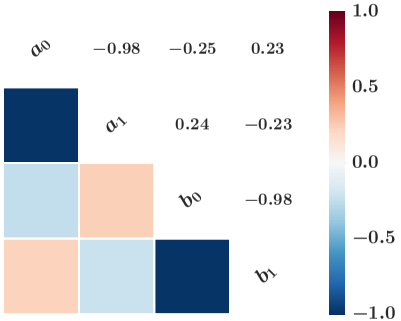

(a) Proton, $0° \leq \theta \leq 30°$

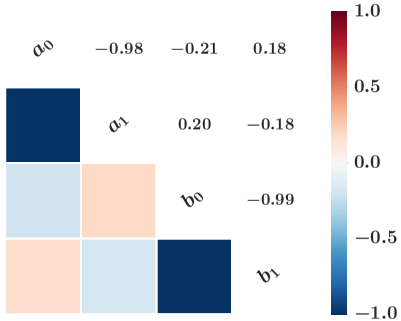

(b) Iron, $0° \leq \theta \leq 30°$

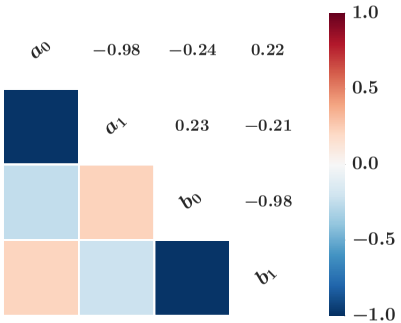

(c) Proton, $30° \leq \theta \leq 45°$

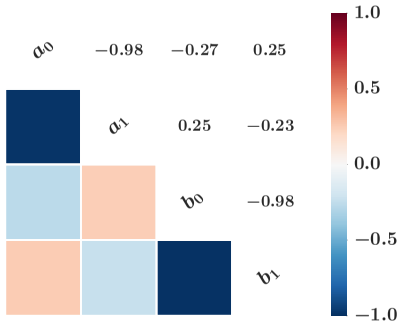

(d) Iron, $30° \leq \theta \leq 45°$

Figure 6.9: Correlation matrices of the LTP fit parameters for simulated extensive air showers with proton and iron primaries divided into the zenith angle ranges $0° \leq \theta \leq 30°$ and $30° \leq \theta \leq 45°$.

	Module combination		
Parameters	$2 \times 5\,\mathrm{m}^2$	$1 \times 10\,\mathrm{m}^2$	Joined
$\mathbf{0^\circ \leq \theta \leq 30^\circ}$			
a_0	5.02 ± 0.42	4.41 ± 0.25	4.56 ± 0.21
a_1	5.62 ± 0.62	5.93 ± 0.36	5.85 ± 0.31
b_0	1.06 ± 0.30	1.01 ± 0.19	1.03 ± 0.16
b_1	0.60 ± 0.44	0.71 ± 0.27	0.68 ± 0.23
$\mathbf{30^\circ \leq \theta \leq 45^\circ}$			
a_0	4.12 ± 0.41	4.44 ± 0.25	4.34 ± 0.21
a_1	5.77 ± 0.58	4.76 ± 0.35	5.06 ± 0.30
b_0	1.59 ± 0.37	1.11 ± 0.18	1.22 ± 0.17
b_1	-0.16 ± 0.51	0.47 ± 0.25	0.34 ± 0.23

Table 6.3: Parameters and uncertainties of the LTP parametrization Eq. (6.5) for AMIGA data for the zenith angle ranges $0^\circ \leq \theta \leq 30^\circ$ and $30^\circ \leq \theta \leq 45^\circ$.

and both module sizes joined for the shower zenith angle range $0^\circ \leq \theta \leq 30^\circ$. The larger LTP for $5\,\mathrm{m}^2$ modules confirms their increased muon counting efficiency in comparison to the $10\,\mathrm{m}^2$ modules.

The LTP observed for data is quite similar to the one in simulations. We explicitly compare the fitted parametrizations for AMIGA data with proton and iron simulations for the energy interval $10^{17.8}\,\mathrm{eV} \leq E \leq 10^{18}\,\mathrm{eV}$ and shower zenith angles $0^\circ \leq \theta \leq 30^\circ$ in Fig. 6.12. The fitted LTP curve for data is close to the one obtained for iron simulations which could be explained by the increased muon content in data compared to simulations which will be discussed in Chapter 7.

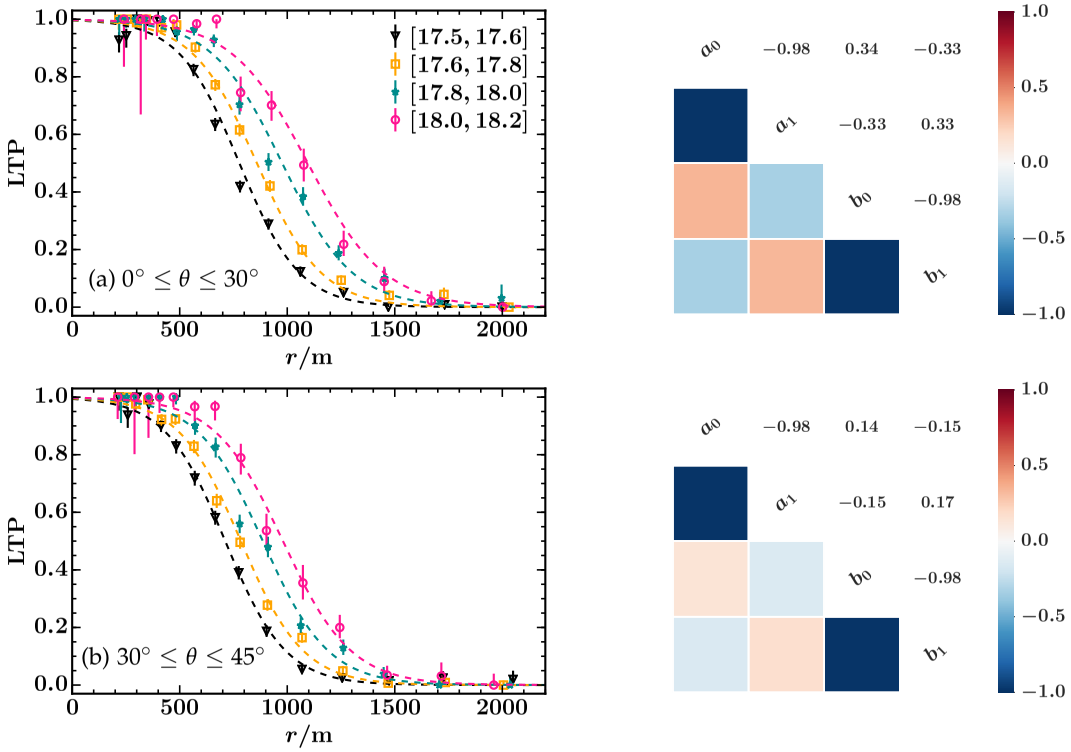

Figure 6.10: Lateral trigger probability within different bins in logarithmic energy (left) and correlation matrices of fit parameters (right) for AMIGA data. Both single 10 m^2 modules and pairs of 5 m^2 modules are taken into account. Top: zenith angle range $30° \leq \theta \leq 45°$ (a), bottom: $30° \leq \theta \leq 45°$ (b).

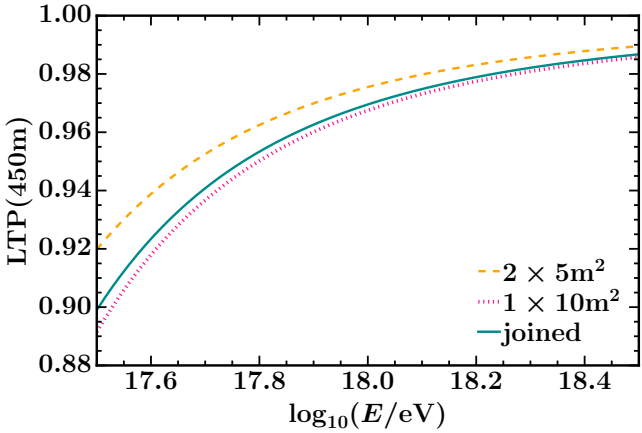

Figure 6.11: LTP at $r = 450\,\mathrm{m}$ as a function of the primary energy for module combinations of $2 \times 5\,\mathrm{m}^2$ (dashed, orange), $1 \times 10\,\mathrm{m}^2$ (dotted, red), and both joined (cyan, solid) for zenith angles $0° \leq \theta \leq 30°$.

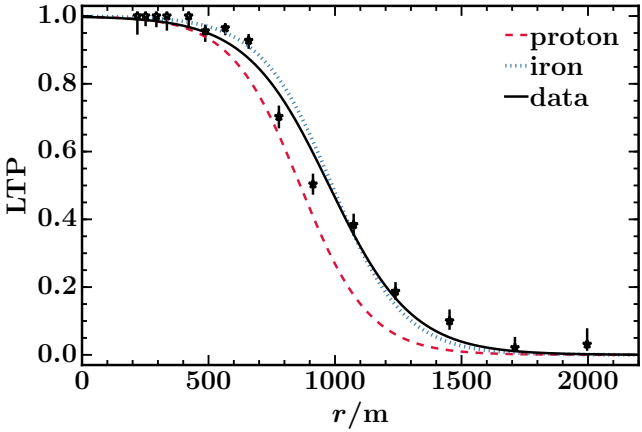

Figure 6.12: Comparison of LTP for AMIGA data with proton and iron simulations for the energy interval $10^{17.8}\,\mathrm{eV} \leq E \leq 10^{18}\,\mathrm{eV}$ and shower zenith angles $0° \leq \theta \leq 30°$.

6.5 ATTENUATION CORRECTION

Depending on the amount of traversed atmosphere, the signal of an extensive air shower measured at ground gets attenuated. In order to remove the zenith dependence of the signal, the atmospheric attenuation has been parametrized for both the SD-1500 and the SD-750 array as a function of the shower zenith angle. The corrected signals S_{38} (SD-1500) and S_{35} (SD-750) are for instance used in the SD estimation of the primary energy.

The attenuation of the SD signal is dominated by the attenuation of the electromagnetic shower component. In contrast, electromagnetic particles do not play any role in the case of AMIGA, since electromagnetic secondaries are almost completely absorbed in the soil layer of 2.3 m depth above the buried scintillator modules. Although muons are only weakly attenuated by the atmosphere, the amount of soil that a muon needs to pass through is increased for inclined showers. This leads to higher zenith-dependent effective muon energy thresholds and hence an attenuation of the muonic signal. In the following, we parametrize the attenuation of the muon density ρ_{450} for AMIGA and introduce a zenith angle-independent estimator ρ_{35} of the muon density at the optimal distance of $r_{\text{opt}} = 450\,\text{m}$.

6.5.1 *Constant intensity cut method*

We employ the constant intensity cut (CIC) method [64] to derive a parametrization of the attenuation of the muonic signal for AMIGA. It is based on the assumption of an isotropic flux

$$J = \frac{\mathrm{d}N}{\mathrm{d}A_{\text{eff}}\,\mathrm{d}t\,\mathrm{d}E\,\mathrm{d}\Omega} \tag{6.10}$$

of cosmic ray particles $\mathrm{d}N$ arriving at earth per effective area $\mathrm{d}A_{\mathrm{eff}} = \mathrm{d}A\cos\theta$, time interval $\mathrm{d}t$, energy $\mathrm{d}E$, and solid angle $\mathrm{d}\Omega$. Since $^{\mathrm{d}J}/_{\mathrm{d}\theta} = 0$ must hold for an isotropic flux,

$$\frac{\mathrm{d}N}{\mathrm{d}E\,\mathrm{d}\cos^2\theta} = \text{const} \tag{6.11}$$

follows with $\mathrm{d}\Omega = \mathrm{d}\cos\theta\mathrm{d}\varphi$. Consequently, integrating over energies above a cut energy E_0, we arrive at a constant number of events

$$\left.\frac{\mathrm{d}N}{\mathrm{d}\cos^2\theta}\right|_{E>E_0} = \text{const} \tag{6.12}$$

with $E > E_0$ in zenith angle bins that are equidistant in $\cos^2\theta$.

The CIC method makes use of the equal number of events ("intensity") in equidistant $\cos^2\theta$ bins to derive a parametrization of the attenuation with zenith angle θ. Cutting horizontally at a fixed intensity is equivalent to cutting at a certain fixed energy. The corresponding signal values in the different zenith angle bins can then be used to fit an attenuation function.

For the SD-750 array, the shower size estimator is the signal size S_{450} at the optimal reference distance of $r_{\mathrm{opt}} = 450\,\mathrm{m}$. The dependence on the primary energy E and the shower zenith angle can be factorized as

$$S_{450}(E,\theta) = S_{35}(E)\cdot f_{\mathrm{att}}(\theta) \tag{6.13}$$

where $S_{35}(E)$ is the energy-dependent signal at $r_{\mathrm{opt}} = 450\,\mathrm{m}$ for the reference zenith angle of $\theta_{\mathrm{ref}} = 35^\circ$ and $f_{\mathrm{att}}(\theta)$ parametrizes the attenuation as a function of θ. The reference angle θ_{ref} is chosen as the median zenith angle

$$\theta_{\mathrm{ref}} = \cos^{-1}\sqrt{\langle\cos^2\theta\rangle} \tag{6.14}$$

in bins of $\cos^2\theta$ for the zenith angle range $0^\circ \leq \theta \leq 55$ which is accessible for the SD-750 array. Originally, the functional form

$$f_{\mathrm{att}}(\theta) = 1 + ax + bx^2 \tag{6.15}$$

of a second order polynomial in

$$x = \cos^2\theta - \cos^2\theta_{\text{ref}} \tag{6.16}$$

with parameters a and b has been chosen to parametrize the observed attenuation for the SD-1500 array [104]. It has been later extended to a third order polynomial with an additional parameter c for both the SD-1500 and SD-750 attenuation parametrizations [65].

For a fixed cut intensity n_{cut}, the parameters of f_{att} can be obtained by a least-squares minimization of

$$\text{LS}(a,b) = \sum_{i=1}^{N_\theta} \frac{1}{\sigma_i^2} \left(S^{\text{cut}}_{450,i} - S^{\text{cut}}_{35} \cdot f_{\text{att}}(\theta_i; a, b) \right) \tag{6.17}$$

where the sum runs over the N_θ zenith angles bins into which the data set is split. In addition to the attenuation parameters a and b, the reference shower size value S^{cut}_{35}, corresponding to the signal at $\theta_{\text{ref}} = 35^\circ$ for the intensity n_{cut}, is a further fit parameter. The signal $S^{\text{cut}}_{450,i}$ is the signal in the ith zenith bin for the chosen cut intensity. The uncertainties σ_i of the $S^{\text{cut}}_{450,i}$ values can be obtained with a bootstrap method [105] by resampling the $S^{\text{cut}}_{450,i}$ values a number of times N_b within each $\cos^2\theta_i$ bin. For each of the N_b generated samples, the cut signal $S^{\text{cut}*}_{450,i}$ is determined by cutting at the predefined intensity cut value. The uncertainty σ_i for the ith zenith bin then corresponds to the standard deviation of the sample cut values $S^{\text{cut}*}_{450,i}$.

6.5.2 *CIC for AMIGA data*

The data set of one year of AMIGA data is much smaller than the ones available for the SD which were used to parametrize the attenuation functions. In contrast to 29585 events above a threshold energy of $10^{17.5}$ eV, which were already available for the SD-750 CIC parametrization for the ICRC 2013 [65], we only dispose about a total number of 3175 events with energies above $10^{17.5}$ eV and zenith angles $\theta \leq 55^\circ$ after applying the previously

described quality cuts. We account for the small data set by using a slightly modified version of the CIC method that has been introduced in Section 6.5.1.

In analogy to Eq. (6.13), we parametrize the attenuation of the muonic signal ρ_{450} at the optimal distance as

$$\rho_{450}\left(E,\theta\right) = \rho_{35}\left(E\right) \cdot f_{\text{att}}\left(\theta\right) \tag{6.18}$$

with f_{att} defined as in Eq. (6.15). However, in contrast to the "original" CIC method, we do not cut at a single fixed level of intensity. Instead, we consider a bin of width 100 (± 50) around the chosen intensity cut value $N_{\text{evs}}^{\text{cut}}$ to be less sensitive to data fluctuations. We hence minimize the modified least-squares expression

$$\text{LS}\left(a,b\right) = \sum_{i=1}^{N_\theta} \sum_{j=N_{\text{evs}}^{\text{cut}}-50}^{N_{\text{evs}}^{\text{cut}}+50} \frac{1}{\sigma_{ij}^2} \left(\rho_{450,\,ij}^{\text{cut}} - \rho_{35,\,j}^{\text{cut}} \cdot f_{\text{att}}\left(\theta_i; a, b\right)\right) \tag{6.19}$$

with an additional sum (index j) over the interval from $N_{\text{evs}}^{\text{cut}} - 50$ to $N_{\text{evs}}^{\text{cut}} + 50$. The muon density $\rho_{450,\,ij}^{\text{cut}}$ corresponds to the density at $r_{\text{opt}} = 450\,\text{m}$ in the i-th θ-bin for the horizontal cut value j. The muon densities at the optimal distance r_{opt} are obtained from MLDF fits with fixed β parameter to reduce statistical fluctuations (cf. Section 5.8). The corresponding reference density $\rho_{35,\,j}^{\text{cut}}$ is given by the muon density at r_{opt} for the reference zenith angle $\theta_{\text{ref}} = 35^\circ$ at this intensity cut value. Different than in Eq. (6.17), we do not fit the $\rho_{35,\,j}^{\text{cut}}$ values, but calculate them in the following way: we take the values $\rho_{450,N_\theta/2\,j}^{\text{cut}}$ of the middle zenith bin with index $i = {}^{N_\theta}/_2$ for the intensity cut value j and normalize them according to

$$\rho_{35,\,j}^{\text{cut}} = \frac{\rho_{450,\,i_{N_\theta/2}\,j}^{\text{cut}}}{f_{\text{att}}\left(\theta_{N_\theta/2}\right)} \tag{6.20}$$

by the attenuation function f_{att} evaluated at the zenith angle $\theta_{N_\theta/2}$ of the middle bin.

The uncertainties σ_{ij} of the muon densities for the different intensity cut values and zenith angle bins are calculated with the bootstrapping method. Within each zenith angle bin (index i), 1000 bootstrap samples of the original density values are generated. For each sample, we cut at the 100 respective numbers of events j within the interval from $N_{\text{evs}}^{\text{cut}} - 50$ to $N_{\text{evs}}^{\text{cut}} + 50$ to obtain the corresponding cut densities $\rho_{450,ij}^{\text{cut}*}$. The uncertainties $\sigma_{450,ij}^{\text{cut}}$ then correspond to the standard deviations of the cut densities $\rho_{450,ij}^{\text{cut}*}$ from the 1000 values obtained from bootstrapping for each i, j combination. Since we use the middle zenith angle bin as a reference, we additionally need to take into account the uncertainties of the reference densities $\rho_{35,j}^{\text{cut}}$. To this end, we normalize the uncertainties of the middle bin by the corresponding attenuation function value as

$$\sigma_{35,j}^{\text{cut}} = \frac{\sigma_{450,i_{N_\theta/2}j}^{\text{cut}}}{f_{\text{att}}\left(\theta_{N_\theta/2}\right)} \tag{6.21}$$

and combine them with $\sigma_{450,ij}^{\text{cut}}$ to the joined uncertainties

$$\sigma_{ij} = \sqrt{\frac{1}{2}\left(\left(\sigma_{450,ij}^{\text{cut}}\right)^2 + \left(\sigma_{35,j}^{\text{cut}}\right)^2\right)}. \tag{6.22}$$

We divide the data set in three zenith bins with equal $\cos^2\theta$ binning within the range $0° \leq \theta \leq 55°$. In each bin, there are approximately 1000 events. Due to the small number of events, a subdivision into more bins is unfortunately not feasible. In Fig. 6.13, the number of events with $\rho_{450} > \rho_{450}^{\text{cut}}$ is shown as a function of ρ_{450}^{cut} in each zenith angle bin. There is an apparent splitting between the different zenith bins. For illustration, vertical lines emphasize the differences in the densities ρ_{450}^{cut} for the same horizontal density cut values (200, 450, 700 events) in different zenith bins. The shaded horizontal band displays the intensity range $200 \leq N_{\text{events}} \leq 700$ that is later used for an averaged fit of the CIC attenuation function (Fig. 6.16).

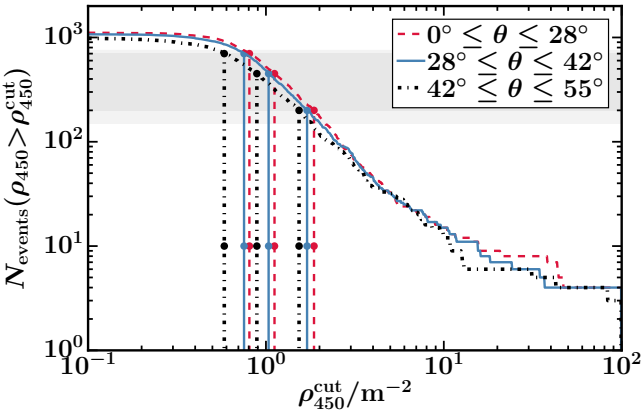

(a) Number of events above cut density

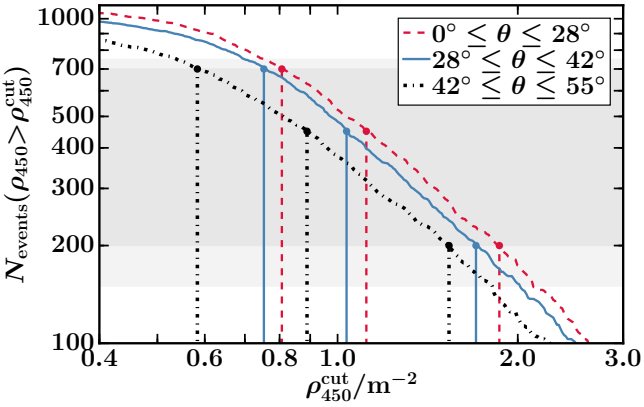

(b) Zoomed version

Figure 6.13: (a) Number of events with $\rho_{450} > \rho_{450}^{\text{cut}}$ as a function of ρ_{450}^{cut} in three bins of zenith angle θ with equal $\cos^2\theta$ binning. The shaded horizontal band displays the range of values $N_{\text{events}}(\rho_{450} > \rho_{450}^{\text{cut}})$ that is used for the fit of the CIC attenuation function. (b) Zoom to intensities above 100 events.

We aim to correct for the attenuation effect such that the corrected densities do not not depend on the zenith angle and the different zenith angle curves lie on top of each other. It has been highlighted in [106, 107], that the obtained parametrization of the attenuation correction depends on the chosen intensity cut value which is closely related to the primary energy. We therefore scan over the range of cut values between 100 and 800 events where the intensity curves show a linear behavior. Below 100 events, the small data set leads to high statistical fluctuations, above 800 events a saturation effect is visible when approaching the total number of events within a zenith bin.

The resulting parameter scan is shown in Fig. 6.14. We have varied the cut intensities within the range from 100 to 800 in steps of 5. For each cut intensity $N_{\text{evs}}^{\text{cut}}$, we have minimized the LS expression of Eq. (6.19) to obtain the optimal fit parameters a and b. The uncertainties in a and b are determined by bootstrapping the complete data set (all zenith angles) 1000 times. For each generated bootstrap sample, the optimal attenuation parameters are fitted. The covariance matrix of the parameters a and b, and hence the individual 1σ uncertainties, are calculated from the set of 1000 best fit parameters.

Due to the small number of zenith angle bins, there is not much information on the bending of the attenuation function for small zenith angles. This is reflected in the large uncertainties of b, while the uncertainties are relatively small for the parameter a. The parameters a and b follow opposite trends; while a slightly decreases, b increases for increasing muon density cut values (decreasing intensity cut values). This could be a consequence of the implicit change in primary energy. However, we do not dispose of enough data to derive any conclusions here.

In addition to the parameter scan in Fig. 6.14, best fit parameters for intensity cut values in the range from 200 to 700 are given in Table 6.4. The corresponding attenuation functions, demonstrating the dependence on the chosen intensity cuts, are plotted in Fig. 6.15. In order to derive a parametrization of the attenu-

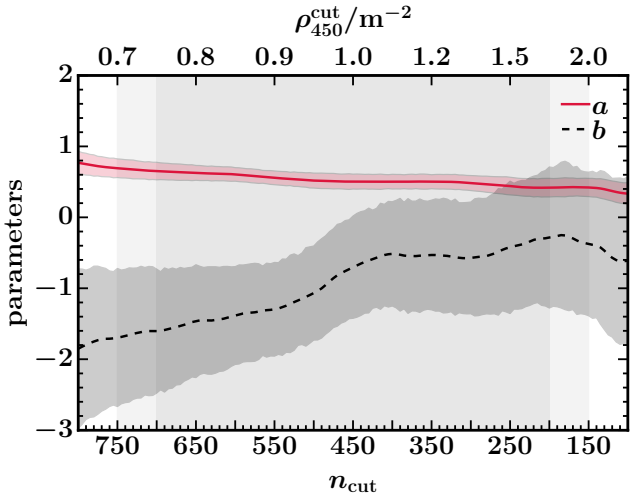

Figure 6.14: Scan of the CIC function parameters a and b over the intensity cut values n_{cut} (lower x-axis). The corresponding density cut values $\rho_{450}^{\mathrm{cut}}$ are given at the upper x-axis. Shaded bands denote the 1σ uncertainties of the parameters obtained by bootstrapping.

	Parameters	
n_{cut}	a	b
200	0.42 ± 0.14	-0.28 ± 0.98
300	0.48 ± 0.10	-0.57 ± 0.79
400	0.50 ± 0.10	-0.52 ± 0.75
500	0.52 ± 0.10	-1.07 ± 0.68
600	0.61 ± 0.10	-1.38 ± 0.72
700	0.65 ± 0.12	-1.60 ± 0.86

Table 6.4: CIC fit parameters with uncertainties for different intensity cuts n_{cut} within the linear range from 200 to 700 events.

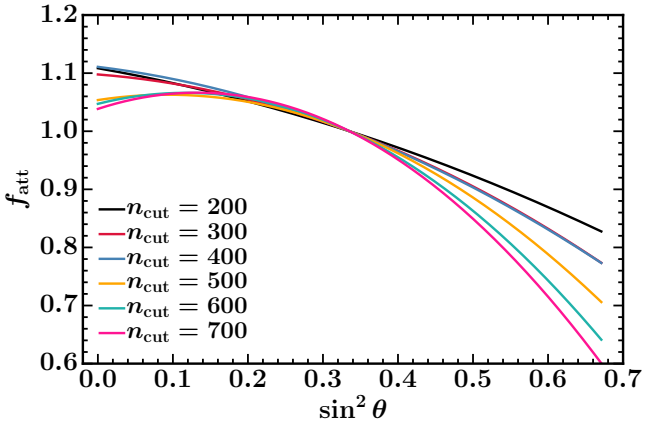

Figure 6.15: CIC attenuation functions plotted over $\sin^2\theta$ for different cuts in the number of events n_{cut}.

ation which fits best the complete considered linear range from $200 \leq n_{\text{cut}} \leq 700$, we perform a least-squares minimization of

$$\text{LS}(a,b) = \sum_{i=1}^{N_\theta} \sum_{j=200}^{700} \frac{1}{\sigma_{ij}^2} \left(\rho_{450,ij}^{\text{cut}} - \rho_{35,j}^{\text{cut}} \cdot f_{\text{att}}(\theta_i; a, b) \right)^2 \tag{6.23}$$

taking into account all intensity cut values from 200 to 700. The resulting attenuation curve is displayed in Fig. 6.16. The best fit parameter values of

$$\begin{aligned} a &= 0.54 \pm 0.10 \\ b &= -1.02 \pm 0.69 \end{aligned} \tag{6.24}$$

correspond approximately to the average values in the scanned region (cf. Fig. 6.14).

We apply the derived average attenuation function to correct the zenith-dependent muon densities ρ_{450} by

$$\rho_{35}(E) = \frac{\rho_{450}(E,\theta)}{f_{\text{att}}(\theta)}. \tag{6.25}$$

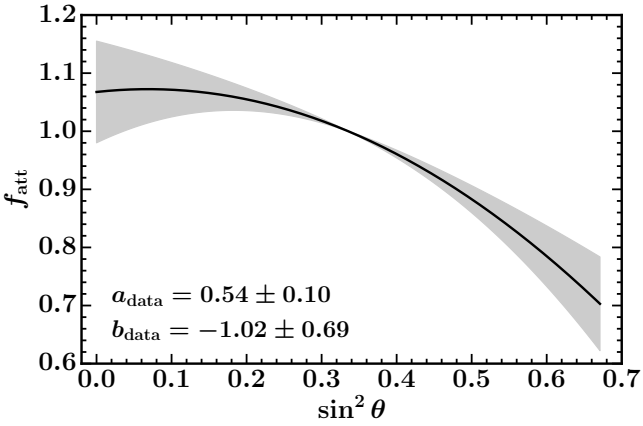

Figure 6.16: Average attenuation function f_{att} obtained from a CIC fit over the linear intensity range $200 \leq n_{\mathrm{cut}} \leq 700$.

In Fig. 6.17, the number of events within the three considered zenith angle bins are plotted over the corrected ρ_{35} values for intensities above 100 events. Although the intensity curves for the different zenith start differing for intensities below 450 events, their agreement, especially for large intensities, has been significantly improved by the attenuation correction. The corrected density values ρ_{35} agree very well at the mean cut intensity of 450 events.

As an additional test, we check the uniformity of the corrected event distribution by plotting the number of events above certain fixed cut densities as a function of the mean zenith angle θ of the three considered zenith angle bins in Fig. 6.18. For comparison, the previous uncorrected event distribution is shown. Although, most likely as a consequence of the small data set, the event distributions of the different zenith bins do not match perfectly, the improved uniformity due to the attenuation correction is clearly visible.

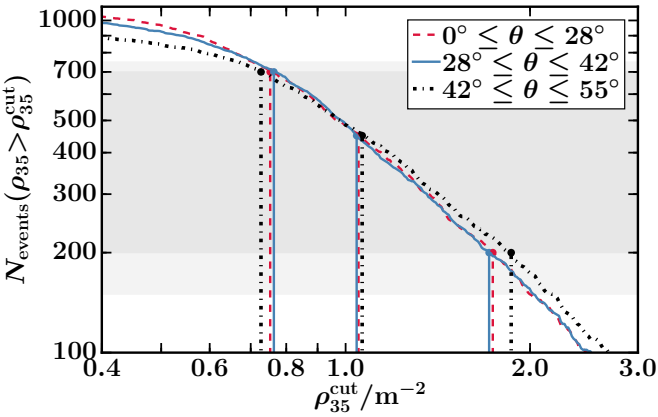

Figure 6.17: Number of events with $\rho_{35} > \rho_{35}^{\text{cut}}$ as a function of ρ_{35}^{cut} in three bins of zenith angle θ with equal $\sin^2\theta$ binning after correcting for the attenuation of signals by $\rho_{35} = \rho_{450}/f_{\text{att}}(\theta)$.

The attenuation of the muonic shower component observed for AMIGA is significantly smaller than the signal attenuation for the SD. This is a consequence of the much stronger attenuation of the electromagnetic component in the atmosphere which makes up a large contribution of the SD signal. The attenuation curves which have been derived with the CIC method from SD and MD data, respectively, are compared in Fig. 6.19. While the attenuation function (parametrization from [108])

$$f_{\text{att}}(x) = 1 + (1.602 \pm 0.039)\, x + (-1.50 \pm 0.10)\, x^2 + (-1.88 \pm 0.53)\, x^3 \tag{6.26}$$

with $x = \cos^2\theta - \cos^2\theta_{\text{ref}}$ and $\theta_{\text{ref}} = 35°$ takes values from 1.3 ($\theta = 0°$) to 0.4 ($\theta = 55°$), corresponding to approximately 30% of the maximum signal value, the MD attenuation function only varies between 1.1 and 0.7, i.e. the muon density at $\theta = 55°$ corresponds still to about 65% of the maximum density value.

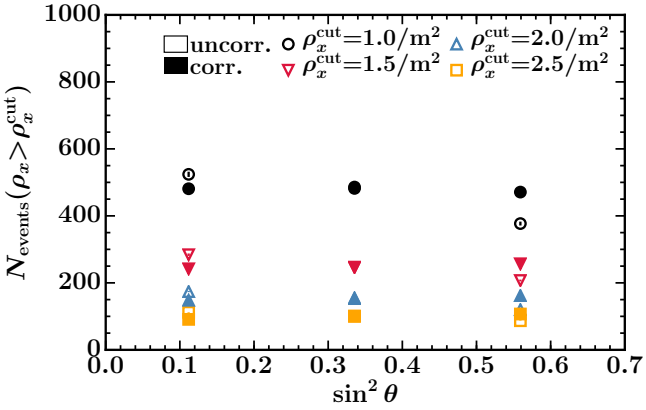

Figure 6.18: Test of constant intensity. Number of events above different cut densities in three bins of zenith angle θ with equal $\sin^2\theta$ binning before ($x = 450$, unfilled markers) and after correcting for the attenuation of signals ($x = 35$, filled markers). Error bars correspond to the Wilson binomial proportion confidence intervals [103].

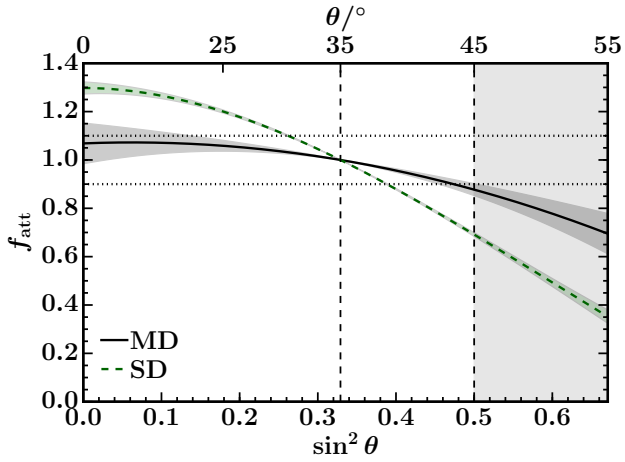

Figure 6.19: Comparison of attenuation curves for SD (Eq. (6.26),[108]) and MD obtained with the CIC method from data.

6.5.3 *Attenuation parametrization for simulations*

To compare the obtained parametrization of the muon attenuation for data with model predictions, we use the library of fixed energy described in Section 5.1 with $N_E = 4$ primary energies of $10^{17.5}$ eV, 10^{18} eV, $10^{18.5}$ eV, and 10^{19} eV and $N_\theta = 7$ zenith angles $0°$, $12°$, $22°$, $32°$, $38°$, $48°$, and $56°$ for proton and iron particles and the two hadronic interaction models QGSJETII-04 and EPOS-LHC. For every setting, 600 showers are available resulting from 120 simulated showers that were tossed five times on the SD-750 array each.

Instead of applying the CIC method, which is suitable for a continuous distribution of showers in primary energy and zenith angle, we parametrize the attenuation of the muon density ρ_{450} as a function of the shower zenith angle θ by

$$\rho_{450}(\theta) = \rho_{35} \cdot f_{\text{att}}(\theta; a, b) \tag{6.27}$$

individually for every hadronic interaction model, primary particle, and primary energy. While the attenuation function f_{att} is defined as in Eq. (6.15), we have an additional fit parameter ρ_{35} specifying the reference muon density at $\theta_{\text{ref}} = 35°$. For each interaction model, primary particle, and energy we obtain the fit parameters a, b and ρ_{35} by a minimization of

$$\text{LS}(\rho_{35}, a, b) = \sum_{i=1}^{N_\theta} \sum_{j=1}^{600} \frac{1}{\sigma_{450,ij}^2} \left(\rho_{450,ij} - \rho_{35} \cdot f_{\text{att}}(\theta_i; a, b)\right)^2 \tag{6.28}$$

taking into account a total number of $N_\theta \times 600 = 4200$ showers. The muon densities $\rho_{450,ij}$ as well as the corresponding uncertainties $\sigma_{450,ij}$ are determined individually for each shower from a fit of the MLDF.

In addition to the individual parametrizations for each primary energy E, we parametrize the muon density at the optimal dis-

tance $r_{\text{opt}} = 450\,\text{m}$ for each primary and hadronic interaction model combination as a function of the energy by

$$\rho_{450}\left(E, \theta; \vec{p}\right) = \rho_{35}\left(E; \vec{p}\right) \cdot f_{\text{att}}\left(E, \theta; \vec{p}\right) \tag{6.29}$$

with $\vec{p} = (a_0, a_1, b_0, b_1, \rho_0, \rho_1)$ and

$$\begin{aligned} \rho_{35}\left(E; \vec{p}\right)/\text{m}^{-2} &= 10^{\left(\rho_0 + \rho_1 \cdot \left(\log_{10}(E/\text{eV}) - 17.5\right)\right)}, \\ a\left(E; \vec{p}\,\right) &= a_0 + a_1 \cdot \left(\log_{10}(E/\text{eV}) - 17.5\right), \\ \text{and} \quad b\left(E; \vec{p}\,\right) &= b_0 + b_1 \cdot \left(\log_{10}(E/\text{eV}) - 17.5\right). \end{aligned} \tag{6.30}$$

We fit the parameter vector $\vec{p}$ by minimizing the LS expression

$$\text{LS}\left(\vec{p}\right) = \sum_{k=1}^{N_E} \sum_{i=1}^{N_\theta} \sum_{j=1}^{600} \frac{1}{\sigma^2_{450,kij}} \left(\rho_{450,kij} - \rho_{450}\left(E_k, \theta_i; \vec{p}\right)\right)^2 \tag{6.31}$$

with an additional sum, compared to Eq. (6.28), over all N_E available primary energies. The resulting best fit parameters for all considered primaries and interaction models are stated in Table 6.5. The uncertainties of the fit parameters $\vec{p}$ are obtained from bootstrapping the data set 500 times and calculating the covariance matrix from the 500 best fit parameters $\vec{p^*}$.

The fit parameters a, b, and $\log_{10}\left(\rho_{35}/\text{m}^{-2}\right)$ that have been obtained for individual energies according to the LS fit of Eq. (6.28) are shown in Fig. 6.20 (markers) together with the results of the energy-dependent parametrization of Eq. (6.30) (solid lines). The parameter correlations for the energy-dependent fit are visualized in Fig. 6.21. As expected, the densities ρ_{35} increase linearly with the energy and are larger for iron than for proton showers due to the higher muon content in iron showers. In contrast, the parameters a and b only show a small dependency on the primary energy E. For proton showers and notably the EPOS-LHC hadronic interaction model, the uncertainties in b are quite large. This is most likely a result of the spread in the position of the shower maximum X_{max}, leading to significant shower-to-shower fluctuations, and the smaller muon densities which increase the statistical uncertainties.

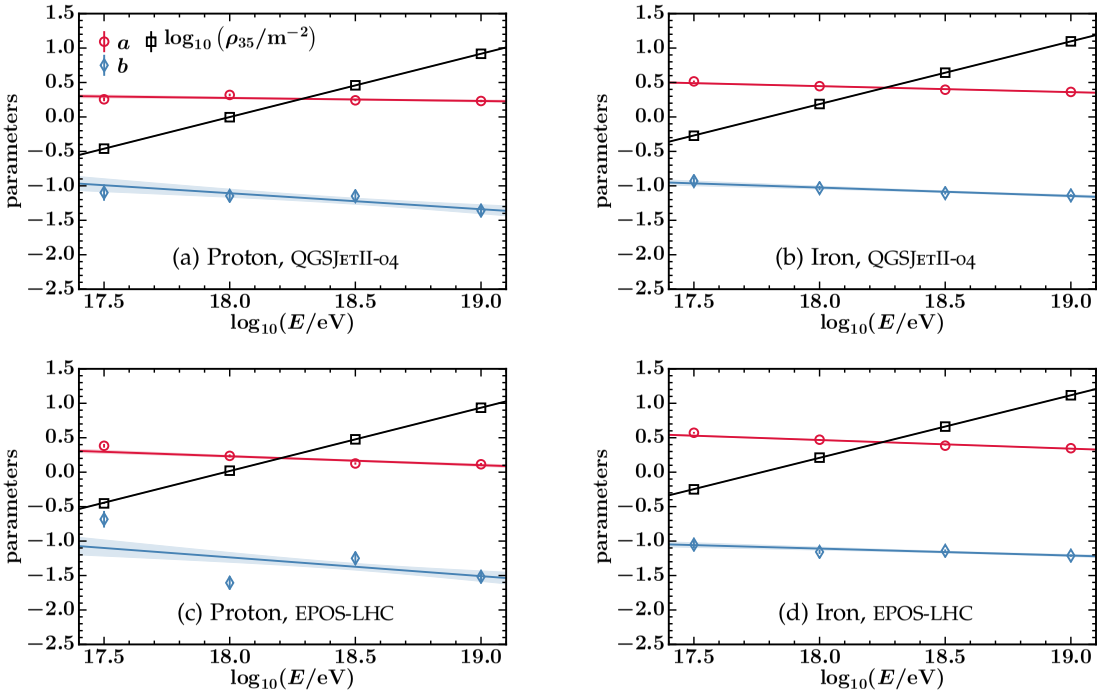

Figure 6.20: Best fit parameters for a, b, and $\log_{10}(\rho_{35}/\mathrm{m}^{-2})$ for different primaries and hadronic interaction models. Markers with error bars (1σ) show the obtained parameters for individual energy fits according to Eqs. (6.27) and (6.28), solid lines display the results for the energy-dependent parametrization of Eq. (6.29).

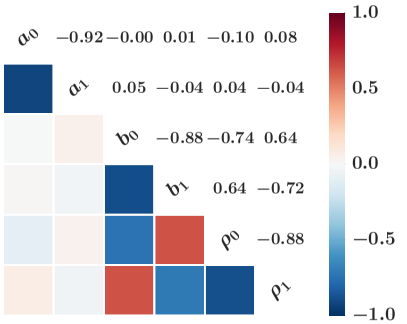

(a) Proton, QGSJetII-04

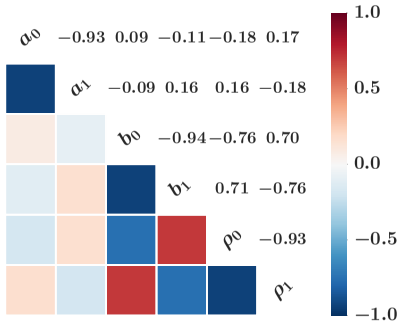

(b) Iron, QGSJetII-04

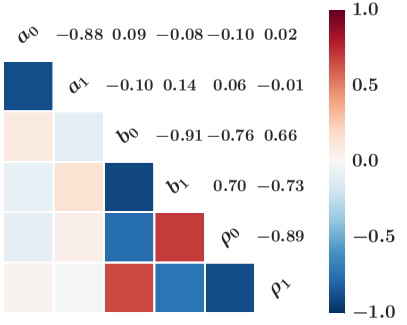

(c) Proton, EPOS-LHC

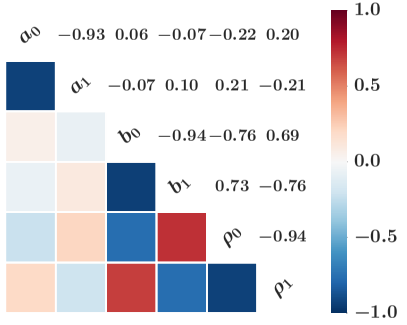

(d) Iron, EPOS-LHC

Figure 6.21: Correlation matrices of the fit parameters $\vec{p} = (a_0, a_1, b_0, b_1, \rho_0, \rho_1)$ for the energy-dependent attenuation parametrization of Eqs. (6.29) and (6.30) for different primary particles and hadronic interaction models.

	QGSJetII-04		EPOS-LHC	
Parameters	Proton	Iron	Proton	Iron
a_0	0.30 ± 0.02	0.49 ± 0.01	0.30 ± 0.02	0.53 ± 0.01
a_1	-0.04 ± 0.02	-0.09 ± 0.01	-0.13 ± 0.02	-0.13 ± 0.01
b_0	-0.99 ± 0.09	-0.96 ± 0.03	-1.10 ± 0.12	-1.06 ± 0.03
b_1	-0.23 ± 0.09	-0.12 ± 0.03	-0.27 ± 0.11	-0.10 ± 0.03
ρ_0	-0.46 ± 0.00	-0.27 ± 0.00	-0.44 ± 0.00	-0.25 ± 0.00
ρ_1	0.92 ± 0.00	0.91 ± 0.00	0.92 ± 0.00	0.91 ± 0.00

Table 6.5: Best fit parameters with 1σ uncertainties of the energy-dependent attenuation parametrization of Eqs. (6.29) and (6.30) for different primary particles and hadronic high-energy interaction models.

The derived attenuation curves f_{att} for the energy-dependent parametrization of Eq. (6.29) are shown in Fig. 6.22 as a function of $\sin^2\theta$ together with the weighted average

$$\langle \rho_{450}/\rho_{35} \rangle_w = {}^1/_{\rho_{35}} \frac{\sum_{i=1}^{n} \rho_{450_i}/(\sigma_{450_i})^2}{\sum_{i=1}^{n} {}^1/(\sigma_{450_i})^2} \tag{6.32}$$

of the normalized densities ρ_{450}/ρ_{35} for every shower zenith angle and primary energy. Despite some differences for the smallest considered energy of $10^{17.5}$ eV where fluctuations are largest, the shape of f_{att} is very similar for the iron simulations of both hadronic interaction models. Proton showers are attenuated stronger than iron showers for zenith angles $\theta \leq 35^\circ$ with $f_{\text{att}} \leq 1$ in comparison to $f_{\text{att}} \geq 1$ for iron showers. The effect is largest for the EPOS-LHC hadronic interaction model which shows a much stronger attenuation at small zenith angles than proton showers that have been simulated with QGSJetII-04. The quality of the attenuation parametrizations is visualized in Fig. 6.23. In case of an optimal correction, the ratio $\rho_{450}/(\rho_{35} \cdot f_{\text{att}})$ should be close to

1. While the weighted average ratios are mostly well contained within $1 \pm 5\%$ for both proton and iron simulations, the deviation and scattering is significantly reduced for iron showers.

For testing purposes, we apply the derived attenuation correction to proton and iron air shower simulations from the continuous QGSJETII-04 simulation library described in Section 5.1.3. The uncorrected (ρ_{450}) and attenuation corrected (ρ_{35}) muon densities at the optimal distance are shown in Fig. 6.24 as a function of θ in logarithmic bins of energy $\log(E/\mathrm{eV}) = [17.6, 17.8, \cdots, 19]$ with logarithmic spacing of 0.2 (bin center values stated in the legend). The shower zenith angles θ have been binned equidistantly in $\sin^2\theta$ in the range $0^\circ \leq \theta \leq 70^\circ$. For zenith angles $\theta \leq 45^\circ$, the attenuation correction is $\leq \pm 10\%$ (Fig. 6.26) and, correspondingly, the corrected and uncorrected muon densities shown in Fig. 6.24 do not deviate strongly. The discrepancy is increased for larger zenith angles. As observed before in Fig. 6.23, the corrected muon densities are slightly biased towards too large densities for $45^\circ \leq \theta \leq 55^\circ$. Since the attenuation parametrization has been done only for zenith angles $\theta \leq 56^\circ$, the correction is not valid for large angles up to 70°, even though the attenuation effect is reduced.

For the subsequent data analyses, we restrict the angular range to $0^\circ \leq \theta \leq 45^\circ$ where the necessary attenuation correction is $\leq \pm 10\%$. One reason for this restriction is that the effective detection areas $A_{\mathrm{eff}} = A\cos\theta$ of the AMIGA modules become very small for larger zenith angles which leads to increased statistical uncertainties. Further, a larger correction of up to 25% for $\theta = 55^\circ$ would cause increased systematic uncertainties in the estimated mean muon densities.

6.5.4 *Comparison of the muon attenuation in simulations and data*

We compare the derived parametrizations for simulations with the average attenuation parametrization that has been obtained for AMIGA data with the CIC method. Since the simulation

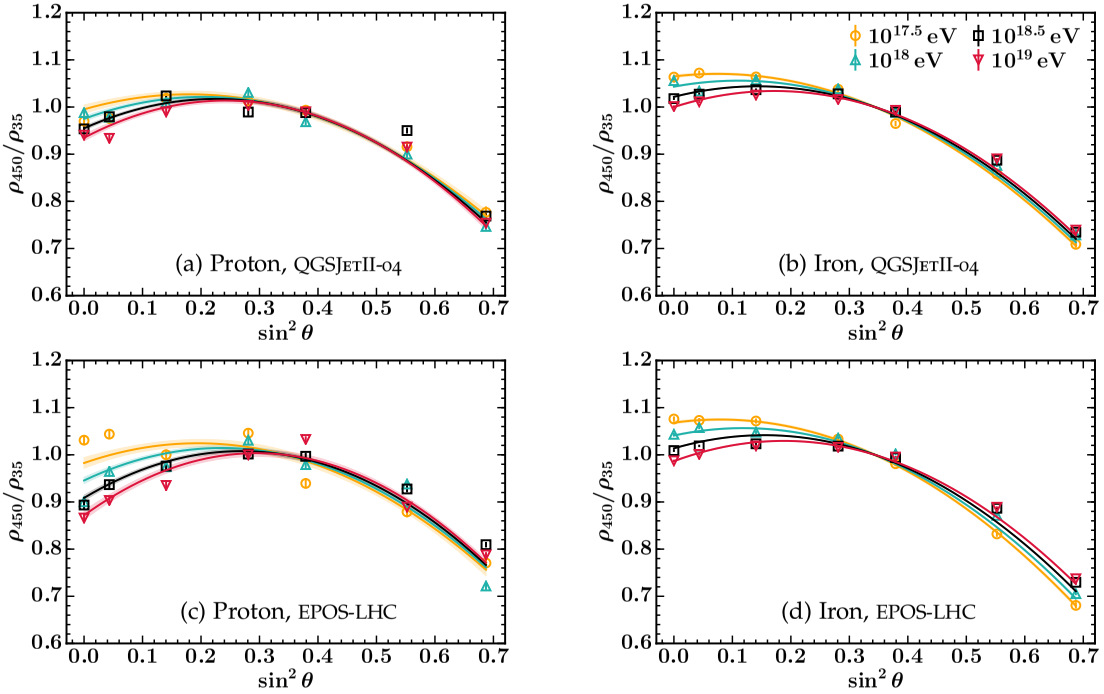

Figure 6.22: Weighted average of the normalized densities ρ_{450}/ρ_{35} (markers) for different primary energies and shower zenith angles; error bars indicate the corresponding standard deviations. Attenuation curves $f_{\text{att}}(E,\theta,\vec{p})$ that have been derived from minimizing Eq. (6.31) are shown as a function of $\sin^2\theta$ for different primary energies.

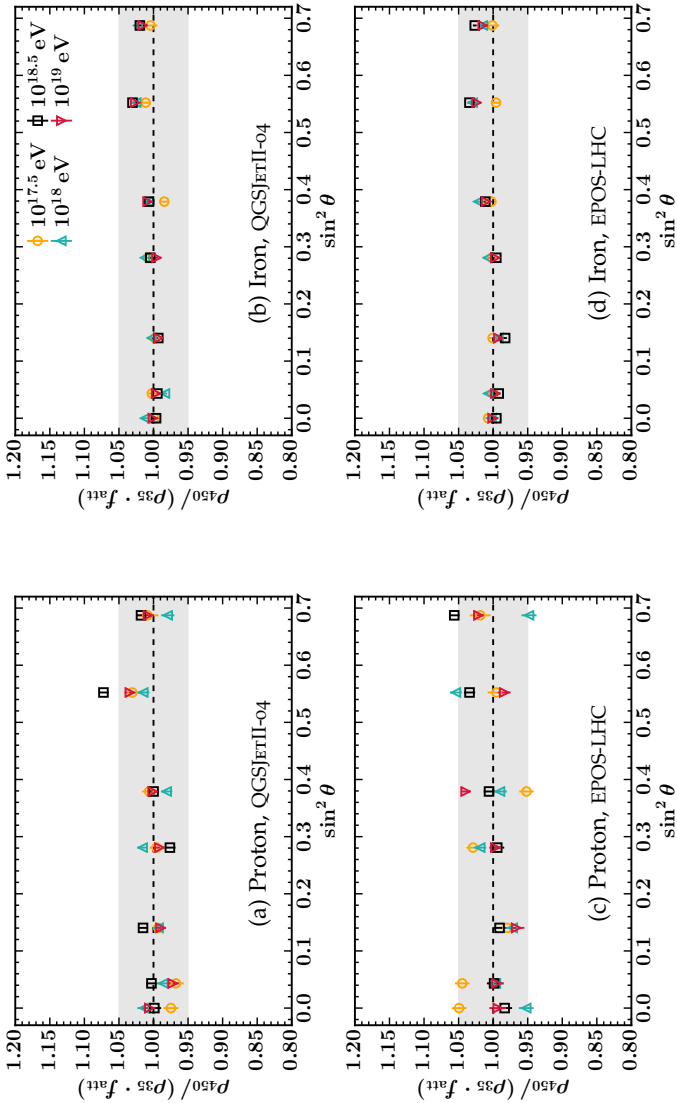

Figure 6.23: Weighted average ratios of $\rho_{450}/(\rho_{35}\cdot f_{\mathrm{att}})$ as a function of $\sin^2\theta$ for different primary energies; error bars indicate the corresponding standard deviations. The deviation of the ratios from 1 shows the quality of the attenuation correction.

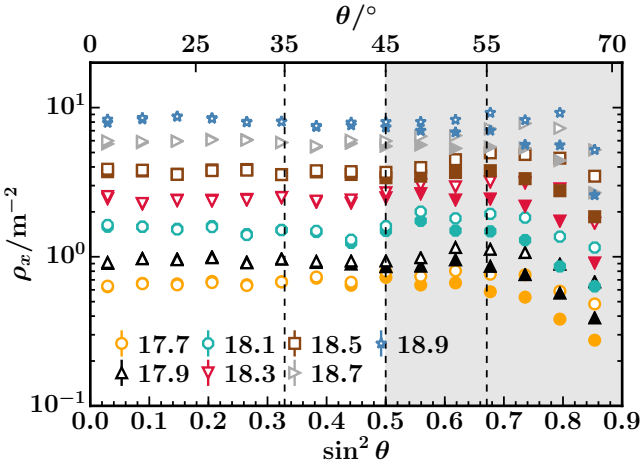

(a) Proton

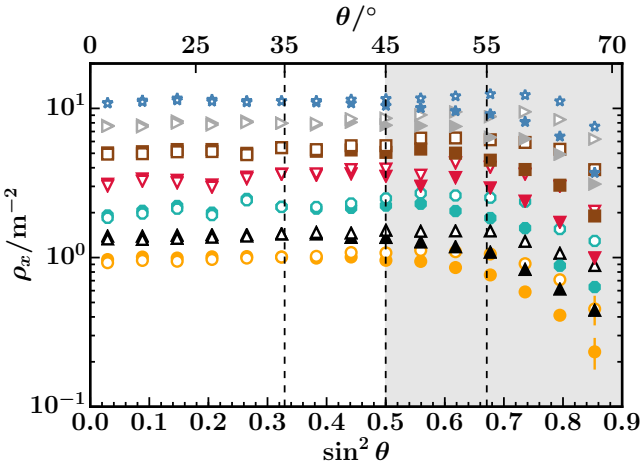

(b) Iron

Figure 6.24: Comparison of uncorrected (filled markers, $x = 450$) and attenuation corrected (unfilled, $x = 35$) muon densities in logarithmic bins of energy $\log(E/\mathrm{eV}) = [17.6, 17.8, \cdots, 19]$ as a function of θ for proton and iron simulations of the continuous QGSJETII-04 library.

parametrizations depend on the primary energy, we need to choose approximately the same energy scale as for data. The CIC parametrization for AMIGA data has been derived by minimizing the LS expression of Eq. (6.23) which takes into account all cut densities within the intensity cut range of $200 \leq n_{\text{cut}} \leq 700$. In order to relate these intensity cut values to the corresponding energy cuts E_{cut}, we plot the number of events with reconstructed energies $E > E_{\text{cut}}$ as a function of the cut energy in Fig. 6.25. The shaded horizontal band displays the intensity range that has been used for the fit of the CIC attenuation function. The mean intensity of $n_{\text{cut}} = 450$ events is associated with a cut energy of $\approx 10^{17.7}$ eV. We choose this energy for a comparison of the attenuation parametrizations for simulations with data.

The attenuation functions for simulations at an energy of $10^{17.7}$ eV are shown for both primaries and hadronic interaction models in Fig. 6.26 in comparison to the average parametrization derived for AMIGA data (cf. Fig. 6.16). The attenuation curves for iron showers are very similar to the attenuation curve for data for both models. In contrast, proton showers are attenuated stronger for zenith angles $\theta \leq 35^\circ$ and less attenuated for $\theta \geq 35^\circ$.

In the following composition analyses, restricted to zenith angles $0^\circ \leq \theta \leq 45^\circ$, we will employ the attenuation parametrization derived from data for the correction of the muon densities measured with AMIGA, and the individual parametrizations for each primary-hadronic interaction model combination for the correction of the muon densities obtained with simulations. The uncertainties of the parameters (a and b for data, a_0, a_1, b_0, and b_1 for simulations) of the attenuation functions will be propagated and treated as systematic uncertainties of the attenuation correction functions f_{att}.

6.6 SYSTEMATIC UNCERTAINTIES

The main sources of systematic uncertainties for AMIGA result from the uncertainty in the calibration of the PMT discriminator

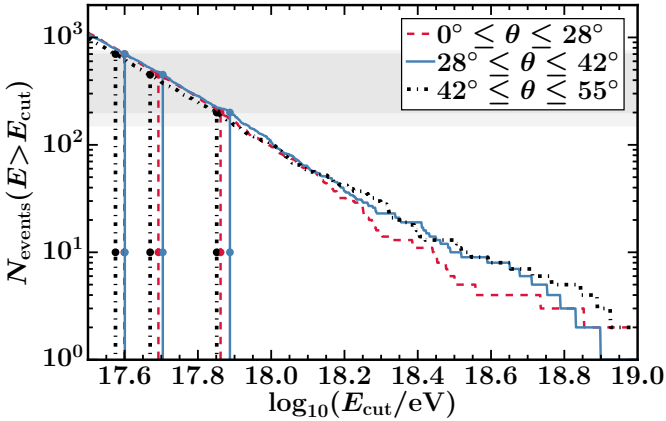

Figure 6.25: Number of events with reconstructed energies $E > E_{\text{cut}}$ as a function of E_{cut}. The shaded horizontal band displays the intensity range that has been used for the CIC fit. The mean intensity of $n_{\text{cut}} = 450$ events corresponds to a cut energy of $\approx 10^{17.7}$ eV.

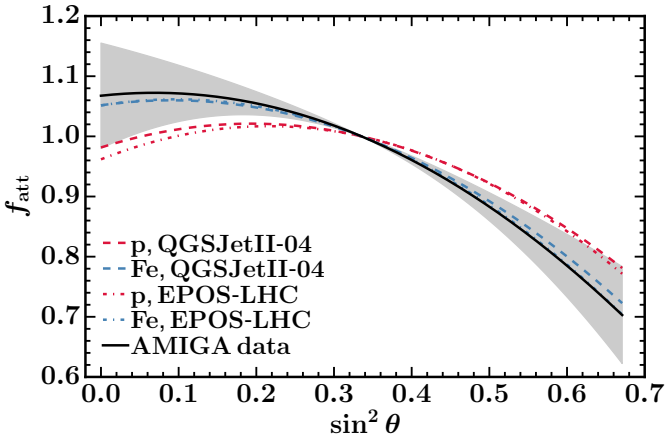

Figure 6.26: Averaged attenuation curves f_{att} obtained from simulations with different primaries and hadronic interaction models for a primary energy of $10^{17.7}$ eV compared to the average attenuation parametrization resulting from a CIC fit to AMIGA data over the intensity range $200 \leq n_{\text{cut}} \leq 700$.

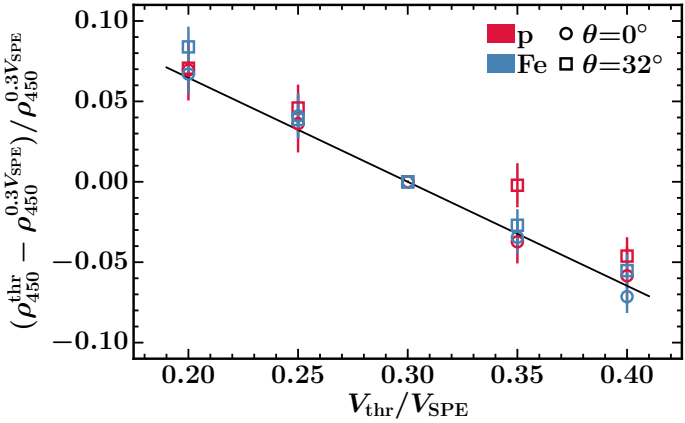

Figure 6.27: Relative difference of the reconstructed $\rho_{450}^{\mathrm{thr}}$ values to $\rho_{450}^{0.3V_{\mathrm{SPE}}}$ (obtained for the target threshold of $0.3V_{\mathrm{SPE}}$) as a function of the discriminator threshold. Markers show the mean relative difference, error bars denote the standard error of the mean. A fit to the data points (black solid line) yields a systematic uncertainty of 3.9% for a 2σ variation of the target threshold.

threshold voltages, the uncertainty of the area-dependent module efficiencies, and the lack of knowledge of the exact density of soil covering the individual modules. Further systematic uncertainties arise from the estimation of the muon density ρ_{450} at the optimal distance to the shower core as a consequence of the unknown true shape of the MLDF on a single event level. Beyond that, the correction of the zenith angle-dependent attenuation of the muon density introduces a small systematic uncertainty.

6.6.1 *Discriminator threshold*

A muon hitting a scintillator bar of an AMIGA module generates a pulse in the PMT at the center of the module. This analog pulse is converted to a binary signal time trace by the underground

electronics as discussed in Section 3.4. For each of the 64 scintillator bars (channels), the discriminator threshold voltage is set to 30% of the mean single photo-electron (SPE) amplitude V_{SPE} such that an SPE is represented by a single 1 or two 1s in the sampled binary trace. The calibration of the discriminator thresholds is done individually for all scintillator channels by an automated background-radiation calibration method in the field.

Measurements with the AMIGA engineering array have shown that the dispersion of the target values of the discriminator threshold is around 10% (see Section 3.4.2) of the mean target value of the discriminator threshold $\langle V_{\mathrm{Thr}} \rangle$ of all channels [8]. To assess the systematic uncertainty related to the setting of the discriminator threshold, we estimate the effect of a 2σ variation of $\langle V_{\mathrm{Thr}} \rangle$, corresponding to thresholds of $(1 \pm 0.02)\langle V_{\mathrm{Thr}} \rangle = (0.3 \pm 0.06) V_{\mathrm{SPE}}$ with simulations.

For this purpose, we use CORSIKA air shower simulations from the library of fixed energy described in Section 5.1.2 with QGSJETII-04 as high-energy hadronic interaction model and a fixed primary energy of 10^{18} eV. For shower zenith angles of $\theta = 0^{\circ}$ and 32°, 120 simulations are available for proton and iron primary particles each. Every simulated EAS is tossed 5 times on the SD-750 array and, subsequently, the detector responses are simulated with Offline for discriminator thresholds of 20%, 25%, 30%, 35% and 40% of V_{SPE}. For each shower, the same core positions are used for all threshold values.

We study the effect of the discriminator threshold on the reconstructed muon density ρ_{450} by fitting the MLDF for each shower and discriminator value. Hereby, we join the 5 shower tosses on the array to increase the number of AMIGA modules with signals and hence reduce sampling fluctuations that are independent of the discriminator threshold settings. The relative difference $\left(\rho_{450}^{\mathrm{thr}} - \rho_{450}^{0.3\mathrm{V_{SPE}}}\right) / \rho_{450}^{0.3\mathrm{V_{SPE}}}$ of the reconstructed $\rho_{450}^{\mathrm{thr}}$ values for the different threshold settings compared to the muon density $\rho_{450}^{0.3\mathrm{V_{SPE}}}$, which is obtained for the target threshold of 30% of the mean SPE amplitude, is calculated on an event-by-event level.

Fig. 6.27 shows the mean relative difference as a function of the discriminator threshold for the considered primaries and shower zenith angles; error bars display the standard error of the mean. For the 2σ variation of $(0.3 \pm 0.06)V_{\mathrm{SPE}}$, a systematic uncertainty of $\sigma_{\mathrm{sys,calib}}/\rho_{450} = 3.9\%$ is obtained by a linear fit to the data points.

6.6.2 *Module efficiency*

The muon counting efficiency of a single detector module is mainly influenced by the light attenuation in the wavelength-shifting (WLS) fibers of the scintillators, leading to under-counting, and the after-pulsing of the PMT, leading to over-counting of muons. Since these effects are not accounted for in the AMIGA detector simulation, their impact cannot be assessed for the spatial and temporal distribution of muons in extensive air showers and the chosen muon reconstruction strategy. However, the muon counting efficiency for single muons was measured in the laboratory and analyzed as a function of the applied window size in the reconstruction procedure (see Section 5.2.2) as shown in Fig. 6.28.

For a window of seven bins, which we use in the muon reconstruction procedure, efficiencies of $\epsilon^{5\mathrm{m}^2}_{\mathrm{win7}} = 104\%$ and $\epsilon^{10\mathrm{m}^2}_{\mathrm{win7}} = 95\%$ are found for the 5 and $10\,\mathrm{m}^2$ modules, respectively. The efficiency of the $5\,\mathrm{m}^2$ modules above 100% is a result of PMT after-pulsing. For the single muons studied in this analysis, the efficiencies approach 94% and 87%, respectively, for large window sizes. Since after-pulsing does not play a role here, these values correspond to the inefficiencies caused by the attenuation in the WLS fibers. Due to the double length of the WLS fibers, the efficiencies are smaller for the $10\,\mathrm{m}^2$ modules.

In air showers, large windows would of course lead to significant under-counting of muons due to simultaneous incident muons. Based on simulations, a window size of seven bins, showing a good balance between under-counting and over-counting effects, is hence chosen for the reconstruction of muons (see Sec-

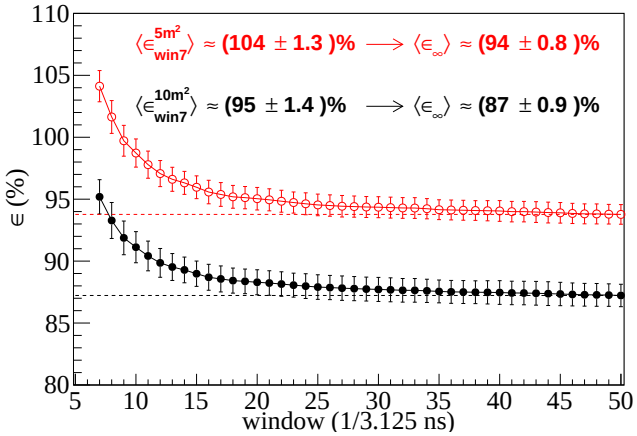

Figure 6.28: Laboratory measurement of the area-dependent module efficiency for 5 and 10 m^2 modules as a function of the applied window size in the reconstruction procedure. The efficiency for 10 m^2 modules is reduced w.r.t. the 5 m^2 modules as a consequence of the increased light attenuation in the wavelength-shiftings fibers. Values of ε above unity are a result of PMT after-pulsing. From [8].

tion 5.4). In our analysis of the data recorded by the AMIGA engineering array, we consequently correct the estimated muon density for each module by the area-dependent efficiency that was derived for a window size of seven bins according to

$$\rho_\mu^{\mathrm{corr}} = \frac{\rho_\mu}{\epsilon}. \tag{6.33}$$

We evaluate the resulting systematic uncertainty of the reconstructed muon density ρ_{450} at the optimal distance with AMIGA data, using the same data set as in Chapter 7. For this purpose, we reconstruct ρ_{450} for each event by a fit of the muon lateral distribution function both for the efficiencies derived for a window size of seven bins and for an infinitely large window ($\epsilon_{\mathrm{inf}}^{5\mathrm{m}^2} = 94\%$ and $\epsilon_{\mathrm{inf}}^{10\mathrm{m}^2} = 87\%$). Averaged over the considered energy range

from $10^{17.4}$ eV to $10^{18.3}$ eV, we find a systematic uncertainty of $\sigma_{\text{sys,eff}}/\rho_{450} = 9.9\%$.

6.6.3 *Soil density*

The AMIGA modules are buried at a vertical depth of 2.3 m in the soil to shield them from electromagnetic shower particles. Although most muons propagate unhampered through the soil layer, it constitutes an effective muon energy threshold of approximately 1 GeV for vertical muons. Position or time-dependent variations in the soil density could lead to variations in the attenuation of the muonic shower component measured by AMIGA. We therefore study the systematic uncertainty in the reconstructed muon density ρ_{450} due to soil density uncertainties with simulations.

The soil density in the area of the Pierre Auger Observatory has been measured at three different positions at latitude, longitude coordinates (451390,6116480), (449890,6113870), and (453640,6112570) in a geological study performed in 2007 [109]. At each position, soil samples were extracted at depths of 1 m, 2 m, and 3 m and the natural densities were evaluated as listed in Table 6.6. The mean soil density is $\rho_{\text{soil}} = 2.38\,\text{g/cm}^3$ with a standard deviation of $\sigma_{\rho_{\text{soil}}} = 0.05\,\text{g/cm}^3$. Individual measurements of the soil densities at the seven positions of the AMIGA unitary cell (UC) have not been performed.

Due to the lack of knowledge of the true soil density at each individual position, the mean soil density ρ is employed in the GEANT4 simulation of the propagation of particles through the 2.3 m soil layer within Offline. We estimate the systematic uncertainty of a density variation of $\pm 3\sigma_{\rho_{\text{soil}}}$ on the reconstructed muon density ρ_{450} with a set of 233 iron shower simulations from the continuous QGSJETII-04 simulation library (Section 5.1.3) with primary energies between $10^{17.5}$ eV and 10^{18} eV and zenith angles in the range $0^\circ \leq \theta \leq 45^\circ$. Each shower is tossed 20 times on the SD-750 array at 5 different core positions (4 tosses per posi-

	Soil density / g cm^{-3}		
Sample depth	Position 1	Position 2	Position 3
1 m	2.43	2.39	2.35
2 m	2.39	2.45	2.40
3 m	2.41	2.32	2.28

Table 6.6: Natural soil densities in the area of the Pierre Auger Observatory that have been determined in a geological study in 2007 at three different positions in the field and for three different soil depths.

tion). The propagation of particles through the soil and the detector response is simulated with $\overline{\text{Off}}\underline{\text{line}}$ for the mean soil density $\rho_{\text{soil}} = 2.38\,\text{g/cm}^3$ and the $\pm 3\sigma_{\rho_{\text{soil}}}$ deviations $\rho^{+}_{\text{soil}} = 2.53\,\text{g/cm}^3$ and $\rho^{-}_{\text{soil}} = 2.23\,\text{g/cm}^3$.

Since the employed CORSIKA simulation library has been produced with a thinning level of $\varepsilon = 10^{-6}$, particles arriving at the ground level have statistical weights w_i [77]. Before the simulation of the detector response in $\overline{\text{Off}}\underline{\text{line}}$, these weighted particles need to be resampled or "unthinned" Following Poissonian statistics, the number and the position of the resampled particles falling into the detection area is generated according to the particle weights and the ratio of sampling and detection area. This randomized particle regeneration procedure is implemented within the CachedXShowerRegenerator module in $\overline{\text{Off}}\underline{\text{line}}$. As particles are regenerated in batches and the random numbers used in the resampling procedure depend on previous actions as the propagation of particles through the soil, artificial fluctuations in the number of muons hitting a specific detector module are introduced in addition to the physical effects of the different soil densities. Consequently, despite the use of equal core positions in the $\overline{\text{Off}}\underline{\text{line}}$ simulations for all soil densities, muon numbers cannot be cannot be compared on an individual module by module level. Instead, we jointly use all tosses of one EAS to fit the

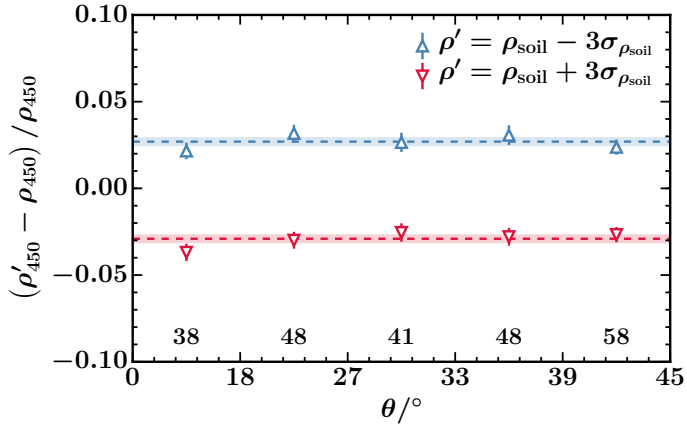

Figure 6.29: Relative difference of the reconstructed muon densities ρ'_{450} at the optimal core distance $r = 450\,\text{m}$ for soil densities $\rho_{\text{soil}} \pm 3\sigma_\rho$ compared to ρ_{450} obtained for the mean soil density ρ_{soil} in bins of shower zenith angle θ. Markers show the mean relative difference, error bars denote the standard error of the mean. Horizontal dashed lines visualize the relative difference averaged over all zenith angles, shaded bands the corresponding standard error of the mean. Numbers at the bottom state the number of events in each zenith bin.

MLDF of the event for each considered soil density to reduce simulation induced fluctuations that are independent of the effect of the attenuation in the soil. We fix the slope parameter β according to the parametrization of Eq. (6.34) as a function of the shower zenith angle θ.

The relative difference of the reconstructed muon densities at the optimal core distance $r = 450\,\text{m}$ for soil densities $\rho^{\pm}_{\text{soil}} = \rho_{\text{soil}} \pm 3\sigma_{\rho_{\text{soil}}}$ compared to ρ_{450} (obtained for the average soil density ρ_{soil}) is shown in Fig. 6.29 as a function of the shower zenith angle θ. Averaged over all considered zenith angles, the variation of the mean soil density ρ_{soil} leads to a variation of the recon-

structed muon density ρ_{450} at the optimal distance to the shower core of $\sigma_{\text{sys,soil}}/\rho_{450} = \mp 2.8\%$.

6.6.4 *MLDF parametrization*

In addition to the uncertainties resulting from the discriminator threshold and the soil density, the use of the MLDF parametrization of Eqs. (5.23) and (5.39) is a further source of systematic uncertainties. To reduce statistical uncertainties leading to a decreased composition sensitivity as discussed in Section 5.8, we fix β to the zenith angle-dependent parametrized values

$$\beta(\theta) = b_0 + b_1 \sec(\theta) \tag{6.34}$$

with parameters $b_0 = 4.4$ and $b_1 = -1.1$ instead of fitting the slope individually on an event-by-event level. However, a systematic uncertainty in the reconstructed muon density ρ_{450} at the optimal core distance arises from fluctuations of the true MLDF shape for individual events. We have estimated this uncertainty in the context of determining the optimal distance from the shower core to evaluate the newly proposed MLDF in Section 5.7. First, we have analyzed the systematic uncertainty in β by calculating the standard deviation $\sigma_\beta^{\text{sys}}/\beta = \sigma\left((\beta - \beta(\theta))/\beta(\theta)\right)$ of the relative difference of β to the parametrization $\beta(\theta)$ as a function of θ. To this end, we have used a set of simulated "high-quality" events with sufficient detector information to leave β as a free fit parameter. For primary energies $E \geq 10^{18}$ eV, we obtain a conservative estimate of the systematic uncertainty of $\sigma_\beta^{\text{sys}}/\beta \leq 15\%$.

In a second step, we have derived an estimation of the systematic uncertainty of ρ_{450} caused by the systematic uncertainty in β by fitting MLDFs with fixed slopes $\beta(\theta) \pm \sigma_\beta^{\text{sys}}(\theta)$ (with $\sigma_\beta^{\text{sys}}(\theta) = 0.15 \cdot \beta(\theta)$) to each event. We conservatively estimate

the systematic uncertainty in ρ_μ for a single event by the averaged muon density difference

$$\Delta\rho_{\mu,i}(r) = \sqrt{\left(\rho_\mu(r;1.15\beta_i) - \rho_\mu(r;\beta_i)\right)^2} + \overline{\left(\rho_\mu(r;0.85\beta_i) - \rho_\mu(r;\beta_i)\right)^2}. \tag{6.35}$$

The mean relative systematic uncertainties $\sigma_{\text{sys,MLDF}}/\rho_{450}$, shown in Fig. 5.33, vary between 7% ($\theta = 48^\circ$) and 10.4% ($\theta = 0^\circ$) of the muon density ρ_{450} at the optimal distance $r_{\text{opt}} = 450\,\text{m}$. Averaging over all angles $\theta \leq 48^\circ$ with weights $w = \sin(\theta)\cos(\theta)$, we account for the uniform distribution of showers in bins of $\sin^2\theta$ for data and obtain a mean relative systematic uncertainty of $\sigma_{\text{sys,MLDF}}/\rho_{450} = \pm 8.8\%$.

6.6.5 *Attenuation correction*

The joined systematic uncertainty

$$\sigma_{\text{sys}}\left(\rho_{450}\right) = \sqrt{\sigma^2_{\text{sys,soil}} + \sigma^2_{\text{sys,thr}} + \sigma^2_{\text{sys,MLDF}}} \tag{6.36}$$

of ρ_{450} due to the mutually independent systematic uncertainties of the soil density, calibration threshold, and the fit of the MLDF is obtained by adding the different uncertainties in quadrature. A further systematic uncertainty arises as a result of the attenuation correction

$$\rho_{35}\left(\theta\right) = {}^1/_{f_{\text{att}}(\theta;a,b)} \cdot \rho_{450} \tag{6.37}$$

discussed in Section 6.5. We calculate the systematic uncertainty of ρ_{35} as

$$\begin{aligned}\sigma_{\text{sys}}\left(\rho_{35}\left(\theta\right)\right) &= \sigma_{\text{sys}}\left({}^{\rho_{450}}/_{f_{\text{att}}(\theta;a,b)}\right) \\ &= {}^{\rho_{450}}/_{f^2_{\text{att}}(\theta)} \cdot \sqrt{{}^{\sigma^2_{\text{sys}}(\rho_{450})}/_{\rho^2_{450}} + {}^{\sigma^2_{\text{sys}}(f_{\text{att}}(\theta))}/_{f^2_{\text{att}}(\theta)}} \\ &= \rho_{35}\left(\theta\right) \cdot \sqrt{{}^{\sigma^2_{\text{sys}}(\rho_{450})}/_{\rho^2_{450}} + {}^{\sigma^2_{\text{sys}}(f_{\text{att}}(\theta))}/_{f^2_{\text{att}}(\theta)}}\end{aligned} \tag{6.38}$$

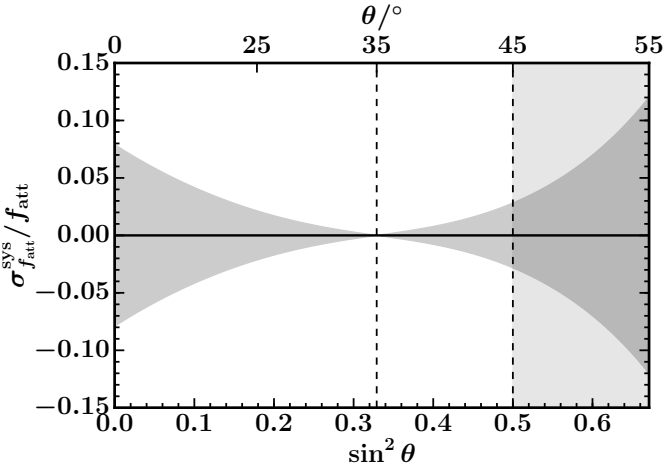

Figure 6.30: Relative systematic uncertainty of ρ_{35} as a function of $\sin^2\theta$ based on the statistical uncertainties of the CIC parameters.

by propagating the independent systematic uncertainties $\sigma_{\text{sys}}(\rho_{450})$ (defined in Eq. (6.36)) and $\sigma_{\text{sys}}(f_{\text{att}}(\theta))$ of the muon density and the attenuation correction.

The systematic uncertainty of the parametrization of f_{att} is caused by the statistical uncertainties of the parameters a and b in Eq. (6.15). The parameter correlations are taken into account by the use of their covariance in the calculation of the systematic uncertainty $\sigma_{\text{sys}}(f_{\text{att}}(\theta))$.

The contribution of the systematic uncertainty of the attenuation correction $\sigma_{\text{sys}}(f_{\text{att}}(\theta))/f_{\text{att}}(\theta)$ to the total systematic uncertainty of ρ_{35} is plotted as a function of θ in Fig. 6.30. It is largest for $\theta = 0°$ (8%), decreases to zero when approaching the reference angle $\theta_{\text{Ref}} = 35°$, and increases again for larger angles up to 3% for the largest considered zenith angle of $\theta = 45°$. The mean systematic uncertainty, averaged over all zenith angles $0° \leq \theta \leq 45°$ for a uniform distribution in $\sin^2\theta$, is $\sigma_{\text{sys},f_{\text{att}}}/f_{\text{att}} = 2.3\%$.

Uncertainty Source	Relative Sys. Unc.	Percentage
Efficiency corr.	$\sigma_{\text{sys,eff}}/\rho_{450}$	9.9%
Discr. thr. (2σ var.)	$\sigma_{\text{sys,thr}}/\rho_{450}$	3.9%
Soil density (3σ var.)	$\sigma_{\text{sys,soil}}/\rho_{450}$	2.8%
MLDF ($\sigma_\beta^{\text{sys}}/\beta$=15%)	$\sigma_{\text{sys,MLDF}}/\rho_{450}$	8.8%
CIC correction	$\sigma_{\text{sys},f_{\text{att}}}/f_{\text{att}}$	2.3%
Total	$\sigma_{\text{sys},\rho_{35}}/\rho_{35}$	**14.3**%

Table 6.7: Averaged systematic uncertainties due to the module area-dependent efficiency correction, the uncertainty in the calibration of the discrimination threshold, the exact soil density at the different counter positions, the lack of knowledge of the true MLDF shape for individual events, and the attenuation correction.

6.6.6 *Total systematic uncertainties*

The average contributions of the previously discussed main systematic uncertainties are summarized in Table 6.7. The systematic uncertainties of the muon density ρ_{450} resulting from the uncertainty of the calibration of the discrimination threshold, the soil density at the different counter positions, and the lack of knowledge of the true MLDF shape for individual events add up in quadrature according to Eq. (6.36). The total systematic uncertainty of the attenuation corrected muon density ρ_{35} is calculated by Eq. (6.38) with an additional term resulting from the systematic uncertainty of the attenuation correction function f_{att}. Averaging over the zenith angle range $0^\circ \leq \theta \leq 45^\circ$ which is considered in the analysis of AMIGA data, we obtain a mean relative systematic uncertainty of $\sigma_{\text{sys},\rho_{35}}/\rho_{35} = 14.3\%$.

In Chapter 7, we will analyze the energy dependence of the muon density ρ_{35}. In this context, we study the energy normalized densities ρ_{35}/E and determine the corresponding mean val-

ues as well as statistical and systematic uncertainties in bins of energy. Since the muon density ρ_{35} and energy E are correlated, we calculate the systematic uncertainty of their ratio by

$$\sigma_{\text{sys}}\left(\frac{\rho_{35}}{E}\right) = \frac{\rho_{35}}{E}\left\{\frac{\sigma^2_{\text{sys}}\left(\rho_{35}\right)}{\rho^2_{35}} + \frac{\sigma^2_{\text{sys}}\left(E\right)}{E^2} - 2\text{corr}\left(\rho_{35}, E\right)\frac{\sigma_{\text{sys}}\left(\rho_{35}\right)}{\rho_{35}}\frac{\sigma_{\text{sys}}\left(E\right)}{E}\right\}^{1/2} \tag{6.39}$$

which takes the correlation of ρ_{35} and E into account.

7

ANALYSIS OF THE MUON DENSITIES MEASURED BY AMIGA

In Chapter 6, we constructed a reliable AMIGA data set by selecting a time period of one year where bad periods for the muon detector were excluded with a newly developed rejection method. Furthermore, we corrected for the different efficiencies of the 5 and 10 m^2 detector modules and applied a correction for the attenuation of the muonic signal in the atmosphere and the soil layer above the scintillators in both data and simulations. Beyond that, the relevant systematic uncertainties for AMIGA were quantified.

In this chapter, we use the corrected data set for the analysis of the muon content of extensive air showers in the energy range from $10^{17.4}$ eV to $10^{18.3}$ eV. In Section 7.1, we fit the energy dependence of the mean muon densities measured by AMIGA. These results are compared with simulations in Section 7.2. We quantify the observed disagreement of the muon content between simulations and data in Section 7.3 by combining the AMIGA muon density measurements with measurements of the mean depth of shower maximum by the fluorescence detector. Additionally, we qualitatively analyze the evolution of the logarithmic mass based on the AMIGA muon measurements in Section 7.4. The obtained mean muon densities are compared with muon measurements of other experiments and previous Auger analyses in Section 7.5. A special focus is set on the comparison with the Auger analysis of horizontal air shower.

7.1 ENERGY DEPENDENCE OF THE MUON DENSITY

For the analysis of the muon densities we consider a sub-sample of events where the SD station with the largest signal lies within the hexagon of the engineering array to ensure that the shower is well sampled by the AMIGA muon detectors. For each event, we reconstruct the muon density ρ_{450} at the optimal distance of $r_{\text{opt}} = 450\,\text{m}$ by fitting the muon lateral distribution function (MLDF) with a fixed slope β according to the new parametrization described in Section 5.6. The minimum distance to the shower core to consider MD modules in the reconstruction is set to $r_{\text{min}} = 100\,\text{m}$ in order to avoid biases due to possible saturation effects close to the shower core where the MLDF is very steep. According to simulations, for larger distances and a window size of 7 bins, no saturation is observed (see Section 5.4). We select showers with zenith angles $0^\circ \leq \theta \leq 45^\circ$ and apply the CIC correction that was developed in Section 6.5 to each event to obtain the zenith corrected muon density estimator ρ_{35}.

7.1.1 *Fit of the energy evolution of ρ_{35}*

We analyze the energy evolution of the muon density within the energy range from $10^{17.4}\,\text{eV}$ to $10^{18.3}\,\text{eV}$. We restrict the analysis to energies below $10^{18.3}\,\text{eV}$ for two reasons. First, while the number of events detected with the MD becomes extremely sparse for higher energies, these events constitute a large lever arm that could bias the fit of the energy evolution. Second, measurements of the depth of maximum by the FD indicate a decrease of the mean logarithmic mass $\langle \ln A \rangle$ within the energy range between $10^{17.2}\,\text{eV}$ and $10^{18.33}\,\text{eV}$ [53]. For higher energies, a change of the elongation rate $\mathrm{d}X_{\text{max}}/\mathrm{d}\log_{10}(E)$ points towards a composition that becomes again heavier. Restricting the analysis to the energy range from $10^{17.4}\,\text{eV}$ to $10^{18.3}\,\text{eV}$, we avoid a distortion of the linear fit of the energy evolution which does not account for a break at the energy where the elongation rate changes.

We fit the evolution of the muon density with energy as a power law

$$\rho_{35}\left(E; a, b\right) = a\left(E/10^{18}\,\mathrm{eV}\right)^{b} \tag{7.1}$$

with a log-likelihood procedure based on the "simplified likelihood method" introduced by Dembinski et al. [110]. This method was developed for the energy calibration of the SD against the FD with hybrid events that were measured by both detectors. Here, the observations $(E_{\mathrm{FD}}, S_{\mathrm{SD}})$, are fitted to the calibration function

$$S\left(E\right) = A\left(E/10^{19}\,\mathrm{eV}\right)^{B}, \tag{7.2}$$

where E_{FD} is the energy estimate from the FD, and S_{SD} the shower size estimator from the SD (S_{38} and S_{35} for vertical showers for the SD-1500 and SD-750 array, respectively, and N_{19} for very inclined showers). The proposed likelihood method includes the uncertainties in both the SD signal and the FD energy estimate and, additionally, takes into account the threshold effect that is caused by the application of an energy cut to the data. We apply this maximum likelihood method to fit the energy evolution of the muon density measured by AMIGA of Eq. (7.1) by replacing $(E_{\mathrm{FD}}, S_{\mathrm{SD}})$ with pairs of $(E_{\mathrm{SD}}, \rho_{35})$ measurements.

The calibration of the SD with the FD includes a fit of the shower-to-shower fluctuations of the SD signal leading to deviations from the expected signal. Being at least an order of magnitude smaller than the SD fluctuations, shower-to-shower fluctuations in the FD are neglected. In contrast, the shower-to-shower fluctuations in E_{SD} and ρ_{35} are strongly correlated as a result of the SD signal consisting of the sum of the electromagnetic and muonic shower component. Consequently, we do not add an additional shower-to-shower fluctuation term for ρ_{35} but simplify the log-likelihood expression of Eq. (12) in Ref. [110] to

$$\ln(L; a, b) = \sum_{k} \ln\left(\sum_{i} e^{-\frac{1}{2}\frac{\left(E_k - E_i\right)^2}{\sigma^2_{E_i}}} e^{-\frac{1}{2}\frac{\left(\rho_{35}(E_k) - \rho_{35}(E_i; a, b)\right)^2}{\sigma^2_{\rho_{35_i}}}}\right), \tag{7.3}$$

where σ_{E_i} denotes the energy uncertainty of the ith event originating from the SD reconstruction. The statistical uncertainty $\sigma_{\rho_{35_i}}$ for a single event is calculated by bootstrapping [101, 102] the AMIGA module data, i.e. the set of radial distance - muon density pairs, 50 times. We then estimate $\sigma_{\text{stat}}(\rho_{35})$ by the standard deviation of the muon densities that are obtained from fits of the MLDF to the bootstrapped module samples.

The index k runs over events $E_{\text{cut}} \leq E \leq E_{\text{max}}$ above the energy cut value of $E_{\text{cut}} = 10^{17.5}$ eV where the SD-750 array becomes fully efficient; the index i runs over all events $E_{\text{min}} \leq E \leq E_{\text{max}}$ within the selected energy range between $10^{17.4}$ eV and $10^{18.3}$ eV. The impact of the choice of the minimum and maximum energies on the fit results is studied in more detail later. The second sum (index i) over events below the full efficiency E_{cut} of the SD-750 array accounts for the migration of events below the threshold value into the accepted energy range.

The statistical uncertainties of the fit parameters are obtained by bootstrapping the data sample 1000 times and calculating the covariance matrix of the bootstrapped data set. The inset plot shows the distribution of the normalized residuals $(\rho_{35} - \langle\rho_{35}\rangle)/\langle\rho_{35}\rangle$. Here, ρ_{35} denotes the reconstructed density for an event and $\langle\rho_{35}\rangle$ the corresponding fit solution at the specific event energy. In addition to the histogram of residuals (round markers), a Gaussian distribution with width $\sigma_{\text{mad}} = 0.30$ of the median absolute deviation (standard deviation $\sigma = 0.43$) is shown which matches well the distribution of the residuals.

We calculate the systematic parameter uncertainties by randomly varying each data point within the systematic uncertainties of the SD energy and the muon density assuming Gaussian uncertainty distributions with normalized widths of $\sigma_{\text{sys},E_{\text{SD}}}/E_{\text{SD}} = 0.14$ and $\sigma_{\text{sys},\rho_{35}}/\rho_{35} = 0.143$. Repeating this procedure 1000 times and fitting the energy dependence each time, we obtain the systematic uncertainties of a and b from the covariance matrix that is calculated from the set of fit results.

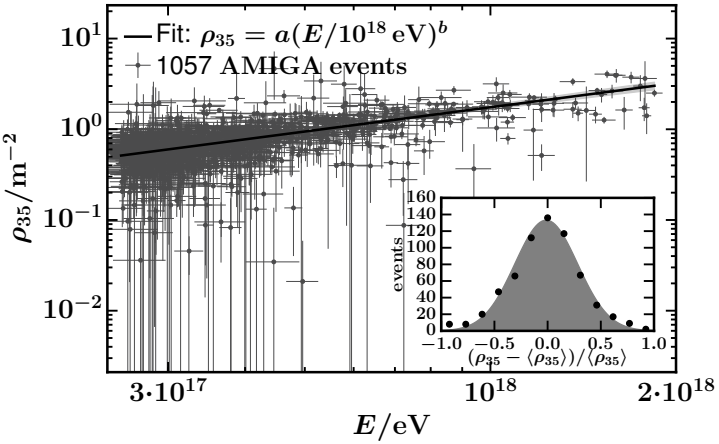

Figure 7.1: Fit of the energy dependence $\rho_{35}\,(E; a, b) = a(E/10^{18}\,\mathrm{eV})^b$ of the attenuation corrected muon density ρ_{35} for AMIGA data in the energy range from $E_{\mathrm{min}} = 10^{17.4}\,\mathrm{eV}$ to $E_{\mathrm{max}} = 10^{18.3}\,\mathrm{eV}$. Vertical and horizontal error bars for single events correspond to the statistical errors of the reconstructed muon densities and SD-reconstructed primary energies which are taken into account in the log-likelihood fit of Eq. (7.3). The added added statistical and systematic uncertainties of the fit are displayed by a grey shaded band. The inset plot shows the distribution of the normalized residuals $(\rho_{35} - \langle\rho_{35}\rangle)/\langle\rho_{35}\rangle$.

The fit of the energy dependence of the attenuation corrected muon density ρ_{35} is shown in Fig. 7.1. The vertical and horizontal error bars for individual events correspond to the statistical errors of the muon densities and SD-reconstructed primary energies which are taken into account in the log-likelihood fit of Eq. (7.3). The best fit solution with parameters

$$a = \rho_{35}(10^{18}\,\mathrm{eV}) = (1.749 \pm 0.048(\mathrm{stat}) \pm 0.048(\mathrm{sys}))\,\mathrm{m}^{-2} \quad \text{and}$$
$$b = \mathrm{d}\ln(\rho_{35}/\mathrm{m}^{-2})/\mathrm{d}\ln(E/\mathrm{eV}) = 0.889 \pm 0.037(\mathrm{stat}) \pm 0.038(\mathrm{sys}) \quad (7.4)$$

is displayed by a solid line with a grey shaded band corresponding to the added statistical and systematic uncertainties.

7.1.2 *Dependence of the fit results on energy and zenith cuts*

The dependence of the fit results on the applied cuts in energy and zenith angle is visualized in Fig. 7.2. We analyze four energy range combinations $[E_{\mathrm{min}}, E_{\mathrm{max}}]$ with $\log_{10}(E_{\mathrm{min}}) \in [17.4, 17.5]$ and $\log_{10}(E_{\mathrm{max}}) \in [18.3, 18.5]$, and three different maximum zenith angles $\theta_{\mathrm{max}} \in [30^\circ, 45^\circ, 55^\circ]$. The relative impact of the selection cuts is shown in Fig. 7.2b where the cut dependent fits of the muon density evolution are normalized by the reference densities ρ_{ref} obtained for the energy range $17.4 \leq \log_{10}(E) \leq 18.3$ and $\theta_{\mathrm{max}} = 45^\circ$. Within the considered energy range of $10^{17.4}$ eV to $10^{18.3}$ eV, the fit curves for different selection cuts in energy and zenith range lie for the most part (except for $\theta_{\mathrm{max}} = 55^\circ$ and the energy range $17.5 \leq \log_{10}(E) \leq 18.3$) within the statistical uncertainties of the reference function which is displayed by the magenta shaded area.

The impact of a variation of the maximum zenith angle θ_{max} and the energy range is demonstrated in Table 7.1 which lists the best fit values of the parameters a and b for a selection of the combinations of maximum zenith angles and energy ranges shown in Fig. 7.2. Shaded blocks highlight the variation of the considered energy for a fixed angle $\theta_{\mathrm{max}} = 45^\circ$, the variation of θ_{max} for a fixed energy range $17.4 \leq \log_{10}(E) \leq 18.3$, as well as the impact of not applying the CIC correction for the reference case of $\theta_{\mathrm{max}} = 45^\circ$ and $17.4 \leq \log_{10}(E) \leq 18.3$.

The impact of the energy range (first shaded block) that is used for fitting the evolution of the muon density with energy can be explained by the dependence of the attenuation of the muon density on the primary energy. As shown in Fig. 6.22 with simulations, the attenuation function $f_{\mathrm{att}}(\theta)$ takes larger values within the zenith angle range $0^\circ \leq \theta \leq 35^\circ$ for smaller energies than for higher ones. However, the mean CIC correction which is

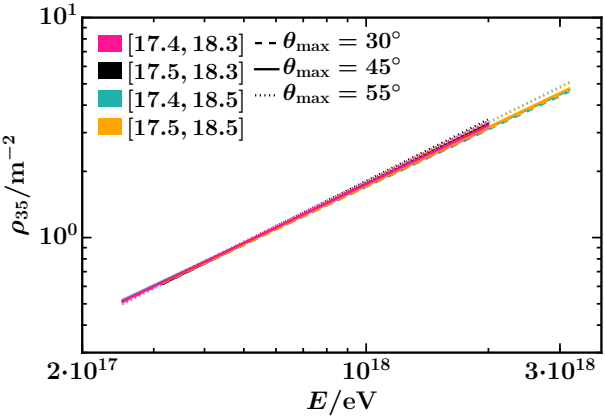

(a) Dependence of fit results on cuts

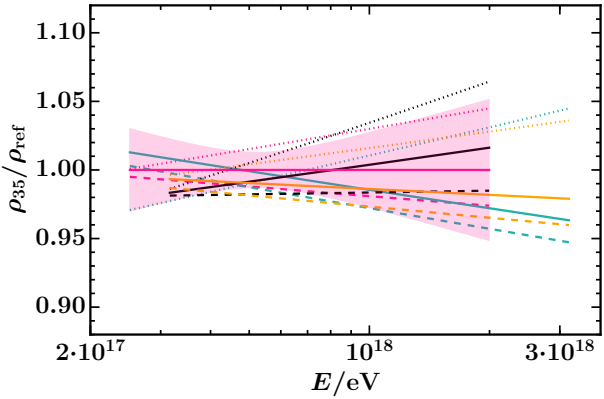

(b) Normalized by reference density

Figure 7.2: Dependence of the fit of $\rho_{35}(E) = a(E/10^{18}\,\mathrm{eV})^b$ on the applied selection cuts, i.e. the variation of the considered energy range $[\log_{10}(E_{\min}), \log_{10}(E_{\max})]$ (colors), and the zenith angle range $[0°, \theta_{\max}]$ (line style). (a) Fitted energy dependence for different selection cuts (b) The selection cut dependent fits are normalized by the reference fit obtained for the energy range $[17.4, 18.3]$ and $\theta_{\max} = 45°$.

Selection cuts				Fit parameters	
E_{min}	E_{max}	θ_{max}	CIC	a / m^{-2}	b
$10^{17.4}$ eV	$10^{18.5}$ eV	45°	✓	1.723 ± 0.047	0.869 ± 0.035
$10^{17.5}$ eV	$10^{18.3}$ eV	45°	✓	1.755 ± 0.048	0.907 ± 0.037
$10^{17.5}$ eV	$10^{18.5}$ eV	45°	✓	1.725 ± 0.044	0.882 ± 0.034
$10^{17.4}$ eV	$10^{18.3}$ eV	30°	✓	1.715 ± 0.052	0.888 ± 0.040
$10^{17.4}$ eV	$10^{18.3}$ eV	45°	✓	1.749 ± 0.048	0.889 ± 0.037
$10^{17.4}$ eV	$10^{18.3}$ eV	55°	✓	1.801 ± 0.053	0.910 ± 0.039
$10^{17.4}$ eV	$10^{18.3}$ eV	45°	✗	1.802 ± 0.052	0.893 ± 0.038

Table 7.1: Best fit parameters a and b with statistical uncertainties for Eq. (7.1), characterizing the dependence of ρ_{35} on the primary energy, for different selection cuts. Shaded blocks highlight the variation of the considered energy range $[\log_{10}(E_{\mathrm{min}}), \log_{10}(E_{\mathrm{max}})]$, the maximum zenith angle θ_{max}, and the application of the CIC correction.

applied to data is not energy-dependent. This leads to a small under-correction, i.e. over-estimation of ρ_{35}, for small energies and an over-correction, i.e. under-estimation of ρ_{35}, for higher energies. Consequently, both an extension of the energy range towards smaller energies and an extension towards higher maximum energies causes a flattening of the slope b. At the same time, the normalization a is slightly reduced. However, the effect leads only to a reduction of about 2% for b and 1% for the parameter a.

With increasing maximum zenith angle θ_{max} (second block), a small increase of the parameters a and b is observed. The steepening of the slope b for larger θ_{max} can be again explained as a consequence of the over- (under-) estimation of ρ_{35} for small (large) energies within the zenith angle range $0° \leq \theta \leq 35°$ due to the applied energy independent CIC correction. Since, in contrast, the energy-dependence of the attenuation is small for larger values

$\theta > 35°$, an extension of the considered angular range leads to a weakening of the effect and hence an increase of the slope b. The impact is, however, very small with variations of less than 3% in a and b compared to the reference case with $\theta_{\max} = 45°$. Equally, leaving out the CIC correction has only a weak influence on the fit results as can be seen from the best fit parameters a and b in the third block in Table 7.1.

In conclusion, the choice of the energy and zenith range as well as the application of the CIC correction do have some effect on the best fit solutions for the parameters a and b, describing the evolution of the muon density with energy. However, all results agree well within the statistical uncertainties of the fit for a maximum zenith angle $\theta_{\max} = 45°$ and the chosen energy range $17.4 \leq \log_{10}(E) \leq 18.3$ which will be considered in the following analyses.

7.2 COMPARISON WITH SIMULATIONS

We compare the fit results for AMIGA data with simulations for proton and iron primary particles. Two simulation libraries are available: the library of continuous energy, and the library of fixed energy described in Section 5.1. The library of continuous energy has a continuous distribution in primary energy and shower zenith angle and was simulated with the QGSJETII-04 hadronic high-energy interaction model. For primary energies between 10^{17} eV and 10^{19} eV, 1000 CORSIKA showers are available for each primary per decade, each being tossed 5 times on the array. In contrast to data, where the spectrum of CRs follows a steeply falling power law, the simulated distribution of showers is flat in E. This difference needs to be accounted for by a reweighting procedure as discussed in Section 5.1.5.

The library of fixed energy comprises simulations for proton and iron primaries for energies of $10^{17.5}$ eV, 10^{18} eV, $10^{18.5}$ eV, and 10^{19} eV, and seven fixed zenith angles from 0° to 56°. For both the QGSJETII-04 and the EPOS-LHC high-energy hadronic interac-

tion model, 120 CORSIKA showers are available for each primary and combination of energy, zenith angle, and interaction model. Tossing every shower 5 times on the detector array leads to a number of 4200 showers per energy, and 16800 showers in total per primary and model. In addition to the availability of both hadronic interaction models, the available number of showers is hence much larger for the fixed than for the continuous energy library.

We used the fixed simulation library to parametrize the energy-dependent attenuation of the muon density in Section 6.5.3. In this context, the evolution of the attenuation corrected muon density ρ_{35} with energy was fitted as $\rho_{35}\left(E;\vec{p}\right)/\mathrm{m}^{-2} = 10^{\left(\rho_0+\rho_1\cdot\left(\log_{10}(E/\mathrm{eV})-17.5\right)\right)}$ (Eq. (6.30)). This parametrization is not the same as the one of Eq. (7.1), but easy to translate to the parameters a and b by $a = 10^{(\rho_0+\rho_1/2)}$ and $b = \rho_1$. The resulting parameters with the corresponding 1σ uncertainties are given in Table 7.2 together with the fit results for the continuous QGSJETII-04 library which will be discussed in the following.

For the fixed library, the slopes b are almost independent of the hadronic interaction models with deviations $< 0.4\%$. With $b = 0.92$ for proton and $b = 0.91$ for iron, the slope difference between the two primary particles is at the order of 1%. In contrast to the slope, describing the evolution of the muon density with energy, the muon content depends on the hadronic high-energy interaction model. The muon densities for proton (iron) primaries of $a_\mathrm{p} = {}^{1.04}/_{\mathrm{m}^2}$ ($a_\mathrm{Fe} = {}^{1.62}/_{\mathrm{m}^2}$) for EPOS-LHC are by 4% (5%) larger than the densities of $a_\mathrm{p} = {}^{1.00}/_{\mathrm{m}^2}$ ($a_\mathrm{Fe} = {}^{1.54}/_{\mathrm{m}^2}$) for QGSJETII-04 at the reference energy of $10^{18}\,\mathrm{eV}$.

In addition to the derived parametrizations from the fixed energy libraries, we fit the energy dependence $\rho_{35}(E) = a\left({}^{E}/_{10^{18}\,\mathrm{eV}}\right)^b$ with the continuous QGSJETII-04 air shower library for proton and iron primary particles. For each simulated event, the reconstructed muon density ρ_{450} is corrected with the primary and energy-dependent attenuation correction function that was

Simulation			Fit parameters	
Primary	Model	Library	a/m^{-2}	b
p	EPOS-LHC	Fixed	1.040 ± 0.006	0.919 ± 0.004
	QGSJETII-04	Fixed	0.997 ± 0.005	0.919 ± 0.003
	QGSJETII-04	Continuous	1.037 ± 0.012	0.916 ± 0.020
Fe	EPOS-LHC	Fixed	1.616 ± 0.003	0.908 ± 0.001
	QGSJETII-04	Fixed	1.537 ± 0.003	0.911 ± 0.001
	QGSJETII-04	Continuous	1.548 ± 0.008	0.918 ± 0.010

Table 7.2: Best fit parameters a and b with 1σ uncertainties for Eq. (7.1) for proton and iron primaries, hadronic interaction models EPOS-LHC and QGSJETII-04, and both simulation libraries (fixed zenith angles and energies, continuous zenith and energy distributions).

parametrized with the fixed energy library (see Section 6.5.3) to obtain the corrected muon density ρ_{35}. The employed log-likelihood

$$\ln(L; a, b) = \sum_k \ln \left(\hat{w}_k e^{-\frac{1}{2} \frac{(\rho_{35}(E_k) - \rho_{35}(E_k; a, b))^2}{\sigma^2_{\rho_{35_k}}}} \right), \qquad (7.5)$$

differs from the one of Eq. (7.3) for data in two respects. Since we use Monte Carlo energies without energy uncertainties, we drop the sum with index i and the corresponding Gaussian accounting for possible energy threshold effects. Furthermore, we reweight each event with $\hat{w}_k = \hat{w}(E_k)$ with the weighting function of Eq. (5.2) to match the steeply falling energy spectrum in data.

The fit results for both proton and iron primaries and the employed data set are shown in Fig. 7.3. Approximately 5000 showers with zenith angles between 0° and 45° within the energy range $10^{17.4}\,\text{eV} \leq E \leq 10^{18.3}\,\text{eV}$ were used for each pri-

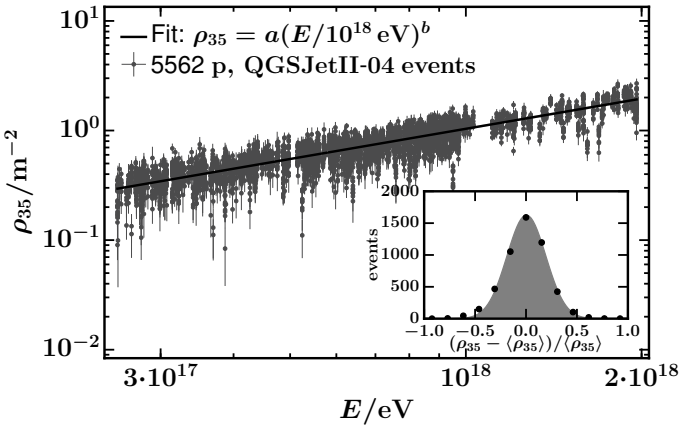

(a) Proton

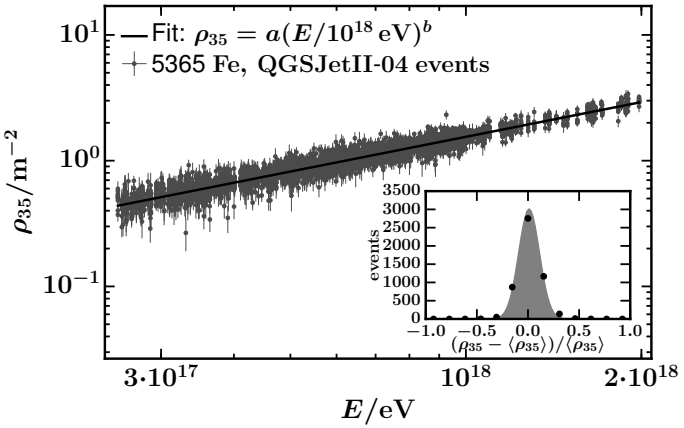

(b) Iron

Figure 7.3: Fit of the energy dependence $\rho_{35}(E) = a(E/10^{18}\,\mathrm{eV})^b$ for simulations of the continuous QGSJetII-04 air shower library for proton (a) and iron (b) primary particles. Since Monte Carlo energies are used, only statistical uncertainties of ρ_{35} (vertical error bars) are considered. Events are weighted according to their energy to match the steeply falling energy spectrum observed in data. The inset plots show the distributions of the normalized residuals $(\rho_{35} - \langle\rho_{35}\rangle)/\langle\rho_{35}\rangle$.

mary. Due to the larger shower-to-shower fluctuations, the spread of the muon densities for proton (median absolute deviation of $\sigma_{\text{mad}} = 0.19$, standard deviation $\sigma = 0.20$), is almost twice as large as the one observed for iron ($\sigma_{\text{mad}} = 0.10$, $\sigma = 0.11$).

The obtained parametrizations of the energy-dependence of ρ_{35} for the fixed and continuous simulation libraries are compared in Table 7.2. A very good agreement between fixed and continuous simulations of the QGSJETII-04 model is observed for iron both in slope ($b = 0.91$) and normalization ($a = 1.54/\text{m}^2$). For proton primaries, the same slope of $b = 0.92$ is obtained for the fixed and continuous library. However, the muon density at 10^{18} eV for the continuous library is 4% larger ($a = 1.04/\text{m}^2$) than for the fixed library ($1.00/\text{m}^2$). The different parametrizations are visualized in Fig. 7.4. To weaken the energy dependence, the mean muon densities are normalized by $E/10^{18}\,\text{eV}$.

The disagreement between the results for the fixed and continuous simulation library for proton showers, in contrast to the perfect agreement for iron showers, could be a result of the larger shower-to-shower fluctuations for proton showers. These affect both the quality of the attenuation parametrization for the library of fixed energy and the fit of the energy dependence for the continuous library. However, the accordance of the more precise iron fit solutions supports that it is well-motivated to employ the parametrizations obtained with the fixed simulation libraries which are based on a much larger data sample compared to the continuous library. Furthermore, in addition to QGSJETII-04, the EPOS-LHC hadronic high-energy interaction model is available for the comparison with data. In the following analyses, we will consequently only display the parametrizations of the fixed energy simulation libraries.

We compare the evolution of the muon content with energy for data with simulations in Fig. 7.5. To soften the strong energy dependence, we normalize the muon densities by the energy. The

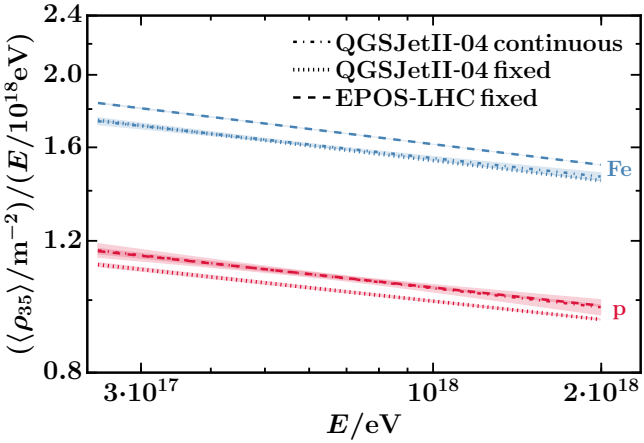

Figure 7.4: Energy-normalized muon densities $\langle\rho_{35}\rangle/(E/10^{18}\,\mathrm{eV})$ as a function of E for simulations for proton and iron primaries, hadronic high-energy interaction models EPOS-LHC and QGSJetII-04, and both considered simulation libraries (fixed zenith angles and energies, continuous zenith and energy distributions).

statistical and systematic uncertainties of the ratio $\langle\rho_{35}\rangle/E$ within bins of energy are calculated by

$$\sigma_{\mathrm{stat/sys}}\left(\frac{\rho_{35}}{E}\right) = \frac{\rho_{35}}{E}\left\{\frac{\sigma^2_{\mathrm{stat/sys}}\left(\rho_{35}\right)}{\rho^2_{35}} + \frac{\sigma^2_{\mathrm{stat/sys}}\left(E\right)}{E^2} - 2\mathrm{corr}\left(\rho_{35}, E\right)\frac{\sigma_{\mathrm{stat/sys}}\left(\rho_{35}\right)}{\rho_{35}}\frac{\sigma_{\mathrm{stat/sys}}\left(E\right)}{E}\right\}^{1/2}, \quad (7.6)$$

taking into account the correlation between ρ_{35} and E. The mean energy-normalized densities $\langle\rho_{35}\rangle/(E/10^{18}\,\mathrm{eV})$ for AMIGA in bins of energy are displayed by round markers, error bars denote the statistical uncertainties. The x-position of the markers corresponds to the mean energy of the events within each energy bin. The

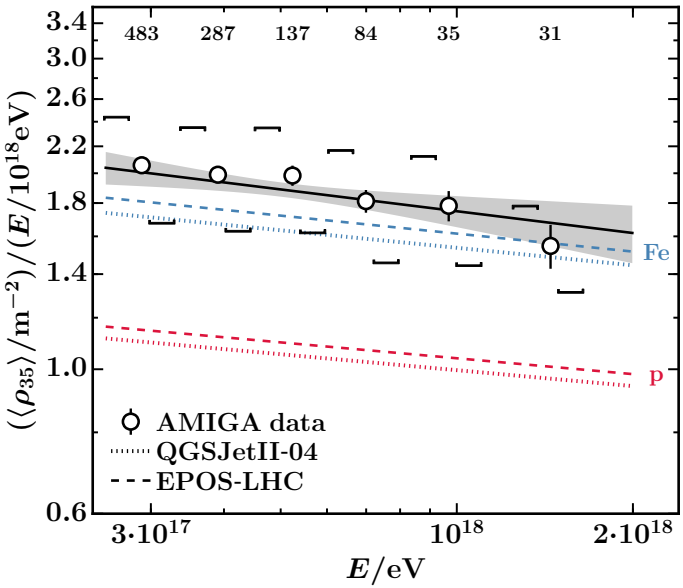

Figure 7.5: Energy-normalized muon densities $\langle\rho_{35}\rangle/(E/10^{18}\,\mathrm{eV})$ as a function of E for AMIGA data compared to expectations from simulations. Mean muon densities for AMIGA in bins of energy are displayed by round markers, error bars denote the statistical uncertainties. Systematic uncertainties are indicated by square brackets that are shifted horizontally due to the systematic uncertainty of the SD energy estimate of 14%. The number of AMIGA events in each energy bin is stated at the top of the figure. The normalized fitted energy dependence $\rho_{35}\,(E)\,/(E/10^{18}\,\mathrm{eV})$ is shown by a black solid line with a shaded band corresponding to the fit uncertainties. For comparison, results are shown for simulations with the EPOS-LHC (dashed) and QGSJetII-04 (dotted) high-energy hadronic interaction models for both proton (red) and iron (blue) primary particles.

Energy	$\langle X_{\mathrm{max}} \rangle / \mathrm{g\,cm^{-2}}$	$\langle \ln(\rho_{35}/\mathrm{m^{-2}}) \rangle$
$10^{17.5}$ eV	$685.2 \pm 1.6^{+8.7}_{-10.7}\,(\mathrm{sys})$	$-0.553 \pm 0.027 \pm 0.143\,(\mathrm{sys})$
10^{18} eV	$724.2 \pm 0.5^{+7.4}_{-10.3}\,(\mathrm{sys})$	$0.465 \pm 0.085 \pm 0.143\,(\mathrm{sys})$

Table 7.3: Mean depths of maximum $\langle X_{\mathrm{max}} \rangle$ measured by the FD [53] and mean logarithmic muon densities $\langle \ln \rho_{35} \rangle$ measured by AMIGA for primary energies of $10^{17.5}$ eV and 10^{18} eV.

systematic uncertainties are indicated by square brackets that are shifted horizontally due to the systematic uncertainty of the SD energy estimate of 14%. The number of AMIGA events in each energy bin is stated at the top of the figure. The normalized fitted energy dependence $\rho_{35}(E)/(E/10^{18}\,\mathrm{eV})$ is shown by a black solid line with a shaded band corresponding to the statistical fit uncertainties. For comparison, simulations results are displayed for the EPOS-LHC and QGSJETII-04 high-energy hadronic interaction models for both proton and iron primary particles.

The energy evolution for AMIGA data with a slope of $b = 0.889 \pm 0.037$ hints at a slight lightening of the composition in the considered energy range from $10^{17.4}$ eV to $10^{18.3}$ eV. With simulations, we find $b = 0.919$ for proton showers for both hadronic interaction models. For iron showers, we obtain $b = 0.908$ and $b = 0.911$ for the EPOS-LHC and QGSJETII-04 model, respectively. Although the logarithmic gain $b = \mathrm{d}\ln\rho_{35}/\mathrm{d}\ln E$ for data is about 2 to 3% smaller than for simulations with a pure composition, within the statistical uncertainties, the fit results agree, however, as well with a pure composition.

In contrast to the similar energy evolution, the observed muon densities in data are larger than for simulated iron showers by 8% for EPOS-LHC and by 14% for the QGSJETII-04 hadronic high-energy interaction model at the reference energy of 10^{18} eV. Although the observed muon densities could be shifted to the region between the proton and iron lines within systematic uncertainties,

the inferred composition would be very heavy. This is in contradiction to X_{max} measurements which predict a light composition in the considered energy range [53]. The observation of a disagreement between the muon content in simulations and data, indicating a "muon deficit" in simulations, was previously made by other muon experiments and Auger analyses as will be discussed in Section 7.5.

7.3 QUANTIFICATION OF THE DISAGREEMENT OF THE MUON CONTENT IN SIMULATIONS AND DATA

We quantify the disagreement between the measured muon densities and model predictions with the help of Auger FD measurements of the mean depth of maximum that were published recently [53]. The previous measurements of the X_{max} distributions [66] were extended by the use of five years of calibrated HEAT data from $10^{17.8}$ eV down to $10^{17.2}$ eV. Since we dispose of simulation libraries for fixed energies of $10^{17.5}$ eV and 10^{18} eV (see Section 5.1.2), we choose these primary energies to compare the muon content of extensive air showers for AMIGA data and simulations.

In Ref. [53], the mean depths of maximum measured by the FD are given in steps of 0.05 in logarithmic energy. We calculate the mean $\langle X_{\mathrm{max}} \rangle$ values for the considered logarithmic energies by averaging the neighboring data points at $\log_{10}(E/\mathrm{eV}) \pm 0.05$. The corresponding mean logarithmic muon densities $\langle \ln \rho_{35} \rangle$ for AMIGA are obtained from averaging the data points within the same energy bins. The measured values and their statistical and systematic uncertainties are given in Table 7.3.

For a comparison of the muon content in data with model predictions, the measured mean depths of maximum need to be related to the mean logarithmic mass $\langle \ln A \rangle$ and the associated logarithmic muon density $\langle \ln \rho_{35} \rangle_A$ in simulations. Both $\langle X_{\mathrm{max}} \rangle_A$ and the logarithmic muon content $\langle \ln N_\mu \rangle_A$, where N_μ is the to-

tal number of muons in an EAS, can be expressed in terms of the mean logarithmic mass $\langle \ln A \rangle$ by

$$\langle X_{\max} \rangle_A = \langle X_{\max} \rangle_{\mathrm{p}} + f_E \langle \ln A \rangle \quad \text{and} \tag{7.7}$$

$$\langle \ln N_\mu \rangle_A = \langle \ln N_\mu \rangle_{\mathrm{p}} + (1 - \beta) \langle \ln A \rangle. \tag{7.8}$$

Due to $N_\mu \propto \rho_{35}$, the total muon number N_μ can be replaced by ρ_{35} [111] yielding

$$\langle \ln \rho_{35} \rangle_A = \langle \ln \rho_{35} \rangle_{\mathrm{p}} + (1 - \beta) \langle \ln A \rangle. \tag{7.9}$$

Employing the relations

$$f_E = \frac{\langle X_{\max} \rangle_{\mathrm{Fe}} - \langle X_{\max} \rangle_{\mathrm{p}}}{\ln 56} \quad \text{and} \tag{7.10}$$

$$\beta = 1 - \frac{\langle \ln \rho_{35} \rangle_{\mathrm{Fe}} - \langle \ln \rho_{35} \rangle_{\mathrm{p}}}{\ln 56}, \tag{7.11}$$

the mean depth of shower maximum $\langle X_{\max} \rangle_A$ and the mean logarithmic muon density $\langle \ln \rho_{35} \rangle_A$ can be calculated for each $\langle \ln A \rangle$ value based on the simulation results for proton and iron showers for a specific hadronic interaction model. The mean depths of maximum $\langle X_{\max} \rangle_{\mathrm{p/Fe}}$ for proton and iron primaries, respectively, are obtained from averaging the CORSIKA Monte Carlo values of all available simulations for the considered hadronic interaction model and primary energy.

Since simulations with a fixed shower zenith angle of $\theta = 35°$ are not available, the mean logarithmic muon densities $\langle \ln \rho_{35} \rangle$ are calculated by means of the fitted energy evolution of $\langle \rho_{35} \rangle$ from Eq. (6.30) that was obtained in the context of the attenuation correction in Section 6.5.3 for proton and iron primaries and both hadronic interaction models. However, since a priori $\langle \ln \rho_{35} \rangle \neq \ln \langle \rho_{35} \rangle$, we do not just take the logarithm of the fitted $\langle \rho_{35} \rangle$ values. Instead, we generate samples of ρ_{35} values by randomly drawing 100.000 times from Gaussian distributions with mean values $\langle \rho_{35} \rangle$ and standard deviations $\sigma(\rho_{35})$ and then compute the average of the logarithmized muon density values.

Primary	Model	$\langle\rho_{35}\rangle/\mathrm{m}^{-2}$	$\sigma^{\mathrm{rel}}_{\rho_{35}}$	$\langle\ln(\rho_{35}/\mathrm{m}^{-2})\rangle$	$\langle X_{\mathrm{max}}\rangle/\mathrm{g\,cm}^{-2}$
$E = 10^{17.5}$ eV					
p	EPOS-LHC	0.361	0.24	-1.053	722.5 ± 1.0
	QGSJETII-04	0.346	0.24	-1.093	714.3 ± 1.1
Fe	EPOS-LHC	0.568	0.15	-0.577	622.9 ± 0.4
	QGSJETII-04	0.539	0.15	-0.630	612.3 ± 0.4
$E = 10^{18}$ eV					
p	EPOS-LHC	1.040	0.20	0.017	751.4 ± 0.9
	QGSJETII-04	0.997	0.19	-0.022	737.3 ± 1.0
Fe	EPOS-LHC	1.616	0.09	0.475	652.1 ± 0.3
	QGSJETII-04	1.537	0.09	0.425	643.6 ± 0.4

Table 7.4: Mean muon densities $\langle\rho_{35}\rangle$, relative standard deviations $\sigma^{\mathrm{rel}}_{\rho_{35}} = \sigma(\rho_{35})/\langle\rho_{35}\rangle$ and the resulting mean logarithmic muon densities $\langle\ln\rho_{35}\rangle$ together with the mean depths of maximum $\langle X_{\mathrm{max}}\rangle$ (uncertainties denote the standard error of the mean) for proton and iron simulations with primary energies of $10^{17.5}$ eV and 10^{18} eV for the EPOS-LHC and QGSJETII-04 hadronic interaction models.

Both the means $\langle\rho_{35}\rangle$ and the standard deviations $\sigma(\rho_{35})$ depend on the type of the primary particle, the energy, and, to a smaller extent, on the hadronic interaction model. We calculate the relative standard deviations $\sigma(\rho_{35})/\langle\rho_{35}\rangle$ in the following way: For a specific primary and hadronic interaction model, the mean attenuation corrected muon density $\langle\rho_{35}\rangle_\theta$ and standard deviation $\sigma(\rho_{35})_\theta$ is calculated for each of the sets of showers for the seven different fixed zenith angles θ between $0°$ and $56°$. Subsequently, the normalized standard deviations $\sigma(\rho_{35})_\theta/\langle\rho_{35}\rangle_\theta$ are averaged over all angles θ with weights $w = \sin\theta\cos\theta$ in order to account for the uniform distribution of showers in bins of $\sin^2\theta$ for data. The mean relative standard deviations $\sigma^{\mathrm{rel}}_{\rho_{35}} = \sigma(\rho_{35})/\langle\rho_{35}\rangle$, are then used together with the mean values $\langle\rho_{35}\rangle$ from the at-

Energy	Model	f_E	β
$10^{17.5}$ eV	EPOS-LHC	-24.76	0.881
	QGSJETII-04	-25.35	0.885
10^{18} eV	EPOS-LHC	-24.67	0.886
	QGSJETII-04	-23.26	0.889

Table 7.5: Parameters f_E and β of Eqs. (7.7) and (7.9) which describe the linear dependence of the mean depth of maximum $\langle X_{\mathrm{max}} \rangle_A$ and the mean logarithmic muon density $\langle \ln \rho_{35} \rangle_A$ on the mean logarithmic mass $\langle \ln A \rangle$ for simulations.

tenuation fit to construct the Gaussian distributions for the calculation of the mean logarithmic muon densities $\langle \ln \rho_{35} \rangle$ for each primary, hadronic interaction model, and energy. The obtained mean muon densities $\langle \rho_{35} \rangle$, the corresponding relative standard deviations $\sigma^{\mathrm{rel}}_{\rho_{35}}$, as well as the resulting mean logarithmic muon densities $\langle \ln \rho_{35} \rangle$ are given in Table 7.4 together with the mean $\langle X_{\mathrm{max}} \rangle$ values for proton and iron simulations and primary energies of $10^{17.5}$ eV and 10^{18} eV.

The resulting values of the parameters f_E and β, which describe the linear dependence of the mean depth of maximum $\langle X_{\mathrm{max}} \rangle_A$ and the mean logarithmic muon density $\langle \ln \rho_{35} \rangle_A$ on the mean logarithmic mass $\langle \ln A \rangle$ according to Eqs. (7.7) and (7.9), are given in Table 7.5. Both parameters vary only slightly for the different energies and hadronic interaction models.

The derived linear relations between $\langle X_{\mathrm{max}} \rangle_A$ and $\langle \ln \rho_{35} \rangle_A$ for simulations are displayed in Fig. 7.6 for primary energies of $10^{17.5}$ eV and 10^{18} eV. The comparison with the mean depths of maximum $\langle X_{\mathrm{max}} \rangle$ and mean logarithmic muon densities $\langle \ln \rho_{35} \rangle$ measured by the FD and AMIGA shows the disagreement between model predictions and data.

The discrepancy of the muon content in data and simulations is quantified in Table 7.6. The mean logarithmic masses $\langle \ln A \rangle$

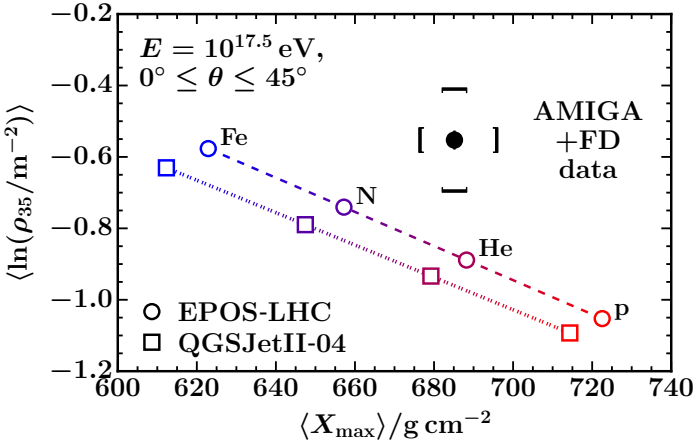

(a) $E = 10^{17.5}$ eV

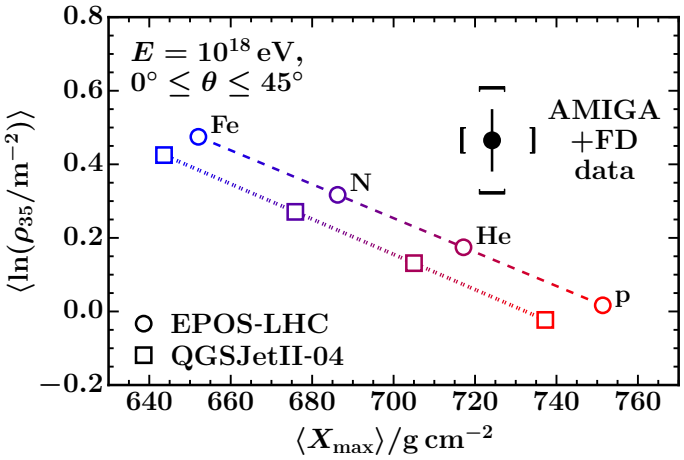

(b) $E = 10^{18}$ eV

Figure 7.6: Average logarithmic muon density $\langle \ln \rho_{35} \rangle$ as a function of the average shower depth $\langle X_{\mathrm{max}} \rangle$ for simulations with primary energies of $10^{17.5}$ eV (a) and 10^{18} eV (b) compared to Auger measurements with the FD ($\langle X_{\mathrm{max}} \rangle$) and AMIGA ($\langle \ln \rho_{35} \rangle$).

Energy	Model	$\langle \ln A \rangle$	$\langle \ln(\rho_{35}/\mathrm{m}^{-2}) \rangle$	f_μ
$10^{17.5}$ eV	EPOS-LHC	1.51	−0.874	$1.38 \pm 0.04 \pm {}^{0.21}_{0.18}(\mathrm{sys})$
	QGSJETII-04	1.15	−0.961	$1.50 \pm 0.04 \pm {}^{0.23}_{0.20}(\mathrm{sys})$
10^{18} eV	EPOS-LHC	1.10	0.142	$1.38 \pm 0.12 \pm {}^{0.21}_{0.18}(\mathrm{sys})$
	QGSJETII-04	0.56	0.040	$1.53 \pm 0.13 \pm {}^{0.23}_{0.20}(\mathrm{sys})$

Table 7.6: Quantification of the disagreement of the muon content between data and simulations. The mean logarithmic masses $\langle \ln A \rangle$ are calculated for simulations with Eq. (7.7) for the measured $\langle X_{\mathrm{max}} \rangle$ values at primary energies of $10^{17.5}$ eV and 10^{18} eV. The corresponding mean logarithmic muon densities $\langle \ln \rho_{35} \rangle$ are obtained with Eq. (7.9). The disagreement between the muon content in data and simulations is quantified by the factor $f_\mu = \exp\left(\langle \ln \rho_{35} \rangle_{\mathrm{AMIGA}} - \langle \ln \rho_{35} \rangle_{\mathrm{sim}}\right)$.

that are associated with the measured $\langle X_{\mathrm{max}} \rangle$ values depend on the hadronic interaction model and are calculated with Eq. (7.7) using the previously determined values of f_E (Table 7.5) and $\langle X_{\mathrm{max}} \rangle_{\mathrm{p}}$ (Table 7.4). They are used together with the parameter β to determine the corresponding mean logarithmic muon densities $\langle \ln \rho_{35} \rangle$ for simulations with Eq. (7.9).

We compute the disagreement between the muon content in data and simulations by the factor

$$f_\mu = \exp\left(\langle \ln \rho_{35} \rangle_{\mathrm{AMIGA}} - \langle \ln \rho_{35} \rangle_{\mathrm{sim}}\right) \tag{7.12}$$

which measures the muon surplus in data w.r.t. model predictions. We obtain that the muon content in simulations would need to be increased by 38% for the EPOS-LHC hadronic interaction model and by 50% − 53%, depending on the considered energy, for the QGSJETII-04 model.

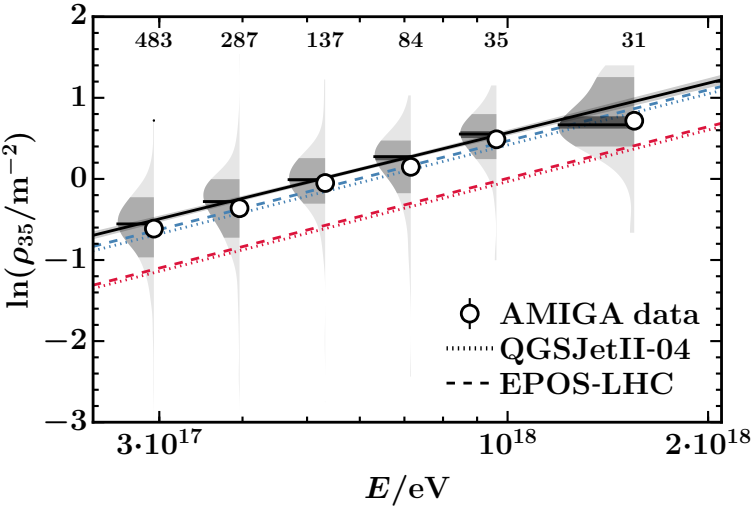

Figure 7.7: Logarithmic muon densities $\ln(\rho_{35}/\mathrm{m}^{-2})$ as a function of E for AMIGA data compared to expectations from simulations. Mean logarithmic muon densities for AMIGA in bins of energy are displayed by round markers, error bars denote the statistical uncertainties. Additionally, shaded violins visualize the event distributions in each bin. The fitted energy dependence is shown by a black solid line with a shaded band corresponding to the fit uncertainties. For comparison, results are shown for simulations with the EPOS-LHC (dashed) and QGSJetII-04 (dotted) high-energy hadronic interaction models for both proton (red) and iron (blue) primary particles.

7.4 MEAN LOGARITHMIC MASS

In addition to the quantification of the disagreement of the muon content in data and simulations, we study the evolution of the mean logarithmic mass according to AMIGA muon measurements in the energy range between $10^{17.4}$ eV and $10^{18.3}$ eV.

The mean logarithmic mass $\langle \ln A \rangle$ is related to the logarithmic muon content $\langle \ln N_\mu \rangle_A$ of an extensive air shower by Eq. (7.9). Since the total muon number N_μ is proportional to ρ_{35} [111], we can estimate $\langle \ln A \rangle$ by

$$\langle \ln A \rangle = \frac{\langle \ln \rho_{35} \rangle_A - \langle \ln \rho_{35} \rangle_\mathrm{p}}{1 - \beta} \tag{7.13}$$

with

$$\beta = 1 - \frac{\langle \ln \rho_{35} \rangle_\mathrm{Fe} - \langle \ln \rho_{35} \rangle_\mathrm{p}}{\ln 56}. \tag{7.14}$$

We derive the mean logarithmic muon contents $\langle \ln \rho_{35} \rangle_{\mathrm{p/Fe}}$ for proton and iron primaries from simulations by means of the fitted energy evolution of $\langle \rho_{35} \rangle$ as explained in Section 7.3 (see Table 7.4 for primary energies of $10^{17.5}$ eV and 10^{18} eV).

The logarithmic muon densities $\ln(\rho_{35}/\mathrm{m}^{-2})$ are shown in Fig. 7.7 as a function of E for AMIGA data compared to expectations from simulations. The fitted energy dependences for both data and simulations deviate only on the per cent level from the previously determined power law parametrizations of $\rho_{35}(E) = a(E/10^{18}\,\mathrm{eV})^b$ in Tables 7.1 and 7.2. The mean values for AMIGA in bins of energy are displayed by round markers, while the event distribution in each bin is visualized by shaded violins.

Since the measured muon densities are higher than those for iron simulations, Eq. (7.13) would yield large values of the mean logarithmic mass $\langle \ln A \rangle$ in contradiction to results from X_max measurements [53]. For this reason, we shift the calculated mean logarithmic masses from AMIGA data by constant offsets of $\Delta \ln A$, depending on the hadronic interaction model (EPOS-LHC: 2.88,

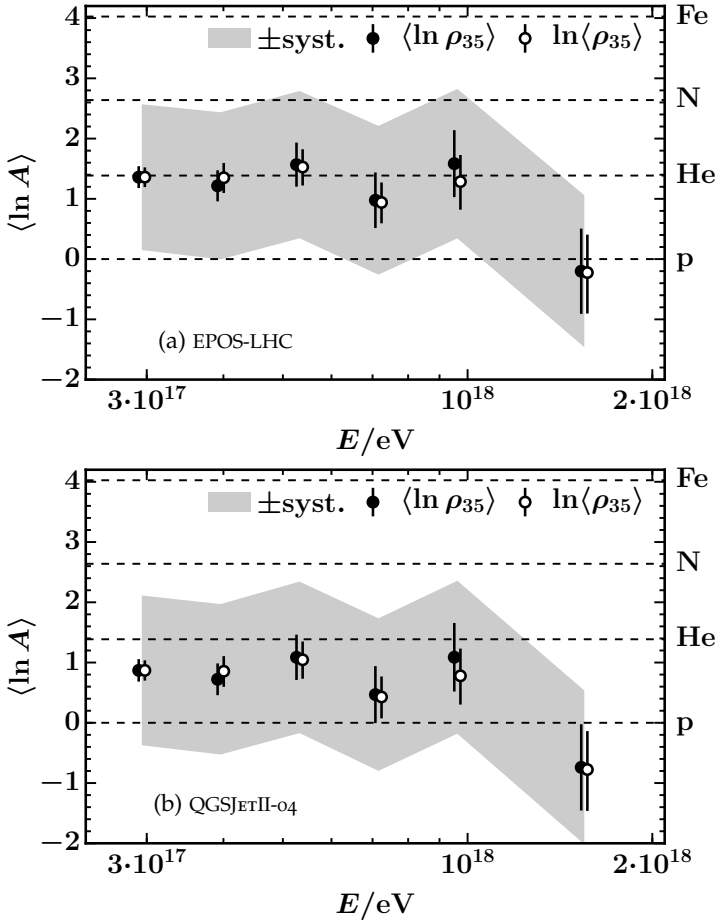

Figure 7.8: Evolution of the mean logarithmic mass $\langle \ln A \rangle$ obtained from AMIGA measurements for the (a) EPOS-LHC and (b) QGSJETII-04 hadronic interaction model. The $\langle \ln A \rangle$ values are shifted by constant offsets to match the results of the $X_{\max}$ analysis in the first bin. Markers show the $\langle \ln A \rangle$ values with statistical uncertainties in bins of energy using the mean logarithmic muon densities $\langle \ln \rho_{35} \rangle$ and, for comparison, using $\ln \langle \rho_{35} \rangle$ instead. Systematic uncertainties are indicated by shaded bands.

QGSJETII-04: 3.87), to match the X_{max} results for the first considered energy bin of $17.45 \leq \log_{10}(E) \leq 17.55$.

The resulting shifted mean logarithmic masses are shown in Fig. 7.8. The statistical errors correspond to the standard error of the mean, systematic uncertainties are indicated by a shaded band. For comparison, the calculations were repeated replacing $\langle \ln \rho_{35} \rangle$ by $\ln \langle \rho_{35} \rangle$. The small differences between both approaches show that there are no strong outliers within the considered energy bins.

The evolution of the mean logarithmic mass in the energy range from $10^{17.4}$ eV to $10^{18.3}$ eV is in agreement with the result of the X_{max} analysis [53] that the mass composition becomes lighter up to an energy of $10^{18.33}$ eV. However, the statistical and systematic uncertainties of the mean logarithmic mass do not yet allow for strong statements on the evolution of the mass composition based on the muon measurements of the AMIGA engineering array.

7.5 COMPARISON WITH OTHER MUON MEASUREMENTS

Comparing the muon densities obtained with the engineering array of AMIGA to simulations in Section 7.3, we found that the muon content in simulations would need to be increased between 38% (EPOS-LHC) and 53% (QGSJETII-04) to match the observations. Similar results of a "muon excess" in data were obtained by other experiments as Yakutsk [112] and HiRes/MIA [113] as well as previous Auger analyses [111, 114, 115]. Recently, both a joint analysis by the SUGAR experiment and Auger [116] and a study of the TA collaboration [117] qualitatively confirmed these findings. In contrast, muon measurements of the EAS-MSU experiment [118] and IceTop [119] agree well with expectations from air shower simulations. Due to the differences of the experiments w.r.t. the primary energy regime, the atmospheric overburden, the detection thresholds of muons as well as the considered shower zenith angles and

distances to the shower core, a comparison and interpretation of these results is however difficult.

Here, we compare the muon densities measured by AMIGA with results of two analyses that were obtained under conditions that are in certain respects similar to the ones for AMIGA. Starting in 1981, direct muon density measurements were carried out at the Akeno experiment in Japan with air shower arrays of different sizes of $1\,\mathrm{km}^2$ (A1), $20\,\mathrm{km}^2$ (A20), and $100\,\mathrm{km}^2$ (A100/Akeno Giant Air Shower Array (AGASA)) in the energy range between $10^{16.5}\,\mathrm{eV}$ and $10^{19.5}\,\mathrm{eV}$ [120]. The muon density of $\rho_\mu(600\,\mathrm{m}) \approx 0.25\,\mathrm{m}^{-2}$ that was measured by AGASA at $3 \cdot 10^{17}\,\mathrm{eV}$ is, despite different atmospheric depths and detection thresholds of muons, consistent with the results of $\rho_\mu(600\,\mathrm{m}) = 0.24 \pm 0.02\,\mathrm{m}^{-2}$ of the HiRes/MIA experiment which reported a muon excess in data w.r.t. simulations [113]. The A1 array at Akeno consisted of scintillation counters on the surface and shielded muon detectors with an identical detection threshold of 1 GeV as AMIGA. With covered energies between $10^{16.5}\,\mathrm{eV}$ and $10^{18.5}\,\mathrm{eV}$ for A1 and $10^{17.4}\,\mathrm{eV}$ to $10^{18.3}\,\mathrm{eV}$ in our analysis of AMIGA data, both the primary energy ranges and the threshold energy of muons agree well and enable a direct comparison of the results of both experiments. Nevertheless, a few differences as the larger atmospheric overburden at Akeno, located at 900 m in comparison to 1450 m above sea level, and, more importantly, the different primary energy reconstructions need to be considered in the interpretation of the results.

In addition to the comparison with the muon densities that were directly measured by Akeno, we focus on a more recent analysis of horizontal air shower (HAS) that were detected by the surface detector of the Pierre Auger Observatory [111]. Since AMIGA is part of the same experiment, both the atmospheric depth and the energy estimation procedure are identical as in this study. However, the HAS analysis uses an indirect method to calculate the relative muon content of a shower by comparing the measured SD signals with a modeled reference muon density profile at ground. Furthermore, the water-Cherenkov detectors have

a lower detection threshold of muons of 300 MeV and the considered zenith angle range from 62° to 80° is distinct from the one that is considered in the analysis of AMIGA data with $\theta \leq 45°$.

7.5.1 *Muons ≥ 1 GeV observed at Akeno*

The A1 1 km^2 array at Akeno was composed of 156 scintillation counters with an area of 1 m^2 each and a mutual spacing of 120 m on the surface [120]. Additionally, eight muon detectors with a total detection area of 25 m^2 each, were installed. The muon detectors, built of 50 rectangular proportional counters each, were shielded by 2 m of concrete, causing a threshold energy of muons of 1 GeV.

The core positions and arrival directions of the detected showers were determined by the surface detectors. The primary energies were estimated with the measured total number of electrons N_e by

$$E = 3.9 \times 10^{15} \left(\frac{N_e}{10^6} \right)^{0.9} \text{ eV}. \tag{7.15}$$

The muon density ρ_μ for each muon detector was calculated by two different methods. The "on-off density" was estimated from the number of impacted counters, assuming that the number of particles hitting each counter follows a Poissonian distribution. In addition, the "analogue density" was calculated from the sum of the energy losses in all counters divided by the average energy loss of a vertically traversing muon.

We compare the muon densities measured by AMIGA with a study of the lateral distribution of muons for core distances ≤ 800 m for extensive air showers with primary energies between $10^{16.5}$ eV and $10^{18.5}$ eV and zenith angles $\theta \leq 24.62°$ that were detected with the A1 array (Section 3.1 of Ref. [120]). Instead of fitting individual MLDFs on an event-by-event level, the measured muon densities of all events are combined to determine the average lateral distributions within bins of the total number

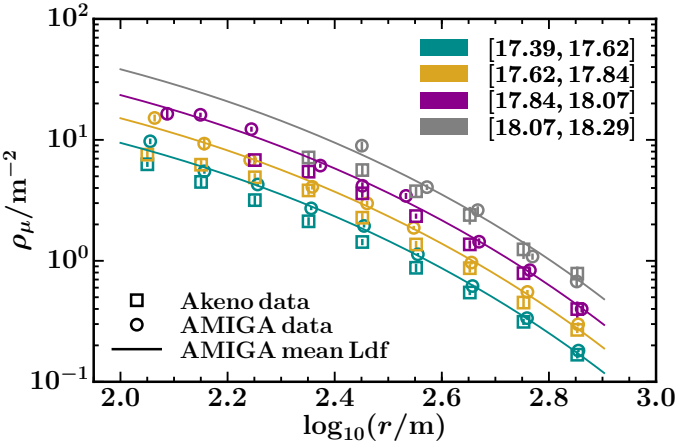

(a) Comparison of Akeno and AMIGA muon densities

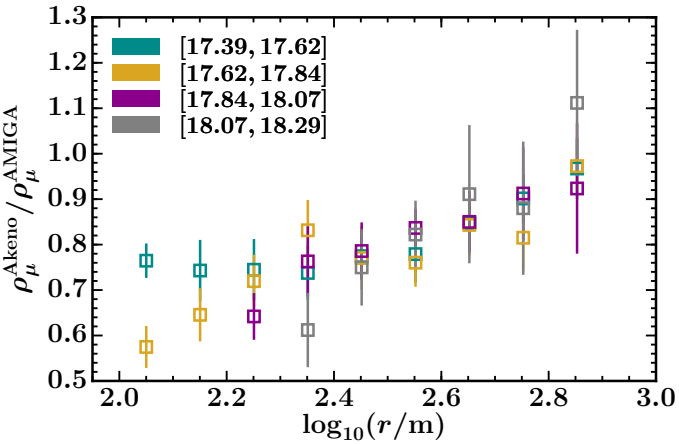

(b) Ratio of Akeno to AMIGA muon densities

Figure 7.9: Comparison of the muon densities measured by the A1 1 km^2 array at Akeno and the engineering array of AMIGA together with fits of the mean MLDFs for AMIGA in bins of primary energy (a). The mean muon densities obtained for A1 in bins of radial core distance are divided by the fitted AMIGA MLDFs in (b).

of electrons N_e with width $\Delta \log N_e = 0.25$. For a comparison with AMIGA data, we calculate the corresponding primary energies with Eq. (7.15) and extracted the average muon densities in bins of radial distance from Fig. 2 in Ref. [120].

The four highest energy bins between $10^{17.4}$ eV and $10^{18.3}$ eV lie within the accessible energy range for AMIGA. We hence perform an identical binning in primary energy, zenith angle, and radial distance for the AMIGA data and jointly plot the results of both experiments in Fig. 7.9. Additionally, the average muon lateral distribution functions (MLDFs) for AMIGA are fitted in each energy bin with the parametrization of Eqs. (5.23) and (5.46) and fixed $\beta = \beta(\langle\theta\rangle)$ parameter according to Eq. (6.34). For a better comparison of the results of both experiments, the mean muon densities obtained for the A1 array in bins of radial core distance are divided by the fitted AMIGA MLDFs in Fig. 7.9b.

The mean muon densities measured by AMIGA are generally higher than the ones obtained in the Akeno analysis. The exact ratio of $\rho_\mu^{\text{Akeno}}/\rho_\mu^{\text{AMIGA}}$ depends however strongly on the radial distance and varies between about 60% for small and 110% for large core distances. For small core distances, the Akeno muon counters most likely suffer from a saturation effect as the radial distance of the nearest considered bin increases with increasing energy. Furthermore, the best agreement between the steeper MLDFs for AMIGA and the Akeno data is found for the lowest energy bin. For the largest radial bin, the muon densities measured by Akeno correspond to more than 90% of the AMIGA muon densities. It is encouraging, but should not be over-interpreted, that the results of both experiments are in quite good agreement considering the different detection techniques, atmospheric depths, and mainly the potential discrepancies in the estimation of the primary energy estimation.

7.5.2 *Auger analysis of horizontal air showers*

The Pierre Auger Observatory has recently published a study of the average number of muons in inclined events with zenith angles $62^\circ \leq \theta \leq 80^\circ$, named horizontal air shower (HAS), above energies of 4×10^{18} eV [111]. The muonic shower component is estimated by a comparison of the measured muon footprint on ground with simulated footprints for a reference model. The study makes use of the fact that the electromagnetic shower component is strongly attenuated for horizontal air showers such that the signal in the water-Cherenkov detectors is largely dominated by muons. We compare the results of this study with the first muon measurements of AMIGA taken with the engineering array. An advantage of AMIGA is that direct measurements of the muon densities are performed and comparisons with simulations are not necessary to obtain an estimator of the muon content.

Summary of the HAS analysis

In the study of horizontal air showers, the muon density ρ_μ at the ground point $\vec{r}$ is modeled as

$$\rho_\mu(\vec{r}) = N_{19}\,\rho_{\mu,19}(\vec{r};\theta,\varphi) \tag{7.16}$$

where $\rho_{\mu,19}$ is the parametrized ground density for a proton shower simulated at a primary energy of 10^{19} eV with the hadronic high-energy interaction model QGSJETII-03 [111]. The relative scale factor N_{19}, relating the observed number of muons to the reference model, is obtained by fitting the parametrization of Eq. (7.16) to the measured muon densities. It is corrected for biases by computing the ratios

$$R_\mu^{\mathrm{MC}} = N_\mu / N_{\mu,19} \tag{7.17}$$

of the total number of muons N_μ at the ground in simulations and the total number of muons $N_{\mu,19}$ that is obtained by integrating the muon density of the reference model (Eq. (7.16)). An

unbiased estimator R_μ of the muon content at ground is obtained by correcting the scale factor $N_{\mu,19}$ by the mean bias that is averaged over different primaries and hadronic interaction models.

The energy dependence of the muon content estimator R_μ is parametrized as

$$R_\mu(E) = a\left(E/10^{19}\,\mathrm{eV}\right)^b \tag{7.18}$$

where a corresponds to the average muon content $\langle R_\mu\rangle(10^{19}\,\mathrm{eV})$ at energy $10^{19}\,\mathrm{eV}$, and b to the logarithmic gain $\mathrm{d}\langle\ln R_\mu\rangle/\mathrm{d}\ln E \approx \mathrm{d}\ln N_\mu/\mathrm{d}\ln E$ of muons with increasing energy. The parameters

$$a = (1.841 \pm 0.029 \pm 0.324(\mathrm{sys})) \quad \text{and} \tag{7.19}$$

$$b = (1.029 \pm 0.024 \pm 0.030(\mathrm{sys})) \tag{7.20}$$

were obtained with a maximum-likelihood method that takes into account both intrinsic shower-to-shower fluctuations and detector sampling fluctuations.

The fitted average muon content $\langle R_\mu\rangle/(E/10^{19}\,\mathrm{eV})$ as well as a bin-wise average of the data are compared with various high-energy hadronic interaction models. In contradiction to studies of the average depth of shower maximum $\langle X_{\max}\rangle$, which predict a mean logarithmic mass $\langle\ln A\rangle$ between proton and iron in this energy range, the measured mean muon numbers are higher than in pure iron showers. The large logarithmic gain of the data in comparison to proton or iron simulations suggests a transition from lighter to heavier elements which is in agreement with the observed $\langle X_{\max}\rangle$ evolution.

The disagreement between model predictions and data is quantified with the help of the mean logarithmic mass $\langle\ln A\rangle$ that is inferred from measurements of the average depth $\langle X_{\max}\rangle$ of the shower maximum. For the measured $\langle\ln A\rangle$ values, the mean logarithmic muon content $\langle\ln R_\mu\rangle$ is predicted and compared with simulations. The minimum deviation of the models w.r.t. data is 1.4σ (EPOS-LHC) and the mean muon number around $10^{19}\,\mathrm{eV}$ would have to be increased by 30% (EPOS-LHC) to 80% (QGSJETII-01) in simulations to match the measurements.

Comparison with AMIGA measurements

For the comparison with the HAS analysis, we define an observable for AMIGA that is comparable to the muon content estimator R_μ. In the analysis of horizontal air showers, the zenith and azimuth dependence is cancelled by dividing the observed muon densities with the parametrized muon density $\rho_{\mu,19}\left(\vec{r};\theta,\varphi\right)$ of the reference model as a function of the radial distance r, the azimuth φ, and the zenith angle θ. This procedure is justified with studies showing that the model and primary dependence of the muon footprint at ground is small for horizontal air showers.

However, since we observe that the attenuation curves for AMIGA depend highly on the primary particle and, to a smaller extent, on the employed hadronic interaction model (see Fig. 6.22), a normalization by the density $\rho_{450}^{19}(\theta)$ of the reference model for the corresponding zenith angle θ would introduce biases in the case of AMIGA.

The distinct situations for AMIGA and the study of horizontal air showers can be explained by two main differences. First, we expect a stronger attenuation of the muonic signal measured by the AMIGA underground detectors resulting from the soil layer of 2.3 m thickness which introduces a zenith-dependent effective muon energy threshold of $1\,\mathrm{GeV}/\cos\theta$. Second, for AMIGA we study vertical showers with zenith angles between 0° and 45° where we observe stronger differences of the attenuation functions for different primaries and models compared to the larger zenith angles of the HAS analysis.

For this reason, we correct the zenith-dependent muon densities $\rho_{450}(\theta)$ for the attenuation effect by calculating ρ_{35} according to Eq. (7.22) before the normalization to the QGSJETII-03 reference model. We hereby employ the attenuation functions that were derived separately for data and simulations for different primary and hadronic interaction models in Section 6.5.3. Subsequently, the attenuation corrected muon densities ρ_{35} are normalized by the corresponding muon density ρ_{35}^{19} of the proton

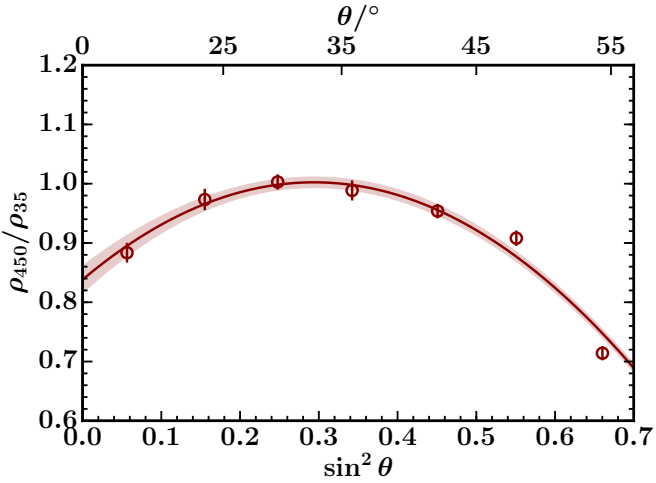

Figure 7.10: Fit of the attenuation curve $f_{\text{att}}(\theta)$ for the reference model (proton, QGSJETII-03, $E = 10^{19}$ eV) to determine the reference density ρ_{35}^{19} at a zenith angle of $\theta = 35°$. The weighted averages of the normalized densities ρ_{450}/ρ_{35} in bins of $\sin^2\theta$ are shown by markers; error bars indicate the corresponding standard deviations. The fit uncertainties are displayed by a shaded band.

QGSJETII-03 reference model with primary energy of 10^{19} eV such that the adapted muon content estimator for AMIGA is defined as

$$R_\mu = \rho_{35}/\rho_{35}^{19}. \tag{7.21}$$

In this way, we perform the appropriate attenuation corrections for for both simulations and data and do not introduce biases due to the use of an incorrect attenuation function derived from the reference model.

Since we do not have simulations of the reference model at 10^{19} eV with a zenith angle of $\theta = 35°$ to calculate the reference density ρ_{35}^{19}, we make use of an available library of proton showers for the QGSJETII-03 model with a continuous energy spectrum

following a flux of E^{-1} and a zenith angle distribution that is uniform in $\cos^2\theta$. We select the energy range $10^{18.95}\,\text{eV} \leq E \leq 10^{19.05}\,\text{eV}$ and parametrize the muon density attenuation by

$$\rho_{450}(\theta) = \rho_{35}^{19} \cdot f_{\text{att}}(\theta; a, b) \tag{7.22}$$

as a function of the shower zenith angle θ according to Eq. (7.22) in Section 6.5. The attenuation function

$$f_{\text{att}}(\theta) = 1 + ax + bx^2 \tag{7.23}$$

is a second order polynomial in $x = \cos^2\theta - \cos^2\theta_{\text{ref}}$ with the reference zenith angle $\theta_{\text{ref}} = 35°$. Minimizing the least squares expression

$$\text{LS}\left(\rho_{35}^{19}, a, b\right) = \sum_{i=1}^{N} \frac{1}{\sigma_{450,i}^2} \left(\rho_{450,i} - \rho_{35}^{19} \cdot f_{\text{att}}(\theta_i; a, b)\right)^2 \tag{7.24}$$

we obtain the reference density

$$\rho_{35}^{19} = (7.22 \pm 0.06)\ \text{m}^{-2} \tag{7.25}$$

and the parameters $a = 0.13 \pm 0.04$ and $b = -1.90 \pm 0.11$.

The parameter uncertainties were determined by bootstrapping the data set 500 times and calculating the covariance matrix from the 500 best fit parameters. The resulting attenuation curve f_{att} is shown as a function of $\sin^2\theta$ in Fig. 7.10. In comparison to proton showers for the EPOS-LHC and QGSJETII-04 models at 10^{19} eV (see Fig. 6.22 in Section 6.5.3), the attenuation curve for the proton QGSJETII-03 simulations has a stronger bending with larger attenuation effects for both the smallest and highest considered zenith angles.

We fit the energy dependence of $R_\mu = \rho_{35}/\rho_{35}^{19}$ with the log-likelihood method described in Section 7.1.1 by minimizing

$$\ln(L; a, b) = \sum_k \ln\left(\sum_i e^{-\frac{1}{2}\frac{(E_k - E_i)^2}{\sigma_{E_i}^2}} e^{-\frac{1}{2}\frac{(R_\mu(E_k) - R_\mu(E_i; a, b))^2}{\sigma_{R_{\mu_i}}^2}}\right), \tag{7.26}$$

Simulation		HAS		AMIGA	
Primary	Model	a	b	a	b
p	EPOS-LHC	1.218	0.944	1.194 ± 0.008	0.919 ± 0.004
	QGSJETII-04	1.176	0.941	1.144 ± 0.006	0.919 ± 0.003
Fe	EPOS-LHC	1.619	0.928	1.810 ± 0.002	0.908 ± 0.001
	QGSJETII-04	1.573	0.925	1.731 ± 0.002	0.911 ± 0.001

Table 7.7: Comparison of the parameters a and b of the parametrization for $R_\mu(E)$ for simulations for the HAS and AMIGA analysis.

in analogy to Eq. (7.3), where σ_{E_i} denotes the energy uncertainty of the ith event originating from the SD reconstruction and $\sigma_{R_{\mu_i}}$ the statistical uncertainty of the muon content estimator. The uncertainties and correlation of the fit parameters a and b are obtained by bootstrapping the data set 1000 times and calculating the covariance matrix from the 1000 best fit parameters. The input data and fit of the energy dependence are shown in Fig. 7.11 for the energy range from $10^{17.4}$ eV to $10^{18.3}$ eV. We find an average muon content of

$$a = 1.872 \pm 0.198(\text{stat}) \pm 0.194(\text{sys}) \tag{7.27}$$

with respect to the proton QGSJETII-03 reference model at 10^{19} eV and a logarithmic gain of

$$b = 0.889 \pm 0.036(\text{stat}) \pm 0.037(\text{sys}), \tag{7.28}$$

which is unchanged compared to the fit of the unnormalized muon densities ρ_{35} as a function of the energy (Eq. (7.4)).

The corresponding parameters a and b for simulations are given in Table 7.7. While the slopes b are equivalent to those listed in Table 7.1 w.r.t. the parametrization $\rho_{35}(E) = a\,(E/10^{18}\,\text{eV})^b$, the normalizations were recalculated as

$$\tilde{a} = a/\rho_{35}^{19} \cdot 10^b \tag{7.29}$$

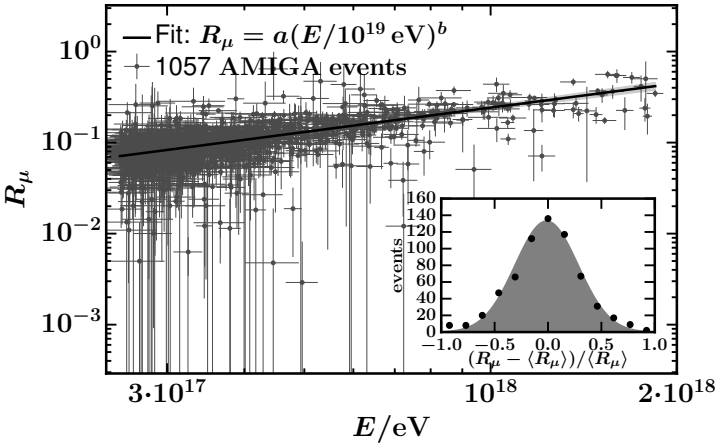

Figure 7.11: Fit of the energy dependence $\langle R_\mu \rangle = a\,(E/10^{19}\,\mathrm{eV})^b$ of the muon content estimator $R_\mu = \rho_{35}/\rho_{35}^{19}$ for AMIGA data. Vertical and horizontal error bars for single events correspond to the statistical errors in R_μ and E. The added added statistical and systematic uncertainties of the fit are displayed by a grey shaded band. The inset plot shows the distribution of the normalized residuals $(R_\mu - \langle R_\mu \rangle)/\langle R_\mu \rangle$.

to match the modified parametrization $R_\mu\,(E) = a\,(E/10^{19}\,\mathrm{eV})^b$ where we write $a(\equiv \tilde{a})$ for simplicity.

The energy-normalized muon content $\langle R_\mu \rangle/(E/10^{19}\,\mathrm{eV})$ is shown in Fig. 7.12 as a function of E for AMIGA data compared to the expectations from simulations. The mean muon content for AMIGA in bins of energy is displayed by round markers with error bars denoting the statistical uncertainties; the normalized fitted energy dependence $R_\mu(E)/(E/10^{19}\,\mathrm{eV})$ is shown by a black solid line with a shaded band corresponding to the fit uncertainties.

We compare the results for AMIGA with those of the study of horizontal air showers in Fig. 7.13. Unfortunately, the energy range of $2.5 \times 10^{17}\,\mathrm{eV} - 2 \times 10^{18}\,\mathrm{eV}$ for AMIGA does not quite reach the energies above $4 \times 10^{18}\,\mathrm{eV}$ that are considered in the SD study

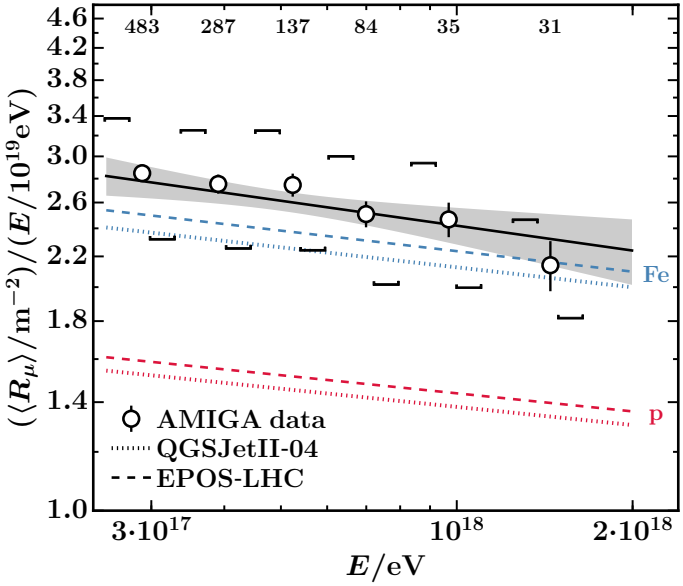

Figure 7.12: Energy-normalized muon content $\langle R_\mu \rangle / (E/10^{19}\,\mathrm{eV})$ as a function of E for AMIGA data compared to expectations from simulations. The muon content R_μ is calculated in reference to proton simulations with the QGSJetII-03 model for a primary energy of 10^{19} eV. The mean muon content for AMIGA in bins of energy is displayed by round markers, error bars denote the statistical uncertainties. Systematic uncertainties are indicated by square brackets that are shifted horizontally due to the systematic uncertainty of the SD energy estimate of 14%. The number of AMIGA events in each energy bin is stated at the top of the figure. The normalized fitted energy dependence $R_\mu(E) / (E/10^{19}\,\mathrm{eV})$ is shown by a black solid line with a shaded band corresponding to the fit uncertainties. For comparison, results are shown for simulations with the EPOS-LHC (dashed) and QGSJetII-04 (dotted) high-energy hadronic interaction models for both proton (red) and iron (blue) primary particles.

Primary	Model	$\langle R_\mu \rangle_{\text{HAS}}$	$\langle R_\mu \rangle_{\text{AMIGA}}$	$\frac{\langle R_\mu \rangle_{\text{AMIGA}}}{\langle R_\mu \rangle_{\text{HAS}}}$
p	EPOS-LHC	0.284	0.289 ± 0.001	1.019 ± 0.004
	QGSJETII-04	0.275	0.277 ± 0.001	1.006 ± 0.001
Fe	EPOS-LHC	0.387	0.446 ± 0.001	1.153 ± 0.004
	QGSJETII-04	0.378	0.425 ± 0.000	1.124 ± 0.001

Table 7.8: Comparison of the average muon content $\langle R_\mu \rangle$ at $10^{18.33}$ eV in simulations for the analysis of HASs and AMIGA.

of horizontal air showers. However, we can compare the logarithmic gains $\mathrm{d}\langle \ln R_\mu \rangle / \mathrm{d} \ln E$ of both analyses and extrapolate the results to an intermediate energy for a direct comparison of the logarithmic muon contents.

Measurements of the mean depth of maximum $\langle X_{\text{max}} \rangle$ show a break of the elongation rate at $10^{18.33}$ eV which is associated to a change in the mass composition of primary cosmic rays [53]. For lower energies between $10^{17.2}$ eV and $10^{18.33}$ eV, the deduced mean logarithmic mass $\langle \ln A \rangle$ decreases, while it increases again for higher energies. The different logarithmic gains of $b = 0.889 \pm 0.037(\text{stat}) \pm 0.038(\text{sys})$ for AMIGA and $b = 1.029 \pm 0.024(\text{stat}) \pm 0.030(\text{sys})$ for the HAS analysis qualitatively fit well to the $\langle X_{\text{max}} \rangle$ results. As discussed previously, the smaller slope b for AMIGA compared to simulations for a pure composition agrees with a lightening of the mass composition in this energy range. On the other hand, the large logarithmic gain which is measured in the HAS analysis between 4×10^{18} eV and 5×10^{19} eV indicates a transition towards heavier elements.

We compare the muon contents for both simulations and data at the intermediate energy of $10^{18.33}$ eV, where a change in the X_{max} elongation rate is observed, by interpolating the results of both studies. The mean muon contents at $10^{18.33}$ eV, stated in Table 7.8 for simulations, only deviate by 1% (QGSJETII-04) to 2% (EPOS-LHC) for proton simulations. For iron primaries, a 12%

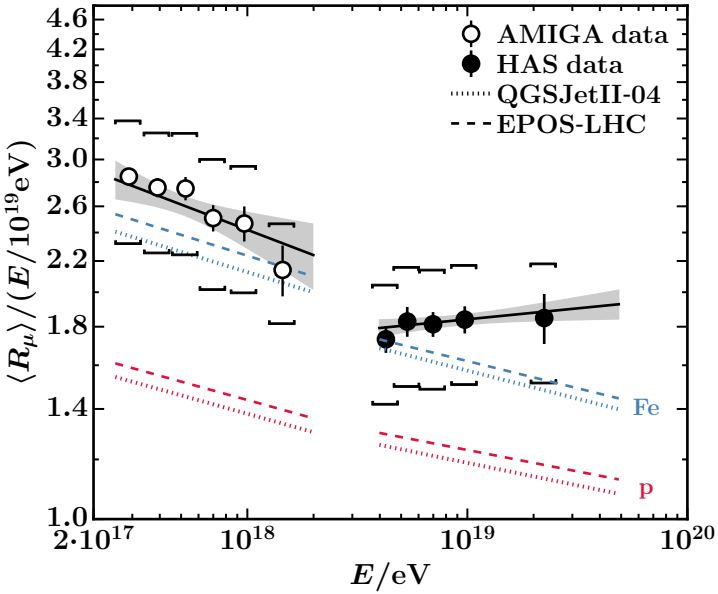

Figure 7.13: Comparison of the energy-normalized muon content $\langle R_\mu \rangle / (E/10^{19}\,\mathrm{eV})$ obtained for AMIGA with measurements of horizontal air showers (HASs) by the surface detector.

(QGSJetII-04) to 15% (EPOS-LHC) larger mean $\langle R_\mu \rangle$ is found in the AMIGA analysis. Extrapolating the measurements of the AMIGA engineering array, we obtain a muon content of

$$\langle R_\mu \rangle_{\mathrm{AMIGA}} = 0.475 \pm 0.025(\mathrm{stat}) \pm 0.022(\mathrm{sys}). \tag{7.30}$$

at $10^{18.33}$ eV in comparison to

$$\langle R_\mu \rangle_{\mathrm{HAS}} = 0.376 \pm 0.015(\mathrm{stat}) \pm 0.069(\mathrm{sys}) \tag{7.31}$$

for the analysis of horizontal air showers. With a ratio of

$$\frac{\langle R_\mu \rangle_{\mathrm{AMIGA}}}{\langle R_\mu \rangle_{\mathrm{HAS}}} = 1.263 \pm 0.083(\mathrm{stat}) \pm 0.237(\mathrm{sys}) \tag{7.32}$$

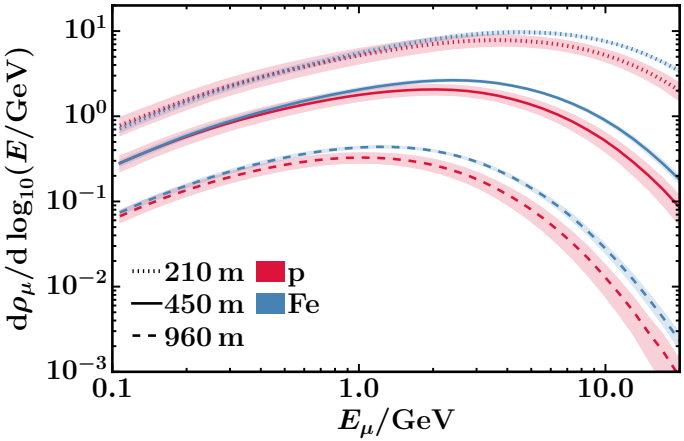

Figure 7.14: Differential muon density spectrum for proton and iron showers as a function of the muon energy E for different radial distances to the shower core for unthinned simulations with the EPOS-LHC hadronic interaction model at a primary energy of $10^{18.5}$ eV and a zenith angle of $\theta = 38°$.

at $10^{18.33}$ eV, AMIGA measures considerably more muons. However, both analyses agree within statistical and systematic uncertainties.

The discrepancy of both analyses in the case of data and iron simulations and, at the same time, an almost perfect agreement for proton simulations can possibly be explained by the different muon energy detection thresholds of the two analyses. In the analysis of HASs measured by the SD, a threshold of 300 MeV of the water-Cherenkov detectors is assumed [111]. The threshold for the buried AMIGA detectors is approximately 1 GeV for vertical muons. Since the energy spectra of the muons detected at ground are different for proton and iron primaries, the ratio of the number of muons for iron showers w.r.t. proton showers at a certain core distance depends on the muon energies. Conse-

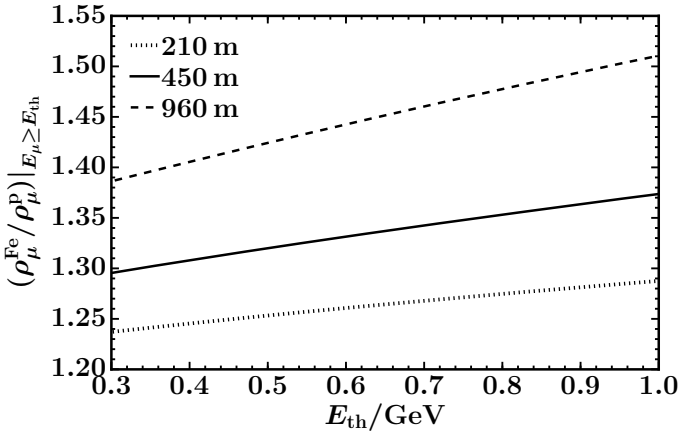

Figure 7.15: Dependence of the ratio $\rho_\mu^{\mathrm{Fe}}/\rho_\mu^{\mathrm{p}}$ of the muon densities of iron to proton showers as a function of the detection threshold of muons E_{th} for different radial distances to the shower core for unthinned simulations with the EPOS-LHC hadronic interaction model at a primary energy of $10^{18.5}$ eV and a zenith angle of $\theta = 38^\circ$.

quently, the mean muon content $\langle R_\mu \rangle$, which is defined in reference to proton simulations at 10^{19} eV with the QGSJETII-03 hadronic interaction model, exhibits a dependence on the detection threshold of muons.

For a qualitative assessment of the impact of the detection threshold, differential muon density spectra for proton and iron showers that were simulated with the EPOS-LHC hadronic interaction model at a primary energy of $10^{18.5}$ eV and a zenith angle of $\theta = 38^\circ$ are shown in Fig. 7.14 for different radial distances to the shower core. We hereby use the unthinned simulations that were produced for the analysis of the impact of the detection threshold of muons on the separability of primary cosmic rays in Chapter 4.

The muon spectra of proton and iron primaries are very similar in the lower energy part, but increasingly deviate towards higher

muon densities for iron showers for high muon energies. Even though the energy spectra depend on the radial distance to the shower core, this effect is seen for all three considered core distances. The impact on the ratio of the muon densities of iron to proton showers is shown in Fig. 7.15 as a function of the detection thresholds of muons E_{th}. Due to the increased muon densities for iron showers, higher muon energy thresholds lead to larger ratios $\rho_\mu^{\mathrm{Fe}}/\rho_\mu^{\mathrm{p}}$. The observed larger muon content for AMIGA for iron simulations and data could thus be a result of the larger detection threshold of the AMIGA detectors compared to the WCDs used in the analysis of horizontal air showers.

We test this assumption by converting the measured muon densities of the AMIGA and HAS analyses to the z-factor

$$z = \frac{\ln\langle R_{\mu,\mathrm{det}}\rangle - \ln\langle R_{\mu,\mathrm{p}}\rangle}{\ln\langle R_{\mu,\mathrm{Fe}}\rangle - \ln\langle R_{\mu,\mathrm{p}}\rangle}, \tag{7.33}$$

which was proposed to correct for simple biases in the recorded muon densities [121]. By design, the z factors for proton and iron primaries are $z_{\mathrm{p}} = 0$ and $z_{\mathrm{Fe}} = 1$, respectively.

The converted muon densities for AMIGA and the HAS analysis are shown in Fig. 7.16. The very good agreement of the z factors at the intermediate energies between the distinct energy ranges of the two analyses supports the assumption that the differences in the measured muon densities are a result of the different detection techniques and the different detection thresholds of muons of the water-Cherenkov detectors and AMIGA detectors in particular. Moreover, the combined muon measurements of AMIGA and the HAS analysis match the results on the mean logarithmic mass derived from X_{max} measurements [53] (see Fig. 2.13) which indicate that the composition evolves towards a very light composition between $10^{17.2}$ eV and $10^{18.33}$ eV and becomes heavier again towards higher energies.

Even though both muon measurements agree well after conversion to the z-factor and the energy evolution of the muon content matches the one inferred from X_{max} measurements, the large

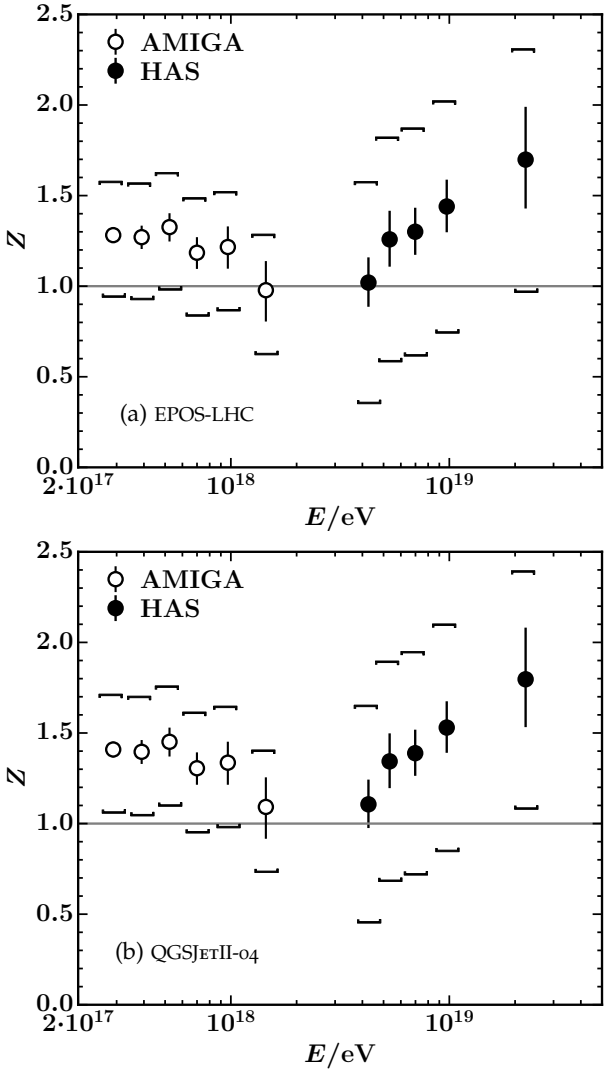

Figure 7.16: Conversion of the muon content measured by AMIGA and for HASs to the z-factor $z = \langle \ln\langle R_{\mu,\mathrm{det}}\rangle - \ln\langle R_{\mu,\mathrm{p}}\rangle\rangle / \langle \ln\langle R_{\mu,\mathrm{Fe}}\rangle - \ln\langle R_{\mu,\mathrm{p}}\rangle\rangle$ for (a) the EPOS-LHC and (b) the QGSJETII-04 hadronic interaction model.

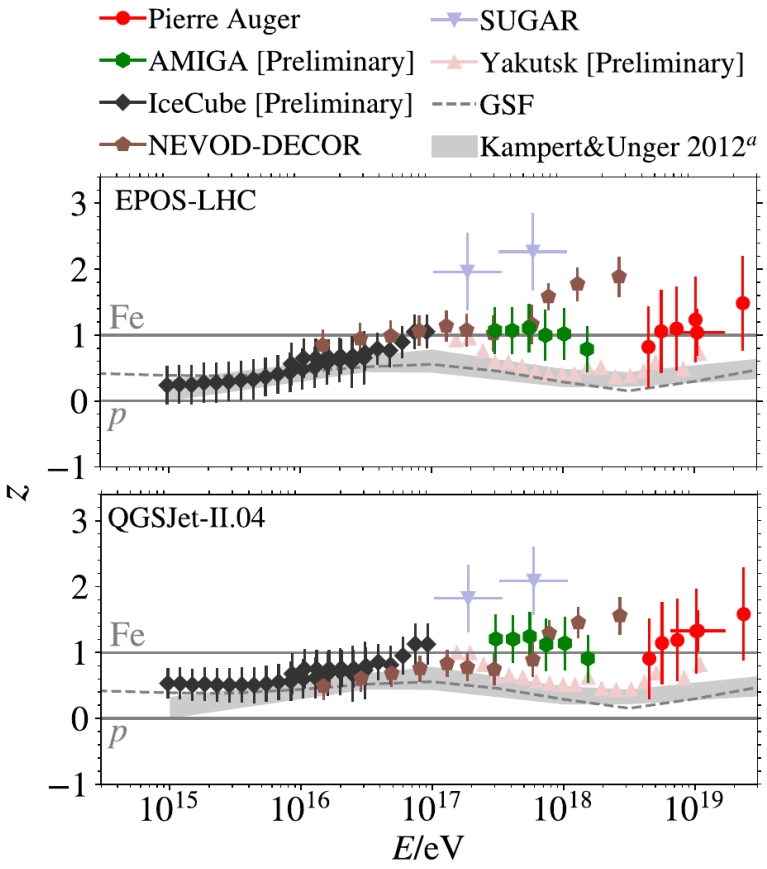

Figure 7.17: Combination of muon measurements after the cross-calibration of their energy scales by conversion to the z-factor $z = (\ln\langle R_{\mu,\mathrm{det}}\rangle - \ln\langle R_{\mu,\mathrm{p}}\rangle)/(\ln\langle R_{\mu,\mathrm{Fe}}\rangle - \ln\langle R_{\mu,\mathrm{p}}\rangle)$. The measurements of this thesis for the AMIGA engineering array are shown by green circles and the measurements of the HAS analysis by red circles. The effect of the changing mass composition is estimated with a Global Spline Fit (GSF) to the cosmic ray flux and composition data (grey dashed-dotted line). In addition, updated composition estimates from X_{max} measurements by Kampert and Unger are shown (grey shaded band). From [121].

muon content in data is at variance with simulations, given the light mass composition inferred from X_{max} measurements. This mismatch of the muonic shower component between data and simulations has been observed by multiple experiments studying the lateral density, production depth, and attenuation of muons. In contrast, there is mostly a good agreement between data and simulations for the electromagnetic shower component (see H. Dembinski for the Working Group on Hadronic interactions and Shower Physics [121] and references therein).

Recently, the muon measurements of multiple experiments, including the AMIGA results of this thesis, have been combined. A good agreement between diverse experiments is obtained after cross-calibrating their energy scales by matching the measured all-particle fluxes as shown in Fig. 7.17 [121]. Subtracting the effect of the changing mass-composition, an energy-dependent discrepancy between data and simulations becomes apparent. While a good agreement is found up to energies of approximately 10^{16} eV, an increasing discrepancy of data and simulations is observed for higher energies. In addition to the primary energy, a dependence of the muonic shower component on the shower age, lateral distance to the shower core, as well as on the energy threshold of the detectors and the shower zenith angles is possible. These observables need to be further investigated by current and future experiments to measure hadronic interaction properties and reconcile simulations with muon data.

8 CONCLUSION

The number of muons in extensive air showers is a crucial observable for measurements of the mass composition of primary cosmic rays. For this reason, the Pierre Auger Observatory is currently being upgraded with new detectors. The AMIGA muon detector extension is an essential part of the upgrade. It consists of buried segmented scintillation counters, which will allow for direct muon density measurements on a shower-by-shower basis.

In this thesis, we performed a simulation study of the impact of muon detection thresholds on the composition separability which has been used to define the specifics of the now deployed upgrade detectors. Furthermore, we improved the existing muon reconstruction procedure for AMIGA and presented a systematic analysis of data from the AMIGA engineering array. We demonstrated the capability of composition analyses with AMIGA and derived first results, based on the muon density measurements, of the mass composition in the energy range from $10^{17.4}$ eV to $10^{18.3}$ eV. The following sections summarize these contributions in detail.

IMPACT OF MUON DETECTION THRESHOLDS As a prerequisite to define the specifics of the upgrade detectors, we analyzed the impact of the detection threshold of muons on the composition separability with simulations. We found that, for ideal detectors, the discrimination power is reduced when lowering the threshold, although the number of detected muons increases. We showed that this observation can be explained by a change of the correlation of the number of muons N_μ with the shower maximum $X_{\max}$ as a function of the muon energy. For increasing thresholds, the overlap of the muon number distributions for

proton and iron primaries is reduced, giving rise to an increased mass separability. We derived the dependence of the $N_\mu - X_{\max}$ correlation on the core distance and the detection threshold of muons qualitatively within a model for hadronic interactions and the shower geometry.

Analyzing the impact of muons that are produced by photon-air collisions, we found that the separability of primaries is additionally reduced as a consequence of the presence of more muons from photonuclear reactions in proton compared to iron showers.

For real detectors of limited size, statistical fluctuations of the detected number of muons lead to a reduced separability in the case of low muon densities. A good separability of distinct mass groups of cosmic rays is only achieved for very large detection areas, or if the depth of shower maximum, as a second mass-sensitive observable, can be inferred from other measurements. Taking these results into account, the Pierre Auger Observatory decided for the installation of plastic scintillation detectors above the existing water-Cherenkov detectors, as the main part of its upgrade. The number of muons will be measured by combining the signals of the two detector types, while the depth of shower maximum can be estimated from the timing of the signals. The direct muon measurements of the AMIGA extension will be used to validate the indirect measurement of the upgrade detectors.

MD RECONSTRUCTION OPTIMIZATION As a part of the upgrade of the Pierre Auger Observatory, the AMIGA muon counter extension will allow for direct muon density measurements. Next to each water-Cherenkov detector on the 750 m sub-array, a segmented scintillation counter, consisting of several modules with a total area of $30\,\mathrm{m}^2$, will be buried at a depth of 2.3 m. The soil shielding constitutes an effective muon energy threshold of approximately 1 GeV for vertical muons. According to our study of the impact of the detection threshold this relatively high threshold improves the separability of different mass groups of cosmic rays.

In order to guarantee an unbiased estimate of the muon density based on the measurements of the AMIGA muon counters, we optimized and extended the existing reconstruction procedure. The muon counting strategy relies on the identification of patterns in the binary time traces for each scintillator bar within time windows of fixed length. Comparing the simulated with the reconstructed number of muons, we found that a window length of seven bins yields unbiased results for all radial distances and considered primary energies.

Muons falling onto the detector from an inclined direction most likely deposit signals in neighboring scintillator bars which leads to over-counting. We developed a geometrical correction procedure for such *corner-clipping* muons that makes use of the orientation of the individual modules as well as the shower zenith and azimuth angle as an approximation of the muon momentum direction. The bias of the estimated muon density of up to 25% is thereby reduced to $\pm 3\%$ for all considered zenith angles, primaries, energies and hadronic interaction models.

The corner-clipping correction ensures the unbiased estimation of the muon density for individual muon counters. However, to compare the muon content between extensive air showers, a muon lateral distribution function needs to be fitted to the measured muon densities as a function of the radial distances of the detectors, which is usually evaluated at an optimal distance where the systematic uncertainties are minimal. The lateral distribution function should be parametrized such that it describes the data well; in particular, it should not be biased at the distance of its evaluation. To meet these requirements, we derived a new parametrization of the existing KASCADE-Grande-like muon lateral distribution function by performing a fit of its shape parameters r^*, α, γ, and $\beta(\theta, E)$ with proton and iron simulations for different primary energies, zenith angles, and hadronic interaction models. The resulting parametrization describes the muon densities better than the previous standard one. Notably, at intermediate distances between 400 and 600 m, an undershooting of

the muon density for proton showers by the former muon lateral distribution function is strongly reduced.

We obtain the best composition sensitivity when parametrizing the slope β of the muon lateral distribution function as a function of the shower zenith angle. This is a result of the drastically reduced fluctuations of the estimated muon density in comparison to fits with free β parameter. We determined that the muon lateral distribution function should be evaluated at $r_{\text{opt}} = 450\,\text{m}$, where the systematic uncertainty of the estimated muon density is minimal.

DATA SELECTION AND SYSTEMATICS The engineering array for AMIGA, consisting of a hexagon of seven muon detectors of $30\,\text{m}^2$ area each, has been operational since February 2015. We selected a reliable sample of one year of calibrated data by developing a bad period rejection for the muon detector, excluding faulty modules, and correcting for the different efficiencies of the $5\,\text{m}^2$ and $10\,\text{m}^2$ AMIGA modules.

We derived a zenith-independent estimator ρ_{35} of the muon density for both simulations and data by parametrizing the attenuation of the muonic signal ρ_{450} due to the atmosphere and soil layer above the buried muon detectors. For data, we employed the constant intensity cut method, which is based on the assumption of an isotropic flux of cosmic rays arriving at earth. For simulations, we parametrized the attenuation of ρ_{450} for every hadronic interaction model and primary particle as a function of the shower zenith angle and the primary energy. In the subsequent analyses, we employed the attenuation parametrization derived from data for the correction of the muon densities measured with AMIGA, and the individual parametrizations for each primary-hadronic interaction model combination for the correction of the muon densities obtained with simulations.

We analyzed the main sources of systematic uncertainties for AMIGA and estimated their contribution to the total systematic uncertainty. As a result of light attenuation in the wavelength-

shiftings in the scintillator modules and PMT after-pulsing, a module area-dependent efficiency correction needs to be applied to the measured muon densities. We estimated that the systematic uncertainty of this correction translates to an uncertainty of $\sigma_{\text{sys,eff}}/\rho_{450} = 9.9\%$. For each of the 64 scintillator bars of one module, the discriminator threshold voltage is set to 30% of the mean single photo-electron amplitude V_{SPE}, such that a single photo-electron is represented by a single 1 in the sampled binary trace. We estimated the effect of a 2σ variation of the target value of the discriminator threshold with simulations and obtained a systematic uncertainty of $\sigma_{\text{sys,calib}}/\rho_{450} = 3.9\%$. Additionally, we evaluated the systematic uncertainty of the reconstructed muon density ρ_{450} that is caused by a variation of the density of the soil above the buried detectors with simulations. For a variation of $\pm 3\sigma_{\rho_{\text{soil}}}$, we found a systematic uncertainty of $\sigma_{\text{sys,soil}}/\rho_{450} = \mp 2.8\%$. The systematic uncertainty arising from the unknown shape of the true muon lateral distribution function gives a contribution of $\sigma_{\text{sys,MLDF}}/\rho_{450} = 8.8\%$. For the estimation of the systematic uncertainty of the attenuation corrected muon density ρ_{35}, we treated the statistical uncertainties of the function parameters as systematic uncertainties of the parametrization. Averaged over all zenith angles $0^\circ \leq \theta \leq 45^\circ$, we found $\sigma_{\text{sys},f_{\text{att}}}/f_{\text{att}} = 2.3\%$. Combining all considered systematic uncertainties, we obtained a mean total systematic uncertainty of $\sigma_{\text{sys},\rho_{35}}/\rho_{35} = 14.3\%$.

ANALYSIS OF THE MEASURED MUON DENSITIES We used the corrected data set to fit the energy dependence of the mean muon densities measured by AMIGA, to quantify the observed disagreement of the muon content between simulations and data, and to analyze the evolution of the logarithmic mass based on the AMIGA measurements. Furthermore, we compared the obtained mean muon densities with results from other experiments and Auger measurements of the other detector types.

We fitted the evolution of the corrected muon density ρ_{35} with energy, measured by the surface detector, as a power law

$$\rho_{35}\,(E; a, b) = a(E/10^{18}\,\mathrm{eV})^{b},$$

with an unbinned log-likelihood method. We restricted the analysis to the energy range from $10^{17.4}$ eV to $10^{18.3}$ eV to allow for the migration of events below the full efficiency of $10^{17.5}$ eV of the SD-750 array into the accepted energy range and to avoid a distortion of the linear fit by measurements at higher energies where the X_{max} elongation rate changes. We found that the energy evolution of ρ_{35} indicates a slight lightening of the composition in the considered energy range, although, within the statistical uncertainties, the fit results agree with a pure composition as well.

We quantified the disagreement between the measured muon densities and the model predictions by relating the mean logarithmic muon density $\langle \ln \rho_{35} \rangle_A$ for the mean logarithmic mass $\langle \ln A \rangle$ to the mean depth of maximum $\langle X_{\mathrm{max}} \rangle_A$ with simulations. Comparing measurements of $\langle X_{\mathrm{max}} \rangle$ from the fluorescence detector and measurements of $\langle \ln \rho_{35} \rangle$ from AMIGA at the same energy with simulations, we obtained that the muon content in simulations would need to be increased by 38% for the EPOS-LHC hadronic interaction model and by about 50−53% for the QGSJETII-04 model.

In addition, we estimated the mean logarithmic mass according to AMIGA muon density measurements by

$$\langle \ln A \rangle = \frac{\ln 56 \cdot \left(\langle \ln \rho_{35} \rangle_A - \langle \ln \rho_{35} \rangle_{\mathrm{p}} \right)}{\left(\langle \ln \rho_{35} \rangle_{\mathrm{Fe}} - \langle \ln \rho_{35} \rangle_{\mathrm{p}} \right)}$$

and studied its evolution in the energy range between $10^{17.5}$ eV and 10^{18} eV. Since the measured muon densities are higher than those for iron simulations, we shifted the calculated mean logarithmic masses by constant offsets of $\Delta \ln A$, depending on the hadronic interaction model, to match the results from the X_{max} analysis for the first considered energy bin at $10^{17.5}$ eV. The observation of a light composition in the considered energy range is

qualitatively confirmed by the first data of the AMIGA engineering array, although the large statistical and systematic uncertainties do not allow for conclusive statements.

We compared the muon densities measured by AMIGA with results of the Akeno experiment and a recent Auger analysis of horizontal air shower (HAS). Considering the different detection techniques, atmospheric overburdens, and ways of reconstructing the primary energy, the results of Akeno and AMIGA are in quite good agreement. We defined a muon content estimator $R_\mu = \rho_{35}/\rho_{35}^{19}$ for AMIGA that is comparable to R_μ in the HAS analysis as the ratio of the attenuation-corrected muon density ρ_{35} and the corresponding muon density ρ_{35}^{19} at 10^{19} eV of the QGSJETII-03 reference model. At the intermediate energy of $10^{18.33}$ eV, where a change in the $X_{\max}$ elongation rate has been observed, we found a very good agreement of the muon content of proton showers with deviations $\leq 2\%$ of both studies demonstrating the comparability of the two analysis methods.

The 12% (QGSJETII-04) to 15% (EPOS-LHC) larger mean $\langle R_{\mu,\mathrm{Fe}} \rangle$ values for iron simulations as well as the 26% higher muon content for AMIGA compared to the HAS analysis can possibly be explained by the different muon energy detection thresholds of AMIGA (1 GeV) and the SD (300 MeV). This assumption is supported by the very good agreement of the z factors

$$z = \frac{\ln\langle R_{\mu,\mathrm{det}} \rangle - \ln\langle R_{\mu,\mathrm{p}} \rangle}{\ln\langle R_{\mu,\mathrm{Fe}} \rangle - \ln\langle R_{\mu,\mathrm{p}} \rangle}, \tag{8.1}$$

correcting for simple biases in the recorded muon densities, at the intermediate energies between the distinct energy ranges of the two analyses. Moreover, the combined muon measurements of AMIGA and the HAS analysis match the results on the mean logarithmic mass derived from $X_{\max}$ measurements, indicating that the composition evolves towards a very light composition between $10^{17.2}$ eV and $10^{18.33}$ eV and becomes heavier again towards higher energies.

FUTURE DIRECTIONS We demonstrated that both the AMIGA muon detectors and the data reconstruction and analysis tools are in a good shape for measurements of the muon densities of extensive air showers. After its completion in 2019, AMIGA will record data until 2025. Despite the slight change in the detector design compared to the engineering array—installing silicon photomultipliers instead of photomultiplier tubes—most of the reconstruction improvements and analysis methods developed in this thesis are applicable.

The presented first results based on the analysis of one year of calibrated data taken with the engineering array show the potential of composition analyses with AMIGA. Furthermore, the precise measurement of the muon density and the analysis of its dependence on the primary energy, lateral distance to the shower core, the shower zenith angle, or the detection threshold of muons will enable the investigation of hadronic interaction properties and help to solve the puzzle of the muon deficit in simulations.

ACRONYMS

COSMIC RAYS

AGN	Active galactic nucleus
CIC	Constant intensity cut
CMB	Cosmic microwave background
CORSIKA	COsmic Ray SImulations for KAscade
CR	Cosmic ray
DSA	Diffusive shock acceleration
EAS	Extensive air shower
EBL	Extragalactic background light
EGMF	Extragalactic magnetic field
EM	Electromagnetic
GMF	Galactic magnetic field
GRB	Gamma-ray burst
GZK	Greisen-Zatsepin-Kuzmin
HAS	Horizontal air shower
IGM	Intergalactic medium
ISM	Interstellar medium
LDF	Lateral distribution function
LTP	Lateral trigger probability
MLDF	Muon lateral distribution function
NLDSA	Non-linear diffusive shock acceleration
SN	Supernova
SNR	Supernova remnant
UHECR	Ultra-high energy cosmic ray

PIERRE AUGER OBSERVATORY

AERA	Auger Engineering Radio Array
AMIGA	Auger Muons and Infill for the Ground Array
ASCII	Auger Scintillator for Composition - II
CDAS	Central data acquisition system
FD	Fluorescence detector
HEAT	High Elevation Auger Telescopes
SD-750	750 m SD vertical
MC	Muon counter
MD	Muon detector
SD	Surface detector
SD-1500	1500 m SD vertical
SSD	Surface scintillator detector
UC	Unitary cell
WCD	Water-Cherenkov detector

TECHNICAL

FPGA	Field-programmable gate array
GPS	Global positioning system
GTS	GPS timestamp
LTS	Local time stamp
PMT	Photomultiplier tube
RAM	Random-access memory
SIPM	Silicon photomultiplier
SPE	Single photo-electron
VEM	Vertical-equivalent muon
WLS	Wavelength-shifting

DIRECT DETECTION EXPERIMENTS

AMS	Alpha Magnetic Spectrometer
BESS	Balloon-borne Experiment with Superconducting Spectrometer
ISS	International Space Station
PAMELA	Payload for Antimatter Matter Exploration and Light-nuclei Astrophysics

AIR SHOWER EXPERIMENTS

AGASA	Akeno Giant Air Shower Array
CASA	Chicago Air Shower Array
EAS-MSU	Moscow State University Extensive Air Shower
EAS-TOP	Extensive Air Shower - Top
HEGRA	High Energy Gamma Ray Astronomy
HiRes	High Resolution Fly's Eye
KASCADE	KArlsruhe Shower Core and Array DEtector
MIA	Michigan Muon Array
SUGAR	Sydney University Giant Air-Shower Recorder
TA	Telescope Array

OTHER ACRONYMS

LHC	Large Hadron Collider
LS	Least squares

BIBLIOGRAPHY

[1] M. Unger et al., *Origin of the Ankle in the Ultra-High Energy Cosmic Ray Spectrum and of the Extragalactic Protons below It*, Phys. Rev. D **92**.12 (2015), arXiv: 1505.02153.

[2] S. Müller and M. Roth, "A CORSIKA Study on the Influence of Muon Detector Thresholds on the Separability of Primary Cosmic Rays at Highest Energies", *Proc. 34th Int. Cosmic Ray Conf.* PoS(ICRC2015)419, The Hague, The Netherlands (2015).

[3] S. Müller et al., "Impact of Muon Detection Thresholds on the Separability of Primary Cosmic Rays", *Proc. 35th Int. Cosmic Ray Conf.* PoS(ICRC2017)311, Busan, Korea (2017).

[4] S. Müller et al., *Impact of Muon Detection Thresholds on the Separability of Primary Cosmic Rays*, Astropart. Phys. **97** (2018) 174–185.

[5] B. Wundheiler for the Pierre Auger Collaboration, "The AMIGA Muon Counters of the Pierre Auger Observatory: Performance and Studies of the Lateral Distribution Function", *Proc. 34th Int. Cosmic Ray Conf.* PoS(ICRC2015)324, The Hague, The Netherlands (2015).

[6] J. Figueira for the Pierre Auger Collaboration, "An Improved Reconstruction Method for the AMIGA Detectors", *Proc. 35th Int. Cosmic Ray Conf.* PoS(ICRC2017)396, Busan, Korea (2017).

[7] S. Müller for the Pierre Auger Collaboration, "Direct Measurement of the Muon Density in Air Showers with the Pierre Auger Observatory", *Proc. Ultra High Energy Cosmic Rays 2018*, UHECR2018, Paris, France (2018).

[8] Pierre Auger Collaboration, *The AMIGA Engineering Array at the Pierre Auger Observatory*, Nucl. Instrum. Methods Phys. Res. A (in preparation) (2018).

[9] P. Blasi, *The Origin of Galactic Cosmic Rays*, Astron. Astrophys. Rev. **21**.1 (2013) 70, arXiv: 1311.7346.

[10] A. M. Hillas, "Cosmic Rays: Recent Progress and Some Current Questions", Conference on Cosmology, Galaxy Formation and Astro-Particle Physics on the Pathway to the SKA, Oxford, England (2006), arXiv: astro-ph/0607109.

[11] A. M. Hillas, *The Origin of Ultra-High-Energy Cosmic Rays*, Annu. Rev. Astron. Astrophys. **22**.1 (1984) 425–444.

[12] R. Aloisio, *Acceleration and Propagation of Ultra High Energy Cosmic Rays*, Prog. Theor. Exp. Phys. **2017**.12 (2017), arXiv: 1707.08471.

[13] M. T. Dova, *Ultra-High Energy Cosmic Rays* (2016), arXiv: 1604.07584.

[14] T. K. Gaisser et al., *Cosmic Rays and Particle Physics*, Cambridge University Press (2016).

[15] M. G. Baring, *Diffusive Shock Acceleration: The Fermi Mechanism* (1997), arXiv: astro-ph/9711177.

[16] P. O. Lagage and C. Cesarsky, *The Maximum Energy of Cosmic Rays Accelerated by Supernova Shocks*, Astron. Astrophys. **125** (1983) 249–257.

[17] E. Amato, *The Origin of Galactic Cosmic Rays*, Int. J. Mod. Phys. D **23**.07 (2014) 1430013, arXiv: 1406.7714.

[18] K. Kotera and A. V. Olinto, *The Astrophysics of Ultrahigh Energy Cosmic Rays*, Annu. Rev. Astron. Astrophys. **49**.1 (2011) 119–153, arXiv: 1101.4256.

[19] M. Spurio, *Particles and Astrophysics: A Multi-Messenger Approach*, Springer (2014).

[20] K. Dolag et al., *Magnetic Field in the Local Universe and the Propagation of UHECRs*, J. Korean Astron. Soc. **37**.5 (2004) 427–431.

[21] G. Sigl et al., *Ultra-High Energy Cosmic Ray Probes of Large Scale Structure and Magnetic Fields*, Phys. Rev. D **70**.4 (2004), arXiv: astro-ph/0401084.

[22] R. A. Batista et al., *CRPropa: A Public Framework to Propagate UHECRs in the Universe*, EPJ Web Conf. **99** (2015) 13004, arXiv: 1411.2259.

[23] R. A. Batista et al., *Effects of Uncertainties in Simulations of Extragalactic UHECR Propagation, Using CRPropa and SimProp*, J. Cosmol. Astropart. Phys. **2015**.10 (2015) 063–063, arXiv: 1508.01824.

[24] AMS Collaboration, *Precision Measurement of the Boron to Carbon Flux Ratio in Cosmic Rays from 1.9 GV to 2.6 TV with the Alpha Magnetic Spectrometer on the International Space Station*, Phys. Rev. Lett. **117**.23 (2016) 231102.

[25] T. Gaisser, *Challenges for Cosmic-Ray Experiments*, EPJ Web Conf. **145** (2017) 18003, arXiv: 1704.00788.

[26] L. O. Drury, *Galactic Cosmic Rays - Theory and Interpretation* (2017), arXiv: 1708.08858.

[27] O. Adriani et al., *PAMELA Measurements of Cosmic-Ray Proton and Helium Spectra*, Science **332**.6025 (2011) 69–72, arXiv: 1103.4055.

[28] AMS Collaboration, *Precision Measurement of the Helium Flux in Primary Cosmic Rays of Rigidities 1.9 GV to 3 TV with the Alpha Magnetic Spectrometer on the International Space Station*, Phys. Rev. Lett. **115**.21 (2015).

[29] AMS Collaboration, *Observation of the Identical Rigidity Dependence of He, C, and O Cosmic Rays at High Rigidities by the Alpha Magnetic Spectrometer on the International Space Station*, Phys. Rev. Lett. **119**.25 (2017).

[30] AMS Collaboration, *Observation of New Properties of Secondary Cosmic Rays Lithium, Beryllium, and Boron by the Alpha Magnetic Spectrometer on the International Space Station*, Phys. Rev. Lett. **120**.2 (2018).

[31] T. K. Gaisser et al., *Cosmic Ray Energy Spectrum from Measurements of Air Showers*, Front. Phys. **8**.6 (2013) 748–758.

[32] KASCADE Collaboration, *Muon Density Measurements with the KASCADE Central Detector*, Astropart. Phys. **16**.4 (2002) 373–386, arXiv: astro-ph/0103363.

[33] KASCADE Collaboration, *KASCADE Measurements of Energy Spectra for Elemental Groups of Cosmic Rays: Results and Open Problems*, Astropart. Phys. **24**.1-2 (2005) 1–25, arXiv: astro-ph/0505413.

[34] K.-H. Kampert for the KASCADE-Grande Collaboration, *Cosmic Rays in the 'Knee'-Region - Recent Results from KASCADE* - (2004), arXiv: astro-ph/0405608.

[35] EAS-TOP Collaboration, *The Cosmic Ray Primary Composition between 10^{15} and 10^{16} eV from Extensive Air Showers Electromagnetic and TeV Muon Data*, Astropart. Phys. **20**.6 (2004) 641–652.

[36] A. Haungs et al., "High-Energy Cosmic Rays Measured with KASCADE-Grande", *Proc. 33rd Int. Cosmic Ray Conf.* PoS(EPS-HEP2013)398, Rio de Janeiro, Brazil (2013), arXiv: 1308.1485.

[37] A. Hanusch et al., *Acceleration of Cosmic Rays in Supernova Shocks: Elemental Selectivity of the Injection Mechanism* (2018), arXiv: 1803.00428.

[38] M. Unger, *Cosmic Rays above the Knee* (2008), arXiv: 0812.2763.

[39] R. Aloisio et al., *Transition from Galactic to Extragalactic Cosmic Rays*, Astropart. Phys., Cosmic Rays Topical Issue **39-40** (2012) 129–143, arXiv: 1211.0494.

[40] Dmitri Ivanov for the Pierre Auger Collaboration and the Telescope Array Collaboration, "Report of the Telescope Array - Pierre Auger Observatory Working Group on Energy Spectrum", *Proc. 35th Int. Cosmic Ray Conf.* Busan, Korea (2017) PoS(ICRC2017)498.

[41] F. Fenu for the Pierre Auger Collaboration, "The Cosmic Ray Energy Spectrum Measured Using the Pierre Auger Observatory", *Proc. 35th Int. Cosmic Ray Conf.* PoS(ICRC2017)486, Busan, Korea (2017).

[42] V. Verzi et al., *Measurement of Energy Spectrum of Ultra-High Energy Cosmic Rays*, Prog. Theor. Exp. Phys. **2017**.12 (2017) 12A103, arXiv: 1705.09111.

[43] M. Unger for the Pierre Auger Collaboration, "Highlights from the Pierre Auger Observatory", ICRC2017, Busan, Korea (2017), arXiv: 1710.09478.

[44] R. Engel et al., *Extensive Air Showers and Hadronic Interactions at High Energy*, Annu. Rev. Nucl. Part. Sci. **61**.1 (2011) 467–489.

[45] K.-H. Kampert and P. Tinyakov, *Cosmic Rays from the Ankle to the Cut-Off*, Comptes Rendus Phys. **15**.4 (2014) 318–328, arXiv: 1405.0575.

[46] W. Heitler, *The Quantum Theory of Radiation*, 2nd ed., Int. series of monographs on physics, London: Oxford University Press (1944).

[47] J. Matthews, *A Heitler Model of Extensive Air Showers*, Astropart. Phys. **22**.5 (2005) 387–397.

[48] K.-H. Kampert and M. Unger, *Measurements of the Cosmic Ray Composition with Air Shower Experiments*, Astropart. Phys. **35**.10 (2012) 660–678, arXiv: 1201.0018.

[49] J. Linsley, "Proton-Air and Proton-Proton Cross Sections from Air Shower Data", *Proc. 19th Int. Cosmic Ray Conf.* Vol. 6, San Diego, California (1985).

[50] Pierre Auger Collaboration, *Interpretation of the Depths of Maximum of Extensive Air Showers Measured by the Pierre Auger Observatory*, J. Cosmol. Astropart. Phys. **2013**.02 (2013) 026–026, arXiv: 1301.6637.

[51] Eun-Joo Ahn for the Pierre Auger Collaboration, "Inferences about the Mass Composition of Cosmic Rays from Data on the Depth of Maximum at the Auger Observatory", *Proc. 33rd Int. Cosmic Ray Conf.* ICRC2013, Rio de Janeiro, Brazil (2013).

[52] S. Ostapchenko, *Monte Carlo Treatment of Hadronic Interactions in Enhanced Pomeron Scheme: QGSJET-II Model*, Phys. Rev. D **83**.1 (2011).

[53] J. Bellido for the Pierre Auger Collaboration, "Depth of Maximum of Air-Shower Profiles at the Pierre Auger Observatory: Measurements above $10^{17.2}$ eV and Composition Implications", *Proc. 35th Int. Cosmic Ray Conf.* PoS(ICRC2017)506, Busan, Korea (2017).

[54] T. Pierog and K. Werner, *New Facts about Muon Production in Extended Air Shower Simulations*, Phys. Rev. Lett. **101**.17 (2008), arXiv: astro-ph/0611311.

[55] F. Riehn et al., "A New Version of the Event Generator Sibyll", *Proc. 34th Int. Cosmic Ray Conf.* PoS(ICRC2015)558, The Hague, The Netherlands (2015), arXiv: 1510.00568.

[56] Pierre Auger Collaboration et al., *Combined Fit of Spectrum and Composition Data as Measured by the Pierre Auger Observatory*, J. Cosmol. Astropart. Phys. **2017**.04 (2017) 038–038, arXiv: 1612.07155.

[57] R. Engel for the Pierre Auger Collaboration, "Upgrade of the Pierre Auger Observatory (AugerPrime)", *Proc. 34th Int. Cosmic Ray Conf.* PoS(ICRC2015)686, The Hague, The Netherlands (2015).

[58] T. Gaisser, *Cosmic-Ray Showers Reveal Muon Mystery*, Am. Phys. Soc. APS, Physics Viewpoint **9** (2016).

[59] Pierre Auger Collaboration, *The Pierre Auger Cosmic Ray Observatory*, Nucl. Instrum. Methods Phys. Res. Sect. Accel. Spectrometers Detect. Assoc. Equip. **798** (2015) 172–213, arXiv: 1502.01323.

[60] D. Veberič and M. Roth, "Offline Reference Manual: SD Reconstruction", Technical report GAP-2005-035, Pierre Auger Collaboration (2005).

[61] J. Abraham et al., *Trigger and Aperture of the Surface Detector Array of the Pierre Auger Observatory*, Nucl. Instrum. Methods Phys. Res. Sect. Accel. Spectrometers Detect. Assoc. Equip. **613**.1 (2010) 29–39.

[62] K. Greisen, *The Extensive Air Showers*, Prog. Cosm. Ray Phys. **3**.1 (1956).

[63] K. Kamata and J. Nishimura, *The Lateral and the Angular Structure Functions of Electron Showers*, Prog. Theor. Phys. Suppl. **6** (1958) 93–155.

[64] J. Hersil et al., *Observations of Extensive Air Showers near the Maximum of Their Longitudinal Development*, Phys. Rev. Lett. **6** (1961) 22–23.

[65] A. Schulz for the Pierre Auger Collaboration, "The Measurement of the Energy Spectrum of Cosmic Rays above 3×10^{17} eV with the Pierre Auger Observatory", *Proc. 33rd Int. Cosmic Ray Conf.* ICRC2013, Rio de Janeiro, Brazil (2013) 0769.

[66] Pierre Auger Collaboration, *Depth of Maximum of Air-Shower Profiles at the Pierre Auger Observatory: Measurements at Energies above $10^{17.8}$ eV*, Phys. Rev. D **90**.12 (2014), arXiv: 1409.4809.

[67] T. K. Gaisser and A. M. Hillas, "Reliability of the Method of Constant Intensity Cuts for Reconstructing the Average Development of Vertical Showers", *Proc. 15th Int. Cosmic Ray Conf.* Vol. 8, Plovdiv, Bulgaria (1977) 353.

[68] D. Martello for the Pierre Auger Collaboration, "The Pierre Auger Observatory Upgrade", *Proc. 35th Int. Cosmic Ray Conf.* PoS(ICRC2017)383, Busan, Korea (2017).

[69] F. G. Schröder, *Radio Detection of Cosmic-Ray Air Showers and High-Energy Neutrinos*, Prog. Part. Nucl. Phys. **93** (2017) 1–68, arXiv: 1607.08781.

[70] Pierre Auger Collaboration, *Muon Counting Using Silicon Photomultipliers in the AMIGA Detector of the Pierre Auger Observatory*, J. Instrum. **12**.03 (2017) P03002.

[71] Pierre Auger Collaboration, *Prototype Muon Detectors for the AMIGA Component of the Pierre Auger Observatory*, J. Instrum. **11**.02 (2016) P02012, arXiv: 1605.01625.

[72] M. Tanabashi et al., *Review of Particle Physics*, Phys. Rev. D **98** (3 2018) 030001.

[73] O. Wainberg et al., *Digital Electronics for the Pierre Auger Observatory AMIGA Muon Counters*, J. Instrum. **9**.04 (2014) T04003, arXiv: 1312.7131.

[74] B. Wundheiler for the Pierre Auger Collaboration, "The AMIGA Muon Counters of the Pierre Auger Observatory: Performance and First Data", *Proc. 32nd Int. Cosmic Ray Conf.* Vol. 3, Beijing, China (2011) 84.

[75] D. Heck et al., "CORSIKA: A Monte Carlo Code to Simulate Extensive Air Showers", Report FZKA 6019, Forschungszentrum Karlsruhe (1998).

[76] M. Kobal, A. Filipcic and D. Zavrtanik, The Pierre Auger Collaboration, "Thinning of High-Energy Cosmic Ray Air-Showers", *Proc. 8th Int. Conf. on Calorimetry in High Energy Physics (CALOR'99)*, Lisbon, Portugal (1999) 809–816.

[77] P. Billoir, *A Sampling Procedure to Regenerate Particles in a Ground Detector from a "Thinned" Air Shower Simulation Output*, Astropart. Phys. **30**.5 (2008) 270–285.

[78] A. Ferrari et al., *FLUKA: A Multi-Particle Transport Code (Program Version 2005)*, CERN-2005-010 (2005).

[79] K. Werner et al., *Parton Ladder Splitting and the Rapidity Dependence of Transverse Momentum Spectra in Deuteron-Gold Collisions at RHIC*, Phys. Rev. C **74**.4 (2006), arXiv: hep-ph/0506232.

[80] T. Pierog and K. Werner, *EPOS Model and Ultra High Energy Cosmic Rays*, Nucl. Phys. B - Proc. Suppl. **196** (2009) 102–105, arXiv: 0905.1198.

[81] P. D. B. Collins and A. D. Martin, *Hadron Reaction Mechanisms*, Rep. Prog. Phys. **45** (1982) 335.

[82] S. Andringa et al., *The Muonic Longitudinal Shower Profiles at Production*, Astropart. Phys. **35**.12 (2012) 821–827, arXiv: 1111.1424.

[83] N. Kalmykov et al., *Quark-Gluon-String Model and EAS Simulation Problems at Ultra-High Energies*, Nucl. Phys. B - Proc. Suppl. **52**.3 (1997) 17–28.

[84] D. Heck and R. Engel, *The EHISTORY and MUPROD Options of the Air Shower Simulation Program CORSIKA*, KIT-SWP **5** (2009).

[85] S. Ostapchenko, *QGSJET-II: Towards Reliable Description of Very High Energy Hadronic Interactions*, Nucl. Phys. B - Proc. Suppl. **151**.1 (2006) 143–146, arXiv: hep-ph/0412332.

[86] D. Heck and T. Pierog, "Extensive Air Shower Simulation with CORSIKA: A User's Guide (Version 7.6400 from April 20, 2018)", Karlsruhe Institute of Technology.

[87] D. Heck and J. Knapp, "Upgrade of the Monte Carlo Code CORSIKA to Simulate Extensive Air Showers with Energies $> 10^{20}$ eV", 6097B, Forschungszentrum Karlsruhe (1998).

[88] B. Keilhauer et al., *Impact of Varying Atmospheric Profiles on Extensive Air Shower Observation: Atmospheric Density and Primary Mass Reconstruction*, Astropart. Phys. **22**.3 (2004) 249–261.

[89] S. Argiro et al., *The Offline Software Framework of the Pierre Auger Observatory*, Nucl. Instrum. Methods Phys. Res. Sect. Accel. Spectrometers Detect. Assoc. Equip. **580**.3 (2007) 1485–1496, arXiv: 0707.1652.

[90] J. Allen et al., *The Pierre Auger Observatory Offline Software*, J. Phys.: Conf. Ser. **119**.3 (2008) 032002.

[91] R. Bruijn et al., "Study of Statistical Thinning with Fully-Simulated Air Showers at Ultra-High Energies", *Proc. 32nd Int. Cosmic Ray Conf.* Vol. 2, Beijing, China (2011) 39.

[92] S. Agostinelli et al., *Geant4 - a Simulation Toolkit*, Nucl. Instrum. Methods Phys. Res. Sect. Accel. Spectrometers Detect. Assoc. Equip. **506**.3 (2003) 250–303.

[93] F. Sanchez et al., "Efficiency Studies for the Prototype AMIGA Detectors Equipped with Multi-Anode PMTs", Technical report GAP-2016-051, Pierre Auger Collaboration (2016).

[94] B. Wundheiler, "Rayos Cósmicos con Energías entre 10^{17} y 10^{19} eV", PhD thesis: Universidad de Buenos Aires (2013).

[95] D. Ravignani et al., *Reconstruction of Air Shower Muon Densities Using Segmented Counters with Time Resolution*, Astropart. Phys. **82** (2016) 108–116, arXiv: 1606.02531.

[96] W. D. Apel et al., *The KASCADE-Grande Experiment*, Nucl. Instrum. Methods Phys. Res. Sect. Accel. Spectrometers Detect. Assoc. Equip. **620**.2 (2010) 202–216.

[97] D. Newton et al., *The Optimum Distance at Which to Determine the Size of a Giant Air Shower*, Astropart. Phys. **26**.6 (2007) 414–419, arXiv: astro-ph/0608118.

[98] I. C. Maris for the Pierre Auger Collaboration, "The AMIGA Infill Detector of the Pierre Auger Observatory", *Proc. 32nd Int. Cosmic Ray Conf.* ICRC2011, vol. 1, Beijing, China (2011) 267–270.

[99] D. Ravignani and A. D. Supanitsky, *A New Method for Reconstructing the Muon Lateral Distribution with an Array of Segmented Counters*, Astropart. Phys. **65** (2015) 1–10, arXiv: 1411.7649.

[100] A. D. Supanitsky et al., *Underground Muon Counters as a Tool for Composition Analyses*, Astropart. Phys. **29**.6 (2008) 461–470, arXiv: 0804.1068.

[101] B. Efron and R.J. Tibshirani, *An Introduction to the Bootstrap (Monographs on Statistics & Applied Probability)*, Chapman & Hall/CRC (1993).

[102] B. Efron, *Second Thoughts on the Bootstrap*, Statist. Sci. **18**.2 (2003) 135–140.

[103] E. B. Wilson, *Probable Inference, the Law of Succession, and Statistical Inference*, J. Am. Stat. Assoc. (2012).

[104] R. Pesce for the Pierre Auger Collaboration, "Energy Calibration of Data Recorded With the Surface Detectors of the Pierre Auger Observatory: An Update", *Proc. 32nd Int. Cosmic Ray Conf.* ICRC2011, vol. 2, Beijing, China (2011) 214.

[105] H. P. Dembinski and M. Roth, "Constant Intensity Cut Method Revisited: Uncertainty Calculation with the Bootstrap", Technical report GAP-2011-074, Pierre Auger Collaboration (2011).

[106] A. Rivera et al., "On the Energy Dependence of the Constant Intensity Cut", Technical report GAP-2009-123, Pierre Auger Collaboration (2009).

[107] D. Veberič et al., "Constant Intensity Cut: Unbinned Estimation of the Signal Attenuation Function", Technical report GAP-2015-065, Pierre Auger Collaboration (2015).

[108] A. Schulz, "Measurement of the Energy Spectrum and Mass Composition of Ultra-high Energy Cosmic Rays", PhD thesis: Karlsruhe Institute of Technology (2016).

[109] "Realización de Estudios Geológicos Geotécnicos en la Zona de El Sosneado. Malargue Mendoza. Caracterización Básica de Suelos.", Servicio Geológico Minero Argentino, Instituto de Tecnología Minera (2007).

[110] H. Dembinski et al., "Energy Calibration Revisited: The Simplified Likelihood Method", Technical report GAP-2012-090, Pierre Auger Collaboration (2012).

[111] Pierre Auger Collaboration, *Muons in Air Showers at the Pierre Auger Observatory: Mean Number in Highly Inclined Events*, Phys. Rev. D **91**.3 (2015), arXiv: 1408.1421.

[112] A. V. Glushkov et al., *Muon Content of Ultra-High-Energy Air Showers: Yakutsk Data versus Simulations*, JETP Lett. **87**.4 (2008) 190–194, arXiv: 0710.5508.

[113] T. Abu-Zayyad et al., *Evidence for Changing of Cosmic Ray Composition between 10^{17} and 10^{18} eV from Multicomponent Measurements*, Phys. Rev. Lett. **84**.19 (2000) 4276–4279.

[114] Pierre Auger Collaboration, *Testing Hadronic Interactions at Ultrahigh Energies with Air Showers Measured by the Pierre Auger Observatory*, Phys. Rev. Lett. **117**.19 (2016), arXiv: 1610.08509.

[115] R. Engel for the Pierre Auger Collaboration, "Test of Hadronic Interaction Models with Data from the Pierre Auger Observatory", *Proc. 30th Int. Cosmic Ray Conf.* Vol. 4, Merida, Mexico (2007) 111–114, arXiv: 0706.1921.

[116] J. A. Bellido et al., *Muon Content of Extensive Air Showers: Comparison of the Energy Spectra Obtained by the Sydney University Giant Air-Shower Recorder and by the Pierre Auger Observatory* (2018), arXiv: 1803.08662.

[117] Telescope Array Collaboration, *Study of Muons from Ultra-High Energy Cosmic Ray Air Showers Measured with the Telescope Array Experiment* (2018), arXiv: 1804.03877.

[118] Y. A. Fomin et al., *No Muon Excess in Extensive Air Showers at 100-500 PeV Primary Energy: EAS-MSU Results*, Astropart. Phys. **92** (2017) 1–6, arXiv: 1609.05764.

[119] J. G. Gonzalez for the IceCube Collaboration, *Measurement of the Muon Content of Air Showers with IceTop*, J. Phys. Conf. Ser. **718** (2016) 052017.

[120] N. Hayashida et al., *Muons ($\geq$ 1 GeV) in Large Extensive Air Showers of Energies between $10^{16.5}$ eV and $10^{19.5}$ eV Observed at Akeno*, J. Phys. G Nucl. Part. Phys. **21**.8 (1995) 1101.

[121] H. Dembinski for the Working Group on Hadronic interactions and Shower Physics, "Report on Tests and Measurements of Hadronic Interaction Properties with Air Showers", *Proc. Ultra High Energy Cosmic Rays 2018*, UHECR2018, Paris, France (2018).